The formation and evolution of discs around young stars

Daniel Elsender

Submitted by Daniel Elsender to the University of Exeter as a thesis for the degree of Doctor of Philosophy in Physics, March, 2024.

I certify that all material in this thesis which is not my own work has been identified and that any material that has previously been submitted and approved for the award of a degree by this or any other University has been acknowledged.

Signed: 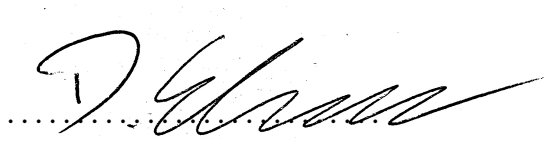

Daniel Elsender

Date: 28/03/2024

Abstract

In this thesis I use three-dimensional radiation hydrodynamic calculations to provide an insight into the properties of protostellar discs, and how their environment can impact them. Through the use of large star-cluster formation calculations, I find some of the ways the metallicity of the molecular cloud can impact discs. The statistical properties of discs formed in one of these calculations match those of observational surveys very well. Motivated by the ability of hydrodynamic calculations to make comparisons with observations I extend the existing numerical methods to model the dynamics of small dust grains in an astrophysical context.

When considering the effects of metallicity on discs I find discs in low metallicity environments tend to be smaller and less well aligned with spin of their protostar. This is due to the low opacity caused by low metallicity and the increased cooling rates because of this. This leads to an enhanced rate of small scale fragmentation. The fragmentation causes an increase in stellar multiplicity and causes the truncation of disc radii.

Using a star-cluster formation calculation at solar metallicity I study the occurrence rate of circumbinary discs. I find that for a given sample of binaries one would expect around 35 per cent of systems to host a circumbinary disc. However, circumbinary discs around binaries with a semi-major axis greater than 100au are predicted to be very rare. I compare the distribution of all known observed of mutual inclination angles between the circumbinary disc and its host binary orbit with those formed in the calculation. The underlying distributions of the two samples are in good agreement.

I have developed an implicit algorithm to model the dynamics of small dust grains. I find this method to be fast, accurate, and avoids several issues there are present with the current dust-as-mixture method in smoothed particle hydrodynamics. This method is applied to dusty discs with an embedded planet. In these calculations, I confirm the discovery of a vertical dust transport mechanism that has only been recently identified by other authors.

Contents

List of Figures

List of Tables

Declaration

This thesis contains work that has been published that was cooperatively written by myself and Matthew R. Bate.

Chapter 3 has been published in *Monthly Notices of the Royal Astronomical Society* , Volume 508, Issue 4, December 2021, Pages 5279–5295.

Chapter 4 has been published in *Monthly Notices of the Royal Astronomical Society*, Volume 523, Issue 3, August 2023, Pages 4353–4364.

Chapter 5 has been accepted by *Monthly Notices of the Royal Astronomical Society* in March 2024 and is currently in press.

Acknowledgements

I am indebted to the guidance of my mentor, Matthew Bate. His advice, wisdom, and great patience he afforded me put me on a path far less difficult to follow had he not been there. The pragmatic approach he takes to solving problems has taught me a great deal about how to be an effective researcher and has given me skills that I will take into wider life. I, and the other members of my office, often found much joy in the visits he would pay when he was overcome with his administrative duties. Over the course of my PhD he has given me the confidence and tools that I have needed, for this I thank him.

I must also thank Tom Bending for his patience with the hundreds of questions I have asked him, academic and otherwise. Also for showing me the proper way to make instant ramen. He is a fantastic human, and it is an honour to be his friend. I am grateful to the refreshingly cheerful Daniel Price for his extensive documentation of SPH, his SPLASH program, and many conversations in Greece. Thank you to my office mates: Ben, Tom, Adrien, and Andy for providing countless hours of distractions and for answering my, sometimes ridiculous, questions. I am grateful to Issy Codron for her commitment to mid-afternoon sweet treat culture and for being a great friend. My friends in Boonk have made life such a joy and have provided a sanctuary away from all things PhD related, at all times of the day.

The Exeter astrophysics group would not function without Emma, who I thank for her unique ability to get things done. And Krisztian for ensuring we have all the computing resources we need at our disposal. I also want to thank the members of the group, there are too many to name, who have made this experience so enjoyable and relaxed.

A huge thank you to my family, my mum, and my sister who have always encouraged me academically when I was growing up. Even though when talking about the subjects I was passionate about they never really understood but they listened anyway. I am fortunate and grateful to have them in my life. A thanks to my grandma who fostered in me a passion for the natural world. To my late father, who taught me so much about life and always encouraged me to surpass my limits, it was a blessing to be his son.

I thank Michelle Fabienne Bieger. She has truly made my time in Exeter a wonderful chapter in my life. She has supported me ferociously, and together we made a home here. I know that all my future endeavours will be made smaller with her in my life. And finally I thank the Bieger family for taking me in as one of their own and welcoming me into their home.

Daniel Elsender

Exeter, U.K.

28th March 2024

Chapter 1

Introduction

"Damn, I had something for this"

— Sterling Archer

1.1 Circumstellar Discs

The formation of circumstellar discs is a natural consequence of the process of star formation due to the conservation of angular momentum. These rotationally supported structures provide a reservoir of material for further star and planet formation. Whilst these discs are a common feature for young stellar objects they exist only for a small fraction of the lifetime of the star, a few million years. It is in this time that the initial diffuse cloud of gas and solids can evolve into entire planetary systems. These discs have long been hypothesised to be associated with the origin of the solar system, theories put forward by René Descartes and Immanual Swedenborg are among the earliest. However, Immanuel Kant and Simon-Pierre Laplace are more often credited as being the originators of such a theory on the formation of the solar system; this theory is referred to as the Nebula Hypothesis. In the following centuries we have been able to detect and observe these discs, first via an excess in infrared emission in their spectral energy distributions (e.g. Aumann et al. 1984; Smith and Terrile 1984; Strom et al. 1989) and then onto direct images of discs (e.g. Beckwith et al. 1984; O'Dell et al. 1993; McCaughrean and O'Dell 1996; McCaughrean et al. 2000). More recently facilities such as the Spectro-Polarimetic High contrast

imager for Exoplanets REsearch (SPHERE) instrument at the Very Large Telescope (VLT) has allowed for images of star light scattered off the disc to be captured (e.g. van Boekel et al. 2017; Avenhaus et al. 2018; Beuzit et al. 2019; Valegard et al. 2024; Garufi et al. 2024). These recent images from SPHERE provide unprecedented detail of circumstellar discs, and their environment. The work of Garufi et al. (2024) is a fantastic example of the abilities of the SPHERE instrument. Whilst SPHERE is a fantastic instrument it only gives us a glimpse of the surfaces of discs as it detects scattered light, and there is no way to see deeper into the disc. The task of looking within the disc itself is more suited to the Atacama Large (sub)Millimetre Array (ALMA). In the past decade ALMA has been the workhouse of disc observations, and has been utilised to study hundreds of circumstellar discs. The instrument works by detecting the thermal emissions of dust grains within the disc, typically grains around one millimetre in size. These grains are thought to mostly exist near the midplane of the disc. In 2014 the poster image of ALMA was released (ALMA Partnership et al. 2015), it did not take long before structures in discs were being observed (Flock et al. 2015; Isella et al. 2016) and even surveys of local star forming regions were being conducted (Ansdell et al. 2016; Long et al. 2018). In the context of discs it is the detection of substructures and population statistics of disc that are the most significant results from ALMA.

1.1.1 Formation

Stars form in relatively diffuse molecular clouds that have angular momentum (Arquilla and Goldsmith 1986; Goodman et al. 1993). As angular momentum is conserved in the collapsing cloud of gas it flattens out into the net angular momentum plane of the cloud, forming a disc. The initial properties of the discs and their evolution are influenced by environmental factors such as stellar radiation, accretion, dynamical interactions with other objects.

Until recently, spatially resolving these discs was difficult and so measurements of disc were taken from inferences derived from unresolved spectral energy distributions (SEDs), the distribution of flux as a function of wavelength. These Young Stellar Objects (YSOs) are divided up into four (or five) classes depending on the form the infrared region

of their SED via

$$\alpha_{\rm IR} \equiv \frac{\Delta \log(\lambda F_\lambda)}{\Delta \lambda}. \tag{1.1}$$

The magnitude of the $\alpha_{\rm IR}$ parameter dictates into which class the YSO is placed into (Lada and Wilking 1984; Lada 1987; Andre et al. 1993). A typical classification scheme looks like this:

1. **Class 0**: undetectable at $\lambda < 10\mu$m, SED peaks in the far-IR.
2. **Class I**: $\alpha_{\rm IR} \geq -0.3$, SED peaks between near- and mid-IR. Sometimes this class is split up further including the flat spectrum sources.
3. **Class II**: $-1.6 \leq \alpha_{\rm IR} \geq -0.3$, SED has a steep slope in near- to mid-IR.
4. **Class III**: $\alpha < -1.6$, SED is essentially that of a stellar photosphere.

The Class 0 objects are the most embedded one, and usually thought to be the youngest and least evolved objects. These clouds are optically thick and so any protostar in the centre is difficult to detect. In the past decade or so, advancements in radio interferometers have allowed us to probe into these objects and even detect discs within them (e.g. Tobin et al. 2012; Yen et al. 2015; Segura-Cox et al. 2016; Aso et al. 2017). The detection of discs in this early stage of star formation implies that discs form rapidly. Numerical models suggest that discs form within a few 10^4 years (Yorke et al. 1993; Machida and Matsumoto 2011; Tsukamoto and Machida 2013), and in some instances even before the star forms, these objects are termed pre-stellar discs (Bate 1998, 2011).

1.1.2 Structure

The study of discs has a rich history with numerous reviews and pedagogical texts which have become very popular sources of fundamental knowledge. Here, I make use of such sources. Specifically, the review of Pringle (1981) and textbook of Frank et al. (1992) which discuss the importance of accretion in astrophysics and provides a good account of the theory required to study discs in astrophysics. Here we give a summary of the main results relevant to this thesis.

1.1.2.1 Vertical structure

Obtaining the structure of a disc via finding a steady state solution to the equations of hydrodynamics and Poisson equation of gravitational potential is not trivial, nor is it guaranteed to be stable (Papaloizou and Pringle 1984). Instead, some assumptions are made to make things more straightforward. Consider an optically thick, low mass ($\simeq 0.01 M_{\rm star}$), geometrically thin disc that is supported by gas pressure. In this case we do not have to worry about the gravity from the disc itself. Then by assuming the disc is vertically isothermal with constant sound speed, the vertical density profile can be found by balancing the force of gravity and pressure. An isothermal disc has sound speed $c_s^2 = k_B T/\mu m_H$ and pressure $P = \rho c_s^2$, where k_B is Boltzmann's constant, T is disc temperature, μ is mean molecular weight, m_H is the atomic mass of hydrogen, and ρ is the gas density of the disc. The condition for vertical hydrostatic equilibrium at height z above the mid-plane of the disc at a radius r is

$$\frac{\mathrm{d}P}{\mathrm{d}z} = -\rho g_z = -\frac{GM_*}{r^2+z^2}\sin(\theta)\rho, \tag{1.2}$$

where G is the gravitational constant, M_* is the stellar mass, and θ is the angle opened between the point that is a height z and a distance r from the central star. For a thin disc $z \ll r$ and substituting in the equation for P, Eq. 1.2 becomes

$$c_s^2 \frac{\mathrm{d}\rho}{\mathrm{d}z} = \frac{GM_*}{(r^2+z^2)^{3/2}} z\rho. \tag{1.3}$$

Keplerian angular velocity in the mid-plane is defined as $\Omega_{\rm K} \equiv \sqrt{GM_*/r^3}$ and so Eq. 1.3 can be written as

$$c_s^2 \frac{\mathrm{d}\rho}{\mathrm{d}z} = -\Omega_{\rm K}^2 \rho z, \tag{1.4}$$

the solution to which is

$$\rho(z) = \rho_0 \exp\left(-z^2/2H^2\right), \tag{1.5}$$

where ρ_0 is the density at the mid-plane and $H \equiv c_s/\Omega_{\rm K}$ is the vertical scale height. By defining the surface density $\Sigma = \int \rho \mathrm{d}z$ the mid-plane density can be written as

$$\rho_0 = \frac{1}{\sqrt{2\pi}}\frac{\Sigma}{H}. \tag{1.6}$$

How does the mass of the disc affect this approximation? Consider an infinite disc, Gauss' theorem states that the gravitational acceleration is independent from height above the mid-plane,

$$g_z = 2\pi G\Sigma, \tag{1.7}$$

this is the contribution from the disc itself. Equating this with the contribution from the stellar host at $z = H$ we see that the stellar gravity dominates if

$$\Sigma < \frac{M_* H}{2\pi r^3}. \tag{1.8}$$

From this we have a regime in which self-gravity of the disc is negligible,

$$\frac{M_{\rm disc}}{M_*} < \frac{H}{2r}, \tag{1.9}$$

where $M_{\rm disc} \sim \pi r^2 \Sigma$. For typical values for circumstellar discs this implies when $M_{\rm disc}/M_* \sim H/r$ our current description of disc vertical structure breaks down and the disc self-gravity must be considered. Typically this is the case when $M_{\rm disc}/M_* \gtrsim 10^{-2}$, in addition to this there is a criterion upon the cooling time scale of the gas disc, when the this timescale is shorter than the orbital timescale a disc is more likely to fragment (Gammie 2001). Given this criterion it is usually cool discs that are susceptible to fragmentation. For a disc orbiting a solar mass star that is accreting at a rate $10^{-6}\mathrm{M}_\odot\ \mathrm{yr}^{-1}$ the temperature at which this instability occurs is $\lesssim$ 20K.

1.1.2.2 Radial structure

Unlike in the vertical direction, the density profile of a disc in the radial direction can not be derived so easily. In particular, the transport of angular momentum must be dealt with. However, with given surface density and temperature profiles we can learn something about the azimuthal velocity of the gas, v_ϕ. Consider the momentum equation of an inviscid fluid

$$\frac{\partial \mathbf{v}}{\partial t} + (\mathbf{v}\cdot\boldsymbol{\nabla})\mathbf{v} = -\frac{1}{\rho}\boldsymbol{\nabla}P - \boldsymbol{\nabla}\Phi, \tag{1.10}$$

where **v** is gas velocity, and Φ is gravitational potential. From the radial component of this, the orbital velocity of the gas is given by

$$\frac{v_\phi^2}{r} = \frac{GM_*}{r^2} + \frac{1}{\rho}\frac{\mathrm{d}P}{\mathrm{d}r}. \tag{1.11}$$

In the above equation the values are for the mid-plane of the disc. However, the pressure in the mid-plane usually decreases with radius meaning the second term on the righthand side is negative; this means the orbital velocity of gas is less than Keplerian. Using fiducial profiles for surface density and temperature of $\Sigma \propto r^{-1}$ and $T \propto r^{-1/2}$ then, $c_s \propto r^{-1/4}$, $\rho \propto r^{-9/4}$ and $P \propto r^{-11/4}$. Substituting and approximating $\mathrm{d}P/\mathrm{d}r \sim -P/r$ into Eq. 1.11 and using $H \equiv c_s/\Omega_\mathrm{K}$ gives,

$$v_\phi = v_\mathrm{K}\left[1 - \frac{11}{4}\left(\frac{H}{r}\right)^2\right]^{1/2} \tag{1.12}$$

where $v_\mathrm{K} = \sqrt{GM_*/r}$. From this we note that the deviation from Keplerian velocity is $O(H/r)^2$. For a thin disc with $H/r = 0.05$ at 1 au the difference between disc azimuthal velocity and Keplerian is about 0.25%. This is small however, this velocity is lower than that of solid bodies, this induces an aerodynamic drag on solids in the disc which can have profound effects. The reason that solids flow at Keplerian velocity is that they do not feel the radial pressure gradient like the gas.

1.1.3 Evolution

From observations we know that discs are not static objects. They change over time, gas is accreted onto the central object, and gas is also dispersed. Yet theoretically, the dominant physical process for disc evolution remains unclear. Considering again a thin, low mass disc, the specific angular momentum is given by

$$l(r) = rv_\phi \approx \sqrt{GM_* r}. \tag{1.13}$$

Note that this is an increasing function with radius, however we know from observations that gas is accreted via the disc, how can this be? There must be some mechanism through

which the disc loses angular momentum. Identifying a dominant mechanism is a central problem in accretion disc physics.

In the classical approach (Lynden-Bell and Pringle 1974; Pringle 1981) the disc is treated as a vertically thin, axisymmetric sheet of viscous fluid. The presence of viscosity allows the gas parcels to transfer their angular momentum and spiral inward toward the central object to be accreted. This approach leads to a relatively simple equation for the evolution of disc surface density $\Sigma(r,t)$. Now, this viscosity is not simply molecular viscosity, the angular momentum transport is too low, but rather the outcome of turbulence in the disc.

Given a surface density $\Sigma(r,t)$, radial velocity $v_r(r,t)$ and angular velocity $\Omega(r)$ the evolution of a flat, circular, thin viscous disc follows from the continuity equation and the azimuthal component of the momentum equation. Consider an annulus of gas with a radial extent between r and $r+\Delta r$, the mass of the annulus is $2\pi r\Delta r\Sigma$ and has angular momentum $2\pi r\Delta r\Sigma r^2\Omega$. The rate of change of the mass of the annulus is equal to the net flow into it,

$$\begin{aligned}\frac{\partial}{\partial t}\left(2\pi r\Delta r\Sigma\right) =& v_r(r,t)2\pi r\Sigma(r,t)\\ &- v_r(r+\Delta r,t)\cdot 2\pi\left(r+\Delta r\right)\cdot\Sigma\left(r+\Delta r,t\right),\end{aligned}$$

in the limit as $\Delta r\longrightarrow 0$ this becomes,

$$r\frac{\partial\Sigma}{\partial t}+\frac{\partial}{\partial r}\left(r\Sigma v_r\right)=0, \tag{1.14}$$

which is the continuity equation. The derivation of the angular momentum is similar, except we must include the transport due to viscous torques $G(r,t)$. We have

$$\begin{aligned}\frac{\partial}{\partial t}\left(2\pi r\Delta r\Sigma r^2\Omega\right) =& v_r(r,t)2\pi r\Sigma(r,t)r^2\Omega(r)\\ &- v_r\left(r+\Delta r,t\right)2\pi(r+\Delta r)\Sigma\left(r+\Delta,t\right)\\ &\cdot(r+\Delta r)^2\Omega(r+\Delta r)+\frac{\partial G}{\partial r}\Delta r,\end{aligned}$$

which in the limit $\Delta r \to 0$ gives

$$r\frac{\partial}{\partial t}\left(\Sigma r^2\Omega\right) + \frac{\partial}{\partial r}\left(r\Sigma v_r r^2\Omega\right) = \frac{1}{2\pi}\frac{\partial G}{\partial r}. \tag{1.15}$$

We have that the rate of change in angular momentum is controlled by the change in surface density due to radial flows and the difference in viscous torques acting on the inner and outer edges of the annulus. For a viscous fluid

$$G(r,t) = 2\pi r\nu\Sigma r^2\frac{\mathrm{d}\Omega}{\mathrm{d}r}, \tag{1.16}$$

where ν is the kinematic viscosity. Using Eq. 1.14 the momentum equation can be simplified to

$$r\Sigma v_r\frac{\mathrm{d}}{\mathrm{d}r}\left(r^2\Omega\right) = \frac{1}{2\pi}\frac{\partial G}{\partial r}, \tag{1.17}$$

under the assumption that $\partial\Omega/\partial t = 0$. Combining this with the continuity equation to get rid of v_r we have

$$r\frac{\partial\Sigma}{\partial t} = -\frac{\partial}{\partial r}\left(\frac{1}{2\pi\left(r^2\Omega\right)'}\frac{\partial G}{\partial r}\right), \tag{1.18}$$

where $(r^2\Omega)'$ denotes the radial derivative. Now, using the assumption of Keplerian angular velocity we have the surface density evolution equation for a geometrically thin disc with internal angular momentum transport

$$\frac{\partial\Sigma}{\partial t} = \frac{3}{r}\frac{\partial}{\partial r}\left(r^{1/2}\frac{\partial}{\partial r}\left[\nu\Sigma r^{1/2}\right]\right). \tag{1.19}$$

This is a diffusion equation for Σ that may or may not be linear depending on the form of ν. If ν is a function of Σ then it is nonlinear. Some headway can be made by assuming that ν is constant. From Eq. 1.19 we have

$$\begin{aligned} r^{1/2}\frac{\partial\Sigma}{\partial t} &= \frac{3\nu}{r}r^{1/2}\frac{\partial}{\partial r}\left(r^{1/2}\frac{\partial}{\partial r}\left[\Sigma r^{1/2}\right]\right) \\ \implies \frac{\partial}{\partial t}\left(r^{1/2}\Sigma\right) &= \frac{3\nu}{r}\left(r^{1/2}\frac{\partial}{\partial r}\right)^2\left(r^{1/2}\Sigma\right). \end{aligned} \tag{1.20}$$

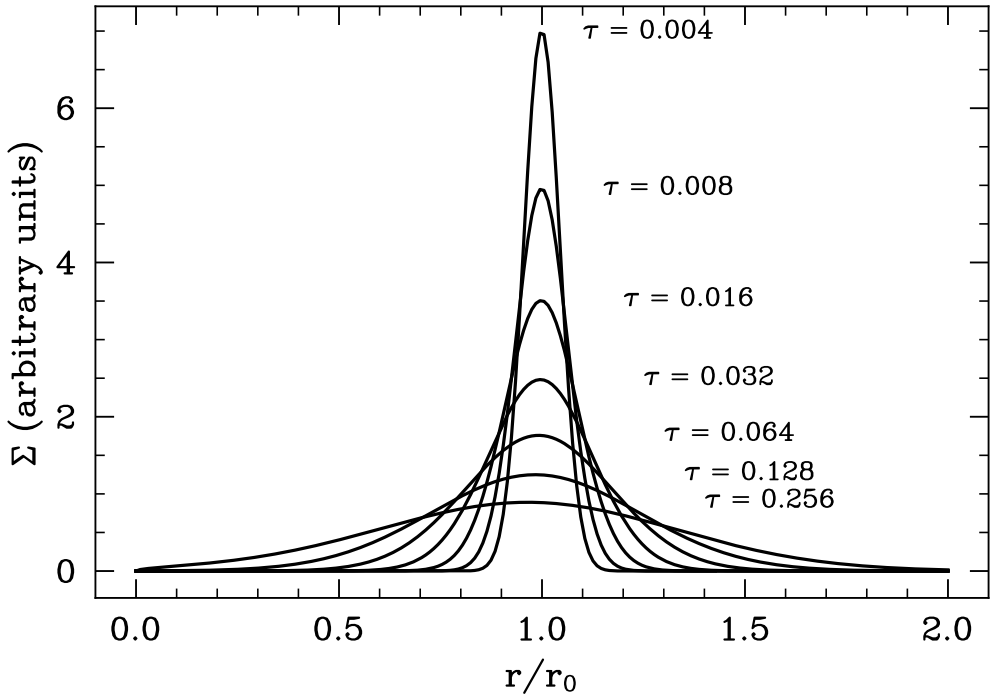

Figure 1.1: Solution to the disc evolution equation with constant ν and increasing τ. It shows the spreading of the initial ring from $r = r_0$.

Now we change variables $X = 2r^{1/2}$ this becomes

$$\frac{\partial}{\partial t}\left(r^{1/2}\Sigma\right) = \frac{12\nu}{X^2}\frac{\partial^2}{\partial X^2}\left(r^{1/2}\Sigma\right), \tag{1.21}$$

and rewriting $r^{1/2}\Sigma = T(t)B(X)$ we have

$$\frac{T'}{T} = \frac{12\nu}{X^2}\frac{X''}{X} = -\lambda^2 = \text{constant}, \tag{1.22}$$

where the functions T and B are exponential and Bessel functions respectively. Using a Green's function solution at time $t = 0$ for gas that lies in a thin rings of mass m and radius r_0

$$\Sigma(r, t = 0) = \frac{m}{2\pi r_0}\delta(r - r_0) \tag{1.23}$$

where $\delta(r - r_0)$ is the Dirac delta function. Using a zero-torque boundary condition at $r = 0$ and allow free-expansion toward $r = \infty$ the solution is expressed as

$$\Sigma(r, t) = \frac{m}{\pi r_0^2}\frac{1}{\tau}x^{-1/4}\exp\left(-\frac{1+x^2}{\tau}\right)I_{1/4}\left(\frac{2x}{\tau}\right), \tag{1.24}$$

where we use dimensionless variables $x = r/r_0$ and $\tau = 12\nu r_0^{-2}t$, and $I_{1/4}$ is a modified Bessel function of the first kind. I plot solutions to Eq. 1.24 at varying τ in Fig. 1.1. As t increases the narrow ring spreads in a diffusive manner on a typical timescale

$$t_{\rm visc} \sim r^2/\nu. \tag{1.25}$$

Whilst this exercise is illustrative we have used a relatively arbitrary choice of viscosity in order to make the mathematics of the problem more straightforward. A more physically motivated approach to dealing with viscosity is that of the α prescription of Shakura and Sunyaev (1973), whereby turbulent motions in the fluid result in the mixing of fluid act as a "turbulent" viscosity. This can be written in the form

$$\nu = \alpha c_s H, \tag{1.26}$$

where H is the scale height of the disc, and α is a dimensionless quantity that measures the efficiency of angular momentum transport due to turbulence. From observations the value of α is estimated to be around $10^{-3}-10^{-2}$ (Hartmann et al. 1998; Andrews et al. 2010b; Rosotti 2023). Angular momentum transport is necessary for the central object to be able to accrete material, of course we know that accretion happens but the question remains as to what this main cause is. The α prescription was devised as a way modelling how turbulence transports angular momentum without saying what the cause of the turbulence is. The source of this turbulence is a controversial topic. One of the proposed sources stems from the interact of the disc with magnetic fields. For a weakly magnetised disc to be linearly unstable the angular velocity must decrease with radius; this is satisfied in a Keplerian disc. This instability is referred to as the magnetorotational instability, this instability had long been known (Chandrasekhar 1961) but only realised in the context of discs by (Balbus and Hawley 1991). In this case small perturbations growth exponentially on dynamic timescales, that leads to self-sustaining turbulence within well ionised discs. But it is exactly this that causes problems for this angular momentum transport mechanism, it is probably not realistic that the entire disc is well ionised and at best they are probably only partially ionised. Along with this and non-ideal magnetohydrodynamics (MHD) effects (in particular Ohmic resistivity) MRI is suppressed in the mid-plane. Another MHD

related mechanism is the layered disc model (Gammie 1996). In this scenario only the active, ionised layer of the disc plays a role in accretion, the surface of the disc is ionised by stellar radiation and cosmic rays, leaving quiescent zones within the disc close to the midplane, which is assumed to have no sources of turbulence. The lack of turbulence in this region will allow dust to settle to the midplane until it creates its own turbulence. In addition to this the quiescent zone causes a bottleneck allowing for the cumulation of gas nearly midplane, leading to higher disc masses at older ages. However, there is no real evidence that these layered discs exist. One other mechanism that has been proposed are so called MHD winds. In this case when a magnetic field threads through a disc a small amount of material is accelerated along the field lines can carried away and a magnetic torque acting on the surface of the disc causes transfer of angular momentum. Given that fields may be weak or discs may not be well ionised, a question remains; can there still be turbulence? Well, yes. If the disc is massive enough for self-gravity to be important then the formation of dense gas clumps due to gravitational instabilities can induce turbulence and transport angular moment away. There are many different, potential, sources of angular momentum transporting turbulence, in reality it is likely a combination of these mechanisms that contribute to angular momentum loss. The broad range of mechanisms are why the α-prescription has been such a successful model. It acknowledges that turbulence is a requirement in angular momentum transport without the practitioner having to worry about its source. But it does not answer the question of where the turbulence comes from.

1.1.4 Dust

Although dust is estimated to be a very small fraction of the mass of circumstellar discs, roughly 1%, it plays an important role in the evolution of discs, the formation of planets, and even observations of discs.

As previously mentioned, solid bodies orbit at Keplerian velocities meaning that they will feel a head wind when in a gas disc. This aerodynamic drag is divided into two regimes defined predominantly by the size of these solids. When the size of the particle is smaller than the mean-free path of the gas molecules in the disc the solid is said to in

the Epstein regime; particles larger than the mean-free path of the gas are in the Stokes regime.

The form of Epstein drag is derived by considering the rate of collisions between the solid particles and gas molecules. Consider a solid, spherical particle of radius s moving at a velocity v relative to the gas. Within the disc the mean thermal speed of gas molecules is

$$v_{\rm th} = \sqrt{\frac{8k_{\rm B}T}{\pi\mu m_{\rm H}}}. \tag{1.27}$$

Assuming a Maxwellian distribution of molecular speeds the drag force acting on solid particles with size $s < \lambda$ and $v \ll v_{\rm th}$ is

$$\mathbf{F}_{\rm D} = -\frac{4\pi}{3}\rho s^2 v_{\rm th}\mathbf{v}. \tag{1.28}$$

For particles that are larger than the mean-free path of the gas, the drag acting on the solids can be expressed in fluid terms where the drag force scales with ram pressure expressed as

$$\mathbf{F}_{\rm D} = -\frac{C_{\rm D}}{2}\pi s^2 \rho v\mathbf{v}, \tag{1.29}$$

where $C_{\rm D}$ is the drag coefficient. When considering non-spherical particles the drag coefficient is not straightforward to assess, however with our assumption of spherical particles $C_{\rm D}$ only depends upon the Reynolds number of the fluid

$$\mathrm{Re} = \frac{2sv}{\nu_{\rm m}}, \tag{1.30}$$

where $\nu_{\rm m}$ is the molecular viscosity of the gas, not the turbulent viscosity of the disc. The standard scaling law of drag coefficient is a piecewise function given by Weidenschilling (1977a)

$$\begin{aligned} C_{\rm D} &\simeq 24\mathrm{Re}^{-1}, \quad \mathrm{Re} < 1 \\ C_{\rm D} &\simeq 24\mathrm{Re}^{-0.6}, \quad 1 \leq \mathrm{Re} \leq 800 \\ C_{\rm D} &\simeq 0.44, \quad \mathrm{Re} > 800. \end{aligned}$$

The two expressions for Epstein and Stokes drag are equivalent if $s = 9\lambda/4$.

A useful parameter to describe the coupling between dust and gas is the stopping time, t_s, which for a spherical particle can be expressed as

$$t_s = \frac{\hat{\rho}_s r_s}{\rho v_{\text{th}}}, \tag{1.31}$$

where $\hat{\rho}_s$ is the density of the particle. The stopping time describes the timescale in which the velocity of solid particles is significantly influenced by the gas.

As previously mentioned the gas orbits more slowly than the solid particles, this difference in velocity has significant implications for the dynamics of solids. One such implication is that of radial drift, realised by Whipple (1972) whereby the headwind felt by solid particles causes them to decelerate and lose angular momentum, spiralling inwards towards the central object. To derive the radial drift speed we consider a disc with a gas orbital velocity as derived in Eq. 1.12. Setting the radial and azimuthal velocities of the particle as v_r and v_ϕ respectively, the equations of motion are

$$\frac{\mathrm{d}v_r}{\mathrm{d}t} = \frac{v_\phi^2}{r} - \Omega_{\text{K}}^2 r - \frac{1}{t_s}\left(v_r - v_{r,\,\text{gas}}\right), \tag{1.32}$$

$$\frac{\mathrm{d}}{\mathrm{d}t}\left(r v_\phi\right) = -\frac{r}{t_s}\left(v_\phi - v_{\phi,\,\text{gas}}\right). \tag{1.33}$$

By assuming the specific angular momentum remains close to Keplerian we have

$$\frac{\mathrm{d}}{\mathrm{d}t} \simeq v_r \frac{\mathrm{d}}{\mathrm{d}r}\left(r v_{\text{K}}\right) = \frac{1}{2} v_r v_{\text{K}}, \tag{1.34}$$

where in this instance v_{K} is defined in Eq. 1.12. The above gives

$$v_\phi - v_{\phi,\,\text{gas}} \simeq -\frac{1}{2}\frac{t_s v_r v_{\text{K}}}{r}. \tag{1.35}$$

Substituting in Ω_K and ignoring higher order terms, yields

$$\frac{\mathrm{d}v_r}{\mathrm{d}t} = -\frac{11}{4}\left(\frac{H}{r}\right)^2 \frac{v_{\text{K}}^2}{r} + \frac{2v_{\text{K}}}{r}\left(v_\phi - v_{\phi,\,\text{gas}}\right) - \frac{1}{t_s}\left(v_r - v_{r,\,\text{gas}}\right). \tag{1.36}$$

From this we obtain the relation

$$v_r = \frac{(r/v_{\rm K})^{-1} v_{r,\,\rm gas} - (11/4)(H/r)^2 v_{\rm K}}{(v_{\rm K}/r)t_s + (r/v_{\rm K})t_s^{-1}}, \tag{1.37}$$

which when written with the Stokes number $\mathrm{St} \equiv t_s \Omega_{\rm K}$ is in the form

$$v_r = \frac{\mathrm{St}^{-1} v_{r,\,\rm gas} - (11/4)(H/r)^2 v_{\rm K}}{\mathrm{St} + \mathrm{St}^{-1}}. \tag{1.38}$$

For particles with $\mathrm{St} \sim 1$ in a disc with the fiducial parameters $\Sigma \propto r^{-1}$, $T_c \propto r^{-1/2}$, and $H/r = 0.03$ the timescale of radial drift at 1 au is one thousand years. This value of Stokes number equates to roughly one metre, this rapid radial drift of metre sized solid objects forms the basis of the "metre-sized barrier", and is a major constraint in planet formation theory.

The above argument is, of course, simplified and excludes turbulence within the disc; this changes the radial transport of solids. Small dust particles that are well coupled with the turbulent gas can diffuse throughout it as well as being advected with the mean gas motion. Consider a disc with surface density of the dust $\Sigma_{\rm d}$, we define the dust to gas ratio as

$$f = \frac{\Sigma_{\rm d}}{\Sigma}. \tag{1.39}$$

If the mass of dust is conserved then

$$\frac{\partial \Sigma_{\rm d}}{\partial t} + \boldsymbol{\nabla} \cdot \mathbf{F}_{\rm d} = 0, \tag{1.40}$$

where $\mathbf{F}_{\rm d}$ is the flux of the dust, this is made up by the advection of dust by the mean gas flow, the diffusion of the dust via turbulence, and radial drift. In the case where gas is vastly more abundant than dust, $f \ll 1$, that the assumption that the gas surface density dominates the diffusive properties of the disc is reasonable and we can write the flux as

$$\mathbf{F}_{\rm d} = \Sigma_{\rm d} \mathbf{v} - D\Sigma \nabla f, \tag{1.41}$$

where $\mathbf{v}$ is the ambient velocity field of the gas disc and D is the turbulent diffusion coefficient (Clarke and Pringle 1988). This can be combined with the mass conservation of Σ

we have the contaminant equation (Morfill and Voelk 1984)

$$\Sigma\left(\frac{\partial f}{\partial t}+\mathbf{v}\cdot\nabla f\right)=\boldsymbol{\nabla}\cdot\left(D\Sigma\nabla f\right). \tag{1.42}$$

In an accretion disc this becomes

$$\frac{\partial f}{\partial t}=\frac{1}{r\Sigma}\frac{\partial}{\partial r}\left(Dr\Sigma\frac{\partial f}{\partial r}\right)-v_r\frac{\partial f}{\partial r}. \tag{1.43}$$

The above is an advection-diffusion equation that describes the evolution of dust to gas ratio. In Chapter 5, I describe a numerical method to solve a diffusion equation for small disc grains in the context of discs around young stars. For a steady disc, away from the boundaries, the radial velocity can be written as (Pringle 1981)

$$v_r=-\frac{3\nu}{2r}. \tag{1.44}$$

1.2 Disc properties

1.2.1 What does theory suggest?

Hydrodynamic simulations are a useful tool in testing the physical models developed to describe astrophysical objects, in the scope of this thesis: discs. Some of the early star formation calculations produced discs (e.g. Tscharnuter 1975; Black and Bodenheimer 1976), although these calculations were axisymmetric. The first calculations, capable of dealing with non-axisymmetric geometries were not until around 20 years later (e.g. Bonnell 1994; Bonnell and Bate 1994; Bate et al. 1995; Whitworth et al. 1995). With greater computational abilities more ambitious star formation calculations were being performed in which entire clusters of stars are being formed (e.g. Bate et al. 2003b; Bate and Bonnell 2005; Bate 2009; Offner et al. 2008; Offner et al. 2009; Bate 2012; Federrath et al. 2014; Cunningham et al. 2018; Lebreuilly et al. 2021). Whilst only few calculations are resolved down to the lengthscales of discs (e.g. Bate et al. 2003b; Bate and Bonnell 2005; Offner et al. 2009) these objects were not the main focus of study. Although most calculations still are not resolved down to the level of the discs themselves, and numerous physical processes are left out

of calculation due to their expense. Some star-formation calculations either zoom in onto selected individual discs (e.g. Kuffmeier et al. 2019) or use 1D disc evolution models (e.g. Qiao et al. 2022). Disc models in 1D are useful to evolve discs over a long period of time and to test certain physics without the expense of simulating a whole disc or when larger simulations do not have the resolution to evolve discs directly, e.g. dust evolution (Birnstiel et al. 2010; Pinilla et al. 2012b; Drążkowska and Alibert 2017; Sellek et al. 2020), planetary migration (Schib et al. 2022), planet formation (Qiao et al. 2023). Given the computational challenges involved in modelling star cluster formation with enough resolution to model the discs that form is it more efficient to simulate discs that form in protostellar collapse (Krumholz et al. 2007; Walch et al. 2010; Joos et al. 2012; Vorobyov et al. 2015) or discs in isolation. Typically, the setup and parameters of discs in isolated calculations are derived from a combination of observations and theory. These calculations fall into two categories; global disc evolution (e.g. Kuffmeier et al. 2021) or local disc evolution where a slice of a disc is simulated (e.g. Ayliffe and Bate 2009a; Bai and Stone 2013).

Calculations of star cluster formation are an important source of data to determine properties of discs. Although as I have mentioned there are relatively few of them. The analysis of Bate (2018) is an early example of protostellar disc synthesis study using a hydrodynamic calculation. The sizes of discs in this study are in very good agreement with observed discs in both Class II and Class 0/I objects. Whilst the masses of discs produced in the calculation are higher than the derived mass of discs from observations they are similar to the masses of discs found in the work of Lebreuilly et al. (2024). In the star cluster formation calculations performed by Wurster et al. (2019) discs of sizes $10 \lesssim r \lesssim 300$au are reported. These calculations include non-ideal MHD. Lebreuilly et al. (2024) performed a suite of star-formation calculations, including MHD, and find a similar distribution of disc sizes to Wurster et al. (2019). They also find that the statistical distribution of disc sizes matches well with observations of the Orion cloud (Sheehan et al. 2022). These works typically find disc masses of <0.01 and 1 $M_{\odot}$. Sellek et al. (2020) found that external photoevaporation can significantly reduced the lifetime of the dust component of young discs, this would inhibit terrestrial planet formation. Additionally, photoevaporation leads to the truncation of discs. Given these results it is important to study the effect of external photoevaporation in star-formation calculations. Wilhelm et

al. (2023) and Qiao et al. (2022) find that most discs are shielded from radiation for at least 0.5 Myr after the formation of the first massive stars. This increases disc lifetimes, allowing for the retention of disc solids potentially aiding planet formation. Gárate et al. (2024) find that if dust is entrained in the photoevaporative winds it may be able to provide a self-shielding effect to the disc.

Many different features of discs and interactions between discs and their environment have been recovered in calculations of star cluster formation; accretion streamers, spirals, arcs, flybys, and warps amongst others. Many of these features are studied in isolation. The SPH calculations of warped α discs of Lodato and Price (2010) agree well with the predictions of Ogilvie (1999). Warps in discs can be responsible for disc tearing (e.g. Nixon and King 2012; Rabago et al. 2023; Young et al. 2023), and features in the dust (Aly et al. 2024). Something that can be done in a calculation that is not possible in observations is knowing the dynamical history of an object. This is useful for studying dynamical encounters such as flybys. Whilst there are a few observations of suspected flybys (e.g Ménard et al. 2020; Dong et al. 2022) they are, like most observations, snapshots in time. There is no way to know the history of these objects. Whereas with calculations we can probe the many effects flybys have upon discs. Breslau et al. (2014) find that discs can be truncated after an interaction with another star. During a flyby, if the perturbing star gets close enough to the outer disc edge it can capture material from the disc. This mass transfer results in a disc forming around the perturber, and also causes significant alteration in the properties of the donor disc (Cuello et al. 2019). Another example of discs interacting with their environments is that of infall. In this scenario material encounters a star after the initial protostellar collapse phase, potentially resulting in a misalignment between inner and out discs or forming second generation disc (Kuffmeier et al. 2021). A key takeaway from star cluster formation calculations is that the process of star-formation is chaotic (Bate et al. 2010) and discs undergo many interactions that have significant impacts upon the evolution of discs and thus the properties of discs. Large star-forming calculations with enough resolution to model discs are a crucial tool in the study of protostellar discs, especially when used in combination with observations.

1.2.2 What do observations tell us?

In order to say something meaningful about the properties of discs, a statistically significant number of observations must be made. Much work has been done to conduct surveys of discs in various different nearby star-forming regions. This has largely been pursued with advent of submillimetre facilities, most notably the Atacama Large (sub)Millimetre Array (ALMA) has been a key instrument in the detection and characterisation of discs (e.g. Huang et al. 2018b; Andrews 2020; Ohashi et al. 2023). The purpose of such surveys are to measure disc masses, sizes, and density profiles in varying environments and evolutionary stages. With such a dataset the dominant physical processes in disc evolution could be worked out.

Given the increasing number of exoplanets being discovered (Gaudi et al. 2021), characterising the objects from which the planets form is fundamental to answering the question of how they formed. The mass of gas and dust from which the Solar System formed is not known, it is, however, possible to derive a lower limit for the amount of material that must have been present during their formation. This is the minimum mass Solar Nebula (Weidenschilling 1977b) and is most commonly taken to be the expression presented by Hayashi (1981),

$$\Sigma(r) = 1.7 \times 10^3 \left(\frac{r}{1\ \mathrm{au}}\right)^{-3/2} \mathrm{g\ cm^{-2}}, \tag{1.45}$$

which when integrated out to 30 au gives $\sim 0.01 M_\odot$. A similar function of the minimum mass of solids required yields a mass of $\sim 1 \times 10^{-4} \mathrm{M}_\odot$. In Fig. 1.2 I plot the gas and dust disc mass from a survey of the discs in Lupus by Ansdell et al. (2016) along with the MMSN values for solids and gas. The mass of dust in a disc is calculated using a relation between it and the sub-millimetre continuum flux at a given wavelength F_ν given by Hildebrand (1983)

$$M_{\mathrm{dust}} = \frac{F_\nu d^2}{\kappa_\nu B_\nu(T_{\mathrm{dust}})}, \tag{1.46}$$

where $B_\nu(T_{\mathrm{dust}})$ is Planck function for a characteristic dust of temperature $T_{\mathrm{dust}} = 20$ K, d is the distance to the star forming region, κ_ν is the dust grain opacity. The calculation of dust mass assume a single grain opacity and dust temperature, this is a big source of un-

certainty for these measurements. There are relatively fewer catalogs of gas disc masses than dust disc masses due to observations in the continuum being less expensive than the spectral line observations required to map gas. Gas masses are trickier to estimate, in this case the line luminosity of ^{13}CO and C^{18}O are compared with the models of Williams and Best (2014). From Fig. 1.2 there appears to be no gas discs with enough mass to satisfy the MMSN. This would leave one to assume that there is not enough mass in discs to form planets, but this deduction is at odds with the occurrence rate of exoplanets. One explanation could be that as these discs are Class II objects and are less massive than at the time of their formation and if planet formation is rapid enough planets may have already formed and all we are detecting is gas left over from this process. Another, more quantifiable, explanation is that the gas masses are underestimated due to the assumptions made during observations: assumptions of optical thinness and disc temperature for example. Recent work by Tung et al. (2024) suggests that dust mass derived from ALMA data may be underestimated by a factor of two, and in the most extreme cases by an order of magnitude. In addition, typical CO tracers might be optically thick causing a systematic underestimation of gas mass, and using an optically thin tracer (e.g. ^{13}C^{17}O, although this is very rare) may a more robust tracer of the gas disc. This has been shown to be the case by Booth et al. (2019) where the gas mass estimate of the disc HD 163269 increases by a factor of 2-6 when using an optically thin tracer.

Using measurements of hundreds of discs in the mm continuum, discs are found to be $\approx 10 - 500$ au in radius and a median radius of $\lesssim 100$ au. Disc radii can calculated via fitted the data to some solution of the steady state disc equation, typically a power-law. The data is fit by minimising some loss function in a Bayesian approach. The model parameters are fit with Monte Carlo Markov Chains converging to a solution (e.g. Tripathi et al. 2017; Tazzari et al. 2017). It is possible that discs may be smaller and that we are seeing a limit due to resolution here. In Fig. 1.3 I have plotted radii of discs taken from the Orion Nebular Cluster (ONC) (Eisner et al. 2018), Ophiuchus and Taurus (Tripathi et al. 2017), Lupus (Tazzari et al. 2017) and the Upper Scorpius OB association (Barenfeld et al. 2017). It is clear that there is variation in the sizes of discs dependent on their environment. In the ONC, for example, stellar density is much higher than the other star forming regions and is in close proximity to the massive star θ^1 Ori C. It is believed that this high stellar density and

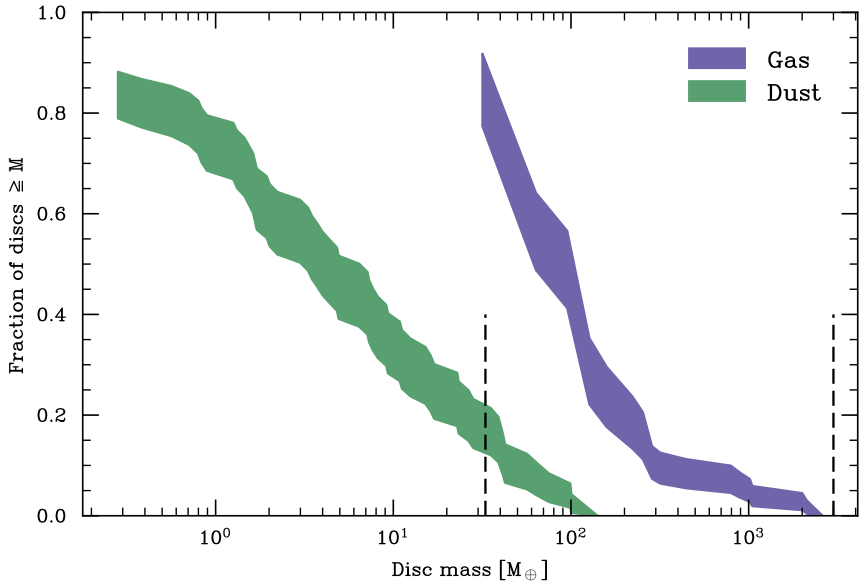

Figure 1.2: Cumulative distribution of disc gas and dust masses taken from the survey of Lupus by Ansdell et al. (2016). The vertical dashed lines indicate the MMSN for solids (left) and gas (right) (Weidenschilling 1977b; Hayashi 1981).

external photoevaporation causes this discs in the ONC to be truncated more than discs in lower density star forming regions (Eisner et al. 2018). Discs that are subjected to external photoevaporation tend to have a comet-like shape, consisting of a bright cusp facing the irradiating source and a tail pointing away from the source, and are termed 'proplyds' (O'Dell et al. 1993; McCaughrean and O'Dell 1996; O'Dell 1998). With the evidence that external photoevaporation influences the evolution of protostellar disc a natural question arises; what other environmental conditions have an effect on the evolution of protostellar discs?

1.2.3 Circumbinary Discs

So far our discussion has only considered discs about a single central object however this is an incomplete picture. Surveys of binary and multiple stellar systems (e.g. Duquennoy and Mayor 1991; Fischer and Marcy 1992; Raghavan et al. 2010; Janson et al. 2012) show that multiplicity is dependent on the mass of the primary star. The multiplicity fraction increases from ≈ 20% for very low mass stars and brown dwarfs, to ≈ 40% for M-dwarfs, and even up to 100% for O-type stars, although the uncertainties for these stars are less well constrained. Binary systems can form via three-body capture, whereby three stars, unbound from each other, pass close to each other and their velocities are significantly

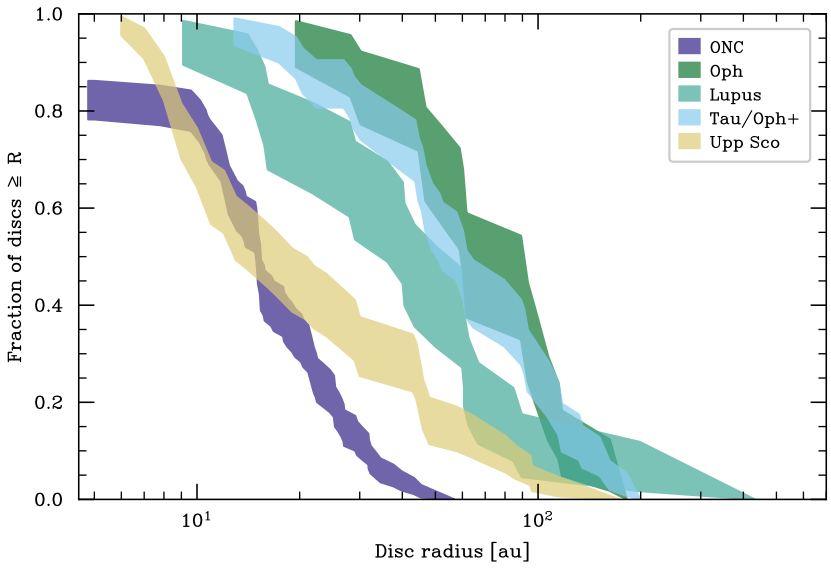

Figure 1.3: Cumulative distributions of the radii of dust discs taken from disc surveys in the Orion Nebula Cluster (Eisner et al. 2018), Ophiuchus (Tripathi et al. 2017), Taurus and Ophiuchus (Tripathi et al. 2017), Lupus (Tazzari et al. 2017), and Upper Scorpius OB association (Barenfeld et al. 2017) regions. Here the distributions are plotted using the Kaplan-Meier estimator to take into account upper limits (unresolved discs) with the shaded region showing a 1σ ($\simeq 68\%$) confidence interval. Adapted from Elsender and Bate (2021).

changed due to their gravitational interactions, and a chaotic dynamical evolution ensues that may result in the formation of a binary system with the excess momentum being carried away by the third star. This process would happen too infrequently to explain the significant binary fraction of stars. In small, dense protostellar groups a similar capture mechanism involving two stars and a circumstellar disc where gravitational perturbations in the disc dissipates some kinetic energy resulting in a binary system. This is possible if the relative velocities of the stars are low, otherwise the second star may just pass by, truncating the circumstellar disc (Clarke and Pringle 1991b, 1991a).

More likely paths to formation are via gravitational fragmentation, either of the collapsing molecular cloud (Boss and Bodenheimer 1979; Boss 1986) or fragmentation of a circumstellar disc (Bonnell and Bate 1994; Bate et al. 1995; Kratter and Matzner 2006). Molecular clouds have been observed to have internal velocity dispersion (Larson 1981) which may lead to non-linear structure in the cloud. If these structures have significant enough density they will collapse faster than the cloud as a whole leading to multiple protostars being formed in a bound system. For disc fragmentation to happen a circumstellar disc must be massive enough and be able to cool faster enough so that it becomes gravitationally unstable. Discs will fragment if $Q < 1$ and if Q is near unity or greater

than it large spiral arms will form, transporting angular momentum outwards. This Q is the Toomre parameter (Toomre 1964) and is defined as $Q = \kappa c_s/(\pi G\Sigma)$ where κ is the epicyclic frequency, c_s is sound speed, and Σ is the surface density of the disc. However, very close binaries, with a semi-major axis of less than 10 au, can not form directly this way (Boss 1986; Bate 1998) due to the opacity limit of fragmentation. Binaries closer than this have likely migrated closer due to dynamical interactions (Artymowicz et al. 1991; Bate et al. 2002). Accretion of material can aid the production of close binaries in two ways. The first being that accretion can directly decrease the separation of the binary orbit if the accreted material does not have a specific angular momentum greater than that of the binary. The second, accretion can destabilise otherwise stable hierarchical multiple systems, forcing the system to undergo dynamical interactions that reduce the binary separation. The orbital evolution of binaries with circumbinary discs has received much attention recently (Miranda et al. 2017; Muñoz et al. 2019; Duffell et al. 2020; Tiede et al. 2020; Heath and Nixon 2020; Zrake et al. 2021; Penzlin et al. 2022; Siwek et al. 2023a). Results from Miranda et al. (2017) suggest than binary systems outspiral during its evolution as accreted angular momentum onto the binary can overcome the disc torques that causes inspiral of the binary. Subsequent studies (Heath and Nixon 2020; Penzlin et al. 2022; Siwek et al. 2023a) have shown that this is only the case when discs are sufficiently thick enough to weaken the torque applied to the disc and sufficiently viscous to allow high mass flow onto the binary causing expansion. The parameters required for the orbit to expand are rather extreme and are not expected to be so common in nature. The orbital evolution is complicated and is a non-trivial function of mass ratio (Duffell et al. 2020; Dittmann and Ryan 2022; Siwek et al. 2023a; Siwek et al. 2023b), eccentricity (Zrake et al. 2021; Siwek et al. 2023b), viscosity (Dittmann and Ryan 2022, 2023), and, as these systems are three dimensional, disc-orbit inclination (Moody et al. 2019; Smallwood et al. 2022; Martin et al. 2024). What is clear this that binary systems are highly dynamic and complicated, and require comprehensive modelling and observations.

Within a binary system discs can form around each stellar object and around the system: circumprimary, circumsecondary, and circumbinary. These discs are truncated by resonances in the system, and a cavity is opened in the circumbinary disc that is related to the semi-major axis of the orbit (Artymowicz and Lubow 1994, 1996). Circumbinary

discs form in a similar way to discs around a single object, whereby infalling gas that has enough angular momentum to form a circular orbit at the distance of the secondary form the centre of mass of the system (Bate and Bonnell 1997).

There are few observations of circumbinary discs relative to discs around single objects. One difficulty arises due to optically thick dust emission that hinders the detection of a companion on scales less than $\lesssim 50$ au in Class 0/I objects (Tobin et al. 2016b). For Class II objects the resolution of the current suite of telescopes remains to be an issue. The typical binary separation is less than the resolution length scale of ALMA in nearby star-forming regions. In addition to this binary systems disrupt parts of their disc, meaning they are not as bright as discs around single objects. All of this means it has not, so far, been possible to gather a statistically significant population of circumbinary discs to learn about their properties, as was the case for circumstellar discs. Typically circumbinary discs are studied as individual objects and as of yet there are few studies on the statistics of circumbinary disc properties. One such study by Czekala et al. (2019) examines the degree of alignment between circumbinary discs and the orbital plane of their hosts. The alignment between circumbinary discs and the orbital plane of the binary, the mutual inclination angle, is defined as

$$\cos\theta = \cos i_{\rm disc} \cos i_* + \sin i_{\rm disc} \sin i_* \cos(\Omega_{\rm disc} - \Omega_*), \tag{1.47}$$

where $i_{\rm disc}$ is the inclination of the disc relative to the line of sight, i_* is similar for the binary orbit, $\Omega_{\rm disc}$ is the longitude of the ascending node, and Ω_* is similar for the binary orbit. The longitude of ascending node can have a degeneracy if the kinematics of the disc is not well constrained and thus two values for the mutual inclination angle is possible. Czekala et al. (2019) show that circumbinary discs can have a large range of mutual inclination angles, with that exception of spectroscopic binaries that typically have a disc that is well aligned with the binary orbital plane.

1.3 Planets in Discs

A central question that is challenging the field of planet formation is; how quickly do they form? The classic theories of planet formation require timescales that may exceed the lifetime of the disc from which they are made. This issue is also connected to the observational problem of discs having a masses lower than the MMSN. We do however know that planets can be formed whilst the disc is still present, for example in the case of PDS 70 (Keppler et al. 2018; Haffert et al. 2019). The most optimistic solution to these inconsistencies is that planet formation is a rapid process. The recent confirmation of the planet TOI-4201b (Delamer et al. 2024) helps to support rapid planet formation based upon the following mass budget and formation efficiency argument. The planet has a mass of $2.59^{+0.07}_{-0.06} M_{\rm J}$, assuming a heavy-element content mass of $\sim 20 M_{\oplus}$ a dust disc mass of $\sim 200 \mathrm{M}_{\oplus}$ would be required, assuming a 10% formation efficiency. Class II disc dust masses around M dwarfs in the Lupus association range from 1 to 50 $\mathrm{M}_{\oplus}$ (Manara et al. 2023), suggesting that the core required to produce a planet such as TOI-4201b must have formed prior to the Class II phase of the disc, under the core accretion model (discussed below). Recent work by Tychoniec et al. (2020) shows that Class 0 discs in the Perseus region have a median dust mass of $158 \mathrm{M}_{\oplus}$, meaning a $\sim$ 15% efficiency would be needed to create the core of TOI-4201b. The dust masses in young systems may contain large enough mass reservoirs to form the seed cores required to form giant planets. During the Class 0/I phase rapid core formation via pebble accretion allows a core massive enough to form within half a million years (Tanaka and Tsukamoto 2019). The rapid formation of these cores could be the answer as to why Class II discs have masses lower than would be expected to form planets: because the planets have already formed.

1.3.1 Giant Planet Formation

When considering the formation of giant planets with substantial gaseous envelopes we must think about the physics of the gas within the protoplanetary disc itself. As it stands there are two dominant theories on the formation of gas giants; the core accretion model, and gravitational instability. The core accretion model first requires a rocky, icy core to have formed, this is in and of itself subject to intense study, that then acquires a gaseous

envelope in three distinct stages. A series of natural questions arise: How quickly can these cores form? What are the barriers to core formation? Gravitational instability requires a massive disc with efficient cooling, this is the same process that takes place for the formation of binaries via gravitational instability.

The core accretion model (Perri and Cameron 1974; Mizuno 1980) relies on a seed cores having already formed, how these cores form is a field in its own right, that are of a mass high enough to trigger a hydrodynamic instability causing the rapid accretion of gas onto it. This critical core mass is of the order $\gtrsim 10M_{\oplus}$. The study of Pollack et al. (1996) exemplifies this model. They consider the formation of Jupiter from a core at a radius of 5.2 au in a disc with a gas surface density of $\Sigma = 700\text{g cm}^{-2}$ and a sold surface density of $\Sigma_p = 10\text{g cm}^{-2}$. In their calculations they use an opacity consistent with a solar mixture of grains that growth of a giant planet in this model happens in three stages:

1. **Core formation**. A core forms due to collisions between solid bodies and runaway accretion of planetesimals. This model assumes a core is already formed. Whilst this core is growing, the mass of the planet envelope remains low and the total mass of the planet is dominated by solids.

2. **Hydrostatic growth**. Once the core has reached its isolation mass, the mass a solid object can attain from the mass reservoir of planetesimals within its vicinity, the envelope begins to contract, as it does so energy is liberated from planetesimals impacting the core and the gravitational potential of the envelope. This energy is transported via radiative diffusion into the surrounding protoplanetary disc. In this phase of growth gas is accreted at a rate faster than that of solid bodies and the planetary envelope mass approaches the mass of the core.

3. **Runaway gas accretion**. Once the envelope mass is greater than that of the core, gas is accreted at a much accelerated rate, limited by the amount of gas the disc can supply.

Fig. 1.4 shows a schematic of the main stages of giant planet formation.

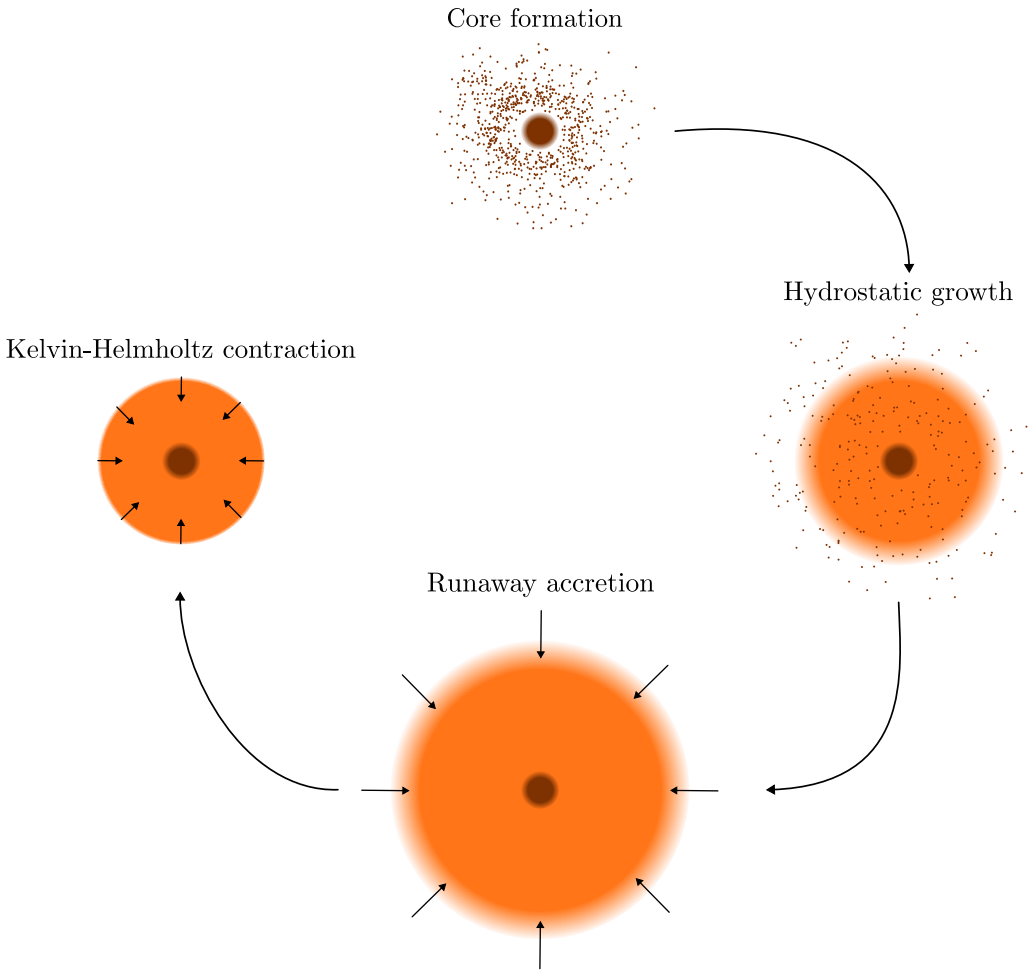

Figure 1.4: The four stages of giant planet formation via the core accretion model.

1.3.2 Interactions with the disc

The study of planet-disc interactions has historically focused on the interactions between planets and the gas discs they are within. This field of study was born from the works of Goldreich and Tremaine (1979, 1980) and Lin and Papaloizou (1979b). Early studies showed that planets migrate inwards when in a disc and can also carve gaps through the gas (Lin and Papaloizou 1986). Planetary migration within a disc is divided into three categories; Types I, II, and III. Type I migration refers to the migration of low mass embedded planets; Type II refers to migration and gap formation by giant planets; Type III refers to rapid migration of intermediate mass planets in relatively massive discs. An issue arises when considering the timescales of migration of planets, they are much shorter than disc lifetimes. In this thesis we consider giant planets and so here I will only focus on Type II migration.

As the mass of a planet increases so does the angular momentum transfer induced by the gravitational interactions with the disc. This transfer of angular momentum can be found by summing over the Linblad resonances (Goldreich and Tremaine 1980), an expression for the rate of angular momentum transfer from the planet to its disc is given by Papaloizou and Lin 1984; Lin and Papaloizou 1986 as

$$\dot{H}_{\rm T} = 0.23 q^2 \Sigma_{\rm p} r_{\rm p}^4 \Omega_{\rm p}^2 \left(\frac{r_{\rm p}}{H}\right)^3, \tag{1.48}$$

where $r_{\rm p}$ is the distance from the centre of the disc to the planet, $\Sigma_{\rm p}$ is the disc surface density in the region of the planet, and H is the thickness of the disc. In order for a planet to carve a gap in the gas disc the torque of the planet acting to open a gap in the disc must be greater than the viscous torque acting to close the gap

$$\dot{H}_{\rm T} \gtrsim \dot{H}_{\nu} \approx 3\pi\nu\Sigma_{\rm p} r_{\rm p}^2 \Omega_{\rm p}. \tag{1.49}$$

This is the case where the tidal torques overcome the that of viscosity. The gaps formed should have a width of at least the Hill radius of the planet. Numerical works in two-dimensions (Bryden et al. 1999; Kley 1999) and three-dimensions (D'Angelo et al. 2002; Bate et al. 2003a) find that only planets with a mass greater then $0.1 M_{\rm J}$ produce perturba-

tions significant enough to open a gap in a disc. The formation of this gap impacts both the growth and migration of the planet. This is because mass can no longer be transferred between the inner and outer regions of the disc as easily as before (Lubow et al. 1999). This affects the migration of the planet and angular momentum is no longer transferred effectively along the spiral arms generated by the planet and the migration of these giant planets is coupled with the viscous evolution of the disc, the timescale of such migration is given by the viscous diffusion timescale of the disc, $\tau_\nu = r_p^2/\nu$. This is the case when the planet has a mass comparable to the local disc. Once the planet is more massive than the local disc the inertia of the planet is enough to slow the migration inwards (e.g Syer and Clarke 1995). It is crucial to note that all of this work is in reference to the interaction between planets and gas discs and, even more pertinent, that most observations of protoplanetary discs are in the continuum , i.e. observations of thermal dust emission, not observations of the gas disc. This is an important distinction as outlined in Section 1.1.4, dust dynamics are different to gas dynamics. Such difference can lead to vastly different structures, for example comparing ^{12}CO emission lines (Huang et al. 2018a; Calahan et al. 2021)and continuum emission (Andrews et al. 2016; Huang et al. 2018a) images of TW Hydrae one significant disparity in not only size, but also in structure. The CO lines trace the gas disc, and show a radial extent of $\sim$ 200 au, whereas in the 870μm continuum there is disc that extends only to around 60 au. Also in the continuum there are substructures that are not present in the gas (Andrews 2020). TW Hydrae is a great example of a disc that has had both its gas and dust disc well studied. It is clear that what we observe in the dust may have little correspondence to the gas disc and vice versa.

In consideration of the dust disc, Paardekooper and Mellema (2004) were the first to simulate low-mass planets opening gaps in dust discs. They found that a planet of mass $0.1 M_J$ can open a gap in the dust but not in the gas, whereas only planets more massive than a Jupiter mass can open gaps in the gas. This gas gap opening dependence on mass is in agreement with the earlier work of Bate et al. (2003a), although this study neglected dust. At the outer edge of the gap cleared in the gas by a massive planet Rice et al. (2006) show that pressure gradients can act as a filter, allowing small grains to pass into the inner disc whilst larger grains remain trapped in the outer disc. Pinilla et al. (2012a) show that millimetre sized grains pile up and accumulate at the outer edge the gas gap in the

pressure bump. Around the same time Ayliffe et al. (2012) showed that the pressure bump at the edge of the gas can trap metre sized solids, allowing to accumulate. Later, Rosotti et al. (2016) found that a gap can be carved in the dust for planets that are able to alter the local gas structure but without creating a pressure maxima. This result was then extended by Dipierro et al. (2016) who provide two mechanisms for opening gaps, and note that a gap in the gas is not a necessary condition for a gap in the dust. The first mechanism is for low-mass planets ($\sim 0.1 M_{\rm J}$) whereby a gap is opened in the dust due to tidal torques with assistance by the drag in the inner disc, without any local perturbations in the radial pressure gradient at the planet location. The second is for massive planets ($\gtrsim 0.5 M_{\rm J}$) that create pressure maxima in the gas, carving a deep gap in the dust and gas. Dipierro and Laibe (2017) provide a criterion for the opening of a gap in the dust based upon balancing the timescales for a gap in the dust to open and to close. They find that the minimum mass to open a gap in the dust is dependent upon the Stokes number of the dust grains.

1.4 The structure of this thesis

This thesis is organised as follows. In chapter 2, I summarise the fundamentals of the numerical method used throughout the thesis in order to study the properties of circmstellar and protoplanetary discs. In chapter 3, I present the analysis of the properties of circumstellar discs formed across four different radiation hydrodynamic calculations of varying metallicity. Here I show how the star-forming environment, in this case the metallicity of the molecular cloud, impacts the formation and evolution of circumstellar discs, and their statistical properties. I compare the results from the calculation with solar metallicity with the properties of discs in local star-forming regions. In chapter 4, I provide statistics of the properties of circumbinary discs that form in a star cluster formation calculation. I calculate the occurrence rate of a given binary system hosting a circumbinary disc as a function of binary separation. In addition to this, I collate all the current known observed circumbinary mutual inclinations and compare the cumulative distribution of observed mutual inclinations with those in the simulation. In chapter 5, I present a new method for solving the dust diffusion equation in the terminal velocity approximation for small dust grain dynamics in SPH. I benchmark this method with the current standard method

in a range of physically motivated and diagnostic tests. Then, in chapter 6, I employ this new method to study the dynamics of small dust grains in the presence of giant planets embedded within protoplanetary discs. Finally, in chapter 7, I summarise the main results of my thesis.

Chapter 2

The Smoothed Particle Hydrodynamics Method

"Man who invented the hamburger was smart; man who invented the cheeseburger was a genius."

— Matthew McConaughey

Smoothed Particle Hydrodynamics (SPH) was initially born out of the drive to study astrophysical problems that do not have spherical symmetry. Indeed it is in this regime where many of the most interesting problems reside. This was the motivation for the invention of SPH, introduced, independently, by both Gingold and Monaghan (1977) and Lucy (1977). The standard way of solving the equations of fluid dynamics is on a grid, computing derivatives via finite difference or finite volumes methods. The grid method has been applied extensively in the context of astrophysics. However, by their very nature, problems in astrophysical fluid dynamics span a vast range in time, space, and density; this requires a great deal of adaptability from numerical methods, something standard grid methods lack. Much effort has been put into solving this issue with the development of adaptive mesh refinement (AMR), though the implementation of this is far from trivial (Springel 2010; Mignone et al. 2012; Stone et al. 2020). In addition to technical difficulties these methods are prone to numerical diffusion due to the grid itself.

The SPH method replaces the grid with a set of particles, which are used as a set interpolation points from which the properties of the fluid can be calculated. It is an intuitive and elegant solution. As SPH is fully Lagrangian the particles move with the density distribution of the fluid as it evolves. This means that SPH has adaptive resolution built into it; denser regions have better resolution and no computational effort is being wasted on regions in which there are no particles. The advantages of this being that no knowledge of which regions will require high resolution is needed beforehand and no complicated mesh refinement needs to take place. SPH also benefits from its ability to use free boundaries (i.e. no fluid can flow 'out' of the computation domain, say for example simulating a disc you may want an accretion boundary and the inner edge but at the outer you are free to not impose any boundary conditions, something that is difficult with grid codes), which crop up in a wide variety of astrophysical problems, with relative ease. All SPH equations can be derived from physical principles with few basic assumptions and it is straightforward to add complicated physics to SPH schemes.

This is not to say that SPH is perfect. Whilst physics is, in principle, straightforward to add into SPH scheme it is often challenging in practice due to numerical issues to do with instabilities. There is an additional computational cost due to the requirement to build neighbour lists. The SPH method which I use in this work uses a binary tree to determine neighbours of particles and to calculate the gravitational forces. The positioning of the particles themselves also causes issues. Initial conditions in SPH are very important and usually require some trial and error to get right, as setups that are not appropriate to the problem can lead to unexpected results. Throughout this thesis I often make use of the reviews of Monaghan (1992) and Price (2012) and the code paper Price et al. (2018b).

2.1 SPH Fundamentals

2.1.1 Interpolation Theory

The basis of SPH is interpolation theory. As mentioned above the points of interpolation are the particles, from which any value can be expressed.

A scalar variable $A(\mathbf{r})$ is defined as

$$A(\mathbf{r}) = \int A(\mathbf{r}')\delta(\mathbf{r} - \mathbf{r}')\mathrm{d}\mathbf{r}' \tag{2.1}$$

where δ is the Dirac delta function. This can be approximated by replacing δ with a smoothing kernel W with a width h where,

$$\lim_{h\to 0} W(\mathbf{r} - \mathbf{r}', h) = \delta(\mathbf{r} - \mathbf{r}'). \tag{2.2}$$

This gives

$$A(\mathbf{r}) = \int A(\mathbf{r}')W(\mathbf{r} - \mathbf{r}')\mathrm{d}\mathbf{r}' + O(h^2) \tag{2.3}$$

where W has the property

$$\int_V W(\mathbf{r} - \mathbf{r}', h)\mathrm{d}V = 1. \tag{2.4}$$

With this Eq. 2.3 can be expressed as a sum over the interpolation points

$$\langle A(\mathbf{r})\rangle = \int \frac{A(\mathbf{r}')}{\rho\mathbf{r}'}W(\mathbf{r} - \mathbf{r}', h)\rho(\mathbf{r}')\mathrm{d}\mathbf{r}' + O(h^2) \tag{2.5}$$

$$\approx \sum_j^{N_{\text{neigh}}} m_j \frac{A_j}{\rho_j}W(\mathbf{r} - \mathbf{r}_j, h), \tag{2.6}$$

where the mass element $\rho\mathrm{d}V$ has been replaced with the mass of the particle m, N_{neigh} is the number of neighbours and j is the neighbour particle index. This summation over discrete points is central to SPH formalism, and can be used to interpolate a quantity $A(\mathbf{r})$ at a point in space $\mathbf{r}$ that is defined in terms of quantities of the particles, e.g. ρ, m. The calculation of gradient terms follows simply by taking the derivative of Eq. 2.5

$$\nabla A(\mathbf{r}) = \frac{\partial}{\partial \mathbf{r}} \int \frac{A(\mathbf{r}')}{\rho(\mathbf{r}')}W(\mathbf{r} - \mathbf{r}', h)\rho(\mathbf{r}')\mathrm{d}\mathbf{r}' + O(h^2), \tag{2.7}$$

$$\approx \sum_j m_j \frac{A_j}{\rho_j}\nabla_i W(\mathbf{r}_i - \mathbf{r}_j, h). \tag{2.8}$$

2.1.2 Smoothing kernels

Any kernel used in SPH must satisfy Eqs. 2.2 and 2.4. The original kernel (Gingold and Monaghan 1977) was the Gaussian and in 3D takes the form

$$W(r,h) = \frac{1}{\pi^{3/2}h^3}\exp\{-q^2\}, \tag{2.9}$$

where $r = |\mathbf{r} - \mathbf{r}'|$, and $q = r/h$. This has the advantage of being spatially everywhere differentiable, which is good for stability. But it also spans the entire spatial domain, which is causes a needless waste of computing time as contributions from particles become rapidly insignificant.

It is far more advantageous to define a kernel with compact support, i.e. a truncation radius. Since Monaghan and Lattanzio (1985) one of the most common kernel is the M4 cubic spline

$$W(r,h) = \frac{\sigma}{h^\nu}\begin{cases} 1 - \frac{3}{2}q^2 + \frac{3}{4}q^3 & \text{if } 0 \le q < 1, \\ \frac{1}{4}(2-q)^3 & \text{if } 1 \le q < 2, \\ 0 & \text{else,} \end{cases} \tag{2.10}$$

where ν is the number of dimensions, and $\sigma = [2/3, 10/7\pi, 1/\pi]$ are the normalisation factors in each dimension. This kernel has compact support over $2h$. Whilst this has the advantage of reduced computation requirements it comes at the cost of reduced accuracy. Usually the cubic kernel is sufficient for most problems in SPH, sometimes a kernel with a larger compact support is needed, for example when including dust in calculations. Such a kernel is the M6 quintic kernel

$$W(r,h) = \frac{1}{120\pi h^3}\begin{cases} (3-q)^5 - 6(2-q)^5 + 15(1-q)^5, & \text{if } 0 \le q < 1, \\ (3-q)^5 - 6(2-q)^5, & \text{if } 1 \le q < 2, \\ (3-q)^5, & \text{if } 2 \le q < 3, \\ 0 & \text{otherwise,} \end{cases} \tag{2.11}$$

this has compact support up to $3h$ and gives virtually identical results as the Gaussian in most problems.

2.1.3 Smoothing length

The term smoothing length refers to the scale over which forces and physical properties of particles are smoothed out over. This is where SPH gets its name, physical properties are smoothed out using a kernel function. A key principle is to keep the number of neighbours that a particle has roughly constant; for the usual cubic spline, for example, this is ≈ 60. This is so that any region of the fluid can be well represented. As a consequence of the Lagrangian nature of SPH keeping the number of neighbours of any given particle roughly constant mean that each particle must have its own smoothing length that is able to vary. The smoothing length of a particle i in 3D can be defined as

$$h_i = \eta \left(\frac{m_i}{\rho_i} \right)^{(1/3)}, \tag{2.12}$$

where η is used to set the number of neighbours for every particle. To obtain about 60 neighbours using a cubic spline $\eta = 1.2$. The choice of value of η is important as it can lead to the pairing instability, where the distribution of particles becomes unstable and particles can fall on top of each other.

2.2 Fluid Equations

Now that the theory of SPH has been laid out the equations of hydrodynamics can be solved. It is pertinent to re-state that SPH is in the Lagrangian frame of reference, as such derivative take the form

$$\frac{\mathrm{d}A}{\mathrm{d}t} = \frac{\partial A}{\partial t} + \mathbf{v} \cdot \boldsymbol{\nabla} A, \tag{2.13}$$

where $\mathbf{v}$ is the velocity of the fluid. This gives the flow rate of a property, A, for a fluid as a function of space and time, opposed to the Eulerian which gives the rate of flow in fixed space.

2.2.1 Continuity equation

Using Eq. 2.6 the density of particle i is

$$\rho_i = \sum_j m_j W_{ij}(h_i). \tag{2.14}$$

Taking the derivative of this yields

$$\frac{\mathrm{d}\rho_i}{\mathrm{d}t} = \sum_j m_j(\mathbf{v}_i - \mathbf{v}_j) \cdot \boldsymbol{\nabla}_i W_{ij}(h_i). \tag{2.15}$$

The continuity equation is the differential form of the conservation of mass of a system defined as

$$\frac{\partial \rho}{\partial t} + \rho \boldsymbol{\nabla} \cdot \mathbf{v} = 0, \tag{2.16}$$

meaning that the rate of change of mass within a fixed volume equals the rate of flow through the boundaries of that volume.

To derive the SPH form of the continuity equation the golden rule of SPH must first be applied, that is to rearrange the continuum equation such that the operators are acting on the density. Applying this golden rule to Eq. 2.16 gives

$$\frac{\partial \rho}{\partial t} + [\boldsymbol{\nabla} \cdot \rho \mathbf{v} - \mathbf{v} \cdot \boldsymbol{\nabla} \rho] = 0. \tag{2.17}$$

Then applying the summation interpolants and rearranging gives

$$\frac{\partial \rho_i}{\partial t} = \mathbf{v}_i \sum_j m_j \cdot \boldsymbol{\nabla} W_{ij}(h_i) - \sum_j m_j \mathbf{v}_j \cdot \boldsymbol{\nabla} W_{ij}(h_i), \tag{2.18}$$

$$= \sum_j m_j(\mathbf{v}_i - \mathbf{v}_j) \cdot \boldsymbol{\nabla}_i W_{ij}(h_i), \tag{2.19}$$

which is identical to Eq. 2.15. Therefore the continuity equation can be replaced by either Eq. 2.14 or Eq. 2.15.

The remainder of the SPH algorithm can be derived from just Eq. 2.14 and the first law of thermodynamics, using a variational principle. This is a wonderful fact as this means that SPH obeys conservation laws exactly.

2.2.2 The Lagrangian

The Lagrangian of hydrodynamics is (Eckart 1960)

$$L = \int \left(\frac{1}{2}\rho v^2 - \rho u\right) \mathrm{d}V, \tag{2.20}$$

where u is the internal energy per unit mass. Applying the summation interpolants to convert this into a SPH equation gives

$$L = \sum_j m_j \left(\frac{1}{2}v_j^2 - u_j(\rho_j, s_j)\right) \tag{2.21}$$

where s is entropy. The equations of motion are given by the Euler-Lagrangian equations for a particle i

$$\frac{\mathrm{d}}{\mathrm{d}t}\left\{\frac{\partial L}{\partial \mathbf{v}_i}\right\} - \frac{\partial L}{\partial \mathbf{r}_i} = 0. \tag{2.22}$$

From this we have

$$\frac{\partial L}{\partial \mathbf{v}_i} = m_i \mathbf{v}_i; \qquad \frac{\partial L}{\partial \mathbf{r}_i} = -\sum_j m_j \left.\frac{\partial u_j}{\partial \rho_j}\right|_{s_j} \frac{\partial \rho_j}{\partial \mathbf{r}_j} \tag{2.23}$$

assuming a constant entropy s (no dissipation). From the first law of thermodynamics

$$\mathrm{d}U = T\mathrm{d}S - P\mathrm{d}V. \tag{2.24}$$

The volume in SPH is not computed directly but estimated by $V = m/\rho$ thus

$$\mathrm{d}V = -\frac{m}{\rho^2}\mathrm{d}\rho, \tag{2.25}$$

$$\implies \mathrm{d}u = T\mathrm{d}s + \frac{P}{\rho^2}\mathrm{d}\rho. \tag{2.26}$$

At a constant entropy this gives the result

$$\left.\frac{\partial u_j}{\partial \rho_j}\right|_{s_j} = \frac{P}{\rho^2}. \tag{2.27}$$

Taking the spatial derivative of the density estimate yields

$$\frac{\partial \rho_j}{\partial \mathbf{r}_i} = \frac{1}{\Omega_j}\sum_k m_k \boldsymbol{\nabla}_i W_{bc}(h_j)\left(\delta_{ji} - \delta_{ki}\right). \tag{2.28}$$

The variability of h across particles needs to be accounted for, as a result we end up with a gradient term for each particle,

$$\Omega_i = 1 - \frac{\partial h_i}{\partial \rho_i} \sum_j m_j \frac{\partial W_{ij}(h_i)}{\partial h_i}, \tag{2.29}$$

where $W_{ij}(h) = W(\mathbf{r}_i - \mathbf{r}_j, h)$. Rearranging and substitution into Eq. 2.22 gives the equation of momentum

$$\frac{\mathrm{d}}{\mathrm{d}t}\{m_i \mathbf{v}_i\} = -\sum_j m_j \frac{P_j}{\Omega_j \rho_j^2} \sum_k m_k \nabla_i W_{jk}(h_b) \left(\delta_{ji} - \delta_{ki}\right), \tag{2.30}$$

upon simplification

$$\frac{\mathrm{d}\mathbf{v}_i}{\mathrm{d}t} = -\sum_j m_j \left(\frac{P_i}{\Omega_i \rho_i^2} + \frac{P_j}{\Omega_j \rho_j^2} \right) \nabla_i W_{ij}(h_i). \tag{2.31}$$

This is the equation of motion in the absence of dissipation and self-gravity. The inclusion of these gives

$$\frac{\mathrm{d}\mathbf{v}_i}{\mathrm{d}t} = -\sum_j m_j \left(\frac{P_i}{\rho_i^2 \Omega_i} \nabla_i W_{ij}(h_i) + \frac{P_j}{\rho_j^2 \Omega_j} \nabla_j W_i j(h_j) \right) + \Pi_{\mathrm{AV}} + \nabla\Phi, \tag{2.32}$$

Π is the artificial viscosity defined in Eq. 2.41, and $\nabla\Phi$ is the acceleration due to self-gravity defined in Eq. 2.39.

2.2.3 Energy equation

The SPH equation for the evolution of internal energy can be simply derived by rearranging Eq. 2.27

$$\frac{\mathrm{d}u_i}{\mathrm{d}t} = \frac{P_i}{\rho_i^2} \frac{\mathrm{d}\rho_i}{\mathrm{d}t}, \tag{2.33}$$

and then taking the time derivative of the density summation to give

$$\frac{\mathrm{d}u_i}{\mathrm{d}t} = \frac{P_i}{\rho_i^2} \sum_j m_j (\mathbf{v}_i - \mathbf{v}_j) \cdot \nabla_i W_{ij}(h_i). \tag{2.34}$$

Taking into account the kernel gradients and dissipation gives and internal energy equation

$$\frac{\mathrm{d}u_i}{\mathrm{d}t} = \frac{P_i}{\Omega_i \rho_i^2} \sum_j m_j (\mathbf{v}_i - \mathbf{v}_j) \cdot \boldsymbol{\nabla}_i W_{ij}(h_i) + \left(\frac{\mathrm{d}u_i}{\mathrm{d}t}\right)^{\mathrm{diss}}, \tag{2.35}$$

I define the contribution to internal energy due to dissipation in Section 2.2.5.

2.2.4 Neighbours and gravity

The reality of finding a particle's neighbour is very computationally expensive and scales as $O(N^2)$ without any optimisation. The code used in this work, SPHNG, uses a binary tree structure originally described in Press (1986) to compute gravity and to find neighbours, this improves efficiency of neighbour finding to $O(N \log N)$. All particles (leaves of the tree) that share a nearest mutual neighbour are paired, the properties of which are combined into a node. All other particles go through the same process until the final two nodes are paired with the root node. To find the neighbours for particle i the tree is walked, ignoring nodes with a sphere of influence that does not fall within the truncation radius of particle i.

The same tree is used to calculate the gravitational force on any given particle. For particles at a distance greater than $2h$ gravitational forces can be computed using the combined contribution of particles, i.e. the nodes themselves. The gravitational forces over these long ranges are calculated using the gravitational monopole and quadrupole terms of distant nodes. All nodes that are within the kernel radius are opened to particle level and the gravitational forces are computed directly. The nodes outside the kernel radius with size to distance ratio $h/r > 0.3$ are opened until their constituent nodes satisfy the criterion $h < 0.3r$. It is an important distinction that SPH particles are not point masses. They are interpolation points that represent a continuous distribution of fluid. Fluid mass contained in overlapping regions represented by these points needs to be accounted for, otherwise the gravitational forces calculated will be too high as this shared mass will counted multiple times. In these cases it is necessary to use a gravitational softening

scheme. The gravitational potential is given by Price and Monaghan (2007)

$$\Phi_i(r) = -G \sum_j m_j \phi(\mathbf{r}_i - \mathbf{r}_j, h_i), \tag{2.36}$$

where ϕ is the softening kernel derived from the density kernel via Poisson's equation. For the cubic spline this is

$$\phi = \int \phi' \mathrm{d}r, \tag{2.37}$$

where

$$\phi' = \frac{4\pi}{r^2} \int_0^r W(r', h) r'^2 \mathrm{d}r'. \tag{2.38}$$

is the force kernel. As a result this adds an additional term onto the equations of motion (see Section 2.2.2)

$$\boldsymbol{\nabla}\Phi_i = -G \sum_j m_j \left[\frac{\phi_{ij}(h_i) + \phi_{ij}(h_j)}{2} \right] \mathbf{r}_{ij} - \frac{G}{2} \sum_j m_j \left[\frac{\zeta_i}{\Omega_i} \boldsymbol{\nabla}_i W_{ij}(h_i) + \frac{\zeta_j}{\Omega_j} \boldsymbol{\nabla}_i W_{ij}(h_j) \right], \tag{2.39}$$

where ζ is the gradient of variable softening length

$$\zeta_i = \frac{\partial h_i}{\partial \rho_i} \sum_j m_j \frac{\partial \phi_{ij}(h_i)}{\partial h_i}. \tag{2.40}$$

The first term in Eq. 2.39 is the softened force due to gravity and the second term is required to conserve energy in the presence of smoothing length gradients.

2.2.5 Artificial viscosity

The presence of shocks in numerical hydrodynamics leads to discontinuities in the fluid as the numerical method can not resolve down to the scale of the mean free path of the gas. In a real fluid kinetic energy is dissipated into heat due to an inherent viscosity. As this viscosity can not be resolved by the numerical method but must be accounted for, an artificial viscosity is included. Viscous terms are added to the fluid equations as was suggested by Von Neumann and Richtmyer (1950). In SPHNG the formulation described

by Monaghan (1997b) is employed as

$$\Pi_{ij} = -\sum_j \frac{m_j}{\rho_{ij}^2}\left[\frac{q_{ij}^i}{\Omega_i}\nabla_i W_{ij}(h_i) + \frac{q_{ij}^j}{\Omega_j}\nabla_j W_{ij}(h_j)\right], \tag{2.41}$$

where ρ_{ij} is the mean density of particles i and j and q_{ij}^i is defined as

$$q_{ij}^i = \begin{cases} -\frac{1}{2}\rho_i v_{\mathrm{sig},i}\mathbf{v}_{ij}\cdot\mathbf{r}_{ij}, & \mathbf{v}_{ij}\cdot\mathbf{r}_{ij} < 0 \\ 0, & \text{else,} \end{cases} \tag{2.42}$$

where signal velocity $v_{\mathrm{sig},i}$ is

$$v_{\mathrm{sig},i} = \alpha_i^{\mathrm{AV}} c_{\mathrm{s},i} + \beta_{\mathrm{AV}}\left|\mathbf{v}_{ij}\cdot\mathbf{r}_{ij}\right|, \tag{2.43}$$

and α_i^{AV} is varied according to the Morris and Monaghan (1997) viscosity switch between $[0.1, 1]$ and $\beta_{\mathrm{AV}} = 2$. The artificial viscosity parameter can be related to the Shakura and Sunyaev α_{SS} in a disc via (Lodato and Price 2010)

$$\alpha_{\mathrm{SS}} \approx \frac{\alpha^{\mathrm{AV}}}{10}\frac{\langle h\rangle}{H}, \tag{2.44}$$

where $\langle h\rangle$ is the mean smoothing length on particles within a cylindrical ring at a given radius.

The β_{AV} term provides provides a second-order Von Neumann & Richtmyer like term that prevents particle interpenetration by dissipating the kinetic energy of particle moving towards each other as heat. The β term is very important in the context of accretion discs where a low α is applied in the absence of shocks. The contribution to the internal energy is given by Price et al. (2018b) as

$$\left(\frac{\mathrm{d}u_i}{\mathrm{d}t}\right)^{\mathrm{diss}} = -\frac{1}{\Omega_i\rho_i}\sum_j m_j v_{\mathrm{sig},i}\frac{1}{2}\left(\mathbf{v}_{ij}\cdot\hat{\mathbf{r}}_{ij}\right)^2 F_{ij}(h_i), \tag{2.45}$$

where $\hat{\mathbf{r}}_{ij}F_{ij} = \nabla_i W_{ij}$.

2.3 Time stepping

2.3.1 Time integration

The SPHNG code uses a second-order Runge-Kutta-Fehlberg integrator (Fehlberg 1969) to evolve the difference equations to be solved. In this scheme the first step is to evaluate the rate of change quantity $\mathbf{A}$

$$k_0 = \dot{\mathbf{A}}(t_n, \mathbf{A}_n), \tag{2.46}$$

where n denotes the timestep counter. The quantity $\mathbf{A}_n$ is predicted at a half timestep $\mathbf{A}_{n+1/2}$ and the derivatives are re-evaluated as

$$k_1 = \dot{\mathbf{A}}\left(t_n + \frac{\Delta t}{2}, \mathbf{A}_{n+1/2}\right), \tag{2.47}$$

k_1 is the predicted gradient of $\mathbf{A}$ at a half timestep. An improved estimate of the derivatives are calculated using a weighted average of k_0 and k_1, this additional accuracy is why the Fehlberg intergrator is second-order even though strictly speaking it is a first-order integrator. The result is

$$\mathbf{A}_{n+1} = \mathbf{A}_n + \left(\frac{1}{256}k_0 + \frac{255}{256}k_1\right)\Delta t. \tag{2.48}$$

2.3.2 Setting timesteps

An essential constraint in any numerical differential equation solver is to satisfy the Courant-Friedrichs-Lewy (CFL) condition, which determines the hydrodynamic timestep. The CFL timestep is defined as

$$\Delta t_{\rm CFL} = C_{\rm CFL}\left(\frac{h}{v_{\rm sig}}\right) \tag{2.49}$$

where $v_{\rm sig}$ is the signal velocity and $C_{\rm CFL}$ is the Courant number, set to 0.3 in SPHNG.

In addition to the CFL constraint there is also a force constraint which is calculated from the ratio of smoothing length to acceleration magnitude $|\mathbf{a}|$

$$\Delta t_{\rm F} = C_{\rm F}\sqrt{\frac{h}{|\mathbf{a}|}} \tag{2.50}$$

where C_F is set to 0.3. Under this condition particles with a high acceleration are given shorter timesteps to maintain accuracy.

In a purely hydrodyanamical calculation these two conditions suffice. When adding in additional physics there may be a requirement to include additional constraints on the timesteps. The timestep for a particle i is set by taking the minimum value of all timestep constraints that are necessary, for example in the purely hydrodynamical case

$$\Delta t_{\min} = \min\left(\Delta t_{\rm CFL}, \Delta t_{\rm F}\right). \tag{2.51}$$

2.3.3 Individual timesteps

To save on computational expense all particles are each given their own timesteps (Bate 1995) . For particles in low density regions it is sufficient to take long timesteps to achieve the required numerical accuracy, whereas for particles in high density regions short timesteps are needed. In practice individual particle timesteps are set into timestep bins. In advance of a calculation a maximum timestep, $\Delta t_{\rm max}$, is chosen and divided by powers of two, upto 2^{30} meaning that the smallest timestep bin is $\approx 10^9$ times smaller than $\Delta t_{\rm max}$. In addition to this particles that share a timestep are evolved together along with particles with other timesteps if they are smaller or if they are a multiple of their timestep.

2.3.4 Sink particles

As density increases, timesteps decrease. At the point when a protostar forms calculations effectively stop due to the very small timesteps required at the location of the protostar. As the interiors of these objects are not of interest in calculations studying discs, all the particles that make up the protostar are replaced by a single, non-gaseous, massive particle with the combined mass, linear momentum and spin of the particles it replaces. Infalling material can be accreted by the particle, alleviating the need for small timesteps. This massive particle is referred to as a sink particle (Bate et al. 1995). The idea has been use previously in finite-difference grid codes to study collapsing clouds past the point of protostellar core formation (Boss and Black 1982; Boss 1987), however these central cells were fixed, the sink particles in SPH can move around.

The sink particles interact with other particles only via gravity. Particles that come within a certain radius of the sink particle, $r_{\rm acc}$ may be accreted if some criteria are satisfied. The accretion radius is set before a calculation is begun and remains at that value throughout the calculation, the accretion radius is not dependent upon the mass of the sink; of course a practitioner would set the accretion radius to a sensible size. Typically an accretion radius is set depending on the resolution desired about a sink particle. The first criterion of accretion is that a particle must be bound to the sink. Second, the specific angular momentum of the particle must be less than required for it to form a circular orbit at the accretion radius about the sink. Finally, the particle must be more tightly bound to that sink than to other sink particles.

2.3.5 Planets with surfaces

In this thesis I make use of the planetary model of Ayliffe and Bate (2009b). In this setup, planetary cores are modelled with a gravitational potential. The method of Ayliffe and Bate (2009b) has been adapted to allow for the use of a gravitational potential to be used in a global disc simulation rather than in a disc section. The main benefit of this model that accretion can be modelled down onto the planet core, allowing the formation of a planetary atmosphere. In order to build this gas atmosphere, gravity is modified near the planet surface. The gravitational potential approaching the surface from outside gradually shallows, and then rapidly increases inside this surface to prevent particle penetration. The gravitational force take the form

$$F_r = -\frac{GM_{\rm c}}{r^2}\left(1 - \left(\frac{2R_{\rm p} - r}{R_{\rm p}}\right)^4\right), \tag{2.52}$$

for $r < 2R_{\rm p}$ where r is the radius from the centre of the planetary core, $R_{\rm p}$ is the radius of the planet core, and $M_{\rm c}$ is the core mass. This results in a net zero force between a particle and the planet core at a radius of $R_{\rm p}$. Inside the core radius the force is outwards and increases with decreasing radius. As a result, particles come to rest close to the core radius. As more particles become bound to the planet core they layer upon top of the inner layer of particles, this gradually forms the planetary atmosphere. Using this method allows for natural growth of a planet, self-gravity, and radiative transfer.

2.3.6 Radiative transfer

With the inclusion of radiative transfer the equations of hydrodynamics must be reformulated. This work uses the flux-limited diffusion of Whitehouse et al. (2005), their method implements the radiation hydrodynamics equations of Mihalas and Mihalas (1984). In solving the radiation hydrodynamic equations it is useful to redefine the specific gas energy into the gas energy density, $e = u\rho$. In the formulation the continuity equation remains the same as in hydrodynamics. The momentum equation now must include radiation pressure

$$\rho \frac{D\mathbf{v}}{Dt} = -\nabla P + \frac{\chi_{\rm F}\rho}{c}\mathbf{F}, \tag{2.53}$$

where $\chi_{\rm F}$ is the flux mean total opacity, and $\mathbf{F}$ is the momentum density flux. The time dependence of the radiation energy density is

$$\rho \frac{D}{Dt}\left(\frac{E}{\rho}\right) = -\boldsymbol{\nabla}\cdot\mathbf{F} - \nabla\mathbf{v} : \mathbf{P} + 4\pi\kappa_{\rm P}\rho B - c\kappa_{\rm E}\rho E, \tag{2.54}$$

where $\kappa_{\rm P}$ and $\kappa_{\rm E}$ are the Planck mean and energy mean absorption opacities, respectively, B is the Planck function, and E is the radiation energy density. The first and second terms on the right hand side are the diffusion of the radiation flux and the work done on the radiation field. The third and fourth terms are the interaction between the radiation and gas fields. The evolution of the gas energy is as follows

$$\rho \frac{D}{Dt}\left(\frac{e}{\rho}\right) = -P\boldsymbol{\nabla}\cdot\mathbf{v} - 4\pi\kappa_{\rm P}\rho B + c\kappa_{\rm E}\rho E. \tag{2.55}$$

The SPH implementation of these equations and the method used to solve them can be found in the work of Whitehouse et al. (2005). In addition to this, the work presented makes use of the thermal evolution model of Bate and Keto (2015) to allow for more accurate treatment of thermal behaviour of molecular clouds at low densities and metallicities. This is done by combining a model of the thermodynamics of a diffuse ISM with radiative transfer in the flux-limited approximation of Whitehouse et al. (2005).

The method I have discussed is applied is perform four star-formation calculations which are then analysed in Chapter 3 in order to extract the properties of protostellar

discs. Additional details of the SPH method are discussed in that chapter, these details are not essential to the SPH method but are required for the physics that is simulated. In Chapter 5 I detail the dynamics of small dust grains in SPH.

Chapter 3

The statistical properties of protostellar discs and their dependence on metallicity

"There are lies, damned lies, and statistics"

— Mark Twain

The formation and evolution of protostellar discs is a key element in the understanding of both star and planet formation. Discs form due to the conservation of angular momentum and dissipation of energy during protostellar collapse. Prior to the advent of interferometers with sub-arcsecond resolution at (sub)-millimetre wavelengths there were relatively few direct images of discs (e.g. Beckwith et al. 1984; O'dell et al. 1993; McCaughrean and O'dell 1996; see the review of McCaughrean et al. 2000). But with radio telescope arrays such as, the Submillimetre Array (SMA), the Atacama Large Millimetre Array (ALMA), and the Very Large Array (VLA), we can now look deep into star-forming regions to resolve many protoplanetary discs. These interferometers have even allowed us to observe discs of embedded Class 0 and I protostars (e.g. Lee et al. 2009; Tobin et al. 2012; Yen et al. 2013; Segura-Cox et al. 2016; Aso et al. 2017; Yen et al. 2017; Tychoniec et al. 2018; Tobin et al. 2020).

With the currently growing catalogue of observed discs it is a good time to compare observed discs with those produced in hydrodynamical calculations. The first such comparison of properties of a large sample of discs formed in a hydrodynamical simulation of a star cluster formation was Bate (2018) who analysed the discs that were formed in the solar-metallicity calculation first published by Bate (2012). Bate studied the large diversity of discs (e.g. disc morphologies, evolutionary processes of discs) and the statistical properties of the discs such as their mass, radii, and disc orientations of bound protostellar pairs. This paper extends this first study to examine the effect metallicity has on the properties of discs.

The radiation hydrodynamical calculations from which we extract the statistics of disc properties were published by Bate (2019) who studied the statistical properties of protostars and their dependence on metallicity. This surpassed the work of Bate (2014) by including additional physical processes (Bate and Keto 2015) to better model low density gas. It is not just opacity that changes with metallicity. In previous star formation calculations dust and gas temperatures were usually assumed to be identical (e.g. Bate 2009; Offner et al. 2009; Bate 2012; Krumholz et al. 2012; Myers et al. 2013; Bate 2014; Cunningham et al. 2018). This is a reasonable approximation when the gas density and/or metallicity are high (e.g. hydrogen number density, $n_{\rm H} > 10^5$ cm^{-3} for solar metallicity; Burke and Hollenbach 1983; Goldsmith 2001; Glover and Clark 2012a). However, at low densities and/or low metallicities the dust and gas temperatures can become uncoupled (Omukai 2000; Tsuribe and Omukai 2006; Dopcke et al. 2011; Nozawa et al. 2012; Chiaki et al. 2013; Dopcke et al. 2013) and gas temperatures are typically higher than dust temperatures (e.g. Glover and Clark 2012b). Only changing the opacity may poorly model star formation as fragmentation and gas accretion rates depend on gas temperature. Improvements to thermal modeling at low densities and metallicities by combining radiative transfer with a thermochemical model of the diffuse ISM were developed by Bate and Keto (2015), see Section 3.1 for further details.

In this chapter, I report the statistical properties of discs from the four radiation hydrodynamical calculations of star cluster formation by Bate (2019) that employ the radiative transfer/diffuse ISM method of Bate and Keto (2015). The calculations have iden-

tical initial conditions except for their metallicity. They have 0.01, 0.1, 1 and 3 times solar metallicity. As each of the molecular clouds collapse, discs form around protostars and I examine the statistical properties of samples of these discs to determine the dependence of disc properties on metallicity. In Section 3.1 I briefly outline the method and initial conditions that were used to perform the calculations. In Section 3.2 I first present an overview of the previous statistical study of discs by Bate (2018), and I then report the new results. In Section 3.3 I provide a discussion of observed disc properties and compare them with the properties of the discs that form in the solar metallicity calculation. Finally, in Section 3.4, I give the conclusions of this study.

3.1 Method

The radiation hydrodynamical calculations analysed in this chapter were previously reported in Bate (2019), but they did not analyse protostellar disc properties. For a complete description of the calculations, see Bate (2019). Here I only provide a brief summary of the method and the physical processes that were included.

3.1.1 Base SPH method

The calculations were performed using the smoothed particle hydrodyanmics (SPH) code, `sphNG`, based on the original version by Benz (1990) and Benz et al. (1990), but substantially modified by Bate et al. (1995), Price and Monaghan (2007), Whitehouse et al. (2005), and Whitehouse and Bate (2006), and parallelised using both `OpenMP` and `MPI`.

Gravitational forces between particles and a particle's nearest neighbours are calculated using a binary tree. The smoothing lengths of particles are allowed to vary in time and space and are set such that the smoothing length of each particle $h = 1.2(m/\rho)^{1/3}$, where m and ρ are the SPH particle's mass and density, respectively (see Price and Monaghan 2007). A second-order Runge-Kutta-Fehlberg method (Fehlberg 1969) is used to integrate the SPH equations, with individual time-steps for each particle (Bate et al. 1995). The artificial viscosity given by Morris and Monaghan (1997) is used with α_v varying between 0.1 and 1 while $\beta_v = 2\alpha_v$ (see Price and Monaghan 2005).

3.1.2 Radiative transfer and diffuse ISM model

To treat the thermodynamics the calculations used a method developed by Bate and Keto (2015) to combine radiative transfer and a diffuse ISM model. Here I only give a brief overview of the physics involved in the calculations, the reader is directed to that paper for further details.

An ideal gas equation of state is used for the gas pressure $p = \rho T_{\rm g} \mathcal{R}/\mu$, where $T_{\rm g}$ is gas temperature, μ is the mean molecular weight of the gas (initially set to $\mu = 2.38$), and $\mathcal{R}$ is the gas constant. Translational, rotational, and vibrational degrees of freedom of molecular hydrogen are taken into account in the thermal evolution. Additionally, molecular hydrogen dissociation and the ionisation of hydrogen and helium are included, with the mass fractions $X = 0.70$ and $Y = 0.28$ for hydrogen and helium, respectively. The contributions of metals to the equation of state are neglected.

Gas, dust, and radiation fields have separate temperatures with the thermal evolution combining radiative transfer in the flux-limited diffusion, described by Whitehouse et al. (2005) and Whitehouse and Bate (2006), with a diffuse ISM model similar to that described by Glover and Clark (2012b) although with much simplified chemical evolution. The dust temperature assumes local thermodynamic equilibrium with the total radiation field and accounts for thermal energy exchanged between the dust and gas during collisions. The calculations used dust-gas collisional energy transfer rates given by Hollenbach and McKee (1989).

Various heating and cooling mechanisms for gas are implemented. Heating by direct collisions with cosmic rays, indirect heating via hot electrons from dust grains due to the photoeletric effect by photons from the interstellar radiation field (ISRF), and heating from molecular hydrogen forming on dust grains are included. The ISRF used is in the form of Zucconi et al. (2001), adapted to include the UV component from Draine (1978) in the energy range $h\nu = 5 - 13.6$eV. Cooling by electron recombination, atomic oxygen and carbon fine structure cooling, and molecular line cooling are included.

The simple chemical model of Keto and Caselli (2008) is used to compute the abundances of C+, C, CO, and the depletion of CO on to dust grains. The carbon chemistry

model is kept very simple but aims to capture the most important thermodynamic behaviour at low gas density. The model of Keto and Caselli (2008) includes the photoelectric effect and allows for both cooling from C^+ at low-densities and treat the depletion of CO at higher densities as they are the primary coolants of gas in their respective density regimes. No other carbon chemistry is calculated in their model. The abundance of atomic oxygen is assumed to scale proportional to $(1 - \mathrm{CO/C})$. The molecular hydrogen formation and dissociation rates used to compute the abundance of atomic and molecular hydrogen are the same as used by Glover et al. (2010).

Opacity is set according to the tables of Pollack et al. (1985) at low temperatures when dust is present and it is assumed opacity scales linearly with metallicity. At higher temperatures the tables of Ferguson et al. (2005) are used with $X = 0.70$, covering heavy element abundances from $Z = 0$ to $Z = 0.1$; the solar abundance is taken to be $Z_\odot = 0.02$. Dust properties may change with different metallicity (e.g., Rémy-Ruyer et al. 2014) but these are not taken into account (see Bate 2019 for further discussion).

3.1.3 Sink particles

During each calculation the protostellar collapse is followed into the second collapse phase caused by the dissociation of molecular hydrogen (Larson 1969). The timesteps become increasingly small, so sink particles (**bate_sphng_1995MNRAS.277..362B**) are inserted after the gas density exceeds 10^{-5} g cm^{-3}. All SPH particles within $r_{\rm acc} = 0.5$ au of the densest particle are replaced by a sink particle with the same combined mass and momentum. If an SPH particle comes within $r_{\rm acc}$, is bound, and has a specific angular momentum less than that required to enter a circular orbit with radius $r_{\rm acc}$, it is accreted by the sink particle. Because of this circumstellar discs can only be resolved if they have a radius greater than ≈ 1 au. The angular momentum of the particles accreted is used to calculate the spin of the sink particles but does not have an effect on the rest of the calculation. The sink particles do not contribute to radiative feedback (Bate 2012, provide a detailed discussion on the limitations of sink particle approximation). Sink particles merge if they pass within 0.03 au of each other.

3.1.4 Initial conditions

For a more complete description of the initial conditions of the four calculations the reader is again directed to Bate (2019). The initial density and velocity structure was identical for all four calculations. A uniform density, spherical cloud of gas contained 500 $M_\odot$ with radius 0.404pc with an initial density of 1.2×10^{-19} g cm^{-3} (hydrogen number density $n_{\rm H} = 6 \times 10^4$ cm^{-3}). The initial free fall time of the gas was $t_{\rm ff} = 1.90 \times 10^5$ yr. An initial supersonic turbulent velocity field was applied to each cloud, in the manner of Ostriker et al. (2001) and Bate et al. (2003b). The velocity field is a divergence-free random Gaussian with a power spectrum $P(k) \propto k^{-4}$, where k is the wavenumber, on a 128^3 uniform grid with particle velocities interpolated from the grid.

For each calculation the dust is initially in thermal equilibrium with the local ISRF, and the gas is in thermal equilibrium with heating from the ISRF and cosmic rays with cooling provide by atomic and molecular line emission and collisional coupling with the dust. This causes a range of initial temperatures for the gas and dust, with dust being warmest on the outside of the cloud and coolest in the centre. For $Z = 3\ Z_\odot$, $T_{\rm dust} = 6.3 - 17$ K, for $Z = Z_\odot$, $T_{\rm dust} = 7.1 - 17$ K, for $Z = 0.1\ Z_\odot$, $T_{\rm dust} = 12 - 17$ K, for $Z = 0.01\ Z_\odot$, $T_{\rm dust} = 16 - 18$ K. The initial gas temperatures vary less with $T_{\rm g} = 9.1 - 9.8$ K.

Each cloud was modelled by 3.5×10^7 SPH particles, providing enough resolution to resolve the local Jeans mass throughout the calculation, necessary to correctly model fragmentation down to the opacity limit (Bate and Burkert 1997; Truelove et al. 1997; Whitworth 1998; Boss et al. 2000; Hubber et al. 2006).

3.1.5 Disc characterisation

The protostellar discs in each calculation continuously evolve due to a variety of processes. Following Bate (2018), I sample the properties of discs at multiple times during the calculation to examine the disc properties statistically. These samples are take every $0.0025 t_{\rm ff}$ ($\approx$ 480yr) for each protostar. The number of instances of discs resulting from each of the four calculations of Bate (2019) and from the calculation of Bate (2012) are found in the second column in Table 3.1. From here on in when referring to discs formed in the Bate (2012) calculation I will usually refer only to Bate (2018).

3.1.5.1 Circumstellar discs

For each protostar (modelled by a sink particle), the SPH gas particles (and other sink particles) are sorted by distance from the sink particle. An SPH particle is considered to be part of the protostellar disc if it has not already been assigned to a disc of a different protostar and if the instantaneous ballistic orbit of the particle has an apastron distance of less than 2000 AU and an eccentricity $e < 0.3$. This is done by starting with the SPH particle closest to the sink particle. The sensitivity to the choice of eccentricity limit is discussed in Bate (2018, section 2.3.3). If these criteria are met, the mass of the particle is added to the mass of the system then the position and velocity of the centre of mass of the system are calculated. This process is repeated with the updated quantities for the next SPH particle. No particles further than 2000 au from the centre of mass are considered – this distance was chosen as it is larger than the apparent radius of any disc studied by Bate (2018), and also applies to the discs of Bate (2019).

If, when moving through the list of particles sorted by distance, a sink particle is encountered (e.g. either as part of a system, or a passing protostar) its identity is recorded and the process of adding mass to the disc is stopped. No particles further away than the nearest sink particle are included. Protostars that do not have a companion within 2000 au are referred to as being isolated and protostars that have never had a companion within 2000 au as having no encounters. A protostar can be single but not isolated – if a protostar has another protostar within 2000 au but the two are not bound then it is single protostar.

The above algorithm gives sensible extraction of discs for both the calculation analysed in Bate (2018) and those analysed here. It is, however, difficult to separate the disc and the envelope of the protostar and sometimes the algorithm finds low mass 'discs' with very large radii. These are not judged to be discs, rather parts of the infalling envelope. To avoid counting these as discs I exclude any 'disc' with a mass < 0.03 M$_\odot$ ($<$ 2100 SPH particles) and the radius that contains 63% (see below for how this is determined) of this mass is $>$ 300 au. Additionally, any 'disc' that has a radius containing 63% of its mass that is three times larger than the radius containing 50% of its mass is excluded. These cuts reduce the number of instances of circumstellar discs that are used for the statistical analysis of the four calculations of Bate (2019) (see the third column in Table 3.1 for the number of

instances that are used and the number of instances used in the disc analysis by Bate 2018). There are more discs identified in the updated solar metallicity calculation compared with the Bate (2012) calculation, this is due to two reasons. First, more stars form in the more recent calculation and so there are more objects for discs to form around. Second, the gas is better modelled in the newer calculation, particularly at low-density, and is typically warmer meaning that discs are less likely to be destroyed by gravitational instabilities.

The truncated power-law disc radial surface density profile

$$\Sigma(r) = \Sigma_{\rm c} \left(\frac{r}{r_{\rm c}}\right)^{-\gamma} \exp\left\{\left[-\left(\frac{r}{r_{\rm c}}\right)^{2-\gamma}\right]\right\}, \tag{3.1}$$

is often used by observers (e.g. Tazzari et al. 2017; Fedele et al. 2017) to fit observed discs. In this function, $r_{\rm c}$ is the characteristic radius of the disc, γ is the power-law slope, and $\Sigma_{\rm c}/e$ is the gas surface density at $r_{\rm c}$. As pointed out by Bate (2018) for $\gamma < 2$, $r_{\rm c}$ is always equal to the radius that contains $(1 - 1/e)$ of the total disc mass (i.e. 63.2%). We note that equation (3.1) only gives sensible profiles for $\gamma < 2$. So if the disc well described by equation (3.1) $r_{\rm c}$ is obtained simply by measuring the radius that contains 63.2% of the total disc mass. Measuring the radii of discs this way is actually a more general way measurement, I find that it also gives reasonable results for discs that have very different surface density profiles. Tripathi et al. 2017 note that using values between 50% and 80% made little difference to their analysis. It is not imperative that a disc is well described by the above surface density profile, as long as the characteristic radius contains $\approx$ 65% of the disc mass then discs tend to be reasonably well characterised. When referring to a disc radius in this chapter I mean $r_{\rm c}$ as defined above.

3.1.5.2 Circum-multiple discs

Many of the protostars in these calculations are found to be in bound multiple systems and thus discs formed in these systems are far more complex than those around a single star. Due to the complexity of these higher order systems we limit our analysis to single, binary, triple, and quadruple systems and to general properties (e.g. disc mass, disc radius, disc/star mass ratios). Systems with an order higher than four that are made up of individual bound systems of order four or less are treat as separate systems. For ex-

Calculation	Instances of discs	Instances of discs used in analysis	Instances of isolated discs used in analysis
Bate 2012	11831	11281	2186
Metallicity 3 $Z_\odot$	18172	17003	3648
Solar Metallicity	16048	15323	2972
Metallicity 0.1 $Z_\odot$	8380	8034	1779
Metallicity 0.001 $Z_\odot$	4809	4585	826

Table 3.1: The instances of discs found in each of the four calculations analysed here and the calculation of Bate (2012) that was analysed by Bate (2018). I apply criteria to determine which instances I consider as 'real' disc that decreases the number of instances of discs I use in this analysis. The largest decrease in instances is 6.4% for the 3 $Z_\odot$ calculation. All calculations were run to 1.20 $t_{\rm ff}$ ($\approx 230,000$ yr). I identify fewer discs with decreasing metallicity.

ample, a septuple system consisting of a quadruple system bound to a triple system will be treat as two individual systems. For protostars bound in pairs, either as a binary or as components of hierarchical higher order systems, I also examine the alignments of the circumstellar discs, protostellar spins, and the orbital plane of the pair.

To compute the total disc mass of a system I sum the total mass of all the discs extracted for a system. Determining the characteristic disc radius for a multiple system is not straight forward. For circumstellar discs, I record the radii containing 2, 5, 10, 20, 30, 40, 50, 63.2, 70, 80, 90, 95, 100 percent of the disc mass. To calculate the characteristic radius for a multiple system I loop over all of the component discs, starting with the smallest of the above radii for each disc, and keep a cumulative sum of the mass contained within a given radius. For example, consider a binary system for which the radii containing 2% and 5% for the disc masses are 4 au and 8 au for the primary's disc, and 3 au and 7 au for the secondary's disc, and 50 au and 75 au for the circumbinary disc. We first sum 2% of the secondary's disc mass with 2% of the primary's disc mass, then with 3% (5% − 2%) of the secondary's disc mass, then with 3% of the primary's disc mass, and so on. The characteristic radius for the system is then the radius at which the cumulative sum first exceeds 63.2% for the total disc mass of the system (again, see Bate 2018 for further details).

The analysis of the protostellar systems uses the same constraints as for circumstellar discs. Any circum-multiple disc which has a total mass <0.03 $M_\odot$ (<2100 SPH particles) and a radius containing 63.2% of the disc mass that is >300 au is excluded. In addition to this any disc with a characteristic radius more than three times great than the radius

containing 50% of the disc mass is also excluded.

3.2 The statistical properties of the discs

Here I discuss the statistical properties of the discs. I begin by providing an overview of the results of the disc analysis reported by Bate (2018). Next I consider the properties of circumstellar discs (orbiting just one protostar), discs of isolated protostars, and discs of protostars that have had no encounters (see the definitions below). I then discuss properties of discs in bound protostellar systems, focusing on the mass and radius of these discs. Finally I investigate the orientation angles between discs, orbital planes, and sink particle spins (angular momenta of protostar and inner disc).

3.2.1 Bate (2018) disc analysis

In this chapter I perform a similar analysis to Bate (2018) to gather statistical properties of discs and investigate their dependence on metallicity. I begin by summarising the main finding of Bate (2018) to put our results in context, and I discuss the different physics used in the calculations (Bate 2012, 2019, 2014).

The calculation analysed by Bate (2018) assumed solar metallicity and employed two-temperature (gas and radiation) radiative transfer in the flux-limited diffusion approximation as developed by Whitehouse et al. (2005) and Whitehouse and Bate (2006). The gas and dust temperatures were assumed to be the same throughout the calculation. By contrast, the Bate (2019) calculations used the Bate and Keto (2015) method to combine radiative transfer with a diffuse ISM model. This method has separate gas and dust temperatures and includes energy transfer between the gas and dust via collisions. The dust temperature is set by assuming it is in local thermodynamic equilibrium with the total radiation field. Initially the density and velocity structure are the same for all of the calculations (both Bate 2012 and Bate 2019), but the initial temperatures are different. The calculation of Bate (2012) had a uniform initial temperature of 10.3 K, while the initial gas and dust temperatures vary both spatially (due to extinction of the ISRF) and due the differing metallicity. During the evolution of the calculations, it is the low-density and/or low-metallicity gas whose temperatures differ most from the temperatures obtained by

Bate (2012). For the solar-metallicity calculation of Bate (2019), because the initial cloud density is quite high ($n_{\rm H} = 6\times10^4$ cm^{-3}) and the gas and dust are reasonably well coupled thermally by collisions, the gas temperatures are similar to those obtained by Bate (2012) who also assumed solar metallicity, except in the outermost parts of the cloud (where star formation does not occur). Therefore, it is expected that the discs of the solar metallicity calculation analysed here should have similar properties to the calculation analysed by Bate (2018).

Bate (2018) show many images of discs formed in the calculation to demonstrate the diversity of discs. The calculations of Bate 2019 also have a wide diversity of discs (see the mosaic animations published as supplementary information with the paper), but in this chapter I only consider their bulk statistical properties. Bate (2018) define an isolated disc as one without a protostellar companion closer than 2000 au. This definition allows for the inclusion of discs that may have been part of multiple systems or had close encounters with other discs, or may become part of a multiple system in the future. Having isolated discs defined this way is consistent with what an observer would see; they would not know the history or future of the disc, only that is is currently isolated. A protostar that has never had an encounter within 2000 au is classified as having no encounters. I categorise discs in the same way to make meaningful comparisons between the calculations.

3.2.1.1 Disc masses and radii

The analysis done by Bate (2018) was the first attempt at protostellar disc population synthesis using a hydrodynamical calculation. Their aims were to show the large diversity of disc types that can be expected around young stars, and to provide statistics on their evolution and properties (e.g. mass, radii, disc alignment). I do not provide a detailed investigation into the evolution of discs – the same evolutionary processes are involved in sculpting the disc populations and in most cases similar evolutionary trends are found.

Bate initially consider the discs around individual protostars (i.e., circumstellar discs), including isolated discs and discs with no encounters as defined above. They find that most ($\approx$ 70%) circumstellar discs are not resolved (i.e. $M_{\rm d} < 0.01{\rm M}_\odot$), largely due to interactions with other protostars or ram-pressure stripping. Protostars that have had

no encounters mostly have resolved discs with the masses of these discs having a clear dependence on the mass of the protostar they are orbiting. The disc mass distributions are subdivided into three protostellar mass ranges: $M < 0.1$ M$_\odot$, 0.1 M$_\odot \leq M < 0.3$ M$_\odot$, and $M > 0.3$ M$_\odot$ and the typical disc mass is found to scale approximately linearly with protostellar mass.

Next Bate (2018) investigate the statistical properties of the discs of stellar systems. When considering the dependency of total system disc mass on stellar system mass they use the same three mass ranges as above. Discs in systems that have a higher total mass tend to be more massive until the mass of the system exceeds ≈ 0.5 M$_\odot$, above which the typical total disc mass is found to be more or less independent of the total stellar mass. More than half of very low mass (VLM) ($M < 0.1$ M$_\odot$) systems have unresolved discs. The discs in the VLM systems tend to be a factor of two times smaller in radius than systems with 0.1 M$_\odot \leq M < 0.3$ M$_\odot$ and a factor of three times smaller than systems with $M > 0.3$ M$_\odot$. The largest discs tend to be found in multiple systems.

3.2.1.2 Disc orientations

Bate (2018) provide a discussion of the relative orientations of discs, orbits, and sink particle spins (this can be thought of as the angular momentum of the star and the inner region of the disc) in bound protostellar pairs. Pairs can be either binary systems or a mutual closest neighbour in a multiple system. To be considered, discs must have a mass of $M_{\rm d} \geq 4.3 \times 10^{-4}$ M$_\odot$. This is equivalent to 30 SPH particles which is enough to calculate the angular momentum vector of the disc.

Discs tend to be more aligned with each other in closer systems, with discs having semi-major axes $\lesssim 100$ au typically being strongly aligned. The discs become more aligned with increasing age, and discs that are part of higher order systems (> 2 protostars) tend to be more well aligned than discs in binary systems. They suggest this is likely because pairs in higher order systems originate from disc fragmentation more often that discs in binary systems, in which discs originate from either disc fragmentaion or star-disc interactions. The alignment between discs and the orbit of the pair has a weaker alignment for close systems and a stronger alignment in wider systems when compared to the alignment

between discs. There is less of a dependence of alignment on age than there was for disc-disc alignment.

The alignment between sink particle spins of pairs (angular momentum of the protostar and inner disc on the scale of $\lesssim 0.5$ au) is similar to the alignment between circumstellar discs. Spin-spin alignment have the same dependencies on age, separation and multiplicity as for disc-disc alignment. The circumstellar discs and sink particle spins of bound pairs show a tendency for strong alignment. Roughly 50% of protostars have misalignments of more than 30° between their resolved outer discs and their sink particle spins (i.e., the combination of their protostellar and inner disc angular momenta). The explanation for this is that the outer part of the discs are continually having their orientations changed more quickly than the spins are. There is a lag for the reorientation of spins through accretion from larger scales of the disc. The alignment of sink particle spins and circumstellar discs do not have the same dependencies on age, separation, and multiplicity as the spin-spin alignment (circumstellar discs and protostellar spins are generally much better aligned with each other than the two spins of a pair of protostars).

3.2.2 Circumstellar discs

In Fig. 3.1 I compare the cumulative distributions of circumstellar disc masses, radii, and disc/star mass ratios from each of the four calculations with different metallicity with the analysis of Bate (2018). The top row gives cumulative distributions for all discs orbiting only one protostar, the middle row gives the corresponding distributions for isolated protostars, and the bottom row gives the distributions for protostars that have never been within 2000 au of another protostar.

We see in the top left panel that most circumstellar discs are unresolved (i.e. $M_{\rm d} < 0.01\,{\rm M}_\odot$), however those discs that are resolved generally follow the same trends and there is no consistent trend with metallicity.

In the middle left panel we see that isolated protostars tend to have mostly resolved discs, with the exception of the lowest metallicity calculation, and there is a consistent trend that a higher proportion of protostars have resolved discs with increasing metallicity.

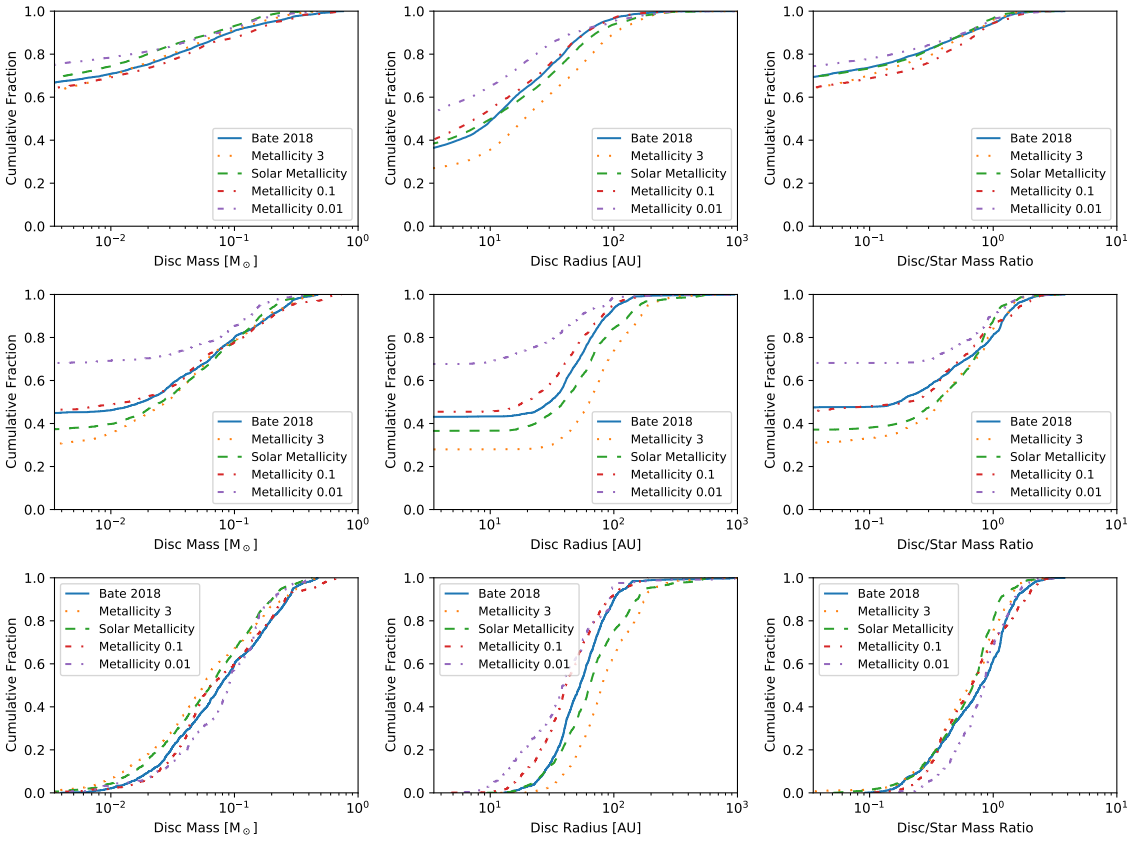

Figure 3.1: Cumulative distributions of disc mass (left), characteristic radius (centre), and disc/star mass ratio (right) for circumstellar discs (top), isolated discs (middle), and discs that have never had a companion protostar pass within 2000 au of the protostar that they orbit (bottom). Here we show the comparison between discs found in the four calculations with differing metallicity and discs found in Bate (2018).

There are also very few massive discs with the lowest metallicity. For protostars never having had another protostar within 2000 au, the vast majority have resolved discs, since they have not been disrupted or truncated by dynamical interactions with other protostars. The mass distributions of these discs have a weak metallicity dependence such that the low-mass discs ($0.01\,M_\odot < M_d < 0.1\,M_\odot$) in the lowest metallicity calculation are typically $\approx$ 50% more massive than those in the highest metallicity calculation. As mentioned above, however, there is also a relative deficit of massive discs in the lowest metallicity calculation ($Z = 0.01\,Z_\odot$).

From the centre column it is very clear that larger discs tend to form with higher metallicity; this is most clear from the bottom centre panel as these no encounter discs are mostly resolved, but the trend is apparent in all of the samples.

As for the cumulative distributions of the ratio between the disc and protostar masses (panels in the right column), there does not appear to be a consistent trend with the metallicity of the molecular cloud, except in the case of the isolated disc sample. For isolated discs, the cumulative distributions becomes steeper with increasing metallicity (i.e. with low metallicity there are many unresolved discs or discs less massive than the protostar).

In Fig. 3.2 the distributions of masses of discs about protostars that have not had an encounter with another protostar within 2000 au are shown. It is clear that disc mass scales with star mass for each metallicity with most disc masses being in the range $\approx$ 0.02-0.2 M_*. There is a slightly greater spread of disc mass across the mass bins in the super-solar metallicity calculation than in the lower metallicities. In Table 3.2 the number of instances of discs about protostars that have had no encounters within 2000 au of an other protostar are given. Note that there are significantly fewer protostars having no encounters of mass $M > 0.3\,M_\odot$ for the lowest metallicity. As discussed in Bate (2019) the lowest metallicity calculation has the highest multiplicity out of the four calculations, making it less likely for protostars to have no encounters within 2000 au. This is also why the $Z = 0.01\,Z_\odot$ calculation has the highest fraction of unresolved discs (Fig. 3.1) – a greater fraction of stars have close companions that disrupt or truncate their circumstellar discs. The reason for the higher multiplicity at low metallicity and the above trends of circumstellar disc

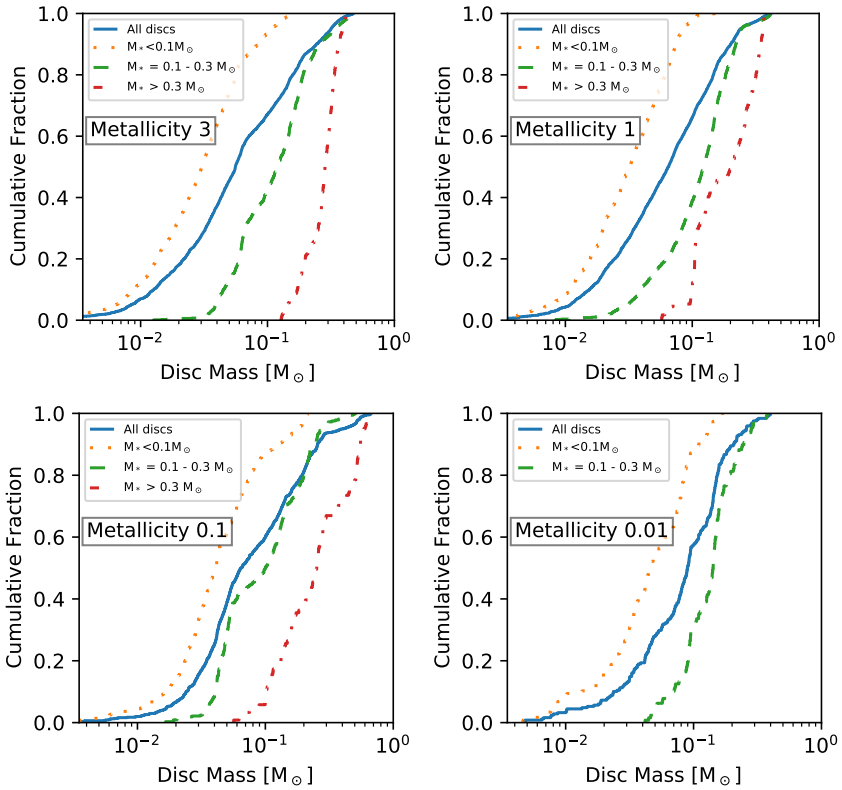

Figure 3.2: The cumulative distributions of circumstellar disc mass for protostars that have never had an encounter within 2000 au. The solid line gives the distribution for no encounter discs, and we also provide the distributions for sub-samples in which the protostellar mass lies in the ranges $M < 0.1$ M$_\odot$, 0.1 M$_\odot$ $< M < 0.3$ M$_\odot$, and $M > 0.3$ M$_\odot$. Discs orbiting more massive stars tend to be more massive. The masses of no encounter discs tend to increase slightly as metallicity decreases. Note that we do not include the cumulative distribution of disc mass for stars of mass $M > 0.3$M$_\odot$ from the $Z = 0.01$ Z$_\odot$ metallicity calculation as there are only two such instances of isolated discs (see Table 3.2).

Calculation		$M < 0.1$ M$_\odot$	0.1 M$_\odot$ $< M <$ 0.3 M$_\odot$	$M > 0.3$ M$_\odot$	Total
Metallicity 3	Instances	1295	859	195	2349
	Percentage	55.1%	36.6%	8.3%	-
Metallicity 1	Instances	896	812	115	1823
	Percentage	49.2%	44.5%	6.3%	-
Metallicity 0.1	Instances	359	329	122	810
	Percentage	44.3%	40.6%	15.1%	-
Metallicity 0.01	Instances	118	129	2	249
	Percentage	47.4%	51.8%	0.8%	-

Table 3.2: The number of instances of discs orbiting protostars that have never had another protostar within 2000 au for each of the four calculations. Provided are the total number, and the numbers in three bins based on protostellar mass. Alongside these are the number of instances in each mass bin as a percentage of the total number of instances of these discs for each calculation. Generally, the proportion of discs decrease as the mass bin increases. This is not case for the lowest metallicity calculation where there is a slight uptick in instances of discs in the intermediate mass bin and almost no instances of discs in the high mass bin. As the metallicity is decreased the number of discs about protostars with no encounters within 2000 au consistently decreases.

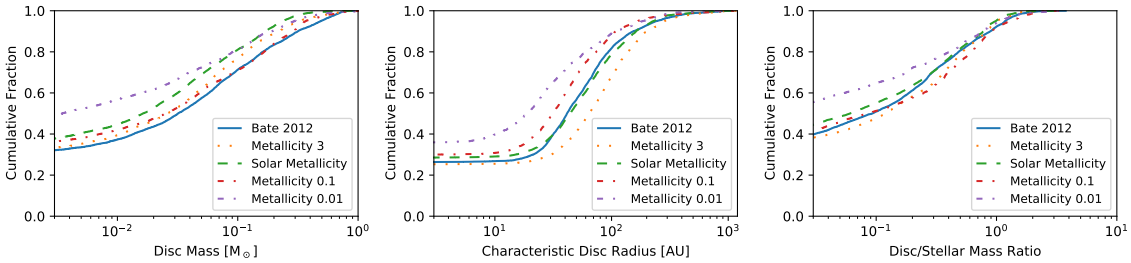

Figure 3.3: Cumulative distributions of protostellar system total disc mass (left), characteristic radius (centre), and total disc mass/total stellar mass ratios (right). Compared are the cumulative distributions from each of the four metallicity calculations with those from the (Bate 2012) calculation. Note that the solar metallicity calculation has similar distributions for disc radius and disc/star mass ratio to the (Bate 2012) calculation (which also assumed solar metallicity), though the system disc masses themselves are typically about a factor of two lower in the newer calculation.

properties with metallicity is discussed in Section 3.3.1.

3.2.3 Discs of bound systems

In this section, I discuss the properties of discs found in bound protostellar systems. These include circumstellar, circumbinary and circum-multiple discs up to and including discs surrounding quadruple systems.

3.2.3.1 Disc masses and radii

In Fig. 3.3 the same three properties across the calculations are compared as in Fig. 3.1 except here discs that are extracted as part of an entire system are considered (see Sec-

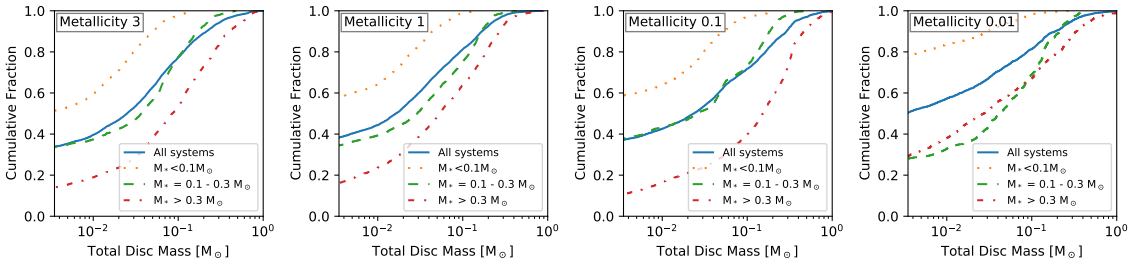

Figure 3.4: The cumulative distributions of total disc masses of protostellar systems for each of the four calculations. We give the distributions of all discs, discs about systems of total stellar mass $M < 0.1$ M$_\odot$, 0.1 M$_\odot$ $< M <$ 0.3 M$_\odot$, and $M >$ 0.3 M$_\odot$. The total disc mass tends to increase as the stellar mass of the system increases, except in the $Z = 0.01$Z$_\odot$ case where the disc masses in the two higher protostellar mass ranges are similarly distributed.

tion 3.1.5.2). Across the calculations the characteristic disc radius tends to increase with metallicity. The median radius of discs in a bound system for the super-solar metallicity calculation is $\sim$ 65 au compared to $\sim$ 20 au in the lowest metallicity calculation. Around 30% of discs in the super-solar metallicity calculation have a characteristic radius larger than 100 au compared to around 10% in the lowest metallicity calculation. This is likely due to the increase of fragmentation due to cooler gas temperatures in the low metallicity calculation (see Section 3.3.1). The characteristic radii tend to be slightly larger for discs in systems than circumstellar discs alone. Note that both circumstellar discs and discs of systems in the Bate (2012) calculation and the solar metallicity Bate (2019) calculation have very similar distributions of disc radii. The circumstellar disc mass distributions are also very similar, although the disc masses of systems are about a factor of two lower in the newer calculation compared to the older calculation. The two different methods employed by these calculations are not expected to show much difference due to the relatively high densities of the initial molecular cloud. The majority of discs across all the calculations have characteristic radii ranging between 20 and 110 au.

The right panel of Fig. 3.3 shows the cumulative distributions of the ratio between the total disc mass and the total protostellar mass of the instances of protostellar systems. Overall the distributions tend to be quite flat indicating a wide range of ratios, but that systems in which the total disc mass exceeds the total protostellar mass are very rare even at these young ages. Again, the lowest metallicity calculation differs slightly from the others in that a greater fraction of systems have low-mass or unresolved discs.

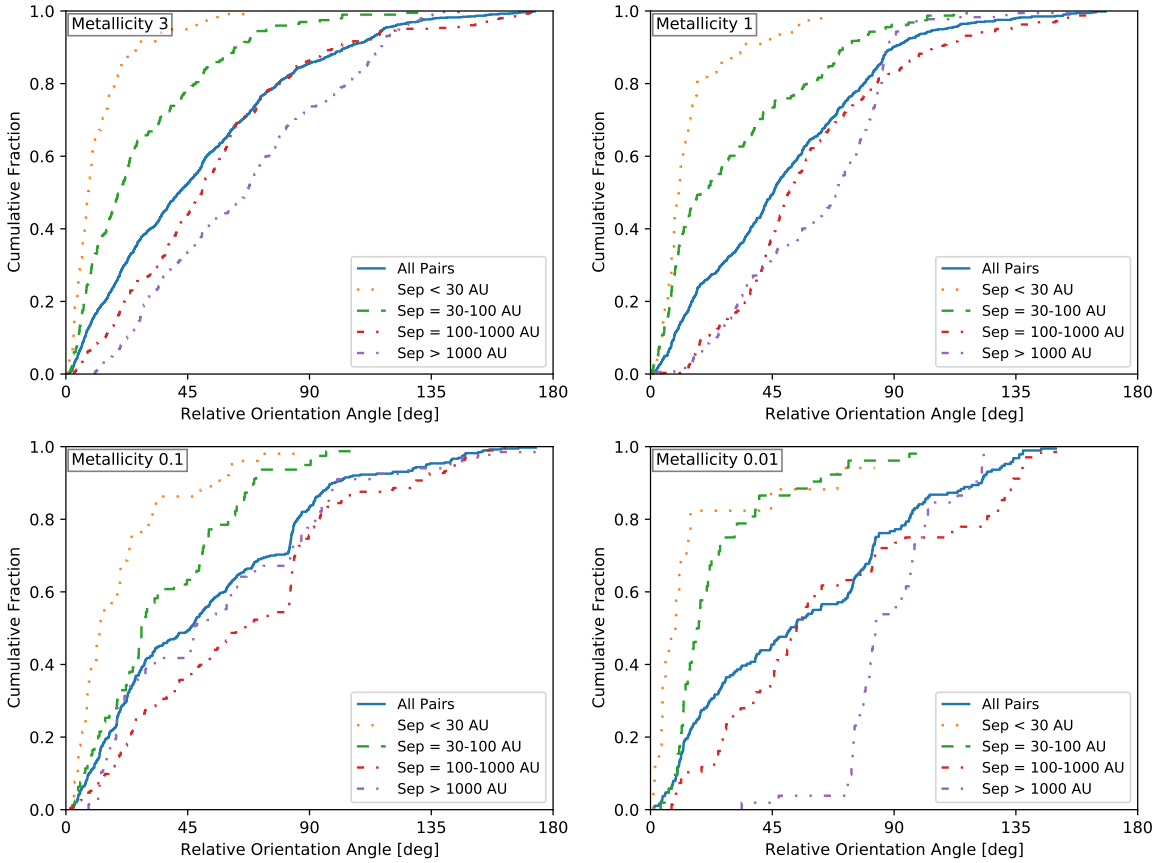

Figure 3.5: The distributions of relative orientation angle between the two circumstellar discs in bound pairs of protostars. The pairs include binaries, and pairs in triple and quadruple systems. Given here are the cumulative distributions for four ranges of the semi-major axis: $a < 30$ au, $30 < a < 100$ au, $100 < a < 1000$ au, and $a > 1000$ au. Also plotted the cumulative distribution of relative orientation angle for all pairs. As metallicity is decreased the alignment between discs also does, except for close systems ($a < 100$ au) at the lowest metallicity ($Z = 0.01\ Z_{\odot}$).

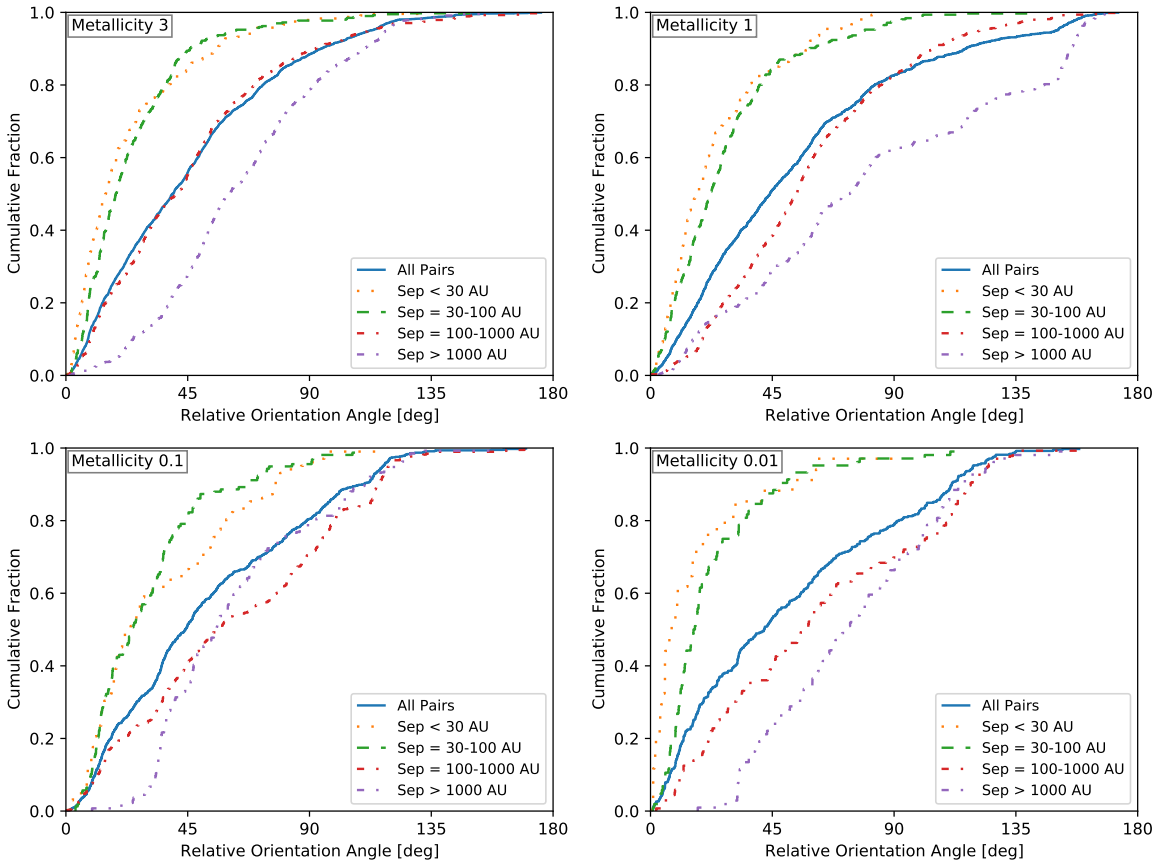

Figure 3.6: The distributions of the relative orientation angle between each circumstellar disc and the orbital plane of the bound protostellar pairs. The pairs include binaries, and pairs in triple and quadruple systems. I give the cumulative distributions for all pairs, and for those in four ranges of the semi-major axis: $a < 30$ au, $30 \leq a < 100$ au, $100 \leq a < 1000$ au, and $a \geq 1000$ au. As the metallicity is decreased the distributions for each given separation ranges tend to become flatter, indicating a more random distribution of orientation angles between discs and the orbital plane of the bound pair. Again, there is an exception for close pairs ($a < 100$ au) at the lowest metallicity.

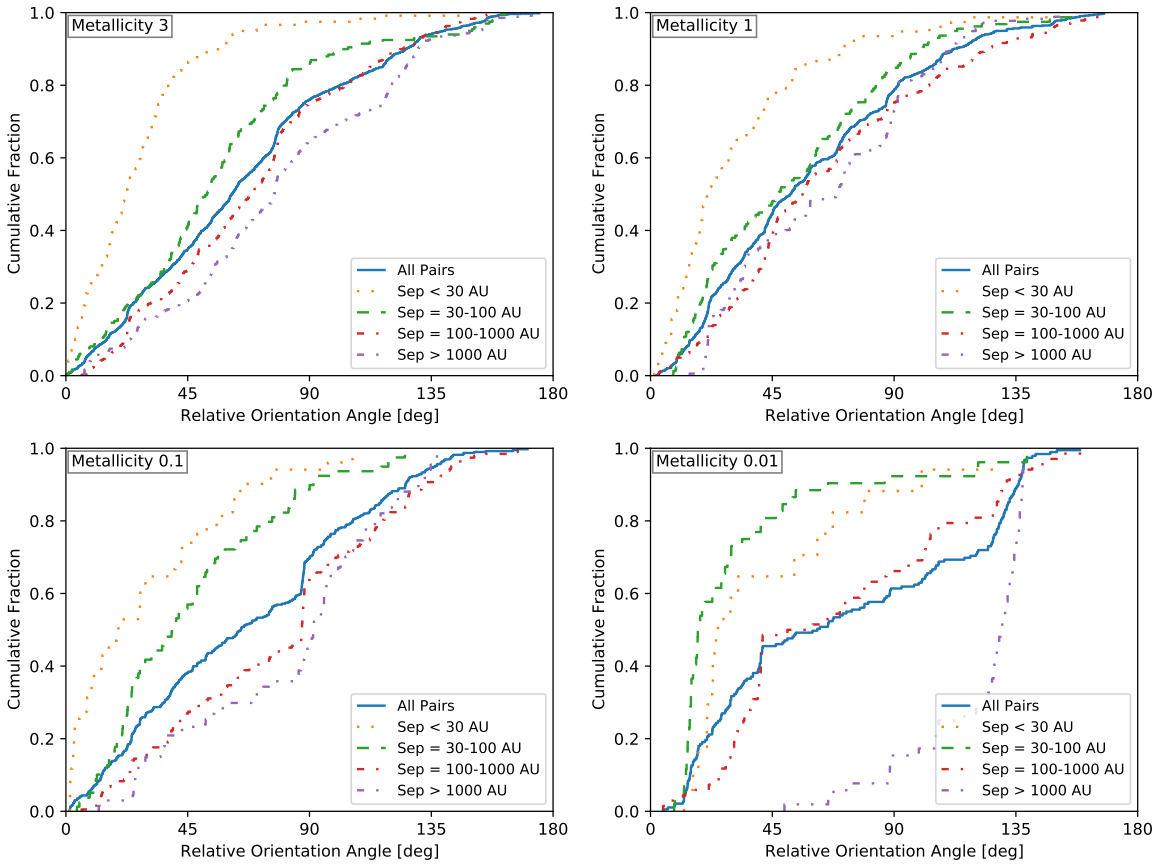

Figure 3.7: The distributions of the relative orientation angle between the two sink particle spins of bound protostellar pairs. The pairs include binaries, and pairs in triple and quadruple systems. I give the cumulative distributions for four ranges of the semi-major axis: $a < 30$ au, $30 \leq a < 100$ au, $100 \leq a < 1000$ au, and $a \geq 1000$ au. Protostellar spins are generally less well aligned with each other than circumstellar discs are with each other or with the orbit.

In Fig. 3.4 I plot the cumulative distributions of total system disc mass separated into mass bins of the total system stellar mass ($M < 0.1$ M$_\odot$, 0.1 M$_\odot$ $< M <$ 0.3 M$_\odot$, and $M >$ 0.3 M$_\odot$). There is a clear trend of increasing total disc mass with increasing total stellar mass, except in the lowest metallicity calculation. Additionally I find that higher order systems have a higher total disc mass, although I do not present that data here. Also note that discs about the stars of mass $M >$ 1 M$_\odot$ in the $Z = 0.1$ Z$_\odot$ metallicity calculation tend to be more massive that the corresponding discs in the other calculations, although the numbers of systems are relatively small. The distributions of disc masses for the three highest metallicity calculations (apart from the highest mass systems) are quite similar to each other and quite different to the distributions in the lowest metallicity case. In the lowest metallicity case, the disc mass distribution of high-mass ($M >$ 0.3 M$_\odot$) systems is quite similar to that of intermediate mass systems (0.1 M$_\odot$ $< M <$ 0.3 M$_\odot$). In other words, massive discs in massive systems are significantly rarer at $Z = 0.01$ Z$_\odot$ than at higher metallicities. Again, this is likely a result of enhanced cooling at low metallicity and, thus, more frequent disc fragmentation. Similarly, more than 80% of discs orbiting very low-mass systems are unresolved, compared to $\approx$ 60% at higher metallicities.

3.2.3.2 Disc orientations of protostellar pairs

In this section, I investigate how relative orientations of protostellar orbits and spins, and discs in bound protostellar pairs depend on metallicity and orbital separation. I find that distributions of relative orientation angle do not vary much with age and are generally similar to those found by Bate (2018). For this reason I do not present any data on the age dependence here. By bound pairs I mean either a binary system or bound pairs in a higher order system. A triple system will always contain one pair (due to the hierarchical way in which systems are identified), and a quadruple system may contain either one or two pairs. For discs to be analysed each protostar must have a circumstellar disc. It is required that each disc to be a mass of $M_d \geq 4.3 \times 10^{-4}$ M$_\odot$ (at least 30 SPH particles) as this is sufficient to determine the angular momentum vector of the disc. For metallicities of $Z = 3, 1, 0.1, 0.01$ Z$_\odot$ the numbers of instances of disc pairs are 1076, 735, 390, and 189 respectively.

First, I investigate the relative orientations of the two circumstellar discs in pairs. In Fig. 3.5, I show the cumulative distributions of the relative orientation angle and its dependence on the separation (semi-major axis) of the protostellar pair for each metallicity calculation. I plot the overall distribution, as well as breaking the samples into four orbital separation ranges: $a < 30$ au, $30 < a < 100$ au, $100 < a < 1000$ au, and $a > 1000$ au. Overall the orientation between discs depends strongly on the separation with a smaller separations leading to a greater degree of alignment between the discs and a larger separation leading to less alignment. In the lowest metallicity case the distribution for all pairs is flatter than for higher metallicity indicating that the disc orientations are starting to become more random. Additionally the differences between the distributions as a function of separation are greatly magnified. In particular, discs in widely separated ($a > 1000$ au) protostellar pairs at the lowest metallicity mostly have relative orientation angles ranging from $70 - 130°$ discs and those with separations $100 < a < 1000$ have close to a random distribution. In the lowest metallicity calculation, discs with separations $30 < a < 100$ au also are more similarly distributed to the discs of separation $a < 30$ au than for higher metallicities. I don't find any age dependence on the alignment of discs. Bate (2018) found a weak age dependence such that older systems were slighly better aligned. An age dependence is what we might expect due gravitational torques acting on the discs from the bound pair slowly aligning them with the orbital plane, and accretion of gas from outside the system causing discs to align with each other. However, we are only able to study evolution on time scales of $\sim 10^4$ years from these hydrodynamical calculations, and the time scale for significant realignment for most systems is likely much longer.

Next, in Fig. 3.6 I investigate the distributions of relative orientation angle of circumstellar discs and the orbital plane of the bound pairs, plotting orientations in the same four ranges of semi-major axis as in Fig. 3.5. Here, there are two values for each bound pair as there are two discs to consider. I find that discs in pairs that are more closely separated than 100 au tend to be well aligned with the orbital plane, although not as well aligned as discs in the closest systems ($a < 30$ au) are with each other. As was seen when considering the orientations between discs, the distributions of relative orientation angle for the pairs separated $a > 100$ au in lowest metallicity calculation tend to be flatter than the other distributions, with essentially a random distribution of relative angles between

zero and 135°. I find no significant dependence of the cumulative distributions of relative orientation angles on age. It may be expected that older systems become more aligned as the gravitational torques from the protostars cause the disc to align with the orbital plane, but again it is likely that the required time scale to see this effect have a significant impact is not covered. Overall, the dependence of the disc-disc relative orientation dependence on separation is somewhat stronger than it is for the alignment of discs with the orbital plane.

In Fig. 3.7 I show the cumulative distributions of the relative orientation angle between the spins of the two sink particles in the bound pairs. The spins are indicative of the angular momenta of the protostar and the inner part of the disc. Overall the spins tend to be less well aligned than the two discs and discs with the orbital plane of the pair. Spin is only effected by accretion, so if two protostars form in different regions and then become bound a greater misalignment would be expected. This is why there is less overall alignment between spins than there is for discs. In the top right panel we see that there is not a strong dependence on separation in the solar metallicity case, except for the closest ($a < 30$ au) pairs which are more well aligned. There is a trend with metallicity such that as the metallicity decreases the spins of sink particles in pairs for which $30 < a < 100$ au become more aligned, with the angles between spins for sink particles with $a < 30$ au and $30 < a < 100$ au becoming very similarly distributed for low metallicities. In the lowest metallicity calculation, I find a dependence on multiplicity such that spins of pairs in triple and quadruple systems are better aligned than in binary systems. I don't find such a dependence on multiplicity in the three highest metallicity calculations. This could be a signature of an enhanced role of disc fragmentation producing pairs at low metallicity.

Finally, I compare the relative orientation angles between the angular momentum vector of the disc and the sink particle spin in Fig. 3.8. Across all four calculations there is a strong preference for alignment. This is to be expected as the spin of a sink particle represents the angular momentum of the protostar and inner part of the disc which accretes from the outer disc. I find that there is no significant dependence of relative orientation distribution between discs and sink particle spin on separation. Each protostar and its disc evolves in a similar manner with accretion and/or gravitational torques reorientat-

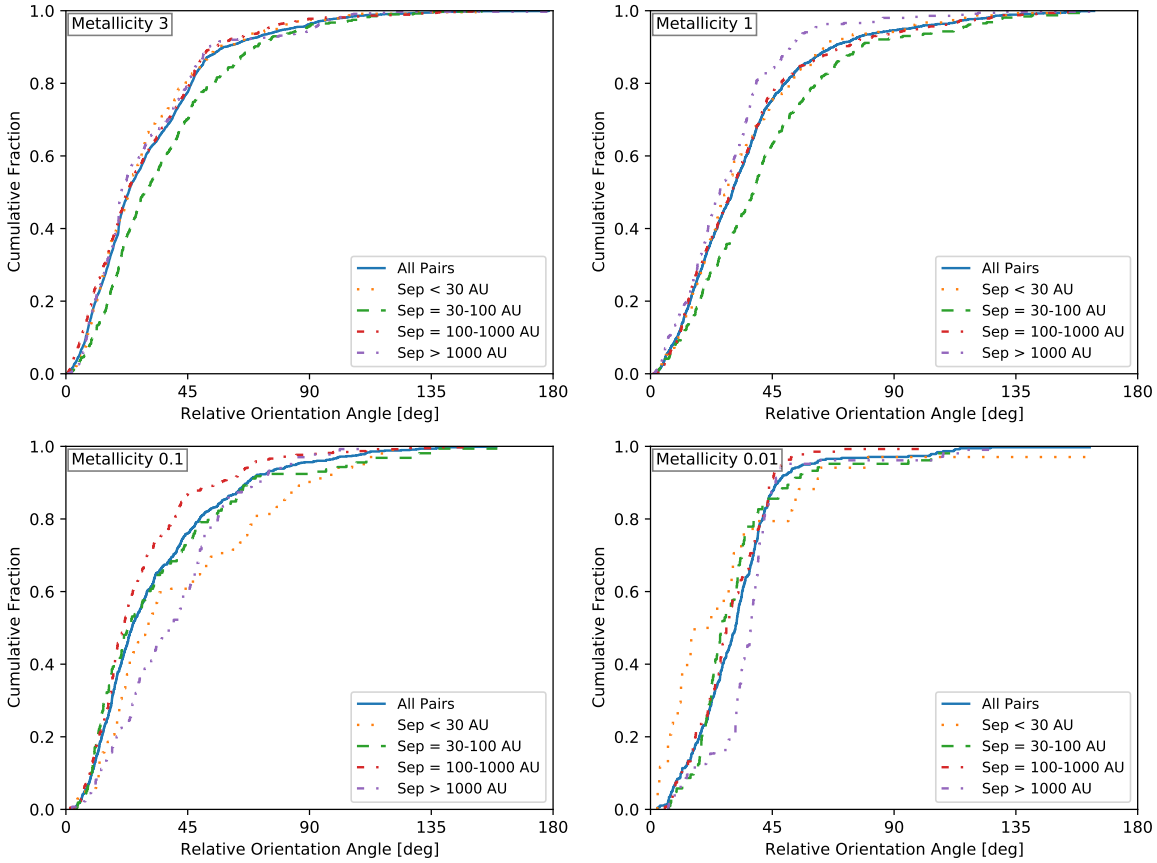

Figure 3.8: The distributions of the relative orientation angle between the circumstellar disc of a protostar and the spin of the sink particle (protostar and inner disc) that it orbits, for protostars in bound pairs. The pairs include binaries, and pairs in triple and quadruple systems. I give the cumulative distributions for four ranges of the semi-major axis: $a < 30$ au, $30 \leq a < 100$ au, $100 \leq a < 1000$ au, and $a \geq 1000$ au. Protostellar discs and spins are generally well aligned with each other, independent of separation of the pair. There is not much variation with metallicity, but in the lowest metallicity calculation in each semi-major axis separation range $\gtrsim 80\%$ of discs and spins are aligned to within 45°, slightly more aligned than the higher metallicity cases.

ing the outer disc and the sink particle spin continually trying to 'catch up' by accreting from the outer disc (see the end of Section 5.3.2 of Bate 2018 for further discussion). With the lowest metallicity I find a slightly better alignment between discs and sink particle spins. As I have previously shown above, a greater fraction of the instances of protostars tend to have low mass (or unresolved) discs in the lowest metallicity calculation. It may be that many of these instances of discs have not had much recent accretion and, therefore, the sink particle spins and outer discs have had time to evolve to become more closely aligned. I don't detect any dependence on age or multiplicity for the relative orientation angles between discs and protostellar spins.

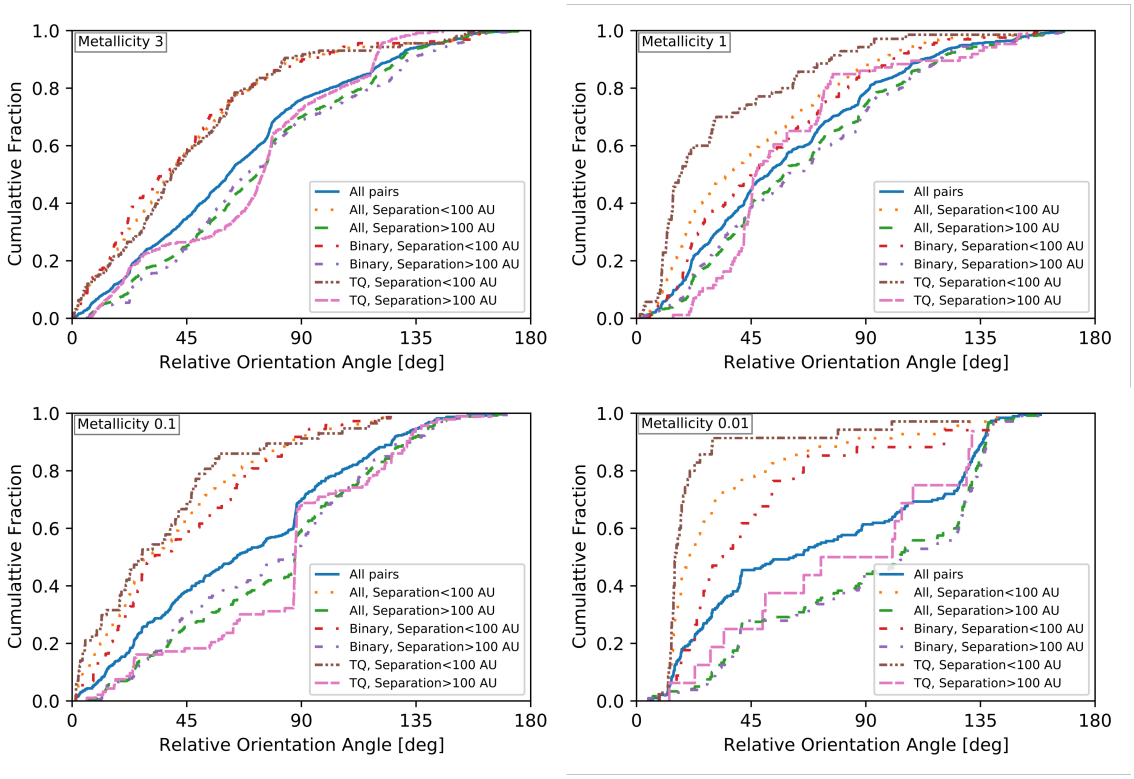

Figure 3.9: Cumulative distributions of protostellar spin orientations in bound pairs for each of the calculations. The distributions are split into bin of multiplicity (binary, and triple and quadruple), and separation (<100 au, and >100 au).

3.2.4 Multiplicity

In the previous section I referred to Fig. 3.7, which shows that in protostellar spin alignment there is dependence on metallicity, i.e. there is better alignment of spins in lower metallicity. Here I show in Fig. 3.9 how the alignment of protostellar (sink particle) spins depends on multiplicity of the system across each of the four calculations. When metallicity is three times that of solar metallicity it matters not the multiplicity of the system in which the bound pair is found. The alignment of the spins are very similar to each other. In contrast to the lowest metallicity setting where bound pairs in triple or quadruple systems are very strongly aligned ($\sim 90\% < 45°$). In binary pairs in the same calculation only when we look at orientations $> 90°$ do we contain $\sim 90\%$ of the pairs. When Bate (2018) analysed the spin alignments in a similar molecular cloud collapse calculation they did not find any dependence on multiplicity.

3.3 Discussion

3.3.1 Effect of opacity

As the metallicity is decreased in the calculations, the opacity is lowered which leads to more rapid cooling of high-density gas (due to reduced optical depths) and fragmentation becomes more likely to occur. Therefore, any given disc should be more gravitationally unstable. When examining the close binary fraction of solar type stars ($M_1 = 0.6-1.5\,\mathrm{M}_\odot$) Moe et al. (2019) find it to be strongly anticorrelated to metallicity. They suggest enhanced disc cooling due to reduced opacity causes an increased rate of disc fragmentation leading to a higher rate of close binaries.

Bate (2019) obtained a similar anticorrelation between the close binary frequency and metallicity in his radiation hydrodynamical calculations. However, when he investigated the cause of the enhanced close binary fraction at low metallicities, he found that classical disc fragmentation (i.e. a circumstellar disc fragmenting into one or more objects which then form a close binary with the original protostar) is not the main cause of the of the anticorrelation. Rather it arises due to enhanced fragmentation on small scales in general – both small-scale fragmentation within collapsing molecular cloud cores and disc fragmentation contribute.

3.3.2 Comparison with previous theoretical results

The trends I find in circumstellar disc mass and size are in general agreement with those found by Bate (2018), and the statistical properties of discs for the solar metallicity calculation in particular are in very close agreement with those obtained by Bate (2018). This isn't too surprising even though the calculations we consider include thermodynamical effects not included in the previous population study of disc properties as the earlier approach is a good approximation at the high densities of the molecular clouds considered in both studies. Similarly, I also find that discs with no encounters are generally more massive and larger than discs that have had interactions. The relative alignments in bound pairs of protostars between discs, the orbital plane, and sink particle spins also have similar dependencies on separation, although unlike Bate (2018) I do not detect a dependence on age of the systems.

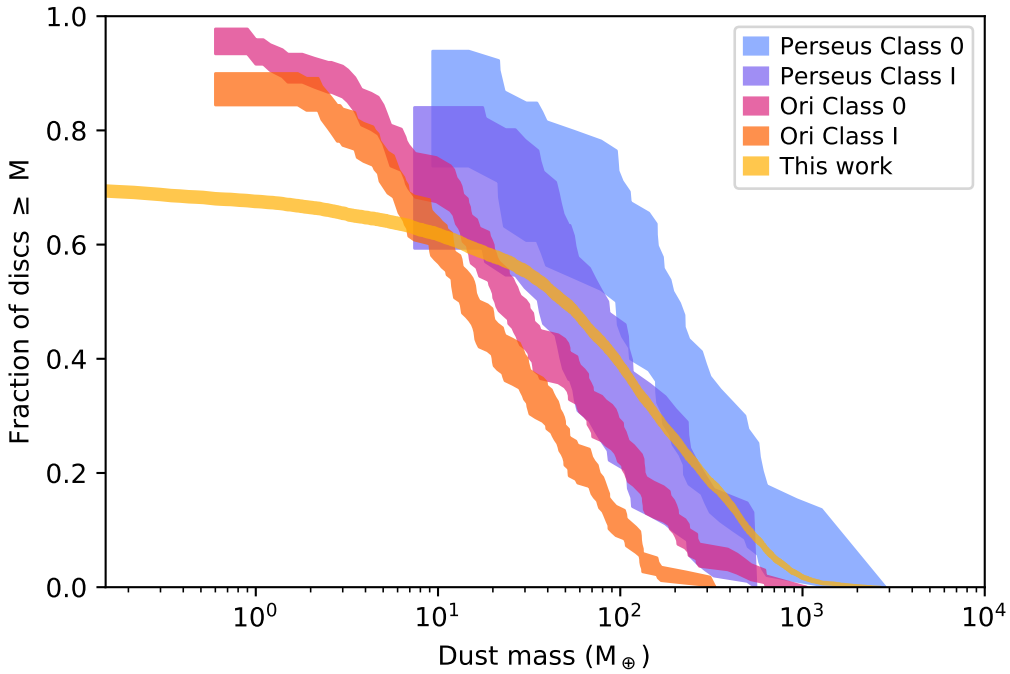

Figure 3.10: Dust mass distributions of discs around protostars in protostellar systems from the solar metallicity calculation of Bate (2019) and for discs of Class 0 and I objects taken from surveys of nearby star-forming regions. I use disc masses from Perseus (Tychoniec et al. 2020) and Orion (Tobin et al. 2020). I make use of the Kaplan-Meier estimate for left censored data as implemented in the Python package *lifelines* (Davidson-Pilon 2019). The shaded regions for the Orion discs and the simulation indicate 1σ confidence intervals, and a confidence intervals of 3σ for Perseus as per Tychoniec et al. (2020).

The new aspect of our study is that I consider whether and how the statistical properties of discs depend on metallicity. This is the first time such a statistical analysis of disc properties at different metallicities has been carried out based on the results of radiation hydrodynamical simulations.

However, studies of how the evolution of individual molecular cloud cores and discs are affected by their metallicity have been carried out before. For example, Machida (2008), Machida et al. (2009), Tanaka and Omukai (2014), and Bate (2014) all showed that fragmentation increases with lower metallicity. Recently, Vorobyov et al. (2020) studied the early evolution of individual protostellar discs in simulations for metallicities ranging $Z = 1 - 0.01$ $Z_\odot$. They focus on the gravitational instability of discs and periodic accretion bursts particularly in low metallicity discs. The accretion rates in the low metallicity discs during the embedded disc phase (40 and 320 kyr for the $Z = 0.01$ $Z_\odot$ and $Z = 0.1$ $Z_\odot$ simulations respectively) are higher in the $Z = 0.01$ $Z_\odot$ simulation. In general agreement with this work, I note that the mean accretion rates of discs at the end of each of the star cluster formation simulations increase as metallicity decreases (Bate 2019, see Table 3). The discs in the cluster simulations are at a similar age to those simulated by Vorobyov et al. (2020).

3.3.3 Comparison with Class 0/I objects

The calculations come with a caveat that the discs that are analysed aren't very old (the oldest is $\sim 10^5$yr). Even though objects don't have a well defined age sequence (Kurosawa et al. 2004; Offner et al. 2012), protostars of this age are generally thought be Class 0 objects. While a Class 0 protostar is defined by observational signatures that indicate the presence of a substantial envelope (Andre et al. 1993), there is now strong evidence that discs can and do grow at this stage (e.g. Yen et al. 2015; Tobin et al. 2020). The catalogue of discs around Class 0 objects is growing with the advent of the Atacama Large Millimeter/submillimeter Array (ALMA). For example, ALMA confirmed the earlier result (Tobin et al. 2012) of a Class 0 object with a rotationally supported disc around L1527 IRS with radius (Ohashi et al. 2014; Sakai et al. 2014; Aso et al. 2017). Currently, the largest observational samples of Class 0 and Class I discs are those from the VLA/ALMA Nascent Disk

and Multiplicity (VANDAM) survey of Perseus protostars (Tychoniec et al. 2018; Tychoniec et al. 2020) and the VANDAM survey of Orion protostars (Tobin et al. 2020). The work of Tychoniec et al. (2020) aims to provide more accurate disc mass determinations than the earlier work of Tychoniec et al. (2018) by considering the effects of large dust grains on the opacities. Therefore, I use the results of the more recent study when making comparisons with the simulations.

3.3.3.1 Disc dust masses

In Fig. 3.10 I plot the cumulative distributions of the disc dust masses from VANDAM surveys of Orion and Perseus Class 0/I protostars, along with the equivalent distribution for instances of discs of protostellar systems from the solar metallicity calculation. I use the Kaplan-Meier estimator, as implemented in the Python package *lifelines* (Davidson-Pilon 2019), with left censoring to account for upper limits on the observed disc masses. I provide shaded 1σ confidence intervals for discs in Orion and the simulations, and 3σ for discs in Perseus (Tychoniec et al. 2020). Dust masses for the simulated discs are determined by using the standard dust to gas ratio of 1:100. The shaded area for the simulated discs is narrow due to the large number of instances of discs that are identified. The Kaplan-Meier estimator is used here as it becoming a standard tool for observational studies of discs.

The form of the mass distribution of simulated discs is similar to the observed distributions. The flattening of the mass distribution of the simulated discs below ≈ 50 $M_\oplus$ is due to the limited resolution of the calculation. Discs that are poorly resolved viscously evolve quicker than they should and, thus, have lower masses than they would at higher resolution (see Bate 2019). Above this mass, the simulated discs are nicely bracketed between the mass distributions of the Perseus and Orion Class 0 objects. The Perseus Class 0 disc dust masses are typically about a factor of two higher than for the simulated discs, and the Orion Class 0 masses are about a factor of two lower. The observed Class I discs have lower masses than the Class 0 discs by factors of 2–3, consistent with them typically being more evolved. The mean disc dust mass for the Class 0 and Class I in Orion are $25.9^{+7.7}_{-4.0}$ and $14.9^{+3.8}_{-2.2}$ $M_\oplus$ respectively and the median disc dust mass for Class 0 and Class I in Perseus are 158 and 52 $M_\oplus$ respectively. The median mass of system discs in the solar

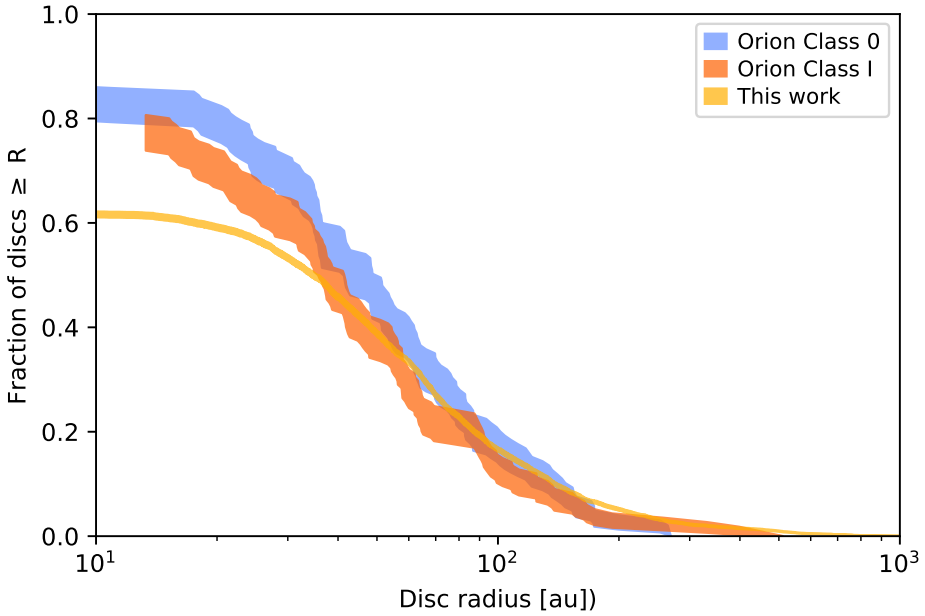

Figure 3.11: Disc characteristic radii distributions from protostellar systems from the solar metallicity calculation of Bate (2019) and for the discs of Class 0 and Class I objects in Orion taken from the VANDAM survey (Tobin et al. 2020). We use the Kaplan-Meier estimate for left censored data where the width shaded region is the confidence interval at 1σ (68%). Observed discs with radii $\leq$ 10au and non-detections are treated as upper limits.

metallicity calculation is 49 $M_\oplus$. Given that there is considerable uncertainty in determining the masses of observed discs (e.g., Tychoniec et al. 2020), the simulated disc masses are in good agreement with the observed Class 0 disc mass distributions.

3.3.3.2 Disc Radii

In Fig. 3.11 I plot the cumulative distributions of Class 0/I dust disc radii from the VANDAM survey of Orion protostars (Tobin et al. 2020), and the equivalent distribution for systems from the solar metallicity calculation. I use the data of all discs from the 0.87mm ALMA observations as at this wavelength the derived radius of a given disc is assumed to be close to the gas radius of the disc. For the observed discs, I treat discs with radii $\leq$ 10 au and non-detections as the upper limits in the analysis.

Immediately it is clear that the radii of discs from the calculation have a remarkably similar distribution to those observed discs for radii $r_c \gtrsim 40$ au. Again, the turnover for the simulated discs at smaller radii is due to the limited numerical resolution of the simulations.

3.3.4 Comparison with Class II objects

Over the past few years, improvements in (sub-)millimetre resolution have given us great ability to conduct large surveys of protoplanetary discs in nearby star-forming regions. Whilst Class II objects are more evolved than any of the protostars I consider in this chapter, it is still useful to compare the empirical trends found from observational studies and those I present.

3.3.4.1 Disc dust mass

Here I compare disc dust masses derived from surveys of various star forming regions with the masses of the simulated discs from the solar metallicity calculation of Bate (2019). Again I use the standard dust to gas ratio of 1:100 to convert the gas masses of the simulated discs into dust masses.

I compare the disc dust masses obtained from the solar metallicity calculation with those derived from observational surveys of Class II objects. I use surveys of: the Lupus star forming region (Ansdell et al. 2016), the Orion Nebula Cluster (ONC) (Eisner et al. 2018), the Orion Molecular Cloud-2 (OMC-2) (van Terwisga et al. 2019), ρ Ophiuchus (Cieza et al. 2019), and λ Orionis (Ansdell et al. 2020). Each derived disc dust mass takes the dust temperature to be $T_{\rm dust} = 20$ K. Note that for the OMC-2 observations I haven't included non-detections, hence the fraction of discs with mass $\geq M_{\rm dust}$ begins at 1.

In Fig. 3.12 I plot the cumulative distributions of disc dust masses from the above surveys and the solar metallicity calculation. I use the Kaplan-Meier estimator with left censoring to account for the upper limits on the observed disc masses. An observation that is deemed to be a non-detection is censored. Plotted in the shaded regions are 1σ ($\approx 68\%$) confidence intervals.

The mean dust masses for Lupus, ONC, OMC-2, ρ Ophiuchus, and λ Orionis are $15 \pm 3\,{\rm M}_\oplus$, $8 \pm 1\,{\rm M}_\oplus$, $67 \pm 9\,{\rm M}_\oplus$, $19 \pm 4\,{\rm M}_\oplus$, and $12 \pm 0.1\,{\rm M}_\oplus$ respectively. The mean dust mass of discs of systems from the solar metallicity calculation is $165\,{\rm M}_\oplus$. It is not surprising that disc dust masses from the simulation are considerably higher than those observed as they are much younger. The most massive discs in the simulation are ~ 1 order of magnitude

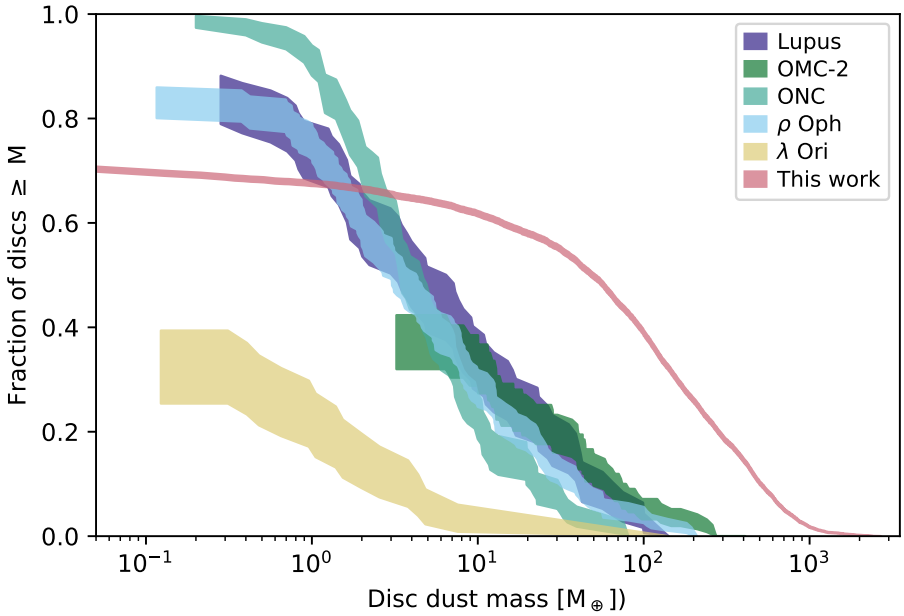

Figure 3.12: Dust mass distributions of discs of protostellar systems from the solar metallicity calculation of Bate (2019) and of the discs of Class II objects taken from surveys of different star forming regions. I use surveys of Lupus (Ansdell et al. 2016), the Orion Nebula Cluster (Eisner et al. 2018), ρ Ophiuchus (Cieza et al. 2019), the Orion Molecular Cloud-2 (van Terwisga et al. 2019), and λ Orionis (Ansdell et al. 2020). I make use of the Kaplan-Meier estimate for left censored data as implemented in the Python package *lifelines* (Davidson-Pilon 2019). The shaded regions indicate a 1σ ($\approx$ 68%) confidence intervals. The observed disc masses of Class II objects tend to be much lower than the simulated discs, as is to be expected if the Class II objects are much more evolved.

more massive than the most massive discs in the Lupus, ONC, ρ Ophiuchus and OMC-2 regions, and around 2 orders of magnitude more massive than the most massive discs in λ Orionis.

3.3.4.2 Disc radii

Here I compare the statistical properties of disc radii in systems formed in the solar metallicity calculation (see Section 3.1.5.2) with the radii derived from observations of Class II objects. I use radii of discs in the ONC (Eisner et al. 2018), Taurus and Ophiuchus (Tripathi et al. 2017), Lupus (Tazzari et al. 2017), Upper Scorpius OB association (Upp Sco) (Barenfeld et al. 2017) regions. Note the survey of Taurus and Ophiuchus (Tripathi et al. 2017) includes 50 discs from the Taurus and Ophiuchus regions, and 9 discs from other regions. Each of these surveys base the disc radii on dust continuum observations. The radii for the ONC, Taurus and Ophiuchus are computed using a Gaussian half width at half maximum whereas Lupus and Upp Sco inferred the radii are from the exponential cutoff radius of a

power-law disc (see Tazzari et al. 2017).

In Fig. 3.13 I plot the cumulative distributions of disc sizes taken from the observational surveys, and of characteristic disc radii of systems from the solar metallicity calculation. Again, I use the Kaplan-Meier estimate with 1σ ($\simeq$68%) confidence intervals. As I have done with the observed discs I left censor simulated discs that are unresolved (i.e. any disc with a gas mass $< 0.01 M_{\odot}$).

Immediately one notes that there is a large dispersion in the observed disc radius distributions from region to region. This dispersion may arise due to the different ages of the regions, different evolutionary processes (e.g. photoevaporation), and/or different initial conditions. The distribution of disc radii from the simulation is slightly less steep than that of the ONC, Lupus, and Taurus and Ophiuchus. The discs in Lupus have a similar radius distribution to the simulated discs. The discs in the ONC are noticably smaller than in the other regions. The ONC has a relatively higher stellar density than, for example, Lupus and Ophiuchus, which may explain the high fraction of compact discs and lack of large discs. However, the initial molecular cloud density for the solar metallicity calculation is also quite high ($n_{\rm H} = 6 \times 10^4$ cm^{-3}) and this does not lead to unusually small discs. The discs in the ONC are also subject to intense radiation from the massive stars so photoevaporation may also be the cause of its smaller discs.

3.3.5 Disc alignments

Observationally, many examples of binary protostellar systems with circumstellar discs that are misaligned with each other have been found over the past couple of decades (see Section 3.2 of Bate 2018 for a recent summary). Early evidence for systems where discs were presumably misaligned with binary orbits when the systems were young came from the observed misalignment of stellar spins and binary orbital planes (Weis 1974; Guthrie 1985). Hale (1994) found a preference for alignment for binary separations $a \lesssim 30$ au and random uncorrelated stellar rotation and orbital axes for wider systems, i.e. the angular momentum of the star rotation is not longer correlated with the angular momentum of the system orbit. Similar dependence of the alignment of protostellar (sink particle) spins on the orbital separation of binaries has been reproduced by past hydrodynamical

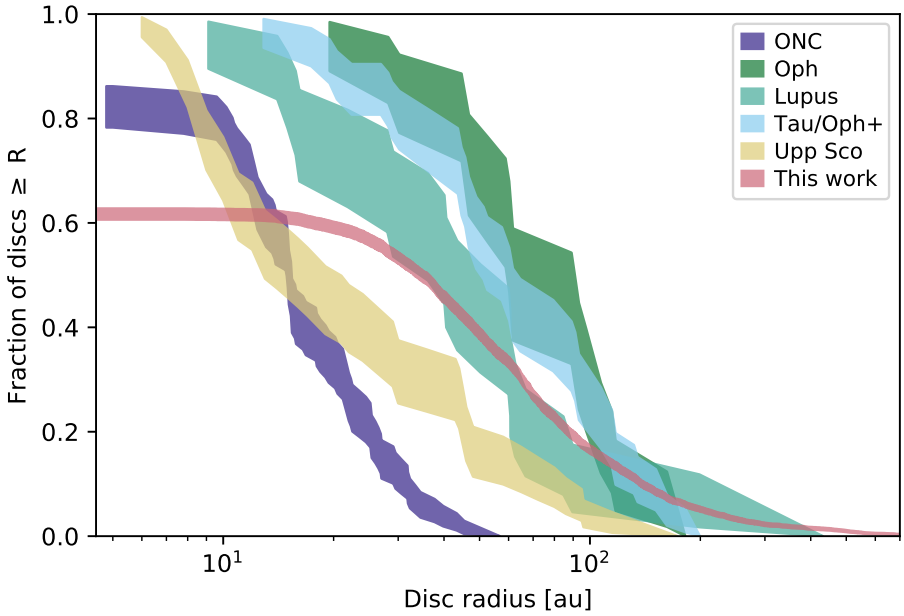

Figure 3.13: Cumulative distributions of the characteristic radii of discs of systems from the solar metallicity calculation of Bate (2019), and discs observed in the Orion Nebula Cluster (Eisner et al. 2018), Ophiuchus (Tripathi et al. 2017), Taurus and Ophiuchus (Tripathi et al. 2017), Lupus (Tazzari et al. 2017), and Upper Scorpius OB association (Barenfeld et al. 2017) regions. I use the Kaplan-Meier estimator to plot the cumulative distributions in order to take into account upper limits (unresolved discs) with the shaded region showing a 1σ ($\simeq 68\%$) confidence interval.

simulations of star cluster formation (e.g. Bate 2012, 2014)

Recently, Aizawa et al. (2020) examined five star forming regions (Lupus, ρ Ophiuchi, Orion, Taurus, Upper Scorpius) to see whether or not discs were aligned with each other on larger scales than bound stellar systems. They find no overall alignment of discs in all regions except in a sub-region of Lupus (Lupus III), where they find 16 discs that differ from random alignment at the 2σ level. These discs appear to be aligned with the filamentary structure of the cloud. Carrying out a similar analysis of discs formed in the calculations analysed here, I find no overall alignment of discs. One expects to find no overall alignment of discs in the calculations as the initial cloud has little net rotation and it does not include magnetic fields.

3.3.6 Discs at low metallicity

The disc fraction in young low metallicity star clusters is observed to be lower than in clusters of higher metallicity at a similar age ($\sim$ 0.5 Myr), providing evidence that discs

have a shorter lifetime at low metallicities (Yasui et al. 2009; Yasui et al. 2016; Yasui et al. 2021). Ercolano and Clarke (2010) show that these observations may be due to the metallicity dependence of disc dispersal by photoevaporation. I am not able to follow discs in the hydrodynamical calculations to these ages (the oldest discs in the lowest metallicity calculation are $\sim 10^4$ yr old), and photoevaporation is not included in the calculations. However, I do find that young discs at lower metallicity have smaller radii and a higher fraction of systems have unresolved or low-mass discs (Fig. 3.3), which may also help to explain the observed metallicity dependence of disc fraction in young clusters.

3.3.7 Planet formation

The occurrence of giant planets orbiting solar type stars has been shown to decrease with decreasing metallicity (Gonzalez 1997; Santos et al. 2001; Fischer and Valenti 2005; Johnson et al. 2010), and the dust mass of debris disc stars with planets correlate with stellar metallicity (Chavero et al. 2019). The core accretion mechanism for giant planet formation has been shown to be less efficient at producing giant planets in metal-poor discs (e.g., Ida and Lin 2004), and Matsumura et al. (2021) find that in low mass and/or low metallicity discs the formation of giant planets is difficult, and planet formation overall tends to be slower. More rapid disc dispersal at lower metallicities would also inhibit giant planet formation (Ercolano and Clarke 2010). If the initial disc properties also depend on metallicity, as found here, with metal-poor discs having smaller radii and a higher fraction of systems have unresolved or low-mass discs (Fig. 3.3), this will also contribute to the paucity of massive planetary systems around metal-poor stars.

3.4 Conclusions

I have presented an analysis of the protostellar discs produced in the four radiation hydrodynamical calculations of star cluster formation with metallicities varying from 1/100 to 3 times solar metallicity first published in Bate (2019). These calculations are have identical initial conditions except for their metallicity and, thus, their initial gas and dust temperatures. This analysis closely follows the analysis of the statistical properties of discs in an earlier solar metallicity calculation Bate (2018). I obtain very similar statistical proper-

ties from the more recent solar metallicity calculation as those that were obtained by Bate (2018), but I am able to explore the metallicity dependence of disc properties.

I have the following conclusions:

1. Higher metallicity typically leads to the formation of larger discs. This is the case for discs of individual protostars, discs of protostars that have never had an encounter within 2000 au, and the discs of stellar systems in general (i.e. single and multiple systems). The discs of protostellar systems in the 3 times solar metallicity calculation have a median characteristic radius of ≈ 65 au and median of ≈ 20 au in the 1/100 time solar metallicity calculation.

2. Discs of protostars that are isolated (they do not have a companion protostar within within 2000 au at the time they are observed) and discs in protostellar systems tend to be slightly more massive with higher metallicity. However, this relation is reversed for discs of protostars that have never had a companion within 2000 au – discs at the highest metallicity ($Z = 3\ Z_\odot$) are typically twice as massive as very low metallicity ($Z = 0.01\ Z_\odot$) discs.

3. Discs in bound pairs (either binaries or components of high-order systems) tends to be well aligned for a semi-major axes $a \lesssim 100$ au across all calculations. In the 1/100 solar metallicity calculation the discs in wide pairs $a \gtrsim 100$ are less well aligned than in the calculations with a higher metallicity with more or less random orientations.

4. In pairs with separations $a \lesssim 100$ au discs tend to be well aligned with the orbital plane of the pairs. Again, discs and orbits in pairs with $a \gtrsim 100$ in the 1/100 solar metallicity calculation, are generally poorly aligned with essentially a random distribution of orientations between zero and 130 degrees.

5. Relative orientation between bound sink particle spins (representative of the angular momentum of the protostar and inner part of the disc) are also sensitive to a change in metallicity. For the super-solar and solar metallicity calculations it is only those pairs closely separated ($a \lesssim 30$au) that tend to be well aligned. For the two sub-solar metallicity calculations spins of pairs separated by $a \lesssim 100$ au tend to be well aligned,

but the spins of wider systems are less well aligned than for higher metallicities with essentially random alignment. For the particular case of pairs with separations $a >$ 1000 au in the 1/100 solar metallicity calculation most of the pairs have retrograde spins relative to each other.

6. Discs and sink particle spins of individual protostars in bound pairs tend to be well aligned in all calculations with no significant dependence on separation. The lowest metallicity calculation has the strongest preference for alignment with $\approx 90\%$ of discs and spins having a relative orientation angle of 45° or less.

7. There is no overall preferential orientation for discs in each simulation as a whole. This is expected as magnetic fields are not included and the overall net rotation of each molecular cloud is very small.

8. The reason that discs sizes tend to be smaller, the fractions of unresolved or low-mass discs are higher, and that the discs, orbits and protostellar spins of wide pairs tend to be less well aligned as the metallicity is decreased is because lower metallicity increases the rate of cooling of high-density gas. This produces more gravitational fragmentation (both of collapsing molecular cloud cores and massive discs), leading to higher multiplicity and a greater role of dynamical interactions between protostars (Bate 2019).

9. The masses of the discs of the systems in the solar metallicity calculation have a similar distribution to the masses of Class 0/I discs observed in the Perseus and Orion star-forming regions. The disc mass distribution from the simulation lies in between the Class 0 disc mass distributions obtained from Perseus and Orion, is similar to the Class I distribution in Perseus, and is roughly 0.6 dex more massive than the Class I discs in the Orion star-forming.

10. The distribution of disc radii of systems in the solar metallicity calculation is in very good agreement with the disc radius distributions of Class 0/I discs observed in the Orion star-forming region.

11. When compared to observations of Class II objects, the disc masses from the solar

metallicity calculation are typically one order of magnitude greater than those estimated from dust observations of the discs in most local star-forming regions, λ Ori excepted. The radii of the discs are similarly distributed to discs observed in the Lupus region.

In the future, the radiation hydrodynamical calculations could be improved by increasing the numerical resolution to resolve lower mass and smaller discs. Furthermore, although the calculations include radiative transfer, separate gas and dust temperatures, and a thermochemical model of the diffuse interstellar medium, they do not include radiative feedback from the protostars themselves. Also, magnetic fields are not included. Despite these limitations, the disc mass and size distributions that are obtained from the calculations are in spectacularly good agreement with those of observed Class 0/I protostars in Perseus and Orion. In particular, this seems to indicate that magnetic braking does not play a large role in determining the properties of protostellar discs (c.f. Seifried et al. 2013; Wurster et al. 2019).

Chapter 4

On the frequencies of circumbinary discs in protostellar systems

"This is getting out of hand. Now there are two of them!"

— Nute Gunray, Viceroy of the Trade Federation

Stars commonly form in binary systems (e.g. Abt and Levy 1976; Duquennoy and Mayor 1991; Ghez et al. 1993; Fisher 2004; Raghavan et al. 2010). It is widely accepted that most stellar binaries form due to fragmentation of the protostellar core, or protostellar discs (e.g. Boss and Bodenheimer 1979; Boss 1986; Bonnell and Bate 1994; Bate et al. 1995; Kratter and Matzner 2006; Clarke 2009). When forming, binaries are not able to form directly with a separation of less than $a \sim 10$ au due to the opacity limit of fragmentation (Boss 1986; Bate 1998). Close binaries ($a < 10$ au) are likely to have migrated inwards due to accretion, interactions with discs, and/or dynamical interactions with other stars (Artymowicz et al. 1991; Bate et al. 2002; Tokovinin and Moe 2020). During the star formation process a binary system may capture gas with high angular momentum from its local environment to form a natal circumbinary disc around a binary. The dynamic interactions between the disc and the binary can dominate the evolution of the natal disc (**lin_tidal_1979.186..799L**; Papaloizou and Pringle 1977; Lin and Papaloizou 1979a). The outcome of such interactions are dependent on properties of the binaries themselves, for example the semi-major axis of the system (a) and the mass ratio of the component stars (q)

(see Artymowicz and Lubow 1994, for example). Binaries with a semi-major axis $a < 50$ au are observed to truncate the outer radius of circumstellar discs (Jensen et al. 1996b) whilst close binaries ($a \lesssim 10$ au) are likely to have circumbinary (CB) discs (Harris et al. 2012). Such discs are also known as discs in the "P"-type configuration (Dvorak 1982).

CB discs were first identified in the 1990s, beginning with a combination of resolved CB discs around multiple systems: GG Tauri (Kawabe et al. 1993; Dutrey et al. 1994), UZ Tauri E (Jensen et al. 1996a; Mathieu et al. 1996), UY Aurigae (Duvert et al. 1998); and inferred discs around known multiple systems: GW Orionis (Mathieu et al. 1995), AK Sco and V4046 Sgr (Jensen and Mathieu 1997), DQ Tau (Mathieu et al. 1997). Over the past 30 years some of the complexities of these systems have been revealed, such as disc size, and system orientation. The discs around GW Ori have been a focus of interest recently due to the geometry of the system (Czekala et al. 2017; Bi et al. 2020; Kraus et al. 2020) with evidence that the disc surrounding this system is inclined $\sim 45°$ to the stellar orbital plane, and Kraus et al. (2020) suggest this misalignment is due to disc warping and tearing. In addition to this some observed features in CB discs have been attributed to disc warps. Marino et al. (2015) discovered a warped inner disc of HD 142527 casting shadows on the outer disc. Warps have previously been proposed to be the cause of non-axisymmetric features of CB discs, as in the case of the T-Tauri disc TW Hya (Rosenfeld et al. 2012). Like discs around single objects, CB discs can extend out to 100s of au, for example the CB disc of V892 Tau has CO gas emission detected at 200 au from the central binary (Long et al. 2021). CB discs can live into the Class II phase, with an approximate lifetime of 2 Myr (Kraus et al. 2012). However, whilst more than forty CB discs have now been detected (see Czekala et al. 2021, and references therein) their detections are relatively scarce compared to discs about single objects. For example, Akeson et al. (2019) detected no new CB discs even in their survey of multiple systems in the Taurus-Auriga star-forming region with a non-detection limit that corresponds to a gas mass of approximately 0.04 Jupiter masses.

It is not known at what rate CB discs should occur, or their typical lifetimes, due to difficulties observing them. On scales $\lesssim 100$ au optically thick dust emission can make it difficult to detect companions separated $\lesssim 50$ au (Tobin et al. 2016b). Despite these difficulties there have been some observations of very young CB discs in embedded Class

0 objects (e.g. Harris et al. 2018; Sadavoy et al. 2018; Hsieh et al. 2020; Belinski et al. 2022). Tobin et al. (2018) find circum-multiple dust emission around eight of the nine Class 0 multiple objects they observed in the Perseus region, although they find none around Class I multiple objects. This may be an indication of the typical lifetime of such discs.

Due to the turbulent nature of molecular clouds, chaotic accretion can take place (Bate et al. 2003b; McKee and Ostriker 2007) and cause misalignments between the binary orbital plane and circumbinary disc (Bate et al. 2010; Bate 2018). There are observations of inclined circumbinary discs, for example KH 15D (Chiang and Murray-Clay 2004) and IRS 43 (Brinch et al. 2016). Recently there has been additional theoretical work done on the evolution of circumbinary disc inclinations. Notably, initially misaligned discs around eccentric binaries can evolve to a polar alignment (Martin and Lubow 2017). Such a disc has been confirmed by observations: the CB disc around the system HD 98800 (Kennedy et al. 2019). Misaligned discs can also occur due to Kozai-Lidov oscillations (Zeipel 1910; Kozai 1962; Lidov 1962), in which disc inclination and eccentricity are exchanged (Martin et al. 2014; Fu et al. 2015; Aly and Lodato 2020). During these oscillations dust that is sufficiently coupled to the gas undergoes oscillations on the same timescale as the gas. The dust may have a different distribution to that of the gas due to a higher radial velocity drift (Zagaria et al. 2021), and during periods of high disc eccentricity the dust may break into rings (Martin and Lubow 2022). Kuruwita and Federrath (2019) suggest that molecular cloud cores that are more turbulent may produce more massive CB discs, potentially extending their lifetimes. This may have an impact on planet formation, if the lifetime of the disc is shorter than the timescale of alignment, and planet formation is sufficiently quick, then the planet may be left misaligned to the binary.

Even though CB disc detections are somewhat uncommon, there is a growing catalogue of circumbinary planets in particular around eclipsing binaries, where the planet transits the binary objects. The eclipsing binary method is an effective way to detect close-in planets around binary objects due to the high likelihood that a planet will transit the objects (see Martin and Triaud 2015). Most of these have been detected by the *Kepler* spacecraft (e.g. Doyle et al. 2011; Welsh et al. 2012), with the *Transiting Exoplanet Survey Satellite* (*TESS*) recently discovering two (Kostov et al. 2020; Kostov et al. 2021). This indicates

that CB discs not only form but can live long enough for planets to grow. Using eclipsing binaries to detect planets mostly relies on the planets being coplanar with the binary orbit. So there is a selection effect. However with the recent detection of a circumbinary planet using radial velocities, which are less restricted to an edge-on configuration, this may change (Standing et al. 2023). If coplanarity is preferred for close binaries then these detections suggest that binaries may have a planet occurrence rate close to that of single stars; if the distribution of planetary orbit inclination is more uniform, then the occurrence rate could be higher than that of single stars (Armstrong et al. 2014). Observing transits of misaligned CB planets becomes a more difficult problem due to the geometry of the system, however there have been efforts to develop a method to detect such planets (see Martin and Triaud 2014, for example).

Given that discs are a natural consequence of star formation, and most stars form in pairs, it is important to understand the statistical properties of CB discs. In addition to this, since there is a growing catalogue of planets orbiting a central binary, the properties of the protoplanetary circumbinary discs also impact planet formation. Knowing how often one expects a disc to form around a binary, how long they tend to live for, and how they are inclined relative to their binary has significant implications for planet formation.

In this chapter I present: a method of characterising these discs from star cluster formation simulations in Section 4.1, the statistics of the circumbinary discs in Section 4.2, a comparison of simulated disc statistics with observed disc statistics in Section 4.3, and the conclusions in Section 4.4. The calculation analysed in this chapter is the solar metallicity calculation from Chapter 3 and has already been discussed in detail. I will not discuss the details of the calculation here.

4.1 Methods

The discs studied in this chapter are from a calculation originally published by Bate (2019). For a full description of the methods used to perform the calculation and the properties of the star cluster the reader is directed there. Here I give only a brief overview of the algorithm used to extract the circumbinary discs and their properties in Section 4.1.1

4.1.1 Disc characterisation

In characterising the properties of the CB discs, I follow the method of Bate (2018). The discs formed in these calculation continually evolve due to a range of hydrodynamical processes (Bate 2018), so to study the properties of the discs I extract properties many times during the calculation. The idea is that if observers examined a very large sample of real protostellar systems the ensemble would consist of systems with many different ages. Snapshots of the discs are taken every $0.0025t_{\rm ff}$ (476 yr) for each protostar. In the solar metallicity calculation this gives 16048 instances of circumstellar discs, and 1515 instances of circumbinary discs.

Previous similar studies of discs (Bate 2018) and the one presented in the previous chapter have found that the basic disc properties (masses and sizes) are in quite good agreement with the observed discs of young (Class 0) protostellar systems. Those studies considered discs in single and multiple systems, however I did not study circumbinary discs in detail. Both Bate and I included CB discs along with discs of triple and quadruple systems (circum-system discs) but CB discs were not studied separately. In this chapter I examine CB discs in much greater detail.

4.1.1.1 Circumstellar discs

In this thesis I have already discussed how discs are characterised and so I will only very briefly layout the most important aspected of disc characterisation

Prior to discussing how I characterise circumbinary discs, first it is essential to discuss how I characterise circumstellar discs as discs can form about either one, or both of the protostars in the binary pair. The discs around individual components are usually referred to as circumstellar discs. First let us consider a single protostar. The SPH gas and sink particles are sorted by distance from the sink particle representing the protostar. Starting with the nearest particle, it is decided this is part of the protostellar disc if:

1. it has not already been assigned to another disc,

2. the instantaneous ballistic orbit of the particle has an apastron distance of less than 2000 au,

3. its orbital eccentricity $e < 0.3$.

If these criteria are met the mass of the particle is added to the system mass, and the position and velocity of the centre of mass of the system are calculated. This is repeated for the next closest particle. Particles are only considered if they are closer than 2000 au. If a sink particle is found when traversing the list of particles the identity of the sink is recorded, and the process of adding mass to the circumstellar disc is ended. In other words, the disc does not include any gas particles more distant than the closest protostar.

Following Bate (2018), when referring to the radius of a disc I mean the characteristic radius, r_c, from the truncated power-law density profile (Fedele et al. 2017; Tazzari et al. 2017)

$$\Sigma(r) = \Sigma_c \left(\frac{r}{r_c}\right)^{-\gamma} \exp\left\{\left[-\left(\frac{r}{r_c}\right)^{(2-\gamma)}\right]\right\}, \tag{4.1}$$

where γ is the power-law radial density profile of the disc, and Σ_c/e is the gas surface density at r_c. When $\gamma < 2$, r_c is always the radius that contains $(1 - 1/e)$ of the total disc mass ($\sim$ 63.2 per cent; Bate (2018)). Equation 4.1 only gives a sensible distribution for $\gamma < 2$. Therefore, I do not fit Equation 4.1 to a disc. Rather, I obtain r_c simply by measuring the radius that contains 63.2 per cent of the total disc mass.

4.1.1.2 Circumbinary discs

Many of the discs formed in these calculation are found to be in bound multiple systems. The scope of this chapter is to discuss the discs surrounding bound 'pairs' of protostars. Sometimes there are binary systems within a higher order system (e.g. a triple system consisting of a binary and a companion). I will be clear whether the binary is a pure binary or a binary within a higher order system when discussing results.

The mass of CB discs is computed in a similar way to that of circumstellar discs. However, instead of searching radially outward from a sink particle I calculate the centre of mass of the binary pair and search radially from there. Note, the sink particles of the bound pair do not cause the radial search to stop in this case. Similarly to the circumstellar discs I list all particles within 2000 au of the centre of mass of the system in order of distance. When going through the list of particlesIignore particles that are contained in

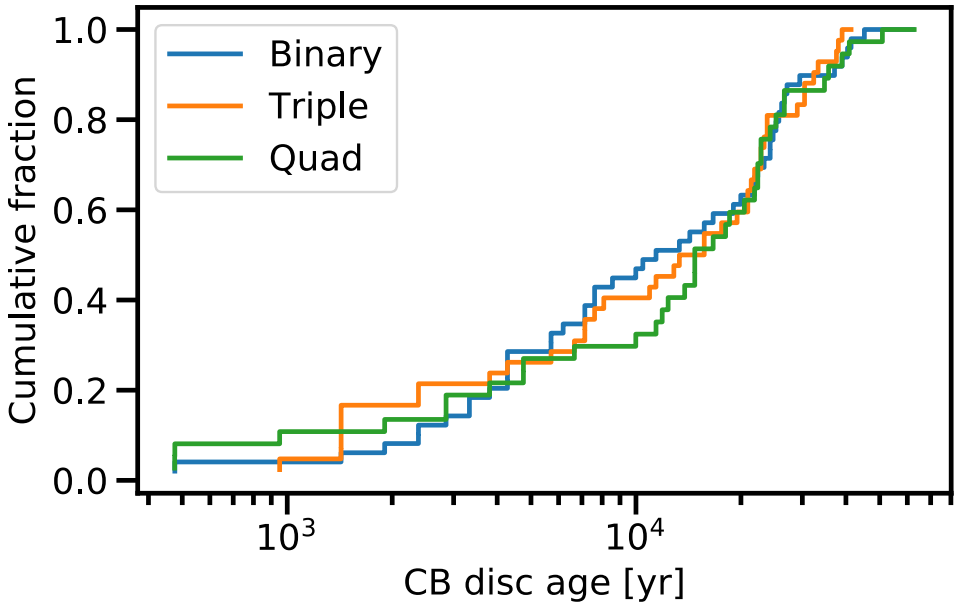

Figure 4.1: Cumulative distributions of the ages of discs taken at either the end of the calculation or at the final snapshot they are recorded in, i.e. the disc is no longer classified or the central object is no longer a binary (e.g., a merger may take place, the binary may become unbound, or another components may exchange into the original binary). Most of the discs in all multiple systems live longer than 10^4 yr. There is no significant multiplicity dependence on the age distributions of the CB discs.

any of the component discs (i.e. circumprimary or circumsecondary). Applying the same criteria as above, I obtain a small number of 'CB discs' that are in fact envelope material. To avoid this I added one more requirement to extract CB discs. I discard any 'CB discs' that contain less than 50 per cent of the total system disc mass (i.e. sum of circumbinary, primary, secondary disc masses). This value was chosen as it means each CB disc will have a significant mass relative to circumstellar discs, and was found to be effective at ignoring envelope material whilst keeping what would usually be considered to be CB discs. This percentage of total mass may seem to be high; this is discussed more in the next section.

Upon incorporating these criteria the number of instances of CB discs is reduced to 1465, from 1515. There are 650, 409, and 406 instances of CB discs in pure binaries, triples, and quadruples respectively.

4.2 Results

In this section I present statistics on CB discs found within the solar metallicity star formation calculation of Bate (2019). In Chapter 3 I studied the disc properties of all four calculations from Bate (2019) and found some dependence on metallicity. Typically disc size decreases with metallicity, and discs and orbits of bound pairs tend to be less aligned at lower metallicity. Therefore one expects there to be some difference in the statistics of CB discs in calculations differing metallicity (e.g. smaller disc size, and a lower occurrence rate of CB discs at lower metallicity), however this is outside the scope of this study.

I summarise the ages of CB discs in the solar-metallicity calculation in Section 4.2.1 and the occurrence rate of CB discs in different systems in Section 4.2.2. In Section 4.2.3 I present the numerous different statistics of the CB discs in the cluster simulations, e.g. radius/mass distributions, disc-orbit mutual inclinations, radius in units of binary separation, disc mass to system mass ratio. The statistics generated from the calculation are from snapshots taken throughout the simulation, every 476 yr. This means that if a disc is present in the calculation for multiple snapshots then the properties of this disc will be included that number of times. Because the discs are continually evolving, the properties of the disc change enough between snapshots that no two snapshots are the same. This does mean, however, that not all instances are strictly independent from each other.

4.2.1 Ages of discs

As the calculation is only run for a set time period (1.20 $t_{\rm ff}$) and the first stars form at 0.606 $t_{\rm ff}$, the oldest protostars can only be $\approx 10^5$ yr old at most. When considering the frequency of CB discs, it would be useful to know how old the discs are. If discs tend to be short lived it would make them less likely to be observed. In Fig. 4.1 I plot the cumulative age distribution of the CB discs at the point where they fail to meet the criteria laid out in Section 4.1.1 for CB discs in binary, triple, and quadruple systems. The distributions in Fig. 4.1 suggest that it does not matter if the disc is around a bound pair in a binary or a hierarchical system; they tend to live, regardless of the system, at least up until ages of $\approx 10^4$ yr. Note that during the simulation discs come and go, i.e. a disc may form around a binary and then cease to be present at a later time. Additionally, sometimes discs may

briefly fail to meet the criteria laid out in the previous section and then go on to satisfy them at a later point. No CB discs found in the simulation have ages greater than 8×10^4 years. The older discs tended to be the most massive ones to form in the simulations (0.1-1 $M_\odot$). These systems are very young compared to those that would typically be observed, however there are some cases of CB discs about comparatively young objects. For example, young CB discs have been observed in L1551 NE (Takakuwa et al. 2012), L1448 IRS3B (Tobin et al. 2016a), IRAS 16293-2422 A (Maureira et al. 2020), and VLA1623 A (Hsieh et al. 2020). This is an indication that CB discs form quickly about protostellar binaries. In the case of L1448 IRS3B, the system is estimated to be less than 150,000 years old.

During their evolution, CB discs can be disrupted in many ways due to the highly dynamic and chaotic process of star formation that can lead to them to having their properties altered or being destroyed entirely (see Bate 2018, which discusses the many processes that can drive disc evolution). This happens on many occasions in this simulation. For example, the CB disc formed around sink particles 3 and 6 (numbered in the order of formation in the calculation) grows in mass until it reaches $\approx 0.4 M_\odot$, after which its mass suddenly decreases by three orders of magnitude. The sudden drop in disc mass is caused by the fragmentation of the CB disc to form a protostar, forming a triple system. CB discs that are misaligned and undergo fragmentation may result in triple systems that are also misaligned. The disc around sinks 9 and 13 is the most massive disc in the simulation ($\approx 0.8 M_\odot$), rapidly growing towards the end of the calculation, until there is a significant increase in dynamical interactions and the disc is completely destroyed. Another example of how CB discs can have their properties altered is the disc around sinks 52 and 176. This disc's mass goes through periodic increases and decreases in mass. This however is not due to periodic busts of accretion, but rather the capture of a third outer star that then orbits the system sweeping through the disc, accreting material away from it but not totally destroying it. These and other events can be viewed in the disc mosaic animation that was published as supplementary material with Bate (2019).

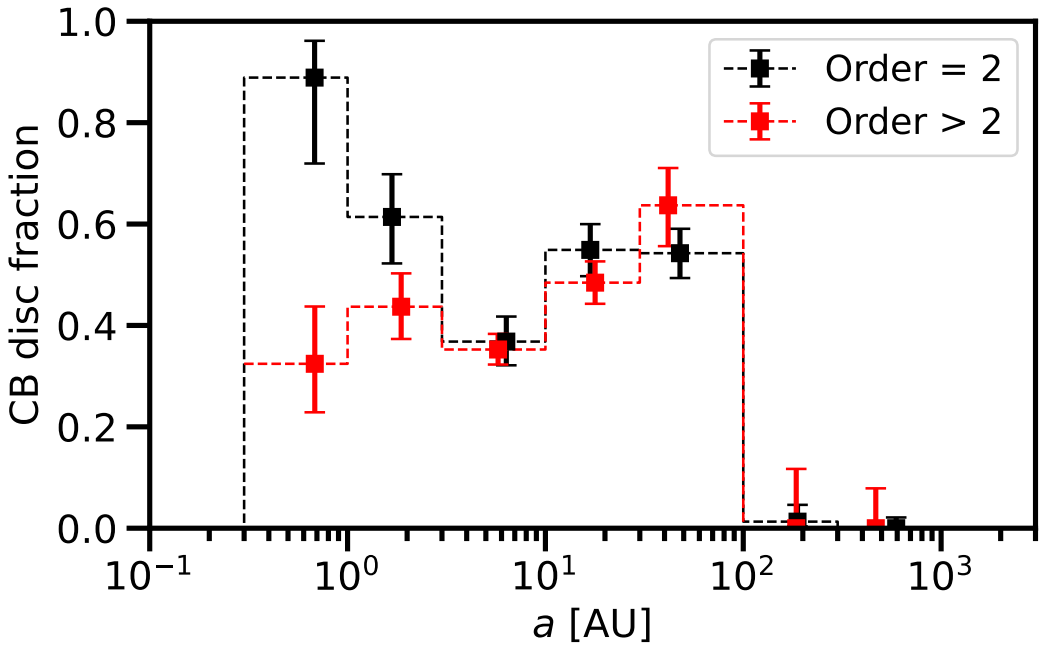

Figure 4.2: The fraction of binaries that host circumbinary discs plotted in bins of binary separation. The fraction of discs in pure binaries if plotted in black, and in red for hierarchical systems. The separation bins are divided as following: 0.3-1, 1-3, 3-10, 10-30, 30-100, and 300-1000; all in au. There are no discs in systems with separation larger than 300 au.

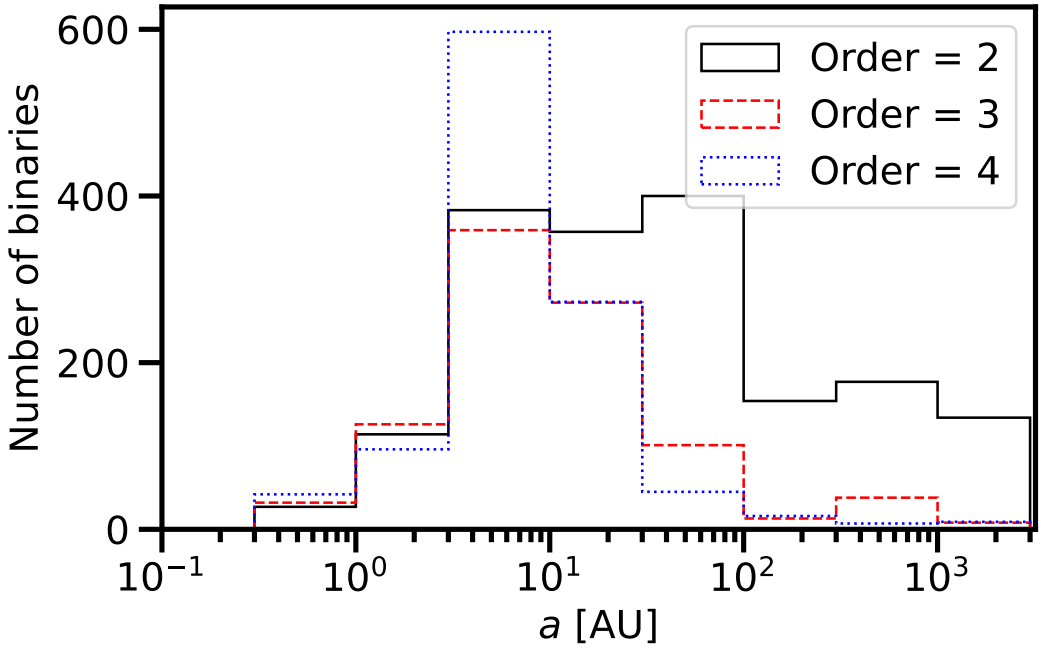

Figure 4.3: Instances of binary systems in bins of binary separation. I plot the number of binaries in each type of system, binary (solid black), and hierarchical triple (dashed red) and quadruple (dotted blue). The separations are binned as following: 0.3-1, 1-3, 3-10, 10-30, 30-100, 100-300, 300-1000, 1000-3000; all in au. There are no binaries with separations larger than 3000 au.

4.2.2 Frequency of discs

Here I consider the fraction of binary systems that host a circumbinary disc. I consider pure binaries and binary pairs in hierarchical systems separately. The separations of the binaries are logarithmically binned every 0.5 dex, and then I count the number of discs about binaries in each bin. The resulting distributions are plotted in Fig. 4.2. The points plotted in Fig. 4.2 are the mean separation of the disc hosting binaries in each bin, and the associated error-bars are calculated using Wilson's interval (Wilson 1927), where the observed probability of a binary having a disc is given by $\hat{p} = (N_{\rm discs}+1)/(N_{\rm binaries}+2)$. The fractions are based upon the instances of binary pairs. I count the number of instances of pairs and the number of pairs with a CB disc across all snapshots and bin them by binary separation. When considering the fraction of pure binaries that host a CB disc one sees a bimodal distribution of CB disc fraction with peaks at $a \approx 0.7$ au, and $a \approx 30$ au in binary semi-major axis. The peak at smaller separations is higher than the peak at larger separations, with 89 per cent of tight binaries hosting a disc compared to around 55 per cent of intermediate separation binaries. Broadly the fractions of binaries in hierarchical systems that host a CB disc are similar except for tight binaries ($a \lesssim 3$ au); for $a > 3$ au there is no significant difference. In hierarchical systems tight binaries are less likely to host a CB disc than strict binary pairs. Note, a in hierarchical systems is the separation between the closest bound pair in the system.

In Fig. 4.3 I show the number of binary system instances in the same separation bins that were used to calculated the CB disc fractions. For separations of $a < 3$ au the number of binary systems are similarly distributed regardless of order. In hierarchical systems the number of binary pairs peaks in the $3 < a < 10$ au separation bin, and then tails off as separation increases with very few pairs with $a > 100$ au. In pure binary systems the number of binaries is roughly uniform in log-separation for $3 < a < 100$ au, then the number of binaries decreases when $a > 100$ au.

The range 3–100 au has the highest total number of binaries (Fig. 4.3). Circumbinary disc hosting binaries with separations $3 < a < 100$ au tend to become more common as the separation increases up to $a \approx 100$ au (Fig. 4.2); the CB disc fraction drops to almost zero when $a > 100$ au in all systems. This suggests that binaries this wide are very rarely able to

form a rotationally supported disc. When taking into account that the binary separation distribution peaks at $\approx$ 30 au, both in the calculation and observations (e.g., Raghavan et al. 2010), CB discs should typically be found around 10 – 100 au binaries.

For pure binaries, systems with $10 < a < 30$ au, and $30 < a < 100$ au roughly host the same fraction of discs. The error-bars give a 2σ confidence interval on the probability of a binary hosting a disc given the number of discs and binaries. Note the caveat that the sample of discs is not strictly independent.

4.2.3 Disc statistics

In Fig. 4.4 I plot the CB disc dust mass against the ratio of the CB disc mass to total system disc mass, with the characteristic radius of the CB discs shown by the colour of the points. Note that all plots in the remainder of the paper are generated from instances of CB discs and/or bound pairs. I assume a dust-to-gas ratio of 0.01 to compute the dust masses. As mentioned in Section 4.1.1 I only consider CB discs that contain at least 50 per cent of the total disc mass. This may seem like a high percentage but considering $\sim$ 87 per cent of CB discs contain more than 95 per cent of the disc mass of the system it captures the vast majority of CB discs. The 'discs' that are discarded with this criterion tend to be of a mass lower than 0.03 $M_\odot$ (100 $M_\oplus$) and have a radius of less than the separation of the binary orbit. This suggests that young binary systems with CB discs tend to have significant discs, and that the discs about the component stars tend to be comparatively low mass. Discs with masses of less than 0.01 $M_\odot$ ($\approx$ 30 $M_\oplus$) are poorly resolved by the calculation, due to too few (< 700) SPH particles modelling them.

When considering the separation of the binary system I find that the radius (r_c) of the CB disc tends to increase with separation. I show this in Fig. 4.5 (left panel) for pure binaries, with the mass of the CB disc shown in the colour map. All binaries that host a CB disc have a separation $a < 110$ au with discs generally smaller than $r_c \lesssim 200$ au. I find the median value of CB disc radius in units of binary semi-major axis, a, is $\sim$ 4.9 in pure binaries, and $\sim$ 5.4 and $\sim$ 6.1 in triple and quadruple systems, respectively (i.e. there is no great difference). Note that I do not find a trend between CB disc mass and CB disc radius.

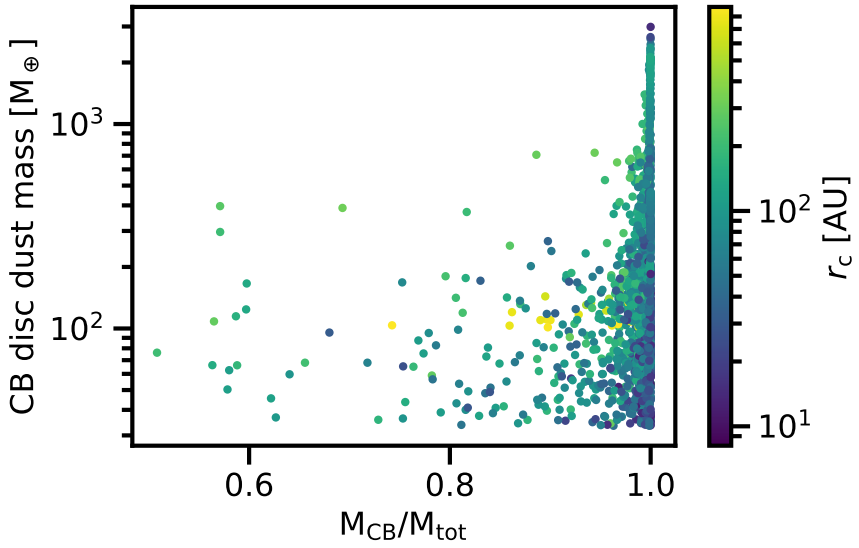

Figure 4.4: Graph of the circumbinary disc dust mass against the fraction of the circumbinary disc mass to the total disc mass. In addition, the radius of the CB disc is shown using the colour of the points. The bulk of the CB discs contain more than 90 per cent of the total disc mass in of the binary. There are only a handful of systems for which more than 20 per cent of the disc mass is in the circumstellar discs. Typically, the lower the CB disc mass, the more likely it holds less of a proportion of the total disc material.

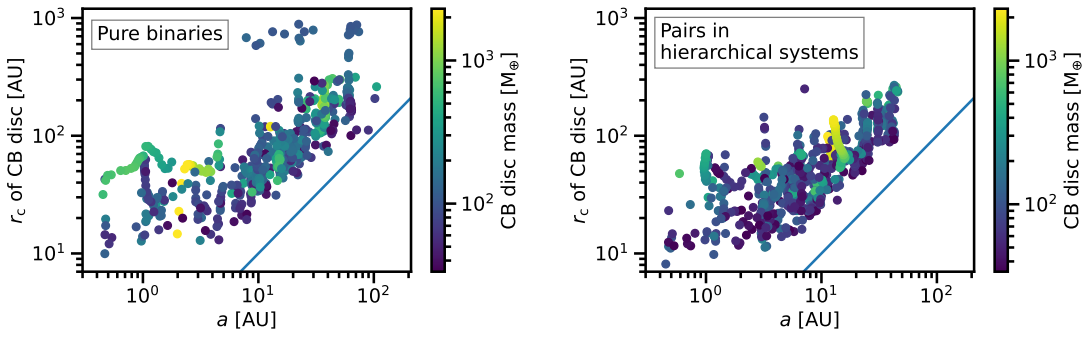

Figure 4.5: The radii of CB discs in pure binaries (top) and hierarchical systems (bottom), and how they depend on binary semi-major axis. The masses of the CB discs are shown using a colour map. The blue line in both plots is where $r_c = a$. As expected, all CB disc radii are greater than the semi-major axis, typically by factors of 3-8 for $a \gtrsim 5$ au.

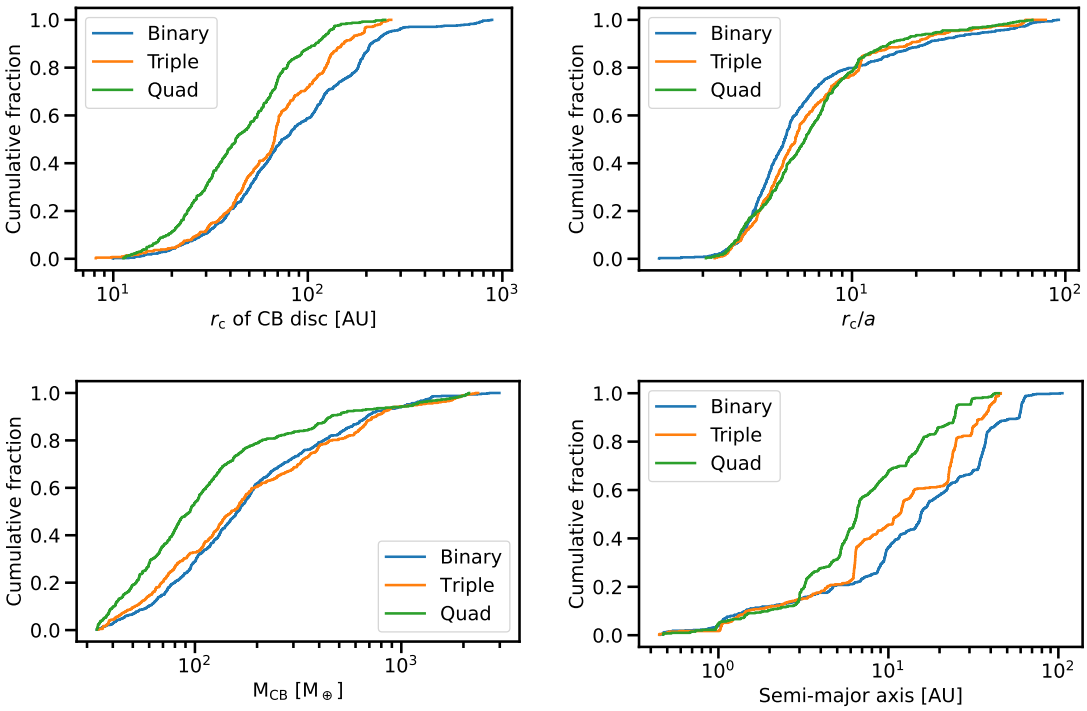

Figure 4.6: The cumulative distribution of CB disc radii measured in au (top) and as a fraction of the binary's semi-major axis (upper middle) in binary, triple, and quadruple systems. I also give the cumulative distributions of CB disc dust masses (lower middle), and semi-major axes of bound pairs in pure binaries and hierarchical systems with CB discs (bottom). The radii of CB discs is lower systematically with increasing order, mainly because the binaries in higher-order systems are systematically closer. The masses of CB discs in pure binaries and in hierarchical triples are very similar, but they are lower in hierarchical quadruples. Semi-major axis of bound pairs tends to decrease with increasing order.

In Fig. 4.5 (right panel) I show a similar trend for binaries in higher-order systems, however the maximum radii of the CB discs appear to be lower. None of the CB discs have a radius $r_c > 300$ au, and there are also no disc-hosting binaries in hierarchical systems with a separation $a > 50$ au. The radii of CB discs in quadruple systems are systematically lower than those in pure binary systems, see Fig. 4.6 (top left). However, this is slightly misleading because whilst the CB discs in hierarchical systems tend to be smaller, the separations of the binaries also tend to be smaller. Therefore, in the top right panel of Fig. 4.6 I show the cumulative distribution of disc radii measured as a fraction of binary separation (i.e., r_c/a). CB discs sizes relative to their binary in all systems are similarly distributed, and thus the disc sizes don't differ significantly for a given binary separation.

I plot the cumulative distribution for CB disc masses in systems of differing order in the bottom left panel of Fig. 4.6; CB discs in triple and binary systems have a very similar distribution of masses, whereas the CB discs in quadruple systems tend to be about a factor of two lower in mass. In the bottom right panel of Fig. 4.6 I show the cumulative distributions of binary semi-major axis for binaries in binary, triple, and quadruple systems. Until binaries become more separated than ~ 3 au the semi-major axes of binary pairs are almost identical across multiplicity. After this point there is a deviation in the distribution of separations. Around 35 per cent of pure binaries instances found are close ($a < 10$ au), with this percentage increasing with multiplicity; more than 60 per cent disc bearing binary instances in quadruple systems are close binaries. The median separation of CB disc hosting binaries is $a \approx 11$ au; this falls below the separation of binaries that one might reasonably expect to be able to observe in optically thick young protostellar systems ($a \approx 50$ au) (Tobin et al. 2016b).

Whilst I find no correlation between binary separation and CB disc mass, I do find a trend between the ratio of CB disc to total disc mass and binary separation. I plot this in Fig. 4.7, with the CB disc mass shown in the colour map. CB disc mass dominates the total disc mass in the system for binaries with a separation $a \lesssim 10$ au. As the binary separation increases past $a = 10$ au, the CB disc to total system (CB including primary and secondary discs) disc mass ratio begins to have values below unity. This is in good agreement with observed binary systems (e.g. Harris et al. 2012). However, in the simu-

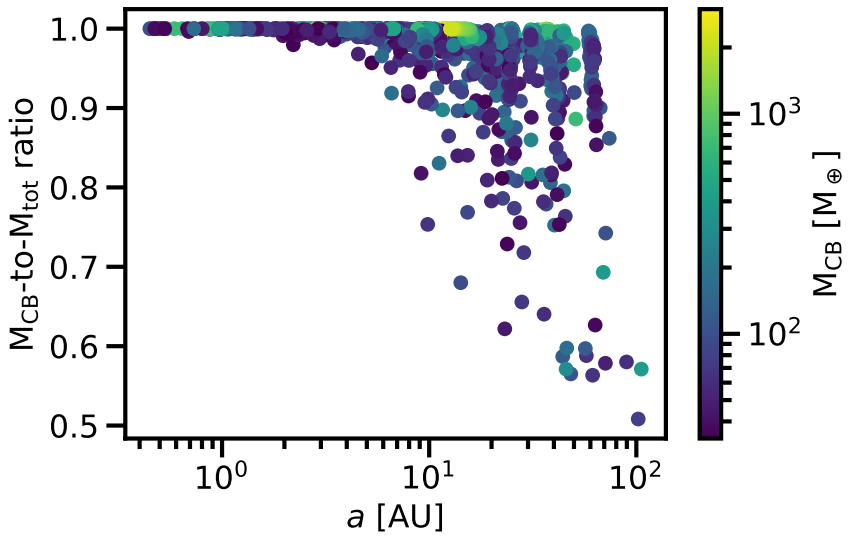

Figure 4.7: The circumbinary disc mass to system disc mass ratio plotted with the binary semi-major axis separation. CB disc mass in shown in the colour map. In systems with $a < 10$ au most CB discs contain > 90 per cent of total disc mass. As a increases the proportion of total disc mass in the CB disc decreases.

lation this is probably largely numerical. The sink particles modelling the protostars have accretion radii of 0.5 au, meaning that circumstellar discs smaller than a few au in radius are poorly modelled. For a binary with a semi-major axis $a = 10$ au, any circumstellar discs would be truncated to a few au in radius or even smaller for eccentric binaries. Such small circumstellar discs would not be numerically resolved.

In Fig. 4.8 I plot the mutual inclination angle between the CB disc plane and binary orbit plane versus the semi-major axis of the binary, with the radius of the CB disc shown in the colour map. Here I show that wider binaries typically have a CB disc that is more well aligned with the binary's orbital plane. The close binaries ($a < 10$ au) have a greater range of mutual inclinations relative to their CB disc. Additionally, these close binaries tend to be more eccentric than the wider binaries. Misaligned discs can cause disc breaking, as has been previously shown in 3D hydrodynamical simulations (e.g. Nixon et al. 2013; Facchini et al. 2013), and may have been observed in the GW Orionis system (Kraus et al. 2020). Highly mutually-inclined small CB discs, such as I find here, can be the cause of asymmetric shadows cast on to outer disc material as detected in scattered light observations (e.g. Benisty et al. 2017; Casassus et al. 2018; Price et al. 2018a).

Martin and Lubow (2017) found a polar alignment mechanism for CB discs that

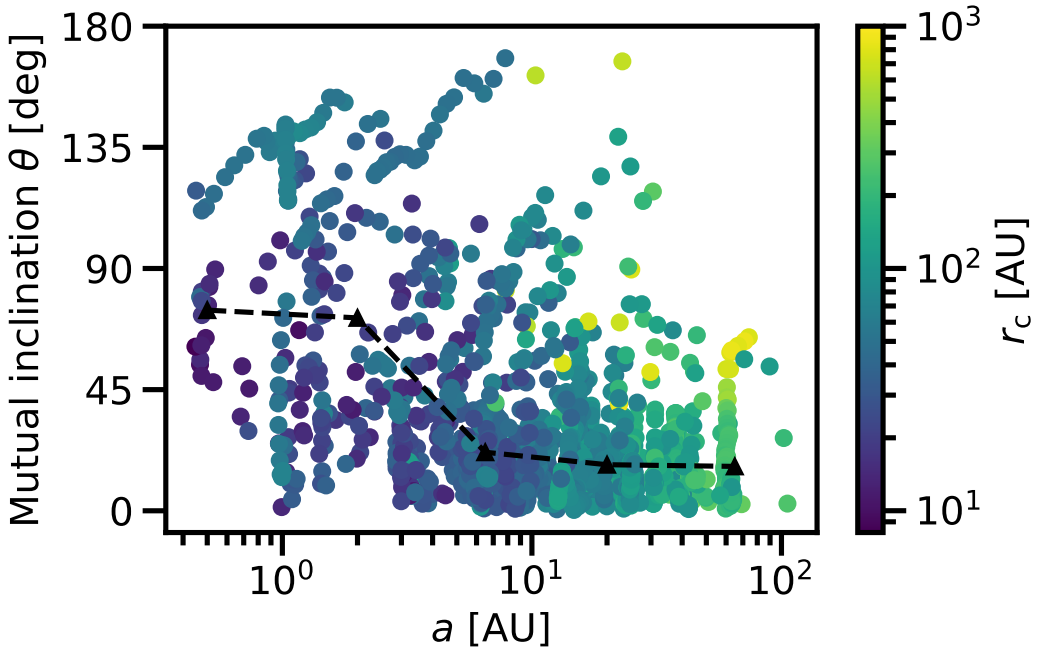

Figure 4.8: The mutual inclination angles of circumbinary discs relative to their binary's orbital plane versus binary orbit semi-major axis. The circumbinary disc radius is plotted in the colour map. The median mutual inclinations of discs binned every 0.5 dex are shown as black triangles. The discs about the very close binaries have a greater range of mutual inclinations. These discs also tend to be relatively small, on the order of 10's of au. These small discs may cast shadows on any outer disc material.

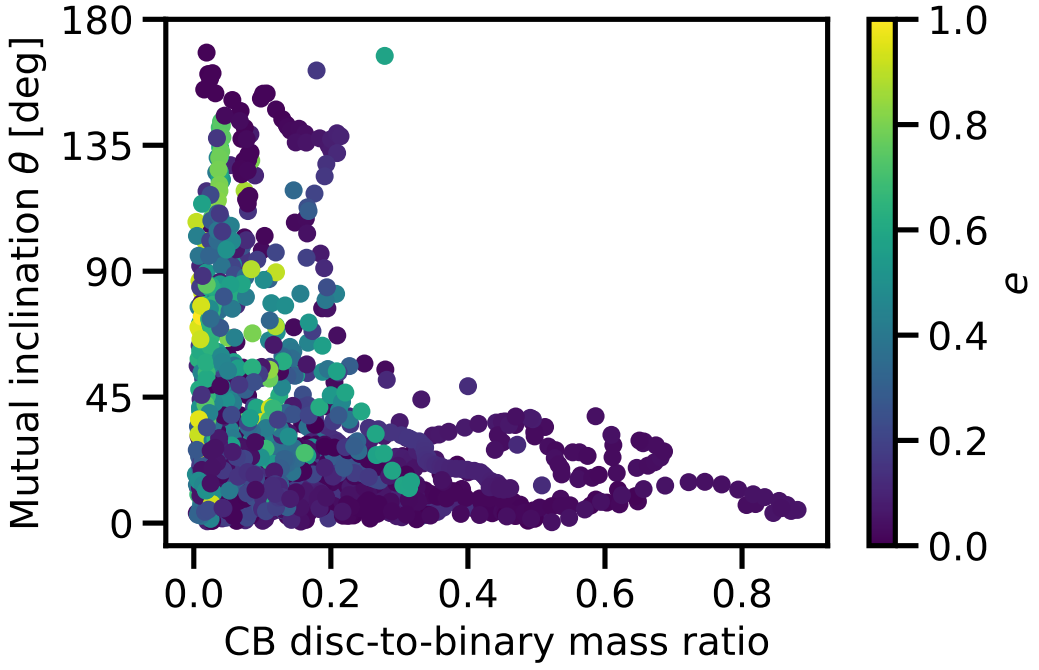

Figure 4.9: The mutual inclination angles of CB discs relative to their binary orbits versus the ratio of the CB disc gas mass to the mass of the binary. The orbital eccentricity of the binary is plotted using the colourmap.

operates best at high binary eccentricity, and low disc mass. Also see Lubow and Martin (2018) and Zanazzi and Lai (2018), and Martin and Lubow (2019). CB discs that are initially mildly misaligned with the binary orbit can evolve to a polar alignment, undergoing nodal libration oscillations of both tilt angle and the longitude of ascending node. They find this process operates above a critical angle of initial misalignment which depends upon the eccentricity of the binary and the mass of the disc. For binaries with eccentricity of 0.5, the process operates for discs with a mass that is just a few per cent of the binary mass with an initial misalignment of at least 40°. In Fig. 4.9 I show disc to binary mass ratios and eccentricities of orbits against mutual inclination. I also find that the most misaligned discs have low disc masses relative to the binary's mass, and tend to have eccentric binaries, in agreement with Martin and Lubow (2017). CB discs whose masses exceed 30 per cent of the binary mass typically have misalignment angles less than 40°.

4.3 Discussion

Here I focus the discussion on the mutual inclinations of the CB discs and their binary orbits, comparing those formed in the calculation with those reported in the literature.

4.3.1 Mutual inclinations

The mutual inclination between a CB disc and the orbit of its binary, θ, is defined as

$$\cos\theta = \cos i_{\rm disc} \cos i_* + \sin i_{\rm disc} \sin i_* \cos(\Omega_{\rm disc} - \Omega_*), \tag{4.2}$$

where $i_{\rm disc}$ is the inclination of the disc relative to the line of sight, i_* is similar for the binary orbit, $\Omega_{\rm disc}$ is the longitude of the ascending node, and Ω_* is similar for the binary orbit. See Fig. 4.10 for a sketch of the geometry. Calculating the mutual inclination between an observed CB disc and the orbit of its binary can be difficult. One needs the orbital parameters of the binary, then one needs good enough observations of the CB disc to find the inclination and the longitude of ascending node.

There are some known mutual inclinations between discs and binaries in the literature. HD 98800B is a near equal-mass binary ($q = 0.86$) with a CB disc in a polar orbit

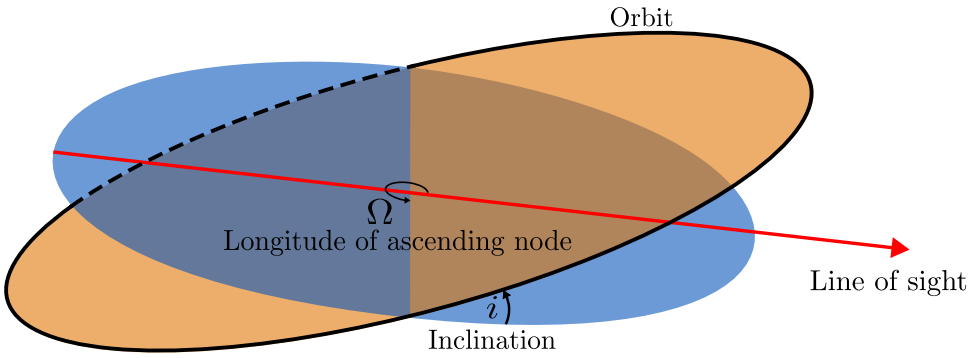

Figure 4.10: A schematic showing angles of ascending node (Ω) and inclination (i) of a body orbiting a central point with respect to the line of sight. The blue disc shows what the orbit would look like if it was in the plane of the observer's view, the orange disc is the orbit with an inclination to the observer's plane, and rotated around the centre point. Determining the angles of the ascending node and the inclination of both the binary and the disc are required to calculate the mutual inclination between the two. Due to the geometry of such systems, often there is a 180° ambiguity of the value of Ω, i.e. it is hard to tell which way the system is 'facing'.

with $\theta = 88.4° \pm 2$ according to Kennedy et al. (2019) and $\theta = 92° \pm 3°$ as reported by Czekala et al. (2019). The disc around HD 142527 B has a mutual inclination that was reported to be $\theta = 35° \pm 5°$ (Biller et al. 2012; Lacour et al. 2016; Boehler et al. 2017; Price et al. 2018a; Claudi et al. 2019; Czekala et al. 2019). However, with improved orbital parameters Balmer et al. (2022) suggest $\theta \approx 46° \pm 2°$ or $\theta \approx 76° \pm 3°$ depending on the value used for the longitude of ascending node as there is a 180° ambiguity with this. Using precise measurements of RV time series and disc dynamical mass Czekala et al. (2019) were able to infer the mutual inclination angles using a hierarchical Bayesian model for four CB discs; V4046 Sgr, AK Sco, DQ Tau, and UZ Tau E, with inferred $\theta < 2.3°$, $< 2.7°$, $< 2.7°$, and $< 2.7°$, respectively. Using the orbital parameters given by Long et al. (2021), V892 Tau has $\theta = 5° \pm 4°$. Another notable mention is the disc around V773 Tau B, which is thought to be in a polar alignment with its binary given the geometry of the system as a whole, but no value for θ has been reported (Kenworthy et al. 2022).

Often when observing CB discs there is a 180° ambiguity with the longitude of ascending node, Ω, for both the disc, $\Omega_{\rm disc}$, and the binary Ω_*. From Fig. 4.10, it is apparent that the geometry of the system will look the same from the observer's point of view if the disc is rotated 180° about the central node. Additional information, such as radial velocities (RVs) or astrometry data, is required to eliminate this ambiguity. In the absence of this, there are two possible values of the mutual inclination between the binary orbit and

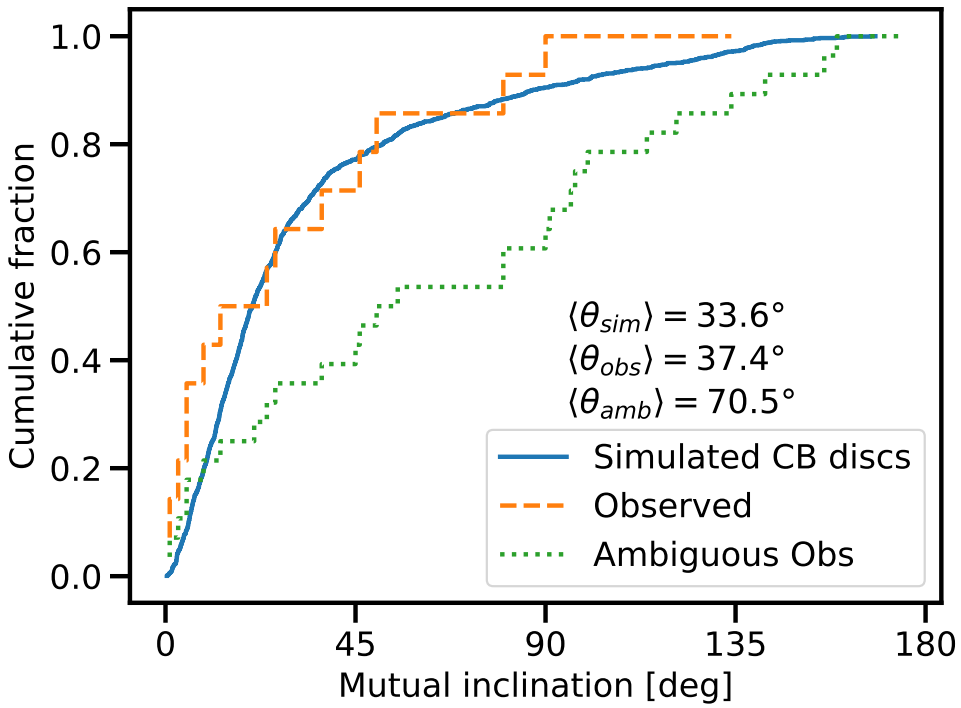

Figure 4.11: Cumulative distributions of the mutual inclination of circumbinary discs with their binaries as formed in the solar metallicity calculation of Bate (2019), and the mutual inclinations of observed discs from Table 4.1. The reported mutual inclinations (θ_1, orange dashed), and both the reported 'fake' values (θ_2) I calculate due to the ambiguity in Ω_*. The mean values of the mutual inclinations for the simulated, reported and ambiguous are 33.6°, 37.4°, and 70.5°, respectively.

the circumbinary disc. When studying the relative orientations of triple systems Sterzik and Tokovinin (2002) note this ambiguity and rather than using one value (even if there are possibly two) to generate statistics they use both values; one "true" and one "false". They do this even for systems that have very well constrained orbital parameters. They find that the mean value of the mutual inclinations does not change, however I believe this is because the distribution of mutual inclination angles for triple systems is close to random. For a set of data that are not random the inclusion of the "false" values will change the mean value. I give mutual inclination results from the calculation both using the actual values of θ, as well as using two values of mutual inclination for each CB disc/binary orbit, since there are only a few observed discs that have a well constrained angle of ascending node.

I use the mutual inclinations of observed CB discs to produce a cumulative distribution to compare with the mutual inclinations of CB discs from our calculations. I provide the data for observed discs, along with the necessary literature values to calculate θ, in Table 4.1. The literature values are given as θ_1, and the values taking into account the ambiguity in Ω_* that I calculate are given as θ_2. I note that I add 180° to Ω_* to obtain the ambiguous values; this choice is arbitrary. I chose to use Ω_* as the value with ambiguity as in the literature there are more systems with ambiguity attached to this value. In Appendix A I provide some extra discussion of how I chose the values for some of the observed systems in Table 4.1.

4.3.1.1 Comparison of simulated and observed mutual inclinations

I produce a cumulative distribution for the simulated discs, reported values for observed discs, and reported and ambiguous values combined for observed discs and plot them in Fig. 4.11. The mutual inclinations of the simulated CB discs have a very similar distribution to the reported observed mutual inclinations, with around half of all CB discs being inclined by less than 25° to the binary's orbit. At around 40° the distribution begins to flatten out, with $\approx$ 20 per cent of CB discs having an inclination of $>$ 45°. Of the simulated CB discs, $\approx$ 10 per cent are retrograde (inclined more than 90° to the binary orbit), compared to 5 per cent of the reported observed discs. When combining the reported values with the alternate values the distribution of mutual inclinations approaches a more random,

uniform distribution, with around 40 per cent of discs possibly being retrograde.

Using a hierarchical Bayesian analysis, Czekala et al. (2019) suggest that $\approx$ 70 per cent of short period spectroscopic binaries have $\theta < 3°$, whereas objects with longer orbital periods (> 30 days) have a much greater range of inclinations, from coplanar to polar. In relation to the calculation discussed in this paper, very close spectroscopic binaries are not produced due to the accretion radii of the sink particles $r_{\rm acc} = 0.5$ au. I do not see such a degree of coplanarity of CB disc and binary orbit in the closest binaries produced by the simulation (see Fig. 4.8). This may be due to the limited gas resolution of the calculation and/or the fact that the simulated systems are all very young (ages $< 10^5$ years) and haven't yet had time to become aligned through the action of gravitational torques and accretion (e.g., Bate et al. 2010).

Name	θ_1 [deg]	θ_2 [deg]	i_* [deg]	$i_{\rm disc}$ [deg]	Ω_* [deg]	$\Omega_{\rm disc}$ [deg]	$\Omega_{*,\rm amb}$ [deg]	References
TWA 3A	9 ± 6	97 ± 1	48.5 ± 0.8	48.8 ± 0.7	104 ± 9	116 ± 0.4	284 ± 9	(1), (2), (3)
AK Sco	3 ± 2	142 ± 2	108.8 ± 2.4	109.4 ± 0.5	48 ± 3	51.1 ± 0.3	228 ± 3	(1), (4), (5)
HD 131511[a]	5 ± 9	175 ± 9	93.4 ± 4.2	90 ± 10	248 ± 3.6	245 ± 5	68 ± 3.6	(6)
alpha CrB[a]	24 ± 28	156 ± 28	88.2 ± 0.1	90 ± 10	330 ± 20	354 ± 20	150 ± 20	(7)
beta Tri[a]	1 ± 8	100 ± 10	130 ± 0.5	130 ± 10	245.2 ± 0.67	247 ± 10	74.5 ± 0.67	(7)
HD 98800B	134 ± 3	91 ± 3	67 ± 3	154 ± 1	343 ± 2.4	196 ± 1	163 ± 2.4	(8), (9)
GW Ori A-B	50 ± 6	45 ± 6	157 ± 7	137 ± 2	263 ± 13	1 ± 1	83 ± 13	(10)
HD 200775	13 ± 8	121 ± 7	66 ± 7	55 ± 1	172 ± 6	180 ± 8	352 ± 6	(11), (12), (13)
V892 Tau	5 ± 4	114 ± 3	59.3 ± 2.7	54.6 ± 1	50.5 ± 9	53 ± 0.7	230.4 ± 9	(14)
GW Ori AB-C	46 ± 5	55 ± 6	150 ± 7	137 ± 2	282 ± 9	1 ± 1	102 ± 9	(10)
99 Her[a]	80 ± 6	21 ± 6	39 ± 2	45 ± 5	221 ± 2	72 ± 10	41 ± 2	(15)
SR 24N	37 ± 6	96 ± 8	132 ± 6	121 ± 7	252 ± 4	297 ± 5	72 ± 4	(16), (17), (18)
GG Tau Aa-Ab	26 ± 6	80 ± 3	132.5 ± 2	143 ± 1	313 ± 10	277 ± 0.2	133 ± 10	(19), (20), (21), (22), (23)
HD 142527	90 ± 2	159 ± 3	126 ± 2	38.2 ± 1.4	142 ± 6	162 ± 1.4	322 ± 6	(24)
IRS 43	>40	-	<30	70 ± 10	-	90 ± 5	-	(25)
V4046 Sgr	<2.3[b]	-	33.5 ± 1.4	-	-	256 ± 1	-	(26), (27), (28), (29)
CoRoT 2239	<5	-	85.1 ± 0.1	81 ± 5	-	-	-	(30), (31), (32)
UZ Tau E	<2.7[b]	-	56.1 ± 5.7	56.15 ± 1.5	-	269.6 ± 0.5	-	(33), (34), (35)
DQ Tau	<2.7[b]	-	158.2 ± 2.8	160 ± 3	-	4.2 ± 0.5	-	(36)
R CrA	>10	-	70 ± 15	35 ± 10	-	180 ± 10	-	(37)

Table 4.1: The mutual inclinations of observed circumbinary discs, with the necessary orbital parameters. The ambiguous values of longitude of ascending node ($\Omega_{*,\rm amb}$) are the reported value ($\Omega_* + 180°$). θ_1 are the reported mutual inclinations, θ_2 are the mutual inclinations calculated using $\Omega_{*,\rm amb}$. The upper section of the table are the objects for which all the necessary orbital parameters required to calculate the mutual inclination have been reported. The lower section of the table are objects for which there has been an inferred, constrained value of mutual inclination reported but for which the full set of orbital parameter has not been reported.

Notes: [a] = Debris disc, [b] = Mutual inclination inferred from hierarchical bayesian model (Czekala et al. 2019)

References: (1) = Czekala et al. (2019); (2) = Andrews et al. (2010a); (3) = Czekala et al. (2021); (4) = Anthonioz et al. (2015); (5) = Czekala et al. (2015); (6) = Kennedy (2015); 7) = Kennedy et al. (2012b); (8) = Kennedy et al. (2019) ;(9) = Zúñiga-Fernández et al. (2021); (10) = Czekala et al. (2017); (11) = Monnier et al. (2006); (12) = Okamoto et al. (2009); (13) = Benisty et al. (2013); (14) = Long et al. (2021); (15) = Kennedy et al. (2012a); (16) = Andrews and Williams (2005); (17) = Fernández-López et al. (2017); (18) = Schaefer et al. (2018); (19) = Andrews et al. (2014); (20) = Di Folco et al. (2014); (21) = Dutrey et al. (2016); (22) = Tang et al. (2016); (23) = Cazzoletti et al. (2017); (24) = Balmer et al. (2022); (25) = Brinch et al. (2016); (26) = Stempels and Gahm (2004); (27) = Rosenfeld et al. (2012); (28) = Kastner et al. (2018); (29) = Kastner (2018); (30) = Gillen et al. (2014); (31) = Terquem et al. (2015); (32) = Gillen et al. (2017); (33) = Simon et al. (2000); (34) = Prato et al. (2002); (35) = Jensen et al. 2007; (36) = Czekala et al. (2016); (37) = Mesa et al. (2019)

The mean mutual inclination angle of CB discs and binary orbits from the simulated systems is $\langle\theta_{\rm sim}\rangle = 33.6°$. For the literature values it is $\langle\theta_{\rm obs}\rangle = 37.4°$ when used the reported observational values, and when using two values for the ambiguity in the geometry of the system it is $\langle\theta_{\rm amb}\rangle = 70.5°$. The literature value of mean mutual inclination angle is similar to the value I find in the simulation; I find a preference for alignment between discs and orbits. I perform a Kolmogorov–Smirnov test to determine whether the underlying distributions of mutual inclination between the observations and simulations differ; I find no evidence at any reasonable significance level to reject the null hypothesis (p-value of 0.561) that they do not differ. When using two values for each disc I find a distribution of mutual inclinations that is closer to a uniform distribution with a very slight preference for alignment. The value of $\langle\theta_{\rm obs}\rangle = 37.4°$ for observed CB discs is close to the peak value of the distribution of mutual inclination of outer objects around binaries that Borkovits et al. (2016) find in a set of *Kepler* triples. Discs that are inclined with their binary that undergo fragmentation could result in a misaligned triple system, similarly for planets forming in misaligned discs. Since the observed frequency of circumbinary planets is similar to the observed frequency of planets around single stars, and circumbinary planets with orbits that are inclined to the binary's orbital plane are more difficult to detect, this may indicate that planets around binaries are more common than those around single stars (Armstrong et al. 2014).

4.4 Conclusions

I have analysed the circumbinary discs formed in a radiation hydrodynamical simulation of star cluster formation and presented their statistics. I have investigated the effect of high-order multiplicity on the properties of the circumbinary discs, and how often one might expect a circumbinary disc to form around a binary given its separation. I have also examined how the geometries of the systems compare to observed systems.

I summarise my findings here:

1. Given a sample of binaries (inclusive of those in hierarchical systems) with orbital semi-major axes less than 100 au, one would expect around 35 per cent of the binaries

to host a CB disc at young ages ($\lesssim 10^5$ years).

2. Close binaries ($a \lesssim 3$ au) without bound companions (i.e. pure binaries) are more likely to host a CB disc than close binaries in hierarchial systems. There is a multiplicity effect.

3. CB discs in hierarchical systems tend to be a bit less massive than those in pure binaries, and the largest discs tend to be smaller than the largest CB discs in pure binaries.

4. The size of the CB disc scales linearly with the binary semi-major axis, a. The median characteristic radius of a CB disc is $\approx 5 - 6\ a$.

5. CB discs of binaries with $a \gtrsim 10$ au tend to be well aligned with the binary's orbit. In addition to this, the binaries in these well-aligned systems tend to have low eccentricity. For binaries with small separations ($a \lesssim 3$ au) that have CB discs, the discs tend to be more randomly orientated. This may be partially due to the finite resolution of the simulations (gas is not modelled within 0.5 au of each protostars), and the extreme youth of the systems.

6. The mutual inclinations of observed binaries and their CB discs are in good agreement with the mutual inclination angles found in the calculation. The underlying distributions of mutual inclination of observed and simulated CB disc do not differ according to a Kolmogorov-Smirnov test (p-value = 0.561). Mutual inclinations from the simulation have a mean value of $\langle \theta_{\rm sim} \rangle = 33.6°$, comparatively the mean value of reported disc-orbit mutual inclinations is $\langle \theta_{\rm obs} \rangle = 37.4°$. When assuming a 180° ambiguity for Ω_* for observed binaries and CB discs the mean value of θ is $\langle \theta_{\rm obs,amb} \rangle = 70.5°$. This good agreement is obtained despite the calculation excluding some physical processes such as magnetic fields and outflows implying that such processes may not play a large role in setting the properties of protostellar discs (Bate 2018 and Chapter 3)

I hope this chapter motivates an increased effort in the detection and cataloguing of circumbinary discs. I have presented evidence from simulations that circumbinary discs

may be more common than what is currently being observed, especially at young ages.

Chapter 5

An implicit algorithm for simulating the dynamics of small dust grains with smoothed particle hydrodynamics

"I hate dust."

— Prof. Matthew R. Bate

5.1 Introduction

Dust emission is the dominant signature in cold astrophysical observations. Small grains absorb ultraviolet/optical light emitted from stars and re-emit this energy in the infrared. Instruments such as the mid-infrared instrument (MIRI) onboard the James Webb Space Telescope (JWST) is primed to detect these emissions from dust. Infrared observations can be used in conjunction with radio observations, such as those using the Atacama Large (sub)Millimeter Array (ALMA), to explore the structures of protoplanetary discs. Within protoplanetary discs it is dust that provides, at least in part, the material from which planets form. In addition to this, dust grains collide with gas particles, altering

the dynamical evolution of both phases. Understanding the dynamics of dust in these environments is crucial for the interpretation of observations that rely upon assumptions about the dust-to-gas ratio, as dust structures can be vastly different to structures in the gas.

Smoothed particle hydrodynamics (SPH) is a popular numerical method for modelling astrophysical fluid dynamics. Previously dust and gas mixtures have been modelled in SPH using separate particles for the dust and gas, originally by Monaghan and Kocharyan (1995), where the dust is coupled to the gas via drag. Such methods are sometimes referred to as two-fluid methods, but are less ambiguously referred to as dust-as-particles. This dust-as-particles method was applied in the context of protoplanetary discs by Maddison et al. (2003) and Barrière-Fouchet et al. (2005). Subsequently, Laibe and Price (2012a, 2012b) presented a new method for simulating dust-as-particles with SPH. Grid codes have also been adapted to model dust-as-particles. Bai and Stone (2010) introduced a hybrid particle-gas scheme to simulate dust-as-particles in dusty gas mixtures with the grid code ATHENA; they also present a fully implicit solver. The grid-code FARGO3D uses an implicit numerical scheme to model multiple species of dust (Benítez-Llambay et al. 2019). Implicit timestepping methods have also been employed in SPH dust-as-particle methods. Monaghan (1997a) modified this method to treat the drag terms implicitly via pairwise interactions. More recently, Laibe and Price (2012b) introduced an implicit timestepping method for their dust-as-particle method based upon the pairwise interaction method of Monaghan (1997a). Lorén-Aguilar and Bate (2014, 2015) developed a semi-implicit approach to dust-as-particle methods in SPH, although this scheme is limited to the use of global timesteps. Stoyanovskaya et al. (2018) and Stoyanovskaya et al. (2020) presented an implicit dust-as-particles SPH method for both linear and non-linear drag regimes.

Modelling the dust as a set of particles in essence doubles the memory required to perform the calculation and usually significantly increases the time to completion compared to an equivalent calculation with only gas. In the past decade much effort has gone into understanding and modelling the dynamics of small dust grains, that are highly coupled with the gas phase. In a series of papers Laibe and Price (2014b, 2014c, 2014a) discuss the limitations of the dust-as-particles method in the high drag (small grain) regime.

To circumvent these issues they developed a dust-as-mixture method (sometimes called one-fluid) for modelling highly coupled dusty gas mixture by framing the equations in the barycentric reference frame of the fluid. Price and Laibe (2015) presented a simplified version by adopting the terminal velocity approximation (Youdin and Goodman 2005) and modelling the dust fraction evolution as a diffusion-like equation. The dust diffusion method is far less computationally expensive than an explicit dust-as-particles method in the limit of small grains. In addition to being deployed in SPH, the dust-as-mixture method for modelling small grain dynamics has been implemented in the adaptive mesh refinement code RAMSES (Lebreuilly et al. 2019).

The dust-as-mixture method of Price and Laibe (2015) has been extended to model the dynamics of multiple small dust grain populations by Hutchison, Price, and Laibe (2018). This dust-as-mixture method is an effective way to simulate the dynamics of small dust grains in the limit of the terminal velocity approximation. However, although the method enforces positivity on the dust fraction, ϵ, (by evolving a variable $s = \sqrt{\epsilon\rho}$), where ρ is the total mass density) it does not limit the dust fraction to less than unity. This issue was solved by Ballabio et al. (2018) who use a different parameterisation of dust fraction in their evolution equations. Namely the dust fraction is defined as

$$\epsilon = \frac{s^2}{1+s^2}, \tag{5.1}$$

and it is the dust variable s that is evolved. An alternative formulation using a dust variable defined by $\epsilon = \sin^2(s)$ was used by Hutchison et al. (2022). This formulation also enforces $\epsilon \in [0, 1]$ and was found to produce more accurate solutions than equation 5.1, but it is more computationally expensive due to the need to evaluate trigonometric functions.

For all of the above formulations, while the positivity of the dust fraction is guaranteed, there is nothing stopping the dust variable, s, itself from becoming negative. In the regions of simulations where there are steep dust fraction gradients, while enforcing exact dust mass conversation, the dust variable can undershoot zero and become negative. If it does so this can cause the dust fraction to become positive in these regions where, otherwise, there should be no dust. This consequence of the mathematics of the model

can be thought of as dust leaking unphysically into these dust sparse regions. This can become a significant issue when modelling dust grains that are moderately coupled to the gas, for example, in protoplanetary discs where larger dust grains would be expected to settle to the midplane of the disc they can 'leak' into or be retained in the upper, and lower, regions of the disc relative to the midplane. This has been avoided in the past by sacrificing exact dust mass conservation and simply neglecting any change in the dust fraction or dust variable that would make it negative (e.g., see section 4.4.2 of Price and Laibe 2015). The resulting dust mass conservation is better when using equation 5.1 or the $\epsilon = \sin^2(s)$ formulations than when using $s = \sqrt{\epsilon\rho}$ or evolving the dust fraction directly, but it is still not ideal.

An additional limitation of the dust-as-mixture method is that it requires a timestep criterion whereby timesteps become small in regions of low dust fraction, or where dust grains become less well coupled (i.e., large). To prevent calculations having prohibitively short timesteps, Ballabio et al. (2018) introduced a mass flux limiter to stop rapid dust diffusion for particles in regions of high dust fraction gradients by artificially limiting the stopping time. The problem with this is that it unphysically modifies the drag acting on the dust during a simulation and, although it provides a numerical solution, the degree to which the solution resembles reality is unclear.

In this chapter, I present an implicit method for solving the dust diffusion equation of Price and Laibe (2015), using the dust variable defined by equation 5.1 (Ballabio et al. 2018). This avoids the need for a dust timestep criterion and negates the need for a stopping time limiter. In addition, it better handles the evolution of the dust variable in regions of large dust gradients due to the iterative nature of the algorithm. Depending on the dust grain sizes, the method also significantly speeds up the time to completion of three-dimensional simulations of protostellar collapse and protoplanetary disc evolution simulations, and yet yields equivalent results to those obtained using the fully explicit method.

The aim of this work is to improve calculations in the limit of small, coupled grains. Although I have applied this to the particle-as-mixture method that uses the terminal velocity approximation, a similar method could be derived to evolve the dust-as-mixture

equations without the additional terminal velocity approximation. Applying such an implicit method to the full dust-as-mixture equations of Laibe and Price (2014b, 2014c) would in principle allow grains with long stopping times to be more accurately modelled. This may be worth investigating in the future, but it is beyond the scope of this paper. Furthermore, while the full set of dust-as-mixture equations can provide a better model for intermediate-sized grains than applying the terminal velocity approximation, the fundamental assumption of a particle-as-mixture method that the velocity field is single valued does eventually break down, as has been shown by Laibe and Price (2014c) and Bate and Loren-Aguilar (2017). Finally, it should be noted that Hutchison et al. (2016) used an implicit method to evolve the the differential velocity between gas and dust in full dust-as-mixture SPH method, but they still solved the dust diffusion equation explicitly.

5.2 Method

5.2.1 The dust-as-mixture dust method

In the derivation of the dust-as-mixture formulation (Laibe and Price 2014b), the continuum equations are rewritten in the barycentric reference frame of the fluid. This involves replacing the velocities of the gas and dust phases with a single barycentric velocity of the mixture,

$$\boldsymbol{v} = \frac{\rho_{\rm g}\boldsymbol{v}_{\rm g} + \rho_{\rm d}\boldsymbol{v}_{\rm d}}{\rho_{\rm g} + \rho_{\rm d}}, \tag{5.2}$$

where $\boldsymbol{v}$ is the velocity, ρ is the density and the subscripts d and g denote the dust and gas quantities, respectively. The differential velocity between the two phases is defined as,

$$\Delta\boldsymbol{v} = \boldsymbol{v}_{\rm d} - \boldsymbol{v}_{\rm g}. \tag{5.3}$$

The total density of the mixture is,

$$\rho = \rho_{\rm g} + \rho_{\rm d}, \tag{5.4}$$

and the dust fraction is defined as,

$$\epsilon \equiv \rho_{\rm d}/\rho. \tag{5.5}$$

The dust-as-mixture equations can then be written in the form

$$\frac{\mathrm{d}\rho}{\mathrm{d}t} = -\rho\left(\boldsymbol{\nabla}\cdot\boldsymbol{v}\right), \tag{5.6}$$

$$\frac{\mathrm{d}\epsilon}{\mathrm{d}t} = -\frac{1}{\rho}\boldsymbol{\nabla}\cdot\left[\epsilon\left(1-\epsilon\right)\rho\Delta\boldsymbol{v}\right], \tag{5.7}$$

$$\frac{\mathrm{d}\boldsymbol{v}}{\mathrm{d}t} = -\frac{\boldsymbol{\nabla}P}{\rho} - \frac{1}{\rho}\boldsymbol{\nabla}\cdot\left[\epsilon\left(1-\epsilon\right)\rho\Delta\boldsymbol{v}^2\right] + \boldsymbol{f}, \tag{5.8}$$

$$\frac{\mathrm{d}\Delta\boldsymbol{v}}{\mathrm{d}t} = -\frac{\Delta\boldsymbol{v}}{t_\mathrm{s}} + \frac{\boldsymbol{\nabla}P}{\left(1-\epsilon\right)\rho} - \left(\Delta\boldsymbol{v}\cdot\boldsymbol{\nabla}\right)\boldsymbol{v} + \frac{1}{2}\boldsymbol{\nabla}\cdot\left[\left(2\epsilon-1\right)\Delta\boldsymbol{v}\Delta\boldsymbol{v}\right], \tag{5.9}$$

$$\frac{\mathrm{d}u}{\mathrm{d}t} = -\frac{P}{\rho_\mathrm{g}}\boldsymbol{\nabla}\cdot\left(\boldsymbol{v}-\epsilon\Delta\boldsymbol{v}\right) + \epsilon\Delta\boldsymbol{v}\cdot\nabla u + \epsilon\frac{\Delta\boldsymbol{v}^2}{t_\mathrm{s}}, \tag{5.10}$$

where P is the gas pressure, $\boldsymbol{f}$ represents non-fluid forces acting on the mixture (e.g., gravity), u is the internal energy of the gas, and t_s is the stopping time of the dust.

The stopping time when the dust is in the Epstein drag regime can be expressed as

$$t_\mathrm{s} = \frac{\hat{\rho}_\mathrm{s} r_\mathrm{s}}{\rho_\mathrm{g} v_\mathrm{th}}, \tag{5.11}$$

where $\hat{\rho}_\mathrm{s}$ is the intrinsic grain density, r_s is the grain radius, and the velocity of the gas molecules due to thermal motion is

$$v_\mathrm{th} = \sqrt{\frac{8k_\mathrm{B}T}{\pi\mu m_\mathrm{H}}}, \tag{5.12}$$

where k_B is Boltzmann's constant, T is the gas temperature, μ is the mean molecular weight of the gas, and m_H is the atomic mass of hydrogen.

This formalism can be simplified when the stopping time is small compared to the hydrodynamic time scale (Price and Laibe 2015). In SPH terms this means $t_\mathrm{s} < h/c_\mathrm{s}$, where h is the SPH particle smoothing (resolution) length and c_s is the sound speed. When this is satisfied, we are in the terminal velocity regime (Youdin and Goodman 2005), i.e. the relative velocity of the dust and gas reaches terminal velocity quickly due to the drag and pressure forces balancing. In this regime the dust-as-mixture equations can be simplified by ignoring the time dependence of the differential velocity, and any terms that are second order in t_s. Then

$$\Delta v = t_\mathrm{s}\frac{\boldsymbol{\nabla}P}{\rho_\mathrm{g}}. \tag{5.13}$$

The continuum equations then become

$$\frac{\mathrm{d}\rho}{\mathrm{d}t} = -\rho\left(\boldsymbol{\nabla}\cdot\boldsymbol{v}\right), \tag{5.14}$$

$$\frac{\mathrm{d}\epsilon}{\mathrm{d}t} = -\frac{1}{\rho}\boldsymbol{\nabla}\cdot\left(\epsilon t_{\mathrm{s}}\boldsymbol{\nabla}P\right), \tag{5.15}$$

$$\frac{\mathrm{d}\boldsymbol{v}}{\mathrm{d}t} = -\frac{\boldsymbol{\nabla}P}{\rho} + \boldsymbol{f}, \tag{5.16}$$

$$\frac{\mathrm{d}u}{\mathrm{d}t} = -\frac{P}{\rho_{\mathrm{g}}}\left(\boldsymbol{\nabla}\cdot\boldsymbol{v}\right) + \frac{\epsilon t_{\mathrm{s}}}{\rho_{\mathrm{g}}}\left(\boldsymbol{\nabla}P\cdot\boldsymbol{\nabla}u\right). \tag{5.17}$$

The inclusion of equation 5.15 means an additional time step criterion is required. Price and Laibe (2015) provide such a criterion in the form

$$\Delta t < C_0\frac{h^2}{\epsilon c_{\mathrm{s}}^2 t_{\mathrm{s}}}, \tag{5.18}$$

where C_0 is the Courant number. This implies that the time steps are constrained when the stopping times are long, i.e. when drag is low / dust grains are not well coupled to the gas. These equations can be discretised into the SPH form. Notably, the continuity and momentum equations have the same discretisation as the gas-only SPH equations. We must have new discretisations for the dust fraction, and the thermal energy evolution equations.

To discretise the dust fraction evolution equation whilst maintaining positivity of the dust fraction, and limiting the fraction to below unity, thus prevents the dust fraction from becoming unphysical, we use the parameterisation of equation 5.1 introduced by Ballabio et al. (2018) resulting in the dust evolution variable

$$s = \sqrt{\frac{\epsilon}{1-\epsilon}}. \tag{5.19}$$

We compute the time evolution of this variable

$$\frac{\mathrm{d}s}{\mathrm{d}t} = \frac{1}{2s\left(1-\epsilon\right)^2}\frac{\mathrm{d}\epsilon}{\mathrm{d}t}, \tag{5.20}$$

using a direct second derivative (Price and Laibe 2015). Substituting Eq. 5.15 into Eq. 5.20

yields

$$\frac{\mathrm{d}s}{\mathrm{d}t} = -\frac{1}{2\rho(1-\epsilon)^2}\{\boldsymbol{\nabla}\cdot[s(1-\epsilon)t_\mathrm{s}\boldsymbol{\nabla}P] + (1-\epsilon)t_\mathrm{s}\boldsymbol{\nabla}P\cdot\boldsymbol{\nabla}s\}. \tag{5.21}$$

Using the implementation of Ballabio et al. (2018), the SPH discretisation of this equation is

$$\frac{\mathrm{d}s_i}{\mathrm{d}t} = -\frac{1}{2\rho_i(1-\epsilon_i)^2}\sum_j\left[\frac{m_j s_j}{\rho_j}(D_i+D_j)(P_i-P_j)\frac{\bar{F}_{ij}}{r_{ij}}\right], \tag{5.22}$$

where $D_i = t_{s,i}(1-\epsilon_i)$, $\bar{F}_{ij} = \left[F_{ij}(h_i) + F_{ij}(h_j)\right]/2$, $r_{ij} = |\boldsymbol{r}_{ij}|$, and $\mathbf{r}_{ij}F_{ij}(h_i) = \boldsymbol{\nabla}_i W_{ij}(h_i)$, where $W_{ij}(h_i)$ is the SPH kernel. This work utilises the M_6 quintic spline kernel.

The energy of the system can be written as

$$E = \sum_i m_i\left[\frac{1}{2}v_i^2 + (1-\epsilon_i)u_i\right], \tag{5.23}$$

which is conserved if

$$\frac{\mathrm{d}E}{\mathrm{d}t} = \sum_i m_i\left[v_i\frac{\mathrm{d}v_i}{\mathrm{d}t} + (1-\epsilon_i)\frac{\mathrm{d}u_i}{\mathrm{d}t} - u_i\frac{\mathrm{d}\epsilon_i}{\mathrm{d}t}\right] = 0. \tag{5.24}$$

Removing the non-dust terms, assuming they conserve energy, and substituting in our parameterisation for dust fraction gives

$$\begin{aligned}\left.\frac{\mathrm{d}E}{\mathrm{d}t}\right|_\mathrm{dust} &= \sum_i m_i(1-\epsilon_i)\left.\frac{\mathrm{d}u_i}{\mathrm{d}t}\right|_\mathrm{dust} \\ &\quad - \sum_i m_i u_i \frac{2s_i}{\left(1+s_i^2\right)^2}\frac{\mathrm{d}s_i}{\mathrm{d}t} = 0,\end{aligned} \tag{5.25}$$

using Eq. 5.22 and rearranging yields

$$\begin{aligned}\left.\frac{\mathrm{d}u_i}{\mathrm{d}t}\right|_\mathrm{dust} = -\frac{1}{2(1-\epsilon_i)}\sum_j m_j\frac{s_i s_j}{\rho_j}\left(D_i+D_j\right) \\ \left(P_i-P_j\right)\left(u_i-u_j\right)\frac{\bar{F}_{ij}}{r_{ij}}.\end{aligned} \tag{5.26}$$

When incorporated into the usual SPH equations for a gas, equation 5.14 can be

expressed as

$$\frac{\mathrm{d}\rho_i}{\mathrm{d}t} = \sum_j m_j(\mathbf{v}_i - \mathbf{v}_j)\cdot\boldsymbol{\nabla}_i W_{ij}(h_i), \tag{5.27}$$

although this equation is not explicitly solved as the density is computed by the usual weighted sum over neighbours, and equations 5.16, and 5.17 become

$$\begin{aligned}\frac{\mathrm{d}\mathbf{v}_i}{\mathrm{d}t} &= -\sum_j m_j\left(\frac{P_i}{\rho_i^2\Omega_i}\boldsymbol{\nabla}_i W_{ij}(h_i) + \frac{P_j}{\rho_j^2\Omega_j}\boldsymbol{\nabla}_j W_{ij}(h_j)\right)\\ &\quad + \boldsymbol{f} + \Pi_{\mathrm{AV}},\end{aligned} \tag{5.28}$$

$$\begin{aligned}\frac{\mathrm{d}u_i}{\mathrm{d}t} &= \frac{P_i}{\Omega_i\rho_i^2}\sum_j m_j(\mathbf{v}_i - \mathbf{v}_j)\cdot\boldsymbol{\nabla}_i W_{ij}(h_i) + \left(\frac{\mathrm{d}u_i}{\mathrm{d}t}\right)^{\mathrm{diss}}\\ &\quad - \frac{1}{2(1-\epsilon_i)}\sum_j m_j\frac{s_i s_j}{\rho_i\rho_j}\left(D_i + D_j\right)\left(P_i - P_j\right)\left(u_i - u_j\right)\frac{\bar{F}_{ij}}{r_{ij}},\end{aligned} \tag{5.29}$$

where Ω_i is the term related to the smoothing length gradients defined as

$$\Omega_i \equiv 1 - \frac{\partial h_i}{\partial\rho_i}\sum_j m_j\frac{\partial W_{ij}(h_i)}{\partial h_i}. \tag{5.30}$$

The Π_{AV} term provides shock capturing via artificial viscosity, which in the SPH code we used is formulated as

$$\Pi_{ij} = -\sum_j \frac{m_j}{\rho_{ij}}\left[\frac{q_{ij}^i}{\rho_i\Omega_i}\boldsymbol{\nabla}_i W_{ij}(h_i) + \frac{q_{ij}^j}{\rho_j\Omega_j}\boldsymbol{\nabla}_j W_{ij}(h_j)\right], \tag{5.31}$$

where q_{ij} is defined as

$$q_{ij}^i = \begin{cases} -\frac{1}{2}\rho_i v_{\mathrm{sig},i}\mathbf{v}_{ij}\cdot\mathbf{r}_{ij}, & \mathbf{v}_{ij}\cdot\mathbf{r}_{ij} < 0\\ 0, & \text{otherwise,}\end{cases} \tag{5.32}$$

where $\rho_{ij} = (\rho_i + \rho_j)/2$, and the signal velocity $v_{\mathrm{sig},i}$ is

$$v_{\mathrm{sig},i} = \alpha_i^{\mathrm{AV}} c_{\mathrm{s},i} + \beta^{\mathrm{AV}}\left|\mathbf{v}_{ij}\cdot\mathbf{r}_{ij}\right|, \tag{5.33}$$

and $\alpha_i^{\mathrm{AV}} \in [0,1]$ and $\beta^{\mathrm{AV}} = 2$. We use the method of Morris and Monaghan (1997) to

evolve $\alpha_i^{\rm AV}$. Finally, the contribution of the artificial viscosity to the gas internal energy is

$$\left(\frac{\mathrm{d}u_i}{\mathrm{d}t}\right)^{\rm diss} = -\frac{1}{\Omega_i}\sum_j \frac{m_j}{\rho_{ij}} v_{{\rm sig},i}\frac{1}{2}(\mathbf{v}_{ij}\cdot\mathbf{r}_{ij})^2 F_{ij}(h_i). \tag{5.34}$$

5.2.2 Implicit dust evolution algorithm

Equation 5.22 is in the explicit form for the evolution of the dust variable, s. Here I present a method for solving the dust diffusion equation implicitly using a backwards Euler method. This formalism uses Gauss-Seidel iterations to solve the implicit dust evolution equation. The idea of using this method to solve the dust evolution equation implicitly was inspired by Whitehouse, Bate, and Monaghan (2005), who used this method to solve the diffusion equation for radiative transfer in the flux-limited diffusion approximation. Using the implicit method detailed below allows us to use timesteps that are not constrained by the stopping time of the dust, instead using the hydrodynamical timestep and so typically speeding up calculations.

To advance a time dependent variable, A, from time $t = n$ to $t = n+1$ the backwards Euler method can be stated as

$$A_i^{(n+1)} = A_i^{(n)} + \mathrm{d}t\left(\frac{\mathrm{d}A_i}{\mathrm{d}t}\right)^{(n+1)}. \tag{5.35}$$

This gives us the implicit equation for A. For interactions between particles i and j, a Gauss-Seidel iterative method $A_i^{(n+1)}$ can be solved for by rearranging the implicit equation to the form

$$A_i^{(n+1)} = \frac{A_i^{(n)} - \mathrm{d}t\sum_j \sigma_{ij}\left(A_j^{(n+1)}\right)}{1 - \mathrm{d}t\sum_j \sigma_{ij}}, \tag{5.36}$$

where σ_{ij} contains quantities other than A. In this scheme $A_j^{(n+1)}$ starts off as $A_j^{(n)}$ and is updated to $A_j^{(n+1)}$ as soon as this value becomes available. Eq. 5.36 is iterated over until some specified convergence criterion is met. Taking Eq. 5.22, and putting it into backwards Euler form we obtain

$$s_i^{(n+1)} = s_i^{(n)} - \mathrm{d}t \left\{ \frac{1 + \left(s_i^{(n+1)}\right)^2}{2\rho_i} t_{s_i} \sum_j s_j^{(n+1)} L_{ij} + \frac{\left(1 + \left(s_i^{(n+1)}\right)^2\right)^2}{2\rho_i} \sum_j \frac{t_{s_j}}{1 + \left(s_j^{(n+1)}\right)^2} s_j^{(n+1)} L_{ij} \right\}, \tag{5.37}$$

where $L_{ij} \equiv \frac{m_j}{\rho_j}(P_i - P_j)\frac{\overline{F}_{ij}}{r_{ij}}$. The implicit equation for $s_i^{(n+1)}$ can be rearranged into a quartic equation of the the form

$$a_4 \left(s_i^{(n+1)}\right)^4 + a_3 \left(s_i^{(n+1)}\right)^3 + a_2 \left(s_i^{(n+1)}\right)^2 + a_1 s_i^{(n+1)} + a_0 = 0, \tag{5.38}$$

where

$$a_4 = \frac{\mathrm{d}t}{2\rho_i} \sum_j \frac{t_{s_j}}{1 + \left(s_j^{(n+1)}\right)^2} s_j^{(n+1)} L_{ij}^{(n+1)},$$

$$a_3 = 0,$$

$$a_2 = \frac{\mathrm{d}t}{\rho_i} \sum_j \frac{t_{s_j}}{1 + \left(s_j^{(n+1)}\right)^2} s_j^{(n+1)} L_{ij}^{(n+1)} + \mathrm{d}t \frac{t_{s_i}}{2\rho_i} \sum_j s_j^{(n+1)} L_{ij}^{(n+1)},$$

$$a_1 = 1,$$

$$a_0 = \frac{\mathrm{d}t}{2\rho_i} \sum_j \frac{t_{s_j}}{1 + \left(s_j^{(n+1)}\right)^2} s_j^{(n+1)} L_{ij}^{(n+1)} + \mathrm{d}t \frac{t_{s_i}}{2\rho_i} \sum_j s_j^{(n+1)} L_{ij}^{(n+1)} - s_i^{(n)}.$$

A solution to Eq. 5.38 can be found with any method of solving quartic equations, e.g. numeric, however as $a_3 = 0$ this is a depressed quartic and we can solve the resolvent cubic (see Appendix B for the analytic solution of the quartic). This analytic solution is preferred as it finds a solution more quickly. Iterating the solution to Eq. 5.38 over all SPH particles until convergence gives the values of the dust variable, s, at the next time step. Again, we note that $s_j^{(n+1)}$ starts off as $s_j^{(n)}$ until we have an updated value for s_j.

5.2.3 Convergence criterion

The value of $s_i^{(n+1)}$ is iterated over until convergence within an accepted tolerance on the $m^{\rm th}$ iteration, i.e. iterations continue until

$$\left| \frac{s_i^{n+1,m} - s_i^{n+1,m-1}}{s_i^{n+1,m}} \right| < \delta, \tag{5.39}$$

where typically $\delta = 10^{-3}$ and $s_i^{n+1,m}$ is the backward Euler form of s_i^{n+1} (equation 5.37) evaluated at iteration m. If the method fails to converge, the timestep is split into two and the iterations begin again. We continue in this manner until convergence is reached, or until the original timestep has been split so many times that it is no longer computationally viable.

In the limit where $\epsilon \geq 2.5 \times 10^{-7}$ ($s > 0.0005$) the equation is solved in this way. If the dust fraction drops below this value equation 5.38 is solved linearly (i.e. simply considering the last two terms on the left-hand side) as the leading order terms of the quartic become vanishingly small. I find no measurable loss of accuracy by solving the diffusion equation linearly in this limit.

5.3 Numerical tests

I have implemented both the implicit and explicit forms of the dust-as-mixture equations using the Ballabio et al. (2018) dust parameterisation into the 3D SPH code SPHNG. Originally SPHNG was developed by Benz (1990) and Benz et al. (1990) and subsequently modified significantly as described in **bate_sphng_1995MNRAS.277..362B<empty citation>**, Whitehouse et al. (2005), Price and Monaghan (2007) and other papers.

To test the dust-as-mixture dust fraction implementations, we used the DUSTYWAVE and DUSTSHOCK tests as outlined in Laibe and Price (2011). In these tests we adopt a stopping time defined as

$$t_{\rm s} = \frac{\epsilon(1-\epsilon)\rho}{K}, \tag{5.40}$$

to be consistent with the literature and analytic solutions, where K is the coefficient of

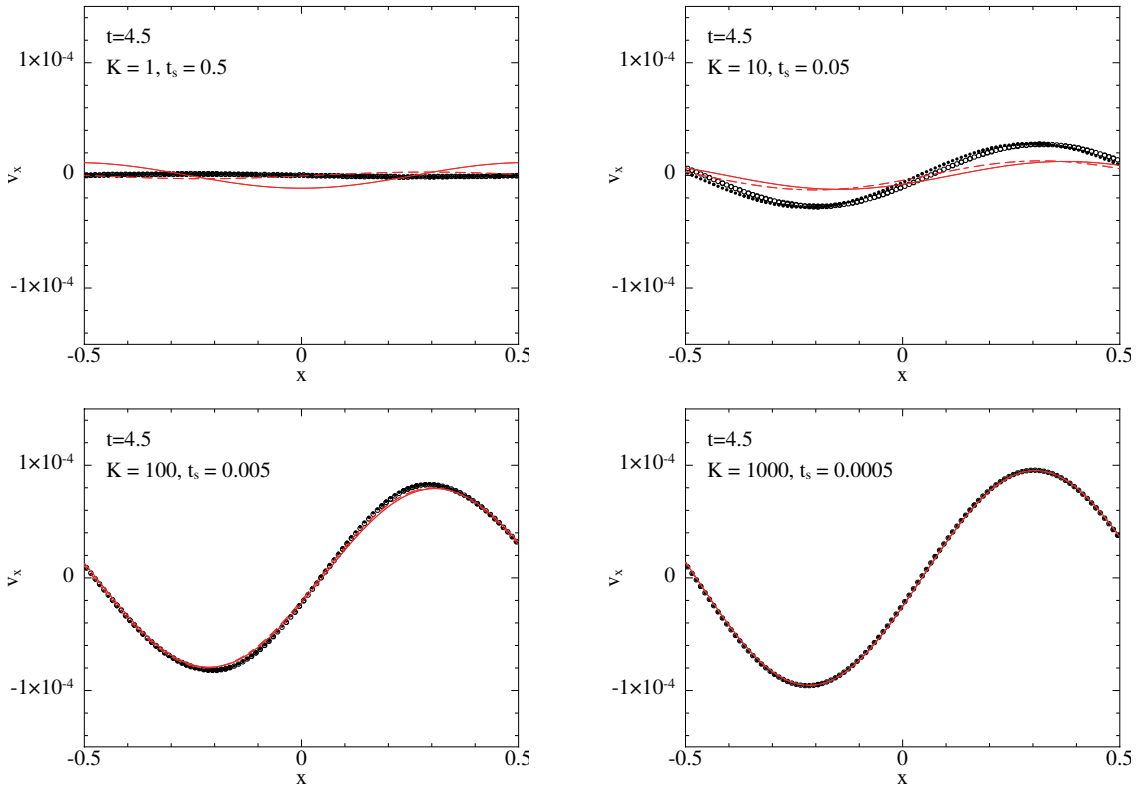

Figure 5.1: Results from the DUSTYWAVE problem performed with our implicit method with a varying drag coefficient $K = 1,\ 10,\ 100,\ 1000$ (from top-left to bottom-right) and a dust-to-gas ratio of 1:1. The analytic solution of the gas velocity is plotted in red as a solid line and the analytic solution of the dust velocity is plotted as a dashed line. The numerical solution of dust and gas velocities are plotted at time $t = 4.5$ as open and filled circles respectively. As with an explicit method, the solution becomes inaccurate at lower drag ($K \lesssim 40$) due to the breakdown of the terminal velocity approximation.

drag between the gas and the dust.

5.3.1 Dustywave

The DUSTYWAVE problem consists of a linear wave propagating through a dust-gas mixture. The problem was originally described for dust-as-particles by Laibe and Price (2011), then in dust-as-mixture by Laibe and Price (2014c). I set the problem up in 3D, but only propagate the wave in the x direction. The problem is initialised with a mixture consisting of equal dust and gas ($\rho_{\rm d} = \rho_{\rm g} = 1$, i.e. $\rho_0 = 2, \epsilon = 0.5$) with a sinusoidal perturbation in both density and velocity of the form $v(x) = v_0 \sin(2\pi x)$ and $\rho(x) = \rho_0 \left[1 + \delta\rho_0 \sin(2\pi x)\right]$. The amplitude of the perturbation is set to $v_0 = \delta\rho_0 = 1 \times 10^{-4}$, with a corresponding perturbation in the energy. An adiabatic equation of state is used where $\gamma = 5/3$ and the sound speed is set to $c_{\rm s} = 1$. The domain is $x,\ y,\ z \in [-0.52, 0.52]$, $[-0.069, 0.069]$, $[-0.073, 0.073]$ respectively, in which 3744 particles are set up in a closed packed lattice, giving a spacing

of $\Delta p = 0.02$, to ensure particle stability throughout the calculation.

As noted by Price and Laibe (2015), there is an inconsistency between the analytic and numerical solution. In the analytic solution $\Delta \boldsymbol{v}$ is assumed to be zero at $t = 0$, however in the terminal velocity approximation $\Delta \boldsymbol{v} = t_{\rm s} \boldsymbol{f}$ is non-zero. This inconsistency causes a small phase difference between the analytic and numerical solution that gets larger as $t_{\rm s}$ gets larger, i.e. less drag / larger grains, and specifically as the terminal velocity approximation breaks down.

The solution is plotted after ≈ 4.5 wave periods in Fig. 5.1 in which both gas and dust velocities are plotted in filled and open circles respectively. These values are reconstructed from the barycentric values for velocity as follows

$$\boldsymbol{v}_{\rm g} = \boldsymbol{v} - \epsilon \Delta \boldsymbol{v}, \tag{5.41}$$

$$\boldsymbol{v}_{\rm d} = \boldsymbol{v} + (1 - \epsilon) \Delta \boldsymbol{v}. \tag{5.42}$$

The results from the implicit method are consistent with those of Price and Laibe (2015) for the explicit method implemented using a direct second derivative. For both explicit and implicit methods, the solutions are very close to the analytic solutions in the regime where the terminal velocity approximation is valid ($K \gtrsim 40$). In lower drag regimes, the terminal velocity approximation gives a solution that is slightly out of phase or is over-dampened in the lowest drag case (see the two upper panels of Fig. 5.1).

5.3.2 Dustyshock

I perform the DUSTYSHOCK (Laibe and Price 2012a) test here with the implicit scheme at high drag. I use the standard Sod (1978) shock tube initial conditions. In the gas for $x \leq 0$ $(\rho_{\rm g}, v_{\rm g}, P) = (1, 0, 1)$, and for $x > 0$ $(\rho_{\rm g}, v_{\rm g}, P) = (0.125, 0, 0.125)$. I use an initial dust-to-gas ratio of unity (i.e., $\epsilon = 0.5$), and an adiabatic equation of state where $\gamma = 5/3$. The domain in 3D is $x,\ y,\ z \in [-0.5, 0.5],\ [-0.012, 0.012],\ [-0.017, 0.017]$ containing 3509 particles, a particle spacing of $\Delta p \approx 6.84 \times 10^{-3}$. The numerical solution is shown in Fig. 5.2 along with the analytic solution for the Sod shock tube in this configuration. The numeric and analytic solutions are in good agreement, with a slight discontinuity in the SPH solution

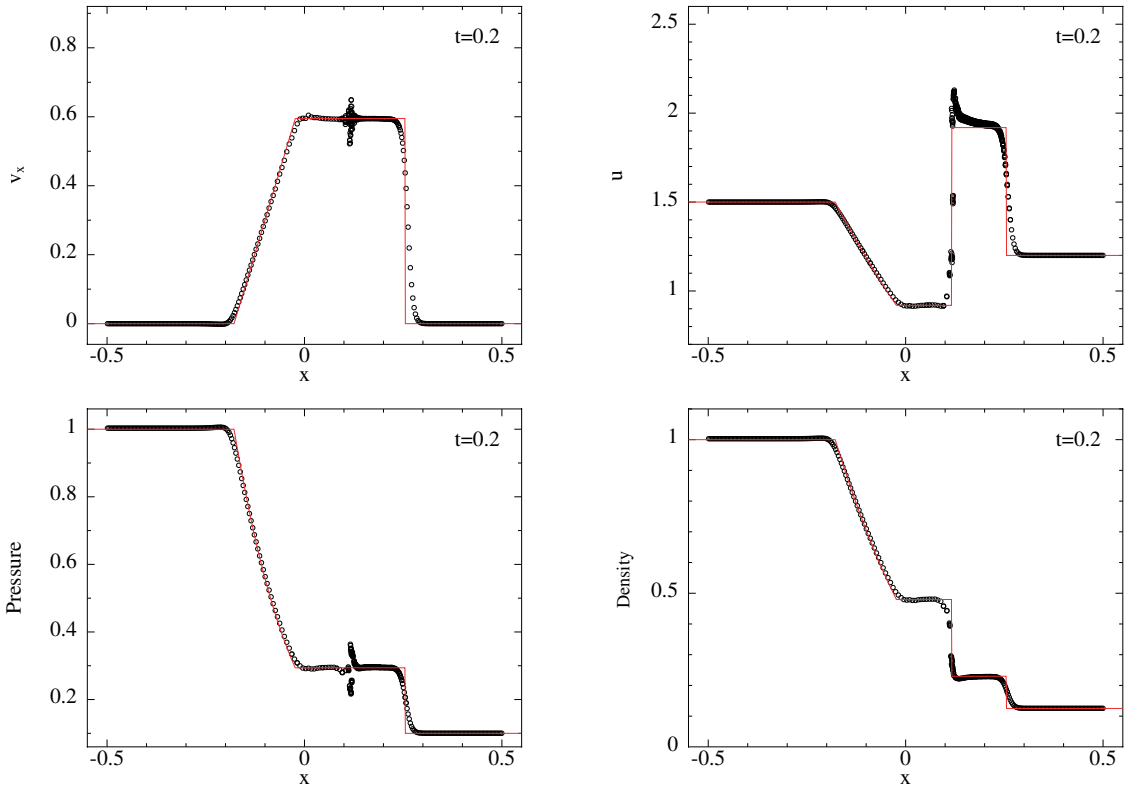

Figure 5.2: Results from the DUSTYSHOCK problem with a high drag coefficient and a high dust-to-gas ratio (1:1). The analytic solution is plotted at time $t = 0.2$ with a solid red line, the numerical solution is plotted with open circles. From upper left going clockwise plotted are: velocity in x direction, internal energy, gas pressure, and total density.

at the contact discontinuity.

5.4 Dusty protostellar collapse

As the first application of this new algorithm for solving the dust diffusion equations in dust-as-mixture SPH, I model the dynamics of small dust grains during the protostellar collapse of a molecular cloud core. We compare the results to those obtained using the semi-implicit dust-as-particles SPH method (Lorén-Aguilar and Bate 2014, 2015) to model the dynamics of the dust grains. The dust-as-particles calculations are almost identical to those presented by Bate and Loren-Aguilar (2017), except that the initial conditions are modified to set the dust particles to their terminal velocity, since by construction the dust-as-mixture SPH method discussed in this paper assumes the terminal velocity approximation (Bate and Loren-Aguilar 2017, took the dust particles to be initially at rest relative to the gas). It should be noted that this implementation of dust-as-particles does not use

the reconstruction of gas and dust velocities of Price and Laibe (2020), so as a result linear waves present in the calculation will tend to be overdamped when the dust particle separation becomes too large to resolve the drag length-scale.

In addition to comparing the results from the dust-as-mixture and dust-as-particles calculations, I perform the dust-as-mixture calculations using both explicit and implicit methods for solving the dust diffusion equation to compare their computational performance.

5.4.1 Initial conditions

Apart from the initial dust velocity being set to its terminal velocity, I replicate the calculations presented in Bate and Loren-Aguilar (2017). I set up unstable Bonnor-Ebert spheres of mass 5 $M_\odot$, radius 0.1 pc, and an inner-to-outer density ratio of 20. I use spherical, reflective boundary conditions. I use initially uniformly rotating clouds, with a rotation rate of 1.012×10^{-13} rad s^{-1}, and a non-rotating cloud. The magnitude of the ratio of rotational to gravitational potential energy for the rotating cloud is $\beta = 0.08$.

I use the same equation of state as Bate and Loren-Aguilar (2017) to model the gas during different phases of collapse, as I do not use radiative transfer. A barotropic equation of state is used for the gas pressure given by

$$P = \begin{cases} c_{\rm s,0}^2 \rho; & \rho < \rho_{\rm c}, \\ c_{\rm s,0}^2 \rho_{\rm c} \left(\rho/\rho_{\rm c}\right)^{7/5}; & \rho_{\rm c} \leq \rho, \end{cases} \tag{5.43}$$

where $c_{\rm s,0} = 1.87 \times 10^4$ cm s^{-1} is the initial isothermal sound speed of gas with a temperature of 10 K (the mean molecular weight is $\mu = 2.38$), and $\rho_{\rm c} = 10^{-13}$ g cm^{-3}. As in Bate and Loren-Aguilar, the calculations only follow the collapse until shortly after the density exceeds $\rho_{\rm c}$, so the gas almost always isothermal at 10 K, except in the centre at the end of the calculations when the temperature begins to rise.

In the dust-as-particles calculations I use 1 million SPH particles to model the gas, and 300,000 to model the dust. Comparatively in the dust-as-mixture calculations I use 1 million SPH particles that model both gas and dust as one fluid in a dust-as-mixture

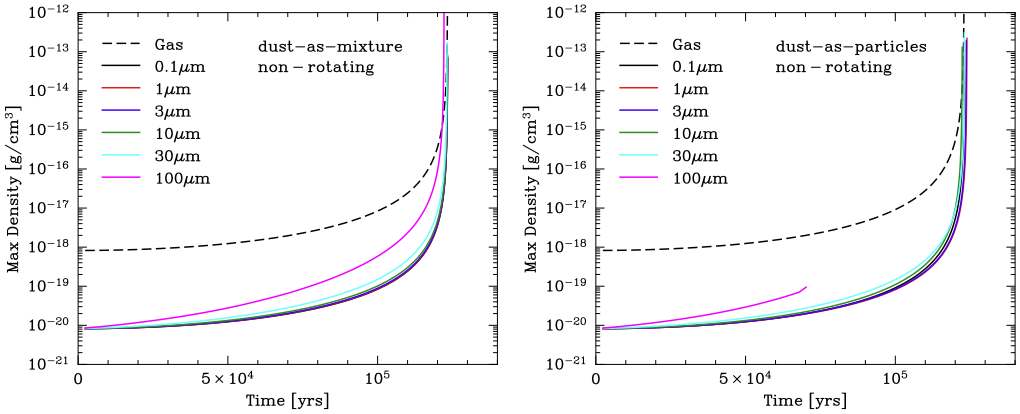

Figure 5.3: Time evolution of the central density of gas and dust during the collapse of non-rotating molecular cloud cores performed using in dust-as-mixture (left) and dust-as-particles (right) methods. There is a monatonic increase in the maximum density of dust with time. The dust-as-mixture and dust-as-particles solutions are similar, except for the largest dust grains. In the dust-as-particles 100μm calculation, the dust in the outer parts of the cloud is collapses more rapidly than in the inner regions, resulting in a 'pile up' of dust. For this case, the terminal velocity approximation of the dust-as-mixture method is only comparable until $t \approx 70,000$ yrs, so we only plot the dust-as-particles solution to this point. The gas density is from the 0.1μm calculations.

model. A uniform initial dust-to-gas ratio of 1:100 is used for all models. Using identical numbers of SPH particles to model the gas components in both sets of calculations means the gas resolutions are the same and the only difference between the calculations is due to the dust implementation.

5.4.2 Results

Here I present the results of the protostellar collapse of a non-rotating cloud and a rotating cloud with $\beta = 0.08$ using both the dust-as-mixture and -particles SPH methods.

In Fig. 5.3 I show the time evolution of the densities of gas and dust at the centre of the collapsing non-rotating clouds. In the dust-as-mixture calculations (left panel) there is a monotonic increase in the density of dust, and the rate of increase is greater for larger dust grain sizes due to the weaker coupling to the gas, although there is little difference for grains of size $r_s \lesssim 10\mu$m. The results are very similar in the equivalent dust-as-particles calculations (right panels), except for the largest grain size. For very small dust grain sizes there is good agreement between the dust-as-mixture and dust-as-particles results that only starts to break down very late in the collapse at very high densities as the first hydrostatic core (Larson 1969) forms; in the the dust-as-particles calculations (unphysical) dust particle clumping occurs late in the collapse. For intermediate dust grain sizes ($r_s \approx$

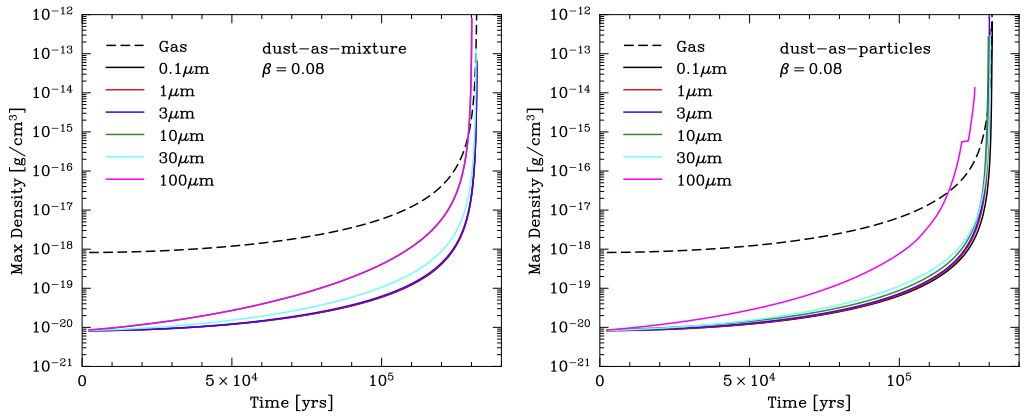

Figure 5.4: Time evolution of the central density of gas and dust in both rotating calculations in dust-as-mixture (left) and dust-as-particles (right). Due to the rotation of the cloud the formation of the hydrostatic core is delayed. The main differences between the two methods is with the largest grains; it is with this size of grain where the underlying assumptions of dust-as-mixture begin to breakdown and a dust-as-particles solution is desirable. The gas density is from the 0.1μm calculations. The slight kink in the 100μm curve is due to numerical noise in the centre on the cloud.

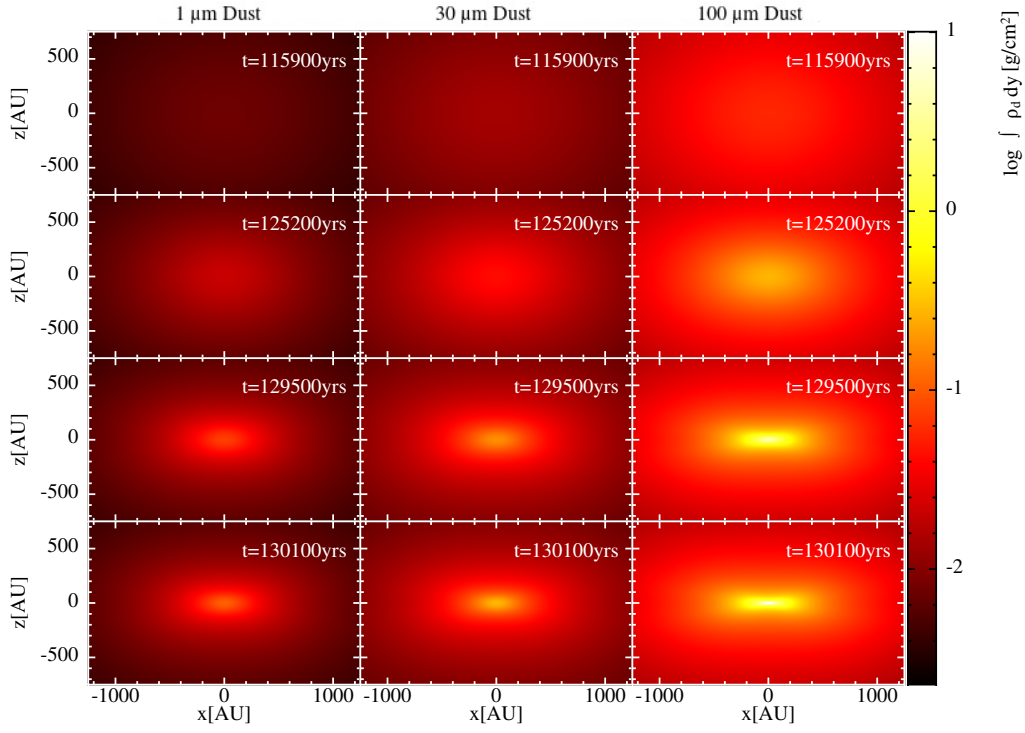

Figure 5.5: Evolution of dust grain column density viewed in the plane of rotation for calculations of molecular cloud core collapse using the dust-as-mixture method. Plotted from left to right are calculations with dust grain sizes r_s = 1μm, 30μm, 100μm. The colour bar is set such that it is the same in each panel of the plot. The small dust grains are coupled to the gas and follow the gas well. The larger grains exhibit different behaviour whereby they collapse more quickly resulting in the central oblate region having a higher dust density. The central obliquity is due to the overall rotation of the gas cloud.

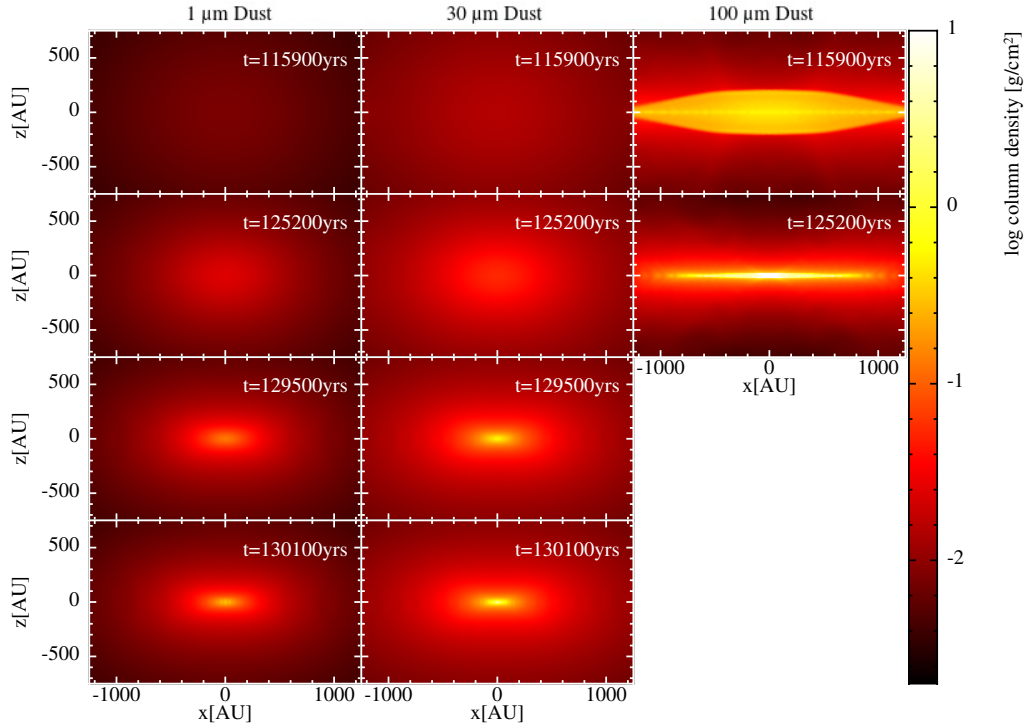

Figure 5.6: Evolution of dust grain column density in the plane of cloud rotation for calculations of molecular cloud core collapse using the dust-as-particles method. Shown from left to right are calculations with dust grain sizes r_s = 1μm, 30μm, 100μm. The colour bar is set such that it is the same in each panel of the plot. In the 100μm calculation the dust grains from the outer regions of the cloud collapse faster than the rest of the grains causing a pile up of grains that pass through each other in the centre of the cloud. These subsequently settle into a dense flat disc, whereupon the calculation grinds to a halt.

$10 - 30$ μm) the central dust density tends to be slightly higher for the dust-as-particles calculations than the dust-as-mixture calculations in the latter third of the collapse, again due to slight dust clumping when using the dust-as-particles method.

In the dust-as-particles calculation with dust grains of size $r_s = 100\mu$m, the initial terminal infall velocities of the dust in the outer regions of the cloud are much higher than in the centre. Therefore, the dust in the outer regions collapses much faster than the dust in dense inner regions causing a 'pile-up' as the dust collapses. This is an extreme case for which the terminal velocity approximation assumed by the dust-as-mixture model quickly breaks down. Therefore, for this case, we present the dust-as-particles results in Fig. 5.3 only until the dust from the outer regions of the cloud catches up with that from the inner part of the cloud. The results between the dust-as-mixture and dust-as-particles for 100μm grains are similar until this point ($t \approx 70,000$ yrs).

In Fig. 5.4 I show the time evolution of the gas and dust densities at the centre of the rotating clouds. In the calculations with dust grains $r_s < 100\mu$m there is little difference in the central densities of dust and gas between the two methods. Again, the dust-as-particles calculations are prone to some dust clumping. Also again, the largest grains (100μm) are less well coupled to the gas and so collapse much more quickly than the small grains. In the rotating case the collapse happens slower than in the non-rotating case, as expected due to centrifugal forces. But again, the dynamics of the large dust grains is better captured using the dust-as-particles method as in this case the terminal velocity approximation is not appropriate.

In Fig. 5.5 I show snapshots of the evolution of the column density of dust in the rotating protostellar collapse calculations containing dust with grain sizes of $r_s = 1\mu$m, 30μm, 100μm. The region shown is the centre of the cloud in the plane of rotation. The small dust grains are tightly coupled to the gas (the morphology of the gas column density looks almost identical to the 1μm dust morphology), whereas the larger grains are not as well coupled and collapse more quickly. This leads to an enhancement in dust-to-gas ratio when larger dust grains are present. The 100μm dust grains collapse fast enough to form a disc-like structure well before the stellar core forms, a consequence of the rotation rate of the cloud. A qualitatively similar result was found by Bate and Loren-

Aguilar (2017), shown in Fig. 3 of their work. I show the equivalent plot of Fig. 5.5 for the dust-as-particles calculations in Fig. 5.6. The dust density for grain sizes 1 and 30μm are similar in both the one- and dust-as-particles calculations, with the exception that in the dust-as-particles calculation the density at the centre of the cloud is slightly denser than in the dust-as-mixture at very late times. The 100μm dust grain calculation using dust-as-particles looks vastly different. In this calculation the dust grains in the outer parts of the cloud are very decoupled from the gas and have such a large initial terminal velocities that they are able to collapse to the centre of the cloud very quickly. Moreover, because the gas drag on them is so weak, even when they get to the denser inner regions the drag is insufficient to slow them to their local terminal velocity so they continue to collapse more quickly than in the dust-as-mixture calculation. This is a case that can not be modelled accurately using the dust-as-mixture terminal velocity approximation. Note that this is an extreme case – such large dust grains are not thought to be abundant in molecular cloud cores. Interstellar dust grains are typically thought to be sub-micron in size.

5.4.3 Comparison with explicit timestepping

In this section I compare the computational performance of the explicit timestepping algorithm of the dust evolution equation as described in Ballabio et al. (2018) with the implicit algorithm described in this work. In their formulation Ballabio et al. (2018) impose a criterion upon the stopping time of the dust to prevent numerical artefacts in regions of low dust-to-gas ratio, namely

$$\tilde{t}_{\rm s} = \min(t_{\rm s}, h/c_{\rm s}). \tag{5.44}$$

The reasoning for adopting this stopping time is to prevent infeasibly slow calculations by limiting the mass flux of particles in regions where there are steep dust density gradients, i.e. at the edge of discs. However this artificially alters the drag and thus the effective size of the dust grains and should be used with caution.

As an example of the problems that altering the stopping time can give, I repeat some of the dust-as-mixture non-rotating protostellar collapse calculations from Section 5.4 using explicit time stepping with the stopping time limiter turned on and off. I compare the results and performance with our implicit algorithm without a stopping time limiter.

In Fig. 5.7 I show the distribution of dust as a function of radius in the collapsing cloud when the maximum gas density reaches $\rho = 10^{-10}$ g cm^{-3} using both the explicit and implicit methods. The explicit results have the stopping time limiter applied, but no stopping time limiter is used for the implicit calculations. I give results for dust grain sizes $r_s = 0.1,\ 100\mu$m. In the explicit, stopping time limited calculations the dust density distribution for both grain sizes is very similar throughout the cloud, and identical in the outer regions where the gas density is low and the stopping time is the longest (i.e. where the stopping time limiter is most likely to be active). The implicit result for the 0.1μm grain size is very similar to the explicit result. However, in the implicit calculation with large grains the dust density is very different. In the outer parts of the cloud, the dust has fallen inwards leaving no dust in the outer parts of the cloud and producing much higher dust densities in the inner regions. Near the centre of the clouds the dust density distributions for the two explicit calculations with the stopping time limiter differ slightly, with the larger grains falling faster leading to a somewhat higher density than the small grains, due to the stopping time limited turning off at the higher gas densities. However the density of the larger grains here is still substantially underestimated compared with the implicit calculation. The large grains in the explicit calculation behave as if they were much smaller due to the timestep limiter. This is why extreme caution is needed if a stopping time limiter is used – a plausible result is obtained for the $r_s = 100\mu$m explicit calculation with the stopping time limiter, but it is a physically incorrect result.

To compare the computational performance between the explicit algorithm and the implicit algorithm, I also ran an explicit calculation without any stopping time limiter for the $r_s = 0.1\mu$m dust grains (a typical size for interstellar dust grains). This increased the calculation time so significantly that it was unrealistic to allow the gas density to reach $\rho = 10^{-10}$g cm^{-3}. I estimate that the implicit algorithm is at least two orders of magnitude (i.e., several hundred times) faster than the explicit algorithm at calculating this protostellar collapse case, because the implicit calculation takes standard hydrodynamical timesteps and does not require the use of a dust-as-mixture dust timestep. When comparing the dust density distributions of these two calculations they are almost identical; our algorithm yields the same result as the explicit algorithm without limiting the stopping time, but does so much more quickly. When using the explicit method with the stopping time

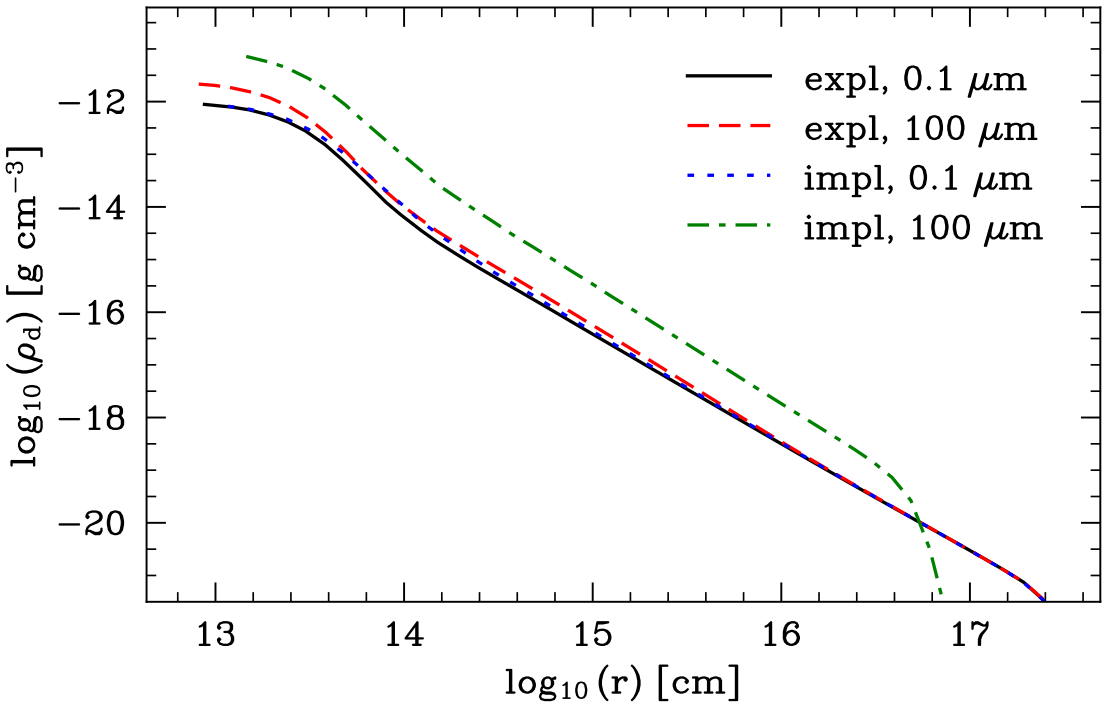

Figure 5.7: Dust density as a function of radius for dust grain sizes 0.1 and 100μm in non-rotating calculations of protostellar collapse when the peak gas density reaches of 10^{-10}g cm^{-3}, just after the first hydrostatic core begins to form. The 'expl' lines denote the dust density from explicit dust-as-mixture calculations with the stopping time limited applied, and 'impl' lines denote the equivalent calculations from implicit dust-as-mixture calculations (without a stopping time limiter). Due to the action of the stopping time limiter the dust density profiles for the two explicit calculations with different grain sizes are very similar, whereas with the implicit method the large grains have evacuated the outer parts of the cloud and migrated much more strongly inward.

limiter for the 0.1μm grain size, the explicit calculation was only about 5 percent faster than the implicit method.

5.5 Protoplanetary discs

In this section I present the results from protoplanetary disc simulations similar to those of Ballabio et al. (2018). The calculations include an embedded planet to study the diffusivity effects of gradients in dust fraction introduced by planet-disc interactions. The idea is that as the planet orbits, gas and dust are flung out into the outer regions of the disc where there are steep dust fraction gradients. It is in these environments that Ballabio et al. found that numerical artefacts in the dust can arise. This is most notable when using earlier formulations that evolved the dust fraction or the dust-to-gas ratio.

For the planet-in-disc test calculations, the initial radial extend of the gas is $r \in [25, 200]$ au and the dust initially extends to 90% of the gas radius. A locally-isothermal equation of state is used, with a radial temperature proportional to $r^{-1/2}$ so that ratio of the disc scale height to radius is a constant, $H/r = 0.1$. The central object is modelled using a gravitational potential of mass 1 $M_\odot$. The surface density of the disc has an initial profile proportional to $r^{-1/2}$. The mass of the disc is 0.0348 $M_\odot$ and the dust-to-gas ratio is set at 0.01. I used 1 million SPH particles to model the disc. The disc contains a 6 Jupiter-mass (M_J) planet at a radius of 140 au. The planet is modelled using a sink particle (Bate et al. 1995), with an accretion radius of 10 au ($\approx$ 0.5 Hill radius). The sink particle only interacts with the gas via gravity and accretion, and the trajectory of the sink particle is integrated with the same Runge-Kutta-Fehlberg integrator that is used for the SPH particles, but with a much lower tolerance.

In Fig. 5.8 I show the time evolution of the dust column density within the protoplanetary disc containing dust grains of size 100μm. The upper panels show the results from a calculation using the implicit dust-as-mixture algorithm to evolve the dust, the low panels show an identical calculation but using the explicit dust-as-mixture algorithm with the stopping time limiter.

The overall dust density distributions are almost identical. However, there are some

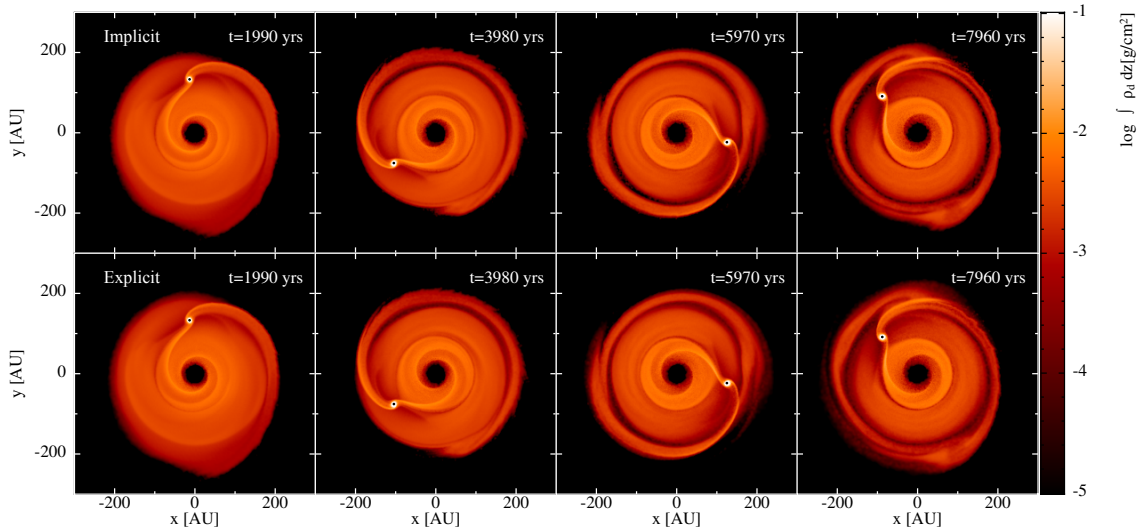

Figure 5.8: The time evolution of the column density of dust in a protoplanetary disc containing a 6 M_J planet. *Upper panels:* Results using the implicit dust-as-mixture dust algorithm. *Lower panels:* Results using the explicit dust-as-mixture dust algorithm with the stopping time limiter. Both calculations contain 100μm dust grains and use the same initial conditions. Similar results are obtained, but the implicit method gives slightly 'sharper' edges to the dust in the gap produced by the planet and at the outer edge of the disc.

differences in regions of high dust density gradient at the dust gap created by the planet and at the outer edge of the dust disc. In the explicit dust-as-mixture calculation the dust density is more smoothed out, whereas in the implicit dust-as-mixture calculation the edges of the dust disc are more sharply defined. This is most easily spotted in the gap in the dust; the dust does not diffuse into the gap as much in the implicit calculation.

I tested the mass conservation of the implicit dust-as-mixture algorithm and find it performs similarly to the explicit stopping time limited algorithm at conserving mass. I performed a similar calculation to the one described above except that we used only 200,000 SPH particles and we modelled the planet and disc in the same way as Ayliffe and Bate (2009b) where gas and dust falls on to and is bound to a planetary surface and remains in the calculation (rather than being accreted by a sink particle). Since all of the mass remains in the calculation (as opposed to being accreted by the sink particle) this allows us to measure more precisely the mass conservation of the respective dust schemes. In the upper panel of Fig. 5.9 I show that we recover the result reported by Ballabio et al. (2018) in which the parameterisation of dust fraction given by Price and Laibe (2015), $\epsilon = s^2/\rho$, does not conserve mass (the dust mass increases with time). In contrast, the implicit dust algorithm maintains the dust mass as well as the explicit algorithm with the Ballabio et al. (2018) dust parameterisation and stopping time limiter. In the lower panel of Fig. 5.9

I focus on just the implicit and explicit calculations to compare how well they converse mass with each other. The implicit calculation slowly loses a small fraction of mass ($\approx$ 0.02 %) initially and then approximately maintains this mass throughout the remainder of the calculation. In the case of the explicit calculation, the initial dust mass very slightly decreases through most of the calculation, but then loses a small fraction of mass towards the end ($\approx$ 0.06%). Overall I find that the dust mass conservation of the two different algorithms is similarly good.

5.6 Negativity of the dust parameter

Whilst the parameterisation of the dust fraction as given by in equation 5.1 ensures that it remains positive and less than one, there is no such constraint on the dust evolution variable, s, itself. During calculations, as the parameter is evolved, it can become negative. The dust fraction itself remains limited to between zero and unity, but a negative dust variable can still produce unwanted, nonphysical effects in the dust fraction. These effects typically manifest as dust seemingly 'leaking out' into regions of low dust fraction, at the edges of discs for example. This was pointed out by Price and Laibe (2015) for earlier versions of the dust parameterisation. They found that the most effective way to counter this issue was to set the dust fraction of the problem particles to zero.

In what follows, I show that the problem of the dust variable going negative can still occur with the newer dust parameterisation of Ballabio et al. (2018). Here we demonstrate the effects of a negative dust variable in both an idealised test case and in a more physically motivated fully 3D simulation. I then demonstrate that another advantage of the implicit dust method is that it avoids this problem entirely.

5.6.1 Dust settling test

For the idealised test case, I use the dust settling test of Price and Laibe (2015) which considers vertical dust settling in a Cartesian box with an acceleration in the 'vertical' (z) direction that mimics a small piece of a protoplanetary disc (i.e., the isothermal gas has a Gaussian density distribution vertically centred on $z = 0$). A full description of the set up the test is given by Price and Laibe (2015) and will not be repeated here. In this case,

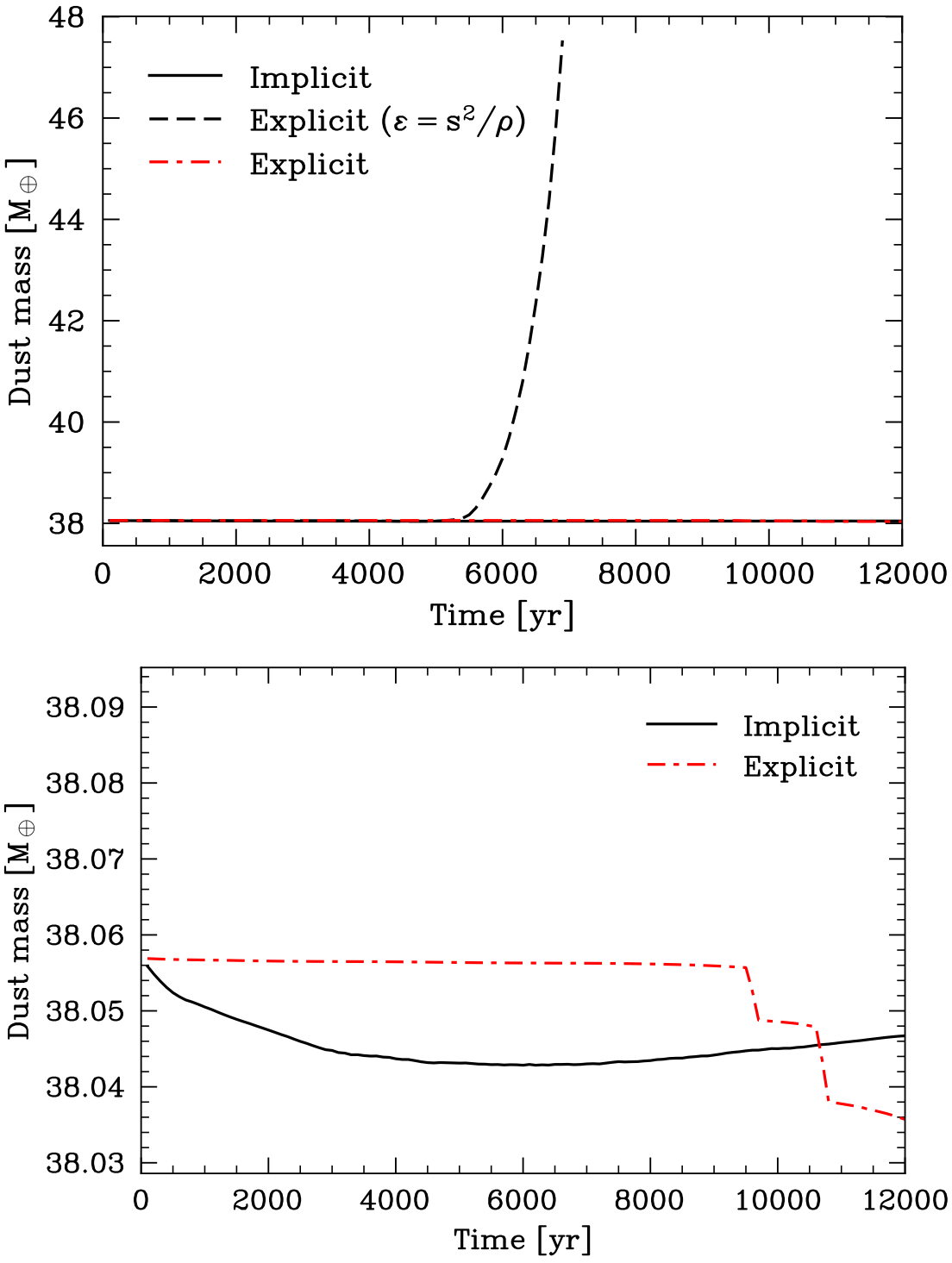

Figure 5.9: Dust mass evolution in a disc with an embedded planet. *Upper*: Dust mass evolution for the implicit and explicit calculations using the Ballabio et al. (2018) dust variable, and an explicit calculation using an alternate dust variable. *Lower*: A zoom in of the results for our implicit dust evolution algorithm and the explicit dust evolution algorithm, both using the Ballabio et al. parameterisation. Both of these calculations conserve dust mass to better than 0.1 percent.

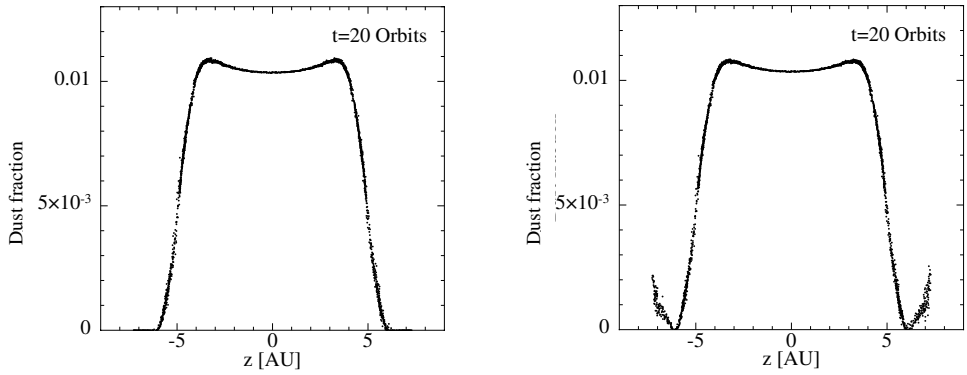

Figure 5.10: The dust settling test with 100μm dust grains after 20 orbital periods. *Left panel*: dust fraction as a function of vertical height in the disc using the implicit method to evolve the dust. *Right panel*: the same except using the explicit method. Using the explicit method, dust 'leaks' out of the dust layer into the low-density atmosphere of the disc ($|z| > 6$ au in the above panels). Using the implicit method gives the same dust profile near the midplane of the disc, but outside the dust layer where the dust fraction should be zero, it is zero as it should be.

I start the test with a dust-to-gas ratio of 1:100 and use a dust grain size of 100μm. The orbital period is 353 years and I show the state of the dust layer after 20 orbits.

As the disc evolves, the dust falls out of the low-density surface regions of the disc to create a dust layer with steep dust gradients at its surface. I show our results in Fig. 5.10 using both the explicit and implicit methods. The problem of the dust variable becoming negative occurs at this sharp gradient at the 'surface' of the dust layer. This is due to the way exact mass conservation of the dust-as-mixture equations is ensured by pairwise SPH particle interactions. The equations 'take' dust from one SPH particle and 'give' it to another. However, if the dust variable of the donor particle is small this can lead to the dust variable of the donor particle becoming negative. Due to the definition of the dust fraction, a negative dust variable still gives a positive dust fraction. However, this means that in regions where no dust is expected, dust diffuses out into these regions in an unphysical manner (lower panel of Fig. 5.10). This can be avoided in the explicit method by explicitly forcing the dust variable to remain positive, but this comes at the expense of sacrificing dust mass conservation.

Using the implicit method, in which the solution to the dust diffusion equation is iterated using the Gauss-Seidel method, the dust variable remains positive and the apparent diffusion of the dust out of the dust layer is avoided (upper panel of Fig. 5.10).

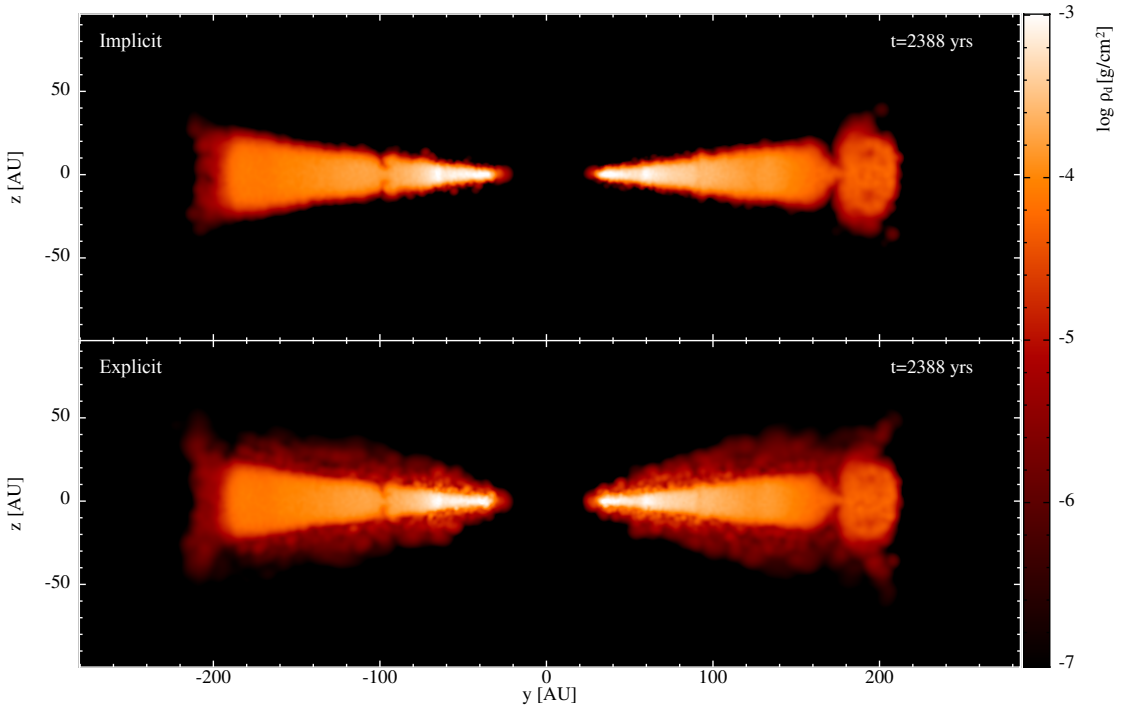

Figure 5.11: Cross section of the dust density in the protoplanetary disc with an embedded planet (slice not taken through planet location) at a radius of 140 au. *Upper panel:* Calculation using the implicit dust algorithm. *Lower panel:* Calculation using the explicit dust algorithm. In the explicit calculation there is an enhancement in dust density above (and below) the bulk of where the dust is expected to be. This is an artefact of the dust variable becoming negative. Using the implicit method avoids this problem.

5.6.2 Protoplanetary disc

Here I demonstrate the effect of the dust variable going negative in regions with a large dust fraction gradient also occurs in more complex simulations. From the same protoplanetary disc calculations that were discussed in Section 5.5 I take a cross section through both discs. This is shown in Fig. 5.11, the upper panel shows the dust density cross section of the disc from the implicit calculation and the lower is the same for the explicit algorithm. Whilst the bulk of the dust across both calculations is settling towards the midplane of the disc, in the calculation that used the explicit dust algorithm there is an apparent excess of dust above and below the the bulk of the dust layer. In addition to this enhancement above and below the midplane, there is also excess dust in the gap carved by the planet. This is due to the dust variable going negative in these regions. This is the same effect as that demonstrated by the simple dust settling test but in a full 3D global simulation. Again, the implicit method for evolving the dust diffusion avoids this problem.

5.7 Conclusions

In this chapter I have described an implicit algorithm to solve the dust-as-mixture dust diffusion equation of Price and Laibe (2015). I have benchmarked this algorithm against standard tests in the literature. The algorithm has also been tested in the settings of the collapse of a dense molecular cloud core and in a protoplanetary disc containing a planet, and compared with results and methods in the literature. The main features of the algorithm I have described are summarised as follows

1. The timestep criterion required by explicit dust diffusion can be avoided meaning that the dust evolution can be evolved on hydrodynamical timesteps which, depending on the dust size, can be much larger.

2. The time to solution compared to a fully explicit solution can be greatly reduced in the regimes of intermediate to large dust grains (by orders of magnitude). Even for very small dust grains, the implicit method is not much slower.

3. Due to the above there is no need to artificially limit the stopping time of dust particles, which has the adverse effect of essentially changing the dust grain size.

4. The iterative solution of the dust diffusion equation in the implicit method naturally avoids the dust variable becoming negative. This avoids dust apparently 'leaking' through strong dust fraction gradients.

Overall I find this implicit algorithm to be fast computationally, to solve the dust diffusion equations accurately, and to avoid several problems that manifest in explicit calculations. However, as with any dust-as-mixture method, the method still fails to give accurate solutions in the limit of large (weakly coupled) grains for which the stopping time is long. Using a dust-as-particles method is more appropriate in such circumstances.

Chapter 6

The Dynamics of Small Dust Grains in the Presence of Giant Planets

"I like the quote for Chapter 5."

— Prof. Matthew R. Bate

Small dust grains are key to performing observations of discs. We know from recent studies that planets can exist within dusty discs (Fedele et al. 2017; Keppler et al. 2018; Hammond et al. 2023), and the detection of these planets has primarily been due to substructures in the dust. Planets in discs in numerical and analytical studies have been known to open up gaps within discs, in both gas and dust (e.g. Lin and Papaloizou 1986; Bate et al. 2003a; Paardekooper and Mellema 2004; Kley and Nelson 2012). Many such structures have been observed recently and seem to be a common feature within dust discs (ALMA Partnership et al. 2015; Long et al. 2018; Huang et al. 2018b). Whilst these features are linked to planet-disc interactions, detection of planet in these young systems remains difficult. Most efforts focus on scattered light images (Dong et al. 2015; Avenhaus et al. 2018), gas kinematics (Pinte et al. 2018; Pinte et al. 2020; Barraza-Alfaro et al. 2024), or continuum emission (Zhang et al. 2018).

Whilst the dynamics of gas and dust are different, in the limit of small grains they are coupled. Dipierro et al. (2016) provide two mechanisms of dust gap opening; one in

the regime of small, coupled grains, and one in the regime of large, uncoupled grains. The small grains move with the gas and therefore a gap is opened in the dust only if a gap is opened in the gas, the larger grains, however, drift towards gas pressure maxima. Later, Dipierro and Laibe (2017) show that for low-mass planets, a gap in the gas is not a necessary condition for a gap in the dust. Any gaps in the gas can act as a filter for dust grains, large grains become trapped at the gap outer edge and small grains can flow into the inner disc (Rice et al. 2006). On longer timescales this ceases to be the case if particles are subjected to collisions (Stammler et al. 2023).

Many observations in the continuum make inferences of planet-disc interaction based upon hydrodynamic models (e.g. Gonzalez et al. 2012; Zhang et al. 2018; Dipierro et al. 2018). Therefore it is crucial to treat the dynamical and thermal evolution more accurately to help develop our understanding of the underlying causes of disc substructures that we see within discs. In this chapter we use a method of evolving dust dynamics developed in the previous chapter along with radiation hydrodynamics and planet models that allow of the accretion of material resolved down to the surface of the planet.

6.1 Methods

To study the dynamics of small grains in the presences of giant planets I use the method described in Chapter 5. This method of solving the dust evolution equation has been implemented in the 3D SPH code SPHNG code. This was originally developed by Benz (1990) and Benz et al. (1990) and significantly modified by Bate et al. (1995), Whitehouse et al. (2005), and Price and Monaghan (2007). The planets in this chapter are modelled using the prescription of Ayliffe and Bate (2009b), in which planet cores are able to accrete gas, and now dust, onto their surface, building an atmosphere. The main difference between the prescription of Ayliffe and Bate (2009b) and my calculations is that here I model the whole disc rather than a section of the disc around the planet. This allows me to model the non-axisymmetric features of the dust. In addition to this the calculations employ flux-limited diffusion radiative transfer method of Whitehouse et al. (2005) and Whitehouse and Bate (2006). I perform calculations of planets in discs orbiting a central star of mass $1 M_\odot$ at Keplarian velocity at a radius 5.2 au. The temperature profile of the disc is $T_g \propto$

r^{-1}, with a scale height of $0.1R$. The surface density of the disc follows a profile $\Sigma_g \propto r^{-0.5}$, where at the radius of the planet the initial unperturbed surface density is 75g cm^{-2}. Each disc is modelled by 1 million particles, and has a radial extent of $r \in (1,\ 20)$ au. I model planets with initial core masses $1M_{Sat}$, $1M_J$, $3M_J$, and $10M_J$. They are modelled by a potential that combines a potential to model their surface with a Newtonian gravitational force

$$F_r = \frac{GM_p}{r^2}\left(1 - \left(\frac{2R_p - r}{R_p}\right)^4\right), \tag{6.1}$$

for $r < 2R_p$ where r is the distance from the planetary core, R_p is the radius of the core, and M_p is the mass of the core. This allows the build up of particles above the surface of the core. In the calculations I use a core radius equal to 3 per cent of the Hill radius. Where the Hill radius is defined as $r_H = a\sqrt[3]{m_2/3(m_1+m_2)}$, where m_1 and m_2 are the masses of the central object and planet, respectively. In these calculations an ideal gas equation of state is employed, $P = \rho_g T_g R_g/\mu$, where ρ is density, T is the temperature, R_g is the gas constant, and μ is the mean molecular mass. Here the subscript g denotes gas values. The translational, rotational, and vibrational degrees of freedom of molecular hydrogen are taken into account. Within the discs there is a single species of dust with sizes varying between calculations. The dust grain sizes used are 10μm, 100μm, 1mm, and 1cm. I perform 16 calculations, with four different core masses ($1M_{Sat}$, $1M_J$, $3M_J$, $10M_J$), and for each of these with four different grain sizes (10μm, 100μm, 1mm, 1cm). Using the equation (Lodato and Price 2010)

$$\alpha_{SS} \approx \frac{\alpha^{AV}}{10}\frac{\langle h\rangle}{H}, \tag{6.2}$$

to relate the SPH artificial viscosity α^{AV} to the Shakura and Sunyaev (1973) parameter I find the discs to have values of $\alpha_{SS} \approx 3\times10^{-2} - 10^{-3}$. The α value peaks near gaps, i.e. at the inner edge of the disc, and either side of the gas gaps, note than only in the $10M_J$ calculation does a gap in the gas being to open up.

6.2 Results

Here I present the results from the planet in disc calculations. In Fig. 6.1 I show the column density of dust within all the simulations after 20 orbits, except in the $10M_J$ calculation where the dust density is shown after 13 obits. From top to bottom in the figure the planet mass increases from $1M_{Sat}$ to $10M_J$ and from left to right the dust grain size increases from 10μm to 1cm. In discs with planets > $1M_J$ and grains of size >1mm a gap readily opens in the dust disc, with a dense arc of dust contained within the horseshoe region of the planetary orbit. For these calculations the beginnings of a gap are stating to appear in the dust discs with the smallest grain sizes. This is due to a gap beginning to form in the gas also. The most clear case of a dust gap is in the most extreme calculation, with the largest planet and largest dust grain size I simulate. In this calculation the dust horseshoe is completely detached from the rest of the dust disc by wide, deep gaps. Here also there are three distinct dust discs: an inner disc around the star that extends to around 4au, a circumplanetary disc, and an outer disc starting from around 8au out to 18au.

In Fig. 6.2 I plot the radial average profile of dust density with 5 degrees of the mid plane of the disc in the z direction. The section of disc that is ±45° from the planet in the azimuthal direction is excluded from the radial average. Gap depth is a function of planet mass and grain size. The difference in density profile for grain sizes 100μm and 10μm is small, indicating that in these environments the 100μm grains are still well coupled to the gas. Once the grains reach sizes of 1mm this is no longer the case and gaps in the dust disc are more extreme than in the gas disc. The peak in dust density in the centre of the gap is the dust that has been trapped in the horseshoe orbit of the disc. The difference in density between the horseshoe and the gap in the $10M_J$ calculation is 2-2.5 orders of magnitude. This decreases to around 1.5 dex with the $3M_J$ planet, and 0.5 dex for the calculation with $1M_J$. I find that no gap opens up in the dust disc when a $1M_{Sat}$ planet is present after 20 orbits (13 for 1cm grains). The gap width is a function of planet mass and grain size. The gap in the dust for a given planet mass is slightly larger with larger dust grains.

In Fig. 6.3 I show the density of gas around the planet location along with the flow of gas after 20 orbits. These snapshots are taken from the calculation with 1mm grains.

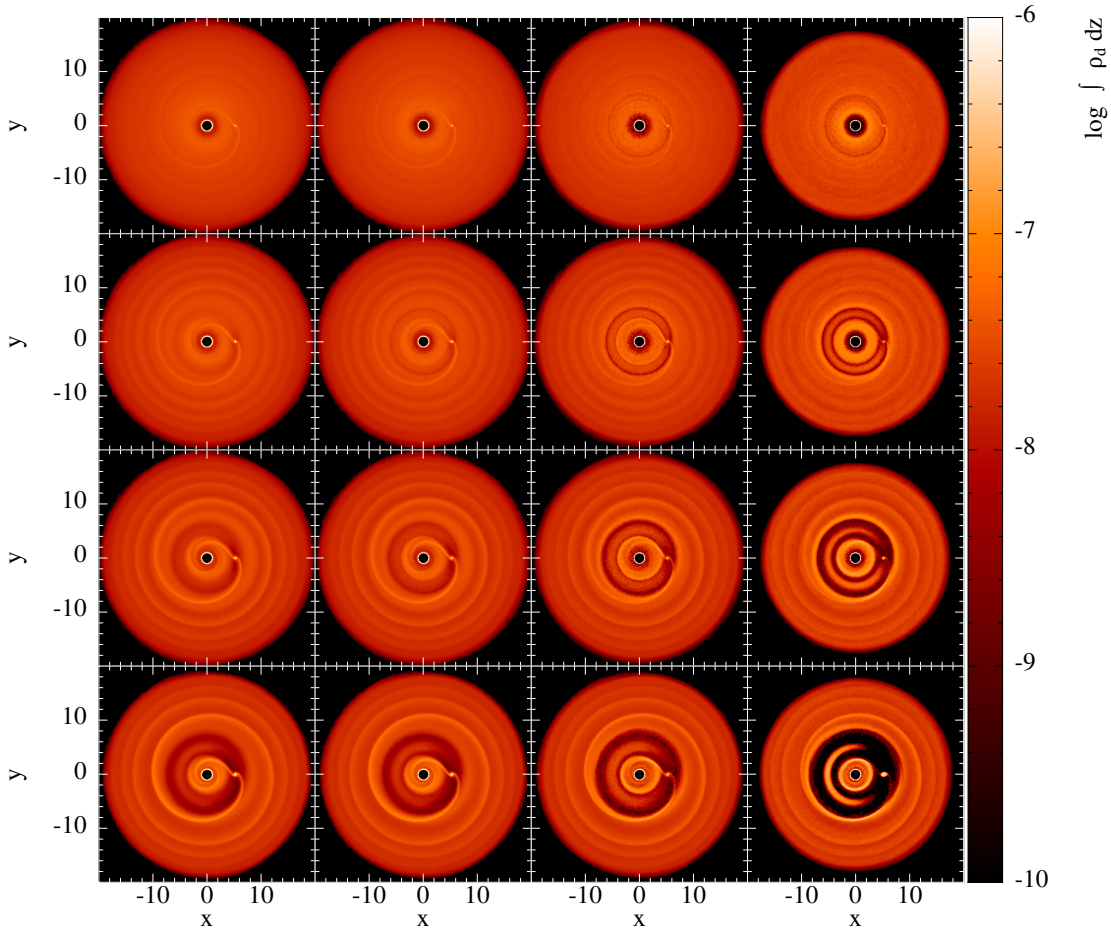

Figure 6.1: Column density of dust after 20 orbits, expect $10M_J$ which has only 13 orbits. Top to bottom planet masses $1M_{Sat}$, $1M_J$, $3M_J$, and $10M_J$. Left to right dust grain sizes 10μm, 100μm, 1mm, and 1cm.

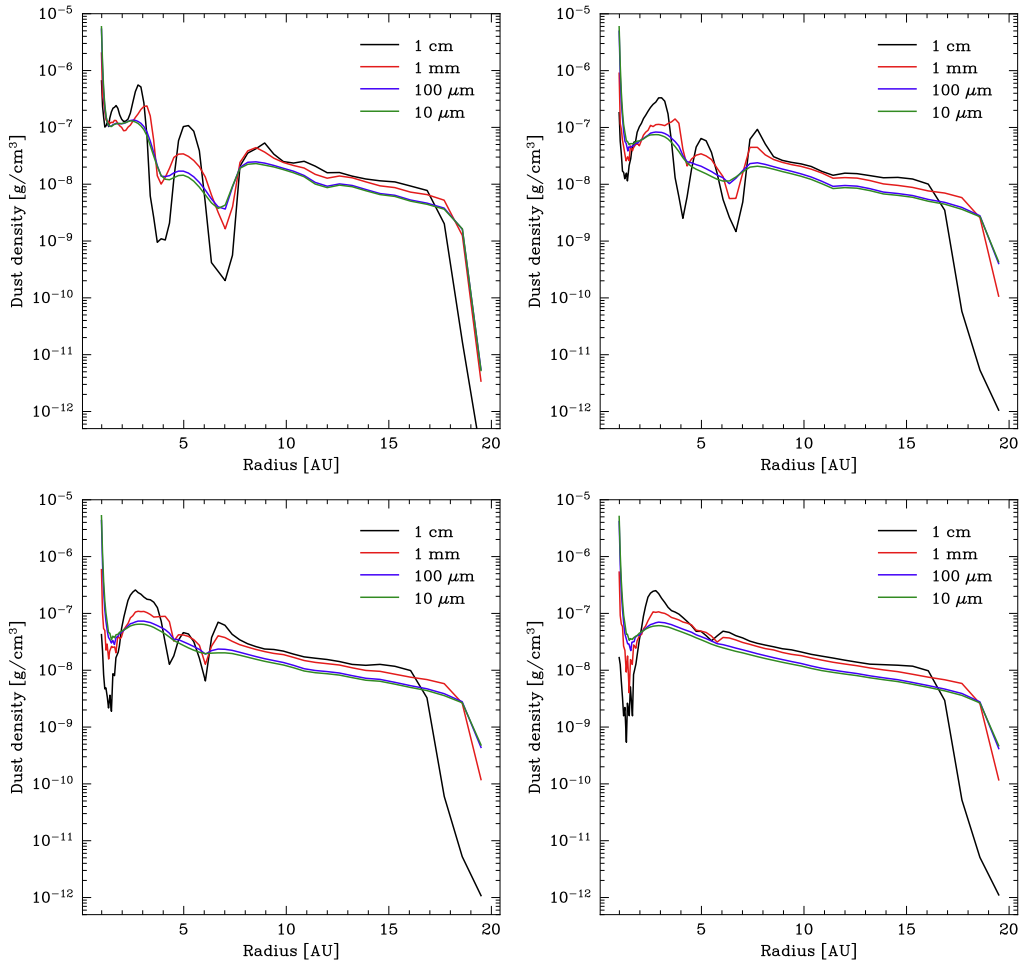

Figure 6.2: From top left going clockwise I show the dust density in the mid plane of discs containing planets of masses $10M_J$, $3M_J$, $1M_J$, and M_{Sat}. In each radial profile the quadrant ±45° from the planet location is excluded. The gaps in dust increase in depth with planet mass and dust grain size. In all cases the planet is located at 5.2au.

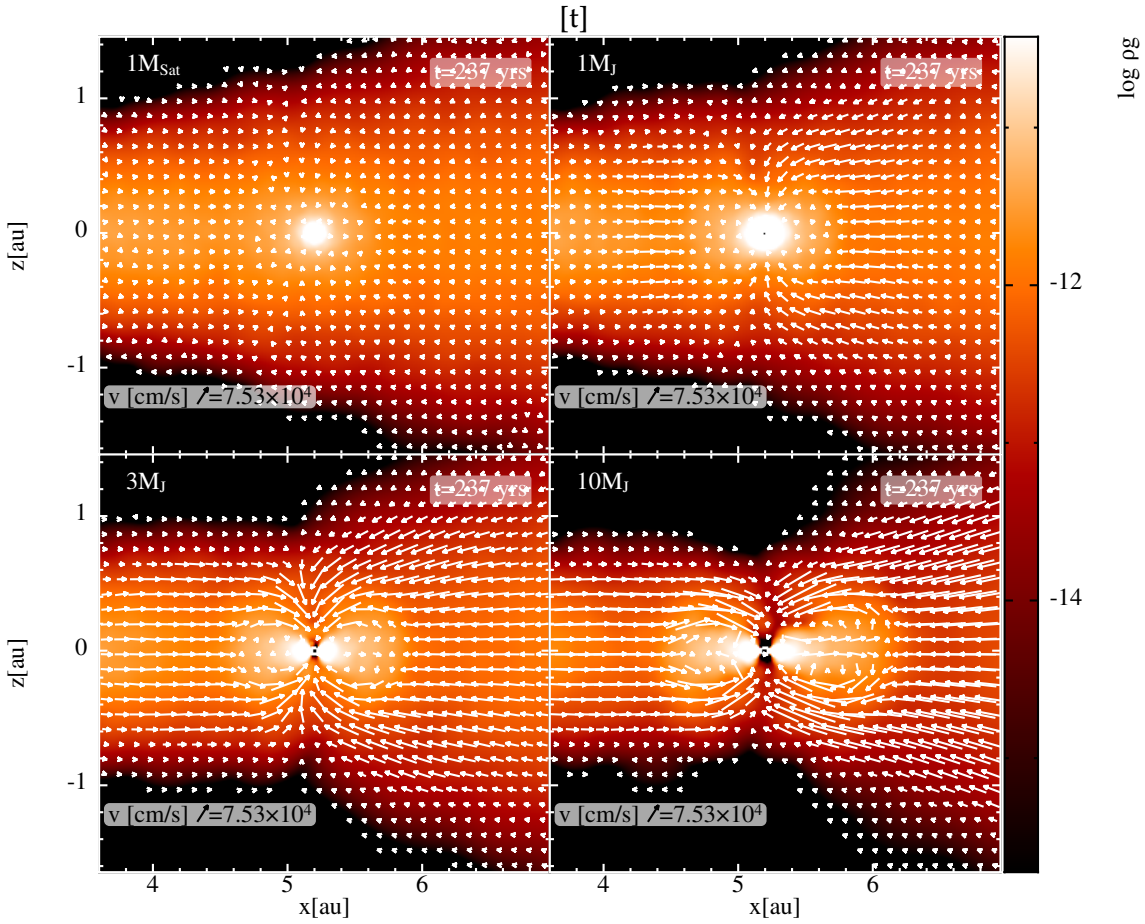

Figure 6.3: Gas density map about the planet location with gas flow direction shown with arrows. The snapshots are cross sections through the $x - z$ axis at the planet location after 20 orbits. The initial planet masses are $1M_{\rm Sat}$, $1M_{\rm J}$, $3M_{\rm J}$, $10M_{\rm J}$ as indicated in the figure panels. The gas flow around the planet strengthens as planet mass increases. The flow of gas onto the planet is dominated by gas from high altitude, and gas flows away from the planet in the midplane.

As the planet mass increases the protoplanetary discs becomes increasingly thinner in the vicinity of the planet. Above and below the planet there are strong flows of gas towards the midplane. These flows of gas are caused by the spiral wakes of the planet, they continuously stir up material that then gets deposited higher up into the disc. The gas flows into the gap and onto the planet. Any gas that is not accreted by the planet flows out into the protoplanetary disc via the circumplanetary disc, through the spiral wakes and rises up again to higher altitudes of the disc (Szulágyi et al. 2014; Fung and Chiang 2016). This is the meridional circulation of gas within a protoplanetary disc (Szulágyi et al. 2014; Morbidelli et al. 2014). Any dust that is coupled to the gas is also influenced by the meridional circulation of the gas (Binkert et al. 2021). The impact of this vertical accretion onto the planets is there is more oxygen rich ice available for accretion onto the planetary atmosphere (Cridland et al. 2020), meaning that in the inner 20 au of the disc it is the chemical composition of the gas that dominates the C/O ratios on planet atmospheres. In this work, the strongest flows are in the discs containing planet of super-Jovian mass. So it would be reasonable to expect that it is in these calculations that moderately coupled dust will feel the largest effect.

In Fig. 6.4 I show dust density of 1mm grains in cross sections of discs that have been rotated about the z axis ±45° with respect to the planet location, i.e. we are looking are the planetary wakes at the inner and outer edges of the gap. The influence of the meridional circulation is most apparent in the two super-Jovian mass calculations. On the left side of Fig. 6.4 there is an enhancement in dust density at the inner edge of the gap, this is where the leading planetary wake is located. At the other side of the gap, in the outer disc, there are two regions in the both discs with a slight enhancement in dust density when compared to the two calculations with less massive planets. The two over densities are located within the trailing spiral wakes of the planet. On the right hand side of Fig. 6.4 the disc is rotated 45° such that the trailing wake is passing through the outer edge of the gap. In the calculation with the $10 M_{\rm J}$ planet we see the vertical height of the dust disc vary between the two spiral wakes. This is where the dust is being stirred up by the wakes. Figure 6.6 shows the vertical velocity of dust in the same cross sections as Fig. 6.4. In the super-Jovian mass calculations there is a strong inversion of vertical dust velocity at the location of the wakes, here the dust is moving away from the midplane. In front of, and

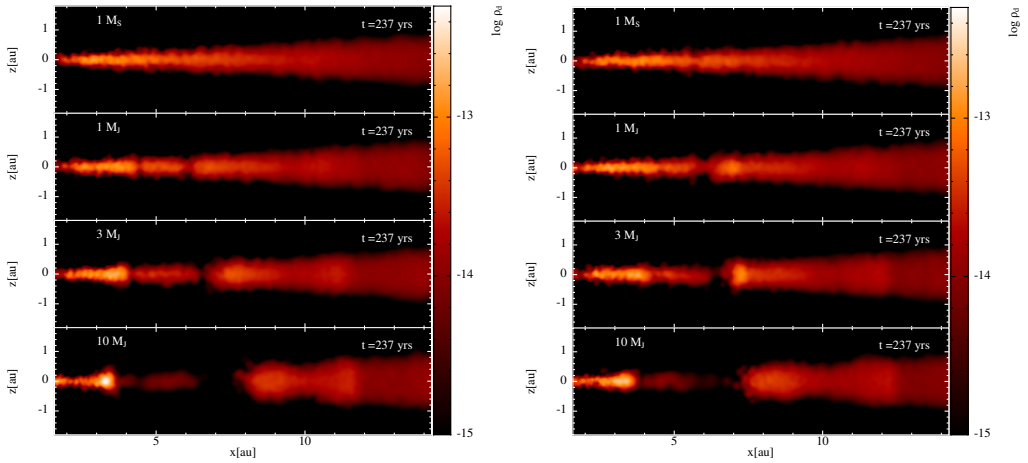

Figure 6.4: *Left*: $\phi = -45°$ from planet location. *Right*: $\phi = +45°$ from planet location. Cross section dust density (g cm^3) of mm-sized grains through disc rotated ±45° from planet location.

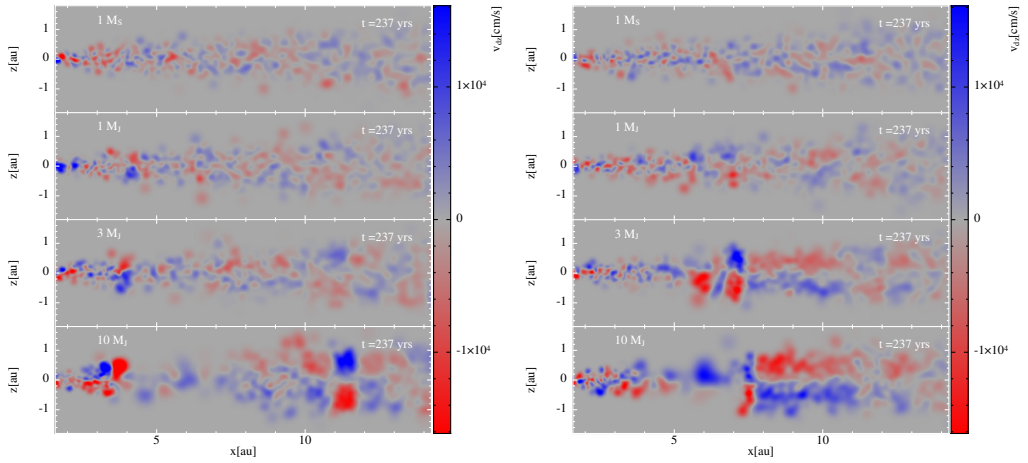

Figure 6.5: *Left*: $\phi = -45°$ from planet location. *Right*: $\phi = +45°$ from planet location. Cross section of vertical dust velocity (cm/s) of mm-sized grains. The vertical velocity of dust is inverted in the spiral wakes of the planet causing dust to be stirred up towards the surface of the disc.

behind, the wakes the dust is settling to the midplane. This vertical transport of the dust results in the alteration of the dust disc geometry that is shown in Fig. 6.4. The vertical transport is efficient enough to allow to mm-sized grains to be found near the surface of the gas disc.

6.3 Discussion

In that past 15 years it has become clear that dust is a key factor in the determination of the geometry of material surrounding a protoplanet, it partially determines whether the planet will host a circumplanetary disc or a more spherical envelope. This affects the accretion rate of the planet, due to the effect of the dust on the opacity and cooling of the gas.

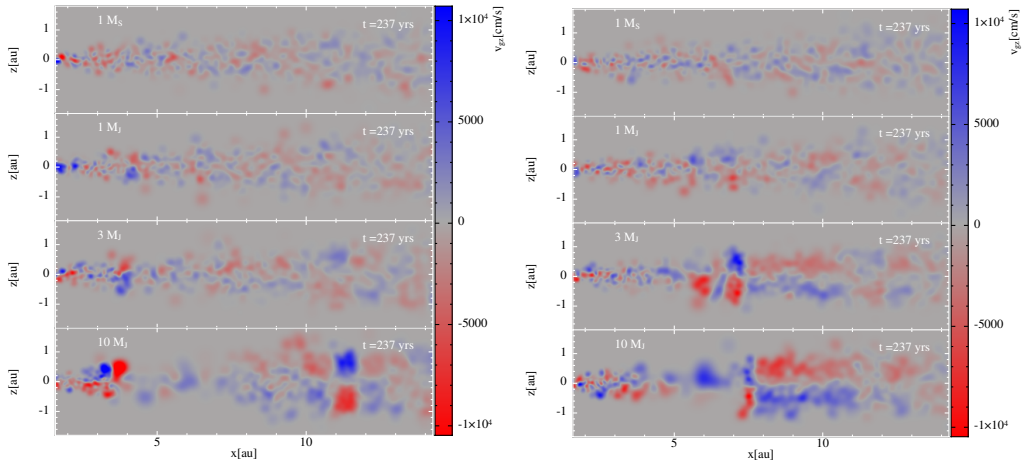

Figure 6.6: *Left*: $\phi = -45°$ from planet location. *Right*: $\phi = +45°$ from planet location. Cross section of vertical gas velocity (cm/s). The vertical velocity of gas is inverted in the spiral wakes of the planet causing gas to be stirred up towards the surface of the disc. This is the meridional gas circulation, a global disc gas flow. Note that the gas velocities are lower than the dust velocities.

In the calculations I present here the average accretion rate over the course of each simulation are: 3.989×10^{-7}, 6.2041×10^{-6}, 1.5266×10^{-5}, and 2.4532×10^{-5} for the $1M_{Sat}$, $1M_J$, $3M_J$, and $10M_J$ mass planets, respectively in units of $M_J\ yr^{-1}$. The planets with a spherical envelope have lower accretion rates than those with discs. The pioneering work of Ayliffe and Bate (2009a) showed that the structure of the material around a protoplanet is dependent upon opacity. The standard picture was that circumplanetary discs were thin discs, however Ayliffe and Bate (2009a) showed that if the grain opacity sufficiently low, only then do disc-like structure form. They also find that discs around more massive planets tend to be flatter than the discs around less massive planets. This is a result recovered in this chapter. When the grain opacity is high the discs are thicker as the thermal pressure supports against the gravitational forces from the planet. Szulágyi et al. (2016) and Szulágyi (2017) investigated the structure of circumplanetary discs and their dependence on temperature, finding that a higher temperature reduces the disc's rotation resulting in a more envelope structure. Recent work by Krapp et al. (2024) agrees with the previous results and find a necessary condition for the formation of circumplanetary discs is that the cooling time is at least one order of magnitude shorter than the orbital time.

Dust gaps are a key sign of evidence that a planet may be present in a disc. The properties of the gap may also give an indication on the properties of the planet, and the dust population (Dipierro and Laibe 2017). In this work I find the dust gap to be deeper

with increasing planet mass for a given grain size, and deeper with increasing grain size for a given planet mass. The width of the gap also changes slightly with grain size for a given planet mass. It is not only the dust gap that the planet has an impact on. The density of dust in the inner disc also appears to depend on both planet mass and grain size. I find that the dust density of the inner disc is higher for small grains, with the exception of the $10M_{\rm J}$ planet. Larger grains are depleted in the inner disc compared to smaller grains. This dust filtration was first identified in the 2D calculations of Rice et al. (2006), and has since been proposed as a mechanism for the long lived inner dust ring in PDS 70 (Pinilla et al. 2024). In this mechanism, small dust grains are coupled to the gas and are able to diffusion across the gap through the gas, replenishing the supply of dust in the inner regions of the disc. This has implications for disc chemistry, water ice that is on small dust grains may get transported from the outer disc into the inner disc and then sublimate, allowing for an efficient water delivery mechanism for water vapour. Ice-bearing particles (sizes 3mm - 1cm) can be prevented from drifting to inner regions of the disc if a gap opens up in the gas (Kalyaan et al. 2021). The blocking of ice particles is most efficient is the gap opens up around 7-15 au from the star, any closer or further away and water-ice can be delivered to the inner regions of the disc, enriching the amount of water vapour present. The depth of the gap is also important, shallower gaps may allow ice-bearing particles to leak through. In addition to this mechanism, low α discs can have a higher an enrichment in water vapour in the inner disc (Kalyaan et al. 2023).

The dust stirring induced by massive planets widens the vertical dust distribution within a disc, this effect is likely to be visible in the observations of the dust (Birnstiel et al. 2018; Zhang et al. 2018). Although this feature will only be visible in close to edge-on discs, it may be an indicator of a massive embedded planet. The dust stirring by massive planets has been identified previously with the grid code JUPITER in the works of Binkert et al. (2021), Szulágyi et al. (2022), and Binkert et al. (2023). The method I use and the initial conditions used in the calculations that I present are different to the those in these previous works. This is an indication that the dust stirring due to the meridional flow induced in the gas via planetary wakes is a robust dust transport mechanism.

6.4 Conclusions

In this chapter I employ the method of dust grain evolution presented in Chapter 5 to examine the influence giant planets have upon the distribution and dynamics of dust grains in protoplanetary discs. The results of this chapter replicate those of previous studies on small dust grains in the presence of giant planets. I summarise the findings below.

1. The impact a planet has upon the distribution of dust within a protoplanetary disc is dependent upon the mass of the planet, and the size of grains in the disc. The gaps that form in the calculations presented have a width of $\sim 5 - 7\ r_{\rm H}$.

2. Small dust grain density in the inner disc is maintained over time, whereas the density of more decoupled grains in the inner disc is reduced over time, with the exception of the calculation with the most massive planet.

3. Spiral wakes generated by massive planets drive strong meridional flows in the gas. This leads to gas falling above and below the planet, with outflows of gas in the circumplanetary disc.

4. Grains of mm-size are stirred up by these meridional flows, enhancing dust density in the spiral wakes of the planet. The dust grains can be stirred up to the surface of the gas disc.

Chapter 7

The Conclusion

"I thought up an ending for my book: 'And he lived happily ever after, unto the end of his days.' "

— Bilbo Bagins

7.1 Concluding Remarks

In this thesis I have presented the analysis of discs formed in hydrodynamic simulations in order to study their properties and how they compare to observations of discs. We are in an era in observational astronomy where is it possible to undertake large surveys within many star-forming regions. This has allowed us to begin to address the questions of how common are discs? How does the environment of a circumstellar disc impact upon the evolution of the disc? What are the statistical properties of discs? How do current hydrodynamic calculations compare with observations? What are the dominant physical processes? These questions are best answered when theory and observations are combined.

In Chapter 3 I present analysis of discs formed four large radiation hydrodynamic calculations of star cluster formation in which metallicity of the calculation is changed. From these calculations I extract the statistics of disc properties, for example; mass, radius, inclination, star-to-disc mass ratios. The metallicities of the calculations are 1/100, 1/10, 1, 3 solar metallicity, in terms of initial conditions this is the only thing that is changed

between the calculations. This is to study the impact the environment of the discs has upon the properties of the disc. When comparing the properties of discs across the calculations it was found that a higher metallicity cloud produces larger discs compared to the low metallicity calculation. In the molecular cloud with the highest metallicity discs have a median characteristic radius of $\approx$ 65 au and in the calculation with the lowest metallicity, discs have median characteristic radius of $\approx$ 20 au. The low metallicity allows for rapid cooling of high density gas leading to more gravitational fragmentation, it is this enhancement in small scale fragmentation that leads to the truncation of discs. This is the same physics that leads to the increase in multiplicity with decreasing metallicity. The change in metallicity has little effect on the masses of discs, with the exception of in the calculation with the lowest metallicity the fraction of unresolved and low-mass discs is much higher. The properties of the discs formed in the solar metallicity calculations are compared with the statistics of disc observations from nearby star-forming regions. I find that the properties, the masses and radii, of the discs formed in this calculation are in very good agreement with the properties of Class 0/I discs in the Orion and Perseus regions. Whereas when comparing the properties of the discs with Class II discs, the masses of the simulated discs are typically an order of magnitude higher, however the radii of simulated discs are comparable to the discs within Lupus. The discs formed in the simulation are closer in evolution to Class 0/I and so are a better comparison over the Class II discs. These calculations do not include magnetic fields, nor do they include feedback from the protostars themselves, despite this, the size and mass distributions of discs formed in the calculation are in good agreement with those obtained from observations. This may indicate that the calculations have captured the dominant physics, and that magnetic braking of discs may not play a big role is setting the properties of protostellar discs.

In Chapter 4 I study the properties of circumbinary discs formed in the solar metallicity calculation discussed in Chapter 3. Binary systems and their discs have recently received an uptick in interest and have been subject to intense study. It is known that binary systems are a very common feature in star-formation, however the occurrence rate of circumbinary discs in young objects is not known. Discs around single objects are almost always expected to form, is the same true of discs around binary systems? There is very little observational data to help answer this question. However, as I demonstrated in

Chapter 3, hydrodynamical calculations are capable of reproducing the statistical properties of protostellar discs derived from observations. It is in Chapter 4 that I make an effort to begin to answer the question of circumbinary disc occurrence rate. Given a sample of young binary systems, inclusive of those in hierarchical systems, that have a semi-major axis of less than 100au it would be expected that around 35 per cent of the binaries would host a circumbinary disc. In these young systems, almost no system with a semi-major axis greater than 100 au hosts are circumbinary disc. In close binary systems ($a \lesssim 3$ au), those without companions are twice as likely to host a circumbinary disc than those with companions. At close separation there is a multiplicity effect, this effect is not apparent in systems with a larger semi-major axis. The sizes of circumbinary discs that form scale linearly with semi-major axis, and have a median radius of 5-6a. Another interesting question one can ask about these systems is how aligned are the circumbinary discs to the orbit plane of their host binaries? Given than discs form due to the conservation of angular momentum, it is reasonable to expect that circumbinary discs will share a similar plane of angular momentum to the binaries and thus be well aligned. I extract the cumulative distribution of the mutual inclination angles between the circumbinary discs and binary orbits and find most systems are reasonably well aligned. I also constructed the cumulative distribution function of all the known mutual inclination angles that were available in the literature to compare with the results from the calculation. I found that the underlying distributions do not differ.

Motivated to extend the capability of the hydrodynamic code that I use in this thesis to simulate protostellar discs, I present a method to evolve the dynamics of small dust grains in Chapter 5. The method builds upon the efforts of the community over the past decade to develop an efficient and accurate method of simulating small dust grain dynamics. I extend the method by developing an implicit numerical scheme that can solve the dust evolution equation quickly and efficiently. I found the method to reproduce the results of the standard explicit scheme, however the implicit method yields the result for larger grains at least two orders of magnitude more quickly. Using the explicit method in practice, when larger grains are present it is, almost, a necessity to artificially limit the stopping time of the dust grains; in essence artificially altering the dust grain sizes, forcing them to be smaller than the practitioner might expect. This is because the timestep crite-

rion for the dust becomes prohibitively small at long stopping time (larger grains). There is no way a priori to know how a stopping time limiter will affect the calculation. This is something that is completely avoided in the implicit method. I found that the implicit scheme is less susceptible to an unphysical solution to the dust diffusion equation. The issue arises due to how the dust fraction is computed. The dust fraction is parameterised by a new variable such that the dust fraction remains between zero and one, however, there is nothing to prevent this new variable from becoming negative. Whilst the result makes sense mathematically, physically this results in dust grains diffusing into a region that they should be diffusing away from and is not a valid physical solution. In the context of a protoplanetary disc this would mean that after dust grains have settled to the midplane they would then diffuse away and become trapped at high altitude in the disc. This issue is significantly avoided with the implicit method. I found this method to be fast, accurate, and to avoid several issues that manifest in the explicit calculations.

In the final Chapter of this thesis I apply this new method for solving the dust diffusion equation in the context of planet formation. I combine planetary models, radiative transfer, and dust dynamics to study the effect giant planets have on the distribution of small dust grains within protoplanetary discs. The larger grains tend to pile up at the outer edge of the gap, whereas the smaller grains tend to have a smoother density profile. Additionally, I found that these calculations reproduce the vertical dust transport induced by the meridional circulation of gas within discs containing giant planets. The dust transport mechanism has been recently discovered in other 3D calculations, here I reproduce these results using different disc parameters and a different numerical method. This strengthens the implication that this dust transport is a robust feature within protoplanetary discs. Whether or not the features in the disc produced by this mechanism are observable deserves to be investigated.

7.2 Future work

One of the aims of this thesis has been to be a part of the answer to how the environment of protostellar discs effects their evolution, and thus their properties. Whilst I have demonstrated that metallicity has an impact upon the properties of the discs, the compar-

isons of the hydrodynamic calculations are with observations of dust. In my analysis the disc radius is based upon the gas disc radius, and I have assumed a 1:100 dust-to-gas ratio when considering dust disc mass. In future, inclusion of small dust grain dynamics in star-formation calculations may allow for a more equatable comparison with observations. An ambitious goal is to couple the method of evolving the dust grains with a method for simulating multiple dust grains at the same time. The coupling of these methods would allow one to study the dynamics of multiple grain species at a reduced computational cost.

The investigation of the vertical dust transport within planet bearing discs should be continued in a with a wider disc parameter space to determine whether certain discs are more susceptible to this effect. I do not present the results of an analysis of the vertical dust transport within discs of different grains sizes, this should be conducted in the future. In addition if the dust dynamics method developed in this thesis can be coupled with a multiple grain evolution model the calculations should be repeated so comparisons between dust grain sizes can be made in the same simulation rather than across calculations. Whilst we find this transport mechanism to be present in a disc containing a single planet, discs with multiple planets could be considered to further test the robustness of this mechanism. I have also kept the orbits of planet fixed, how does planet migration impact the dust transport?

In theory the method I have presented for solving the dust diffusion equation in the limit of terminal velocity could be applied to the full set of dust-as-mixture equations. Given the improvements made to the explicit dust diffusion method it would be worthwhile to investigate the suitability of the implicit method on the full dust-as-mixture method. Such a method would allow for further investigations into the dynamics of small dust grains of a number of astrophysical settings with great accuracy in the limit of large grains. The ultimate goal of developing a fast and accurate dust dynamics method is to couple it with a method for dust growth and fragmentation. With this, one could study the dynamics and growth of dust from sub-micron to mm-sized grains, from protostellar collapse right through to the early evolution of the protostellar disc.

The Appendices

Appendix A

Notes on the mutual inclinations of observed systems

"If a man knows not to which port he sails, no wind is favorable."

— Seneca

In constructing Table 4.1, we have the following notes:

In the case of HD98800B, Zúñiga-Fernández et al. (2021) report two values for $i_{\rm disc}$ ($i_{\rm disc}$ = 26° or 154°). They recover θ = 89 ± 1° when $i_{\rm disc}$ = 26°, and θ = 134 ± 1° when $i_{\rm disc}$ = 154°. The alternate value of θ when $i_{\rm disc}$ = 26° is θ = 46 ± 1°. In our statistics we use the higher value of $i_{\rm disc}$ as it recovers polar (θ = 91 ± 3°) and retrograde values for θ whilst preserving our assumption of 180° ambiguity in Ω_*.

TWA 3A is complicated, there are many degenerate solutions as i for both disc and inner binary are ambiguous. Ω for the disc is constrained, though the disc is either coplanar or polar depending on which i you take. Czekala et al. (2021) claim this disc to be coplanar, however they do not report the mutual inclination angle calculated with the degenerate values of i. When i_* = 48.5 ± 0.5° and $i_{\rm disc}$ = 131.2 ± 0.7°, θ = 83.4 ± 0.9°; when i_* = 131.5 ± 0.8° and $i_{\rm disc}$ = 131.2 ± 0.7°, θ = 9 ± 6°. In the degenerative cases, the disc is either close to coplanar or in polar orbit. Assuming a 180° ambiguity of Ω_* in these cases gives "alternate" values; in the coplanar case it is nearly polar, and in the polar case it is

nearly retrograde. In this paper we use $i_* = 48.5$ and $i_{\rm disc} = 48.8$, and as with the other systems we give a "false" value of θ by assuming 180° ambiguity in Ω_* even though this value has been constrained with RV data (Czekala et al. 2021).

There is no value of Ω_* reported in the literature for R CrA (Mesa et al. 2019; Czekala et al. 2019) and so we do not include it in our statistics.

In the case of HD 142527 B, Balmer et al. (2022) provide updated orbital parameters for this system. The corresponding mutual inclination angles are $\theta = 89.8 \pm 2°$ and $\theta = 158.8 \pm 3°$, so this disc is either polar or retrograde. This is not in agreement with the previous value of theta from Czekala et al. (2019) of $\theta = 35 \pm 5°$. We use the updated orbital parameters from Balmer et al. (2022) in our statistics. The higher inclination is in better agreement with the modelling of Price et al. (2018a).

Appendix B

Solving the quartic analytically

"I can normally tell how intelligent a man is by how stupid he thinks I am."

— Cormac McCarthy

The solutions to the quartic equation

$$P(x) = x^4 + a_3x^3 + a_2x^2 + a_1x + a_0 = 0, \tag{B.1}$$

can be found via solving the resolvent cubic if $P(x)$ is depressed, i.e. $a_3 = 0$. Firstly, the real root, y_1 is found for the resolvent cubic

$$y^3 - a_2y^2 + -4a_0y + 4a_2a_0 - a_1^2 = 0. \tag{B.2}$$

Then the four solutions to the quartic $P(x)$ are given by the four solutions of (Abramowitz and Stegun 1972)

$$z^2 \mp \left(y_1 - a_2\right)^{1/2} z + \left(\frac{y_1}{2} \mp \left(\frac{y_1}{2}\right)^2 - a_0\right) = 0. \tag{B.3}$$

Bibliography

Abramowitz, M., and I. A. Stegun. 1972. *Handbook of mathematical functions*. US Government printing office, January.

Abt, H. A., and S. G. Levy. 1976. 'Multiplicity among solar-type stars.' *The Astrophysical Journals* 30 (March): 273–306.

Aizawa, Masataka, Yasushi Suto, Yoko Oya, Shiro Ikeda, and Takeshi Nakazato. 2020. 'Search for Alignment of Disk Orientations in Nearby Star-forming Regions: Lupus, Taurus, Upper Scorpius, ρ Ophiuchi, and Orion.' *The Astrophysical Journal* 899, no. 1 (August): 55.

Akeson, Rachel L., Eric L. N. Jensen, et al. 2019. 'Resolved Young Binary Systems and Their Disks.' *The Astrophysical Journal* 872, no. 2 (February): 158.

ALMA Partnership, C. L. Brogan, et al. 2015. 'The 2014 ALMA Long Baseline Campaign: First Results from High Angular Resolution Observations toward the HL Tau Region.' *ApJL* 808, no. 1 (July): L3.

Aly, Hossam, and Giuseppe Lodato. 2020. 'Efficient dust ring formation in misaligned circumbinary discs' [in en]. *Monthly Notices of the Royal Astronomical Society* 492, no. 3 (March): 3306–3315.

Aly, Hossam, Rebecca Nealon, and Jean-François Gonzalez. 2024. 'WInDI: a Warp-Induced Dust Instability in protoplanetary discs.' *Monthly Notices of the Royal Astronomical Society* 527 (January): 4777–4789.

Andre, Philippe, Derek Ward-Thompson, and Mary Barsony. 1993. 'Submillimeter Continuum Observations of rho Ophiuchi A: The Candidate Protostar VLA 1623 and Prestellar Clumps.' *The Astrophysical Journal* 406 (March): 122.

Andrews, Sean M. 2020. 'Observations of Protoplanetary Disk Structures.' *Annual Review of Astronomy and Astrophysics* 58 (August): 483–528.

Andrews, Sean M., Claire J. Chandler, et al. 2014. 'Resolved Multifrequency Radio Observations of GG Tau.' *The Astrophysical Journal* 787 (June): 148.

Andrews, Sean M., Ian Czekala, et al. 2010a. 'Truncated Disks in TW Hya Association Multiple Star Systems.' *The Astrophysical Journal* 710 (February): 462–469.

Andrews, Sean M., and Jonathan P. Williams. 2005. 'Circumstellar Dust Disks in Taurus-Auriga: The Submillimeter Perspective.' *The Astrophysical Journal* 631 (October): 1134–1160.

Andrews, Sean M., D. J. Wilner, A. M. Hughes, Chunhua Qi, and C. P. Dullemond. 2010b. 'Protoplanetary Disk Structures in Ophiuchus. II. Extension to Fainter Sources.' *The Astrophysical Journal* 723 (November): 1241–1254.

Andrews, Sean M., David J. Wilner, et al. 2016. 'Ringed Substructure and a Gap at 1 au in the Nearest Protoplanetary Disk.' *ApJL* 820, no. 2 (April): L40.

Ansdell, M., J. P. Williams, et al. 2016. 'ALMA Survey of Lupus Protoplanetary Disks. I. Dust and Gas Masses.' *The Astrophysical Journal* 828, no. 1 (September): 46.

Ansdell, Megan, Thomas J. Haworth, et al. 2020. 'An ALMA Survey of λ Orionis Disks: From Supernovae to Planet Formation.' AJ 160, no. 6 (December): 248.

Anthonioz, F., F. Ménard, et al. 2015. 'The VLTI/PIONIER near-infrared interferometric survey of southern T Tauri stars. I. First results.' *Astronomy and Astrophysics* 574 (January): A41.

Armstrong, D. J., H. P. Osborn, et al. 2014. 'On the abundance of circumbinary planets.' *Monthly Notices of the Royal Astronomical Society* 444 (October): 1873–1883.

Arquilla, R., and P. F. Goldsmith. 1986. 'A Detailed Examination of the Kinematics of Rotating Dark Clouds.' *The Astrophysical Journal* 303 (April): 356.

Artymowicz, P., C. J. Clarke, S. H. Lubow, and J. E. Pringle. 1991. 'The Effect of an External Disk on the Orbital Elements of a Central Binary.' *The Astrophysical Journall* 370 (March): L35.

Artymowicz, Pawel, and Stephen H. Lubow. 1994. 'Dynamics of Binary-Disk Interaction. I. Resonances and Disk Gap Sizes.' *The Astrophysical Journal* 421 (February): 651.

———. 1996. 'Mass Flow through Gaps in Circumbinary Disks.' *The Astrophysical Journal* 467 (August): L77.

Aso, Yusuke, Nagayoshi Ohashi, et al. 2017. 'ALMA Observations of the Protostar L1527 IRS: Probing Details of the Disk and the Envelope Structures.' *The Astrophysical Journal* 849, no. 1 (November): 56.

Aumann, H. H., F. C. Gillett, et al. 1984. 'Discovery of a shell around alpha Lyrae.' *The Astrophysical Journal* 278 (March): L23–L27.

Avenhaus, Henning, Sascha P. Quanz, et al. 2018. 'Disks around T Tauri Stars with SPHERE (DARTTS-S). I. SPHERE/IRDIS Polarimetric Imaging of Eight Prominent T Tauri Disks.' *The Astrophysical Journal* 863 (August): 44.

Ayliffe, Ben A., and Matthew R. Bate. 2009a. 'Circumplanetary disc properties obtained from radiation hydrodynamical simulations of gas accretion by protoplanets.' *Monthly Notices of the Royal Astronomical Society* 397 (August): 657–665.

———. 2009b. 'Gas accretion on to planetary cores: three-dimensional self-gravitating radiation hydrodynamical calculations.' *Monthly Notices of the Royal Astronomical Society* 393 (February): 49–64.

Ayliffe, Ben A., Guillaume Laibe, Daniel J. Price, and Matthew R. Bate. 2012. 'On the accumulation of planetesimals near disc gaps created by protoplanets.' *Monthly Notices of the Royal Astronomical Society* 423 (June): 1450–1462.

Bai, Xue-Ning, and James M. Stone. 2010. 'Particle-gas Dynamics with Athena: Method and Convergence.' *The Astrophysical Journal Supplement Series* 190 (October): 297–310.

Bai, Xue-Ning, and James M. Stone. 2013. 'Wind-driven Accretion in Protoplanetary Disks. I. Suppression of the Magnetorotational Instability and Launching of the Magneto-centrifugal Wind.' *The Astrophysical Journal* 769 (May): 76.

Balbus, Steven A, and John F Hawley. 1991. 'A powerful local shear instability in weakly magnetized disks. I-Linear analysis. II-Nonlinear evolution.' *The Astrophysical Journal* 376:214–233.

Ballabio, G., G. Dipierro, et al. 2018. 'Enforcing dust mass conservation in 3D simulations of tightly coupled grains with the PHANTOM SPH code.' MNRAS 477, no. 2 (June): 2766–2771.

Balmer, William O., Katherine B. Follette, et al. 2022. 'Improved Orbital Constraints and Hα Photometric Monitoring of the Directly Imaged Protoplanet Analog HD 142527 B' [in en]. AJ 164, no. 1 (July): 29.

Barenfeld, Scott A., John M. Carpenter, Anneila I. Sargent, Andrea Isella, and Luca Ricci. 2017. 'Measurement of Circumstellar Disk Sizes in the Upper Scorpius OB Association with ALMA.' *The Astrophysical Journal* 851, no. 2 (December): 85.

Barraza-Alfaro, Marcelo, Mario Flock, and Thomas Henning. 2024. 'Kinematic signatures of planet-disk interactions in vertical shear instability-turbulent protoplanetary disks.' *Astronomy and Astrophysics* 683 (March): A16.

Barrière-Fouchet, L., J. -F. Gonzalez, J. R. Murray, R. J. Humble, and S. T. Maddison. 2005. 'Dust distribution in protoplanetary disks. Vertical settling and radial migration.' *Astronomy and Astrophysics* 443 (November): 185–194.

Bate, M. R. 1995. PhD diss., University of Cambridge.

Bate, M. R., G. Lodato, and J. E. Pringle. 2010. 'Chaotic star formation and the alignment of stellar rotation with disc and planetary orbital axes.' *MNRAS* 401, no. 3 (January): 1505–1513.

Bate, M. R., S. H. Lubow, G. I. Ogilvie, and K. A. Miller. 2003a. 'Three-dimensional calculations of high- and low-mass planets embedded in protoplanetary discs.' *Monthly Notices of the Royal Astronomical Society* 341 (May): 213–229.

Bate, Matthew R. 2018. 'On the diversity and statistical properties of protostellar discs.' *Monthly Notices of the Royal Astronomical Society* 475, no. 4 (January): 5618–5658.

———. 1998. 'Collapse of a Molecular Cloud Core to Stellar Densities: The First Three-dimensional Calculations.' *The Astrophysical Journal* 508 (November): L95–L98.

———. 2009. 'The importance of radiative feedback for the stellar initial mass function.' *Monthly Notices of the Royal Astronomical Society* 392 (February): 1363–1380.

———. 2011. 'Collapse of a molecular cloud core to stellar densities: the formation and evolution of pre-stellar discs.' *Monthly Notices of the Royal Astronomical Society* 417 (November): 2036–2056.

———. 2012. 'Stellar, brown dwarf and multiple star properties from a radiation hydrodynamical simulation of star cluster formation.' *MNRAS* 419, no. 4 (January): 3115–3146.

———. 2014. 'The statistical properties of stars and their dependence on metallicity: the effects of opacity.' *Monthly Notices of the Royal Astronomical Society* 442, no. 1 (July): 285–313.

———. 2019. 'The statistical properties of stars and their dependence on metallicity.' *Monthly Notices of the Royal Astronomical Society* 484, no. 2 (April): 2341–2361.

Bate, Matthew R., and Ian A. Bonnell. 1997. 'Accretion during binary star formation - II. Gaseous accretion and disc formation.' *Monthly Notices of the Royal Astronomical Society* 285 (February): 33–48.

———. 2005. 'The origin of the initial mass function and its dependence on the mean Jeans mass in molecular clouds.' *Monthly Notices of the Royal Astronomical Society* 356 (February): 1201–1221.

Bate, Matthew R., Ian A. Bonnell, and Volker Bromm. 2002. 'The formation of close binary systems by dynamical interactions and orbital decay.' *Monthly Notices of the Royal Astronomical Society* 336 (November): 705–713.

———. 2003b. 'The formation of a star cluster: predicting the properties of stars and brown dwarfs.' *Monthly Notices of the Royal Astronomical Society* 339 (March): 577–599.

Bate, Matthew R., Ian A. Bonnell, and Nigel M. Price. 1995. 'Modelling accretion in protobinary systems.' *MNRAS* 277, no. 2 (November): 362–376.

Bate, Matthew R., and Andreas Burkert. 1997. 'Resolution requirements for smoothed particle hydrodynamics calculations with self-gravity.' *Monthly Notices of the Royal Astronomical Society* 288, no. 4 (July): 1060–1072.

Bate, Matthew R., and Eric R. Keto. 2015. 'Combining radiative transfer and diffuse interstellar medium physics to model star formation.' *MNRAS* 449, no. 3 (April): 2643–2667.

Bate, Matthew R., and Pablo Loren-Aguilar. 2017. 'On the dynamics of dust during protostellar collapse' [in en]. *Monthly Notices of the Royal Astronomical Society* 465, no. 1 (February): 1089–1094.

Beckwith, S., B. Zuckerman, M. F. Skrutskie, and H. M. Dyck. 1984. 'Discovery of solar system size halos around young stars.' *The Astrophysical Journal* 287 (December): 793–800.

Belinski, A., M. Burlak, et al. 2022. 'Orbital parameters and activity of ZZ Tau - a low-mass young binary with circumbinary disc.' *Monthly Notices of the Royal Astronomical Society* 515 (September): 796–806.

Benisty, M., K. Perraut, et al. 2013. 'Enhanced Hα activity at periastron in the young and massive spectroscopic binary HD 200775.' *Astronomy and Astrophysics* 555 (July): A113.

Benisty, M., T. Stolker, et al. 2017. 'Shadows and spirals in the protoplanetary disk HD 100453' [in en]. *Astronomy and Astrophysics* 597 (January): A42.

Benítez-Llambay, Pablo, Leonardo Krapp, and Martin E. Pessah. 2019. 'Asymptotically Stable Numerical Method for Multispecies Momentum Transfer: Gas and Multifluid Dust Test Suite and Implementation in FARGO3D.' *The Astrophysical Journal Supplement Series* 241 (April): 25.

Benz, W. 1990. 'Smooth Particle Hydrodynamics - a Review.' In *Numerical Modelling of Nonlinear Stellar Pulsations Problems and Prospects,* edited by J. Robert Buchler, 269. January.

Benz, W., R. L. Bowers, A. G. W. Cameron, and W. H. . Press. 1990. 'Dynamic Mass Exchange in Doubly Degenerate Binaries. I. 0.9 and 1.2 M_{sun} Stars.' *ApJ* 348 (January): 647.

Beuzit, J. -L., A. Vigan, et al. 2019. 'SPHERE: the exoplanet imager for the Very Large Telescope.' *Astronomy and Astrophysics* 631 (November): A155.

Bi, Jiaqing, Nienke van der Marel, et al. 2020. 'GW Ori: Interactions between a Triple-star System and Its Circumtriple Disk in Action.' *The Astrophysical Journal* 895 (May): L18.

Biller, Beth, Sylvestre Lacour, et al. 2012. 'A Likely Close-in Low-mass Stellar Companion to the Transitional Disk Star HD 142527.' *The Astrophysical Journal* 753 (July): L38.

Binkert, Fabian, Judit Szulágyi, and Til Birnstiel. 2021. 'First 3D grid-based gas-dust simulations of circumstellar discs with an embedded planet.' *Monthly Notices of the Royal Astronomical Society* 506 (October): 5969–5988.

———. 2023. 'Three-dimensional dust stirring by a giant planet embedded in a protoplanetary disc.' *Monthly Notices of the Royal Astronomical Society* 523 (July): 55–79.

Birnstiel, T., C. P. Dullemond, and F. Brauer. 2010. 'Gas- and dust evolution in protoplanetary disks.' *Astronomy and Astrophysics* 513 (April): A79.

Birnstiel, Tilman, Cornelis P. Dullemond, et al. 2018. 'The Disk Substructures at High Angular Resolution Project (DSHARP). V. Interpreting ALMA Maps of Protoplanetary Disks in Terms of a Dust Model.' *The Astrophysical Journal* 869 (December): L45.

Black, D. C., and P. Bodenheimer. 1976. 'Evolution of rotating interstellar clouds. II. The collapse of protostars of 1, 2, and 5 M sun.' *The Astrophysical Journal* 206 (May): 138–149.

Boehler, Y., E. Weaver, et al. 2017. 'A Close-up View of the Young Circumbinary Disk HD 142527.' *The Astrophysical Journal* 840 (May): 60.

Bonnell, I. A. 1994. 'A New Binary Formation Mechanism.' *Monthly Notices of the Royal Astronomical Society* 269 (August): 837–848.

Bonnell, I. A., and M. R. Bate. 1994. 'The Formation of Close Binary Systems.' *Monthly Notices of the Royal Astronomical Society* 271 (December): 999–1004.

Booth, Alice S., Catherine Walsh, et al. 2019. 'The First Detection of 13C17O in a Protoplanetary Disk: A Robust Tracer of Disk Gas Mass.' *The Astrophysical Journal* 882 (September): L31.

Borkovits, T., T. Hajdu, et al. 2016. 'A comprehensive study of the Kepler triples via eclipse timing.' *Monthly Notices of the Royal Astronomical Society* 455 (February): 4136–4165.

Boss, A. P., and D. C. Black. 1982. 'Collapse of accreting, rotating, isothermal, interstellar clouds.' *The Astrophysical Journal* 258 (July): 270–279.

Boss, A. P., and P. Bodenheimer. 1979. 'Fragmentation in a rotating protostar: a comparison of two three-dimensional computer codes.' *The Astrophysical Journal* 234 (November): 289–295.

Boss, Alan P. 1986. 'Protostellar Formation in Rotating Interstellar Clouds. V. Nonisothermal Collapse and Fragmentation.' *The Astrophysical Journals* 62 (November): 519.

———. 1987. 'Protostellar Formation in Rotating Interstellar Clouds. VI. Nonuniform Initial Conditions.' *The Astrophysical Journal* 319 (August): 149.

Boss, Alan P., Robert T. Fisher, Richard I. Klein, and Christopher F. McKee. 2000. 'The Jeans Condition and Collapsing Molecular Cloud Cores: Filaments or Binaries?' *The Astrophysical Journal* 528, no. 1 (January): 325–335.

Breslau, Andreas, Manuel Steinhausen, Kirsten Vincke, and Susanne Pfalzner. 2014. 'Sizes of protoplanetary discs after star-disc encounters.' *Astronomy and Astrophysics* 565 (May): A130.

Brinch, Christian, Jes K. Jørgensen, Michiel R. Hogerheijde, Richard P. Nelson, and Oliver Gressel. 2016. 'Misaligned Disks in the Binary Protostar IRS 43.' *The Astrophysical Journal* 830 (October): L16.

Bryden, G., Xingming Chen, D. N. C. Lin, Richard P. Nelson, and John C. B. Papaloizou. 1999. 'Tidally Induced Gap Formation in Protostellar Disks: Gap Clearing and Suppression of Protoplanetary Growth.' *The Astrophysical Journal* 514 (March): 344–367.

Burke, J. R., and D. J. Hollenbach. 1983. 'The gas-grain interaction in the interstellar medium - Thermal accommodation and trapping.' *The Astrophysical Journal* 265 (February): 223–234.

Calahan, Jenny K., Edwin Bergin, et al. 2021. 'The TW Hya Rosetta Stone Project. III. Resolving the Gaseous Thermal Profile of the Disk.' *The Astrophysical Journal* 908 (February): 8.

Casassus, Simon, Henning Avenhaus, et al. 2018. 'An inner warp in the DoAr 44 T Tauri transition disc.' *Monthly Notices of the Royal Astronomical Society* 477, no. 4 (July): 5104–5114.

Cazzoletti, P., L. Ricci, T. Birnstiel, and G. Lodato. 2017. 'Testing dust trapping in the circumbinary disk around GG Tauri A.' *Astronomy and Astrophysics* 599 (March): A102.

Chandrasekhar, Subrahmanyan. 1961. *Hydrodynamic and hydromagnetic stability.* January.

Chavero, C., R. de la Reza, et al. 2019. 'Emerging trends in metallicity and lithium properties of debris disc stars.' *Monthly Notices of the Royal Astronomical Society* 487, no. 3 (August): 3162–3177.

Chiaki, Gen, Takaya Nozawa, and Naoki Yoshida. 2013. 'Growth of Dust Grains in a Low metallicity Gas and Its Effect on the Cloud Fragmentation.' *The Astrophysical Journall* 765, no. 1 (March): L3.

Chiang, Eugene I., and Ruth A. Murray-Clay. 2004. 'The Circumbinary Ring of KH 15D.' *The Astrophysical Journal* 607 (June): 913–920.

Cieza, Lucas A., Dary Ruíz-Rodríguez, et al. 2019. 'The Ophiuchus DIsc Survey Employing ALMA (ODISEA) - I: project description and continuum images at 28 au resolution.' *Monthly Notices of the Royal Astronomical Society* 482, no. 1 (January): 698–714.

Clarke, C. J. 2009. 'Pseudo-viscous modelling of self-gravitating discs and the formation of low mass ratio binaries.' *Monthly Notices of the Royal Astronomical Society* 396 (June): 1066–1074.

Clarke, C. J., and J. E. Pringle. 1988. 'The diffusion of contaminant through an accretion disc.' *Monthly Notices of the Royal Astronomical Society* 235 (November): 365–373.

Clarke, C. J., and J. E. Pringle. 1991a. 'Star-disc interactions and binary star formation.' *Monthly Notices of the Royal Astronomical Society* 249 (April): 584–587.

———. 1991b. 'The role of discs in the formation of binary and multiple star systems.' *Monthly Notices of the Royal Astronomical Society* 249 (April): 588–595.

Claudi, R., A. -L. Maire, et al. 2019. 'SPHERE dynamical and spectroscopic characterization of HD 142527B.' *Astronomy and Astrophysics* 622 (February): A96.

Cridland, Alexander J., Arthur D. Bosman, and Ewine F. van Dishoeck. 2020. 'Impact of vertical gas accretion on the carbon-to-oxygen ratio of gas giant atmospheres.' *Astronomy and Astrophysics* 635 (March): A68.

Cuello, Nicolás, Giovanni Dipierro, et al. 2019. 'Flybys in protoplanetary discs: I. Gas and dust dynamics.' *Monthly Notices of the Royal Astronomical Society* 483 (March): 4114–4139.

Cunningham, Andrew J., Mark R. Krumholz, Christopher F. McKee, and Richard I. Klein. 2018. 'The effects of magnetic fields and protostellar feedback on low-mass cluster formation.' *Monthly Notices of the Royal Astronomical Society* 476, no. 1 (May): 771–792.

Czekala, I., S. M. Andrews, et al. 2015. 'A Disk-based Dynamical Mass Estimate for the Young Binary AK Sco.' *The Astrophysical Journal* 806 (June): 154.

Czekala, I., S. M. Andrews, et al. 2016. 'A Disk-based Dynamical Constraint on the Mass of the Young Binary DQ Tau.' *The Astrophysical Journal* 818 (February): 156.

Czekala, Ian, Sean M. Andrews, et al. 2017. 'The Architecture of the GW Ori Young Triple-star System and Its Disk: Dynamical Masses, Mutual Inclinations, and Recurrent Eclipses.' *The Astrophysical Journal* 851 (December): 132.

Czekala, Ian, Eugene Chiang, et al. 2019. 'The Degree of Alignment between Circumbinary Disks and Their Binary Hosts.' *The Astrophysical Journal* 883 (September): 22.

Czekala, Ian, Álvaro Ribas, et al. 2021. 'A Coplanar Circumbinary Protoplanetary Disk in the TWA 3 Triple M Dwarf System.' *The Astrophysical Journal* 912 (May): 6.

D'Angelo, G., T. Henning, and W. Kley. 2002. 'Nested-grid calculations of disk-planet interaction.' *Astronomy and Astrophysics* 385 (April): 647–670.

Davidson-Pilon, Cameron. 2019. 'lifelines: survival analysis in Python.' *Journal of Open Source Software* 4 (40): 1317.

Delamer, Megan, Shubham Kanodia, et al. 2024. 'TOI-4201: An Early M Dwarf Hosting a Massive Transiting Jupiter Stretching Theories of Core Accretion.' *The Astrophysical Journal* 962 (February): L22.

Di Folco, E., A. Dutrey, et al. 2014. 'GG Tauri: the fifth element.' *Astronomy and Astrophysics* 565 (May): L2.

Dipierro, G., L. Ricci, et al. 2018. 'Rings and gaps in the disc around Elias 24 revealed by ALMA.' *Monthly Notices of the Royal Astronomical Society* 475 (April): 5296–5312.

Dipierro, Giovanni, and Guillaume Laibe. 2017. 'An opening criterion for dust gaps in protoplanetary discs.' *Monthly Notices of the Royal Astronomical Society* 469 (August): 1932–1948.

Dipierro, Giovanni, Guillaume Laibe, Daniel J. Price, and Giuseppe Lodato. 2016. 'Two mechanisms for dust gap opening in protoplanetary discs.' *Monthly Notices of the Royal Astronomical Society* 459, no. 1 (June): L1–L5.

Dittmann, Alexander J., and Geoffrey Ryan. 2022. 'A survey of disc thickness and viscosity in circumbinary accretion: Binary evolution, variability, and disc morphology.' *Monthly Notices of the Royal Astronomical Society* 513 (July): 6158–6176.

———. 2023. *The Evolution of Accreting Binaries: from Brown Dwarfs to Supermassive Black Holes,* October.

Dong, Ruobing, Cassandra Hall, Ken Rice, and Eugene Chiang. 2015. 'Spiral Arms in Gravitationally Unstable Protoplanetary Disks as Imaged in Scattered Light.' *The Astrophysical Journal* 812 (October): L32.

Dong, Ruobing, Hauyu Baobab Liu, et al. 2022. 'A likely flyby of binary protostar Z CMa caught in action.' *Nature Astronomy* 6 (January): 331–338.

Dopcke, Gustavo, Simon C. O. Glover, Paul C. Clark, and Ralf S. Klessen. 2011. 'The Effect of Dust Cooling on Low metallicity Star forming Clouds.' *The Astrophysical Journall* 729, no. 1 (March): L3.

Dopcke, Gustavo, Simon C. O. Glover, Paul C. Clark, and Ralf S. Klessen. 2013. 'On the Initial Mass Function of Low-metallicity Stars: The Importance of Dust Cooling.' *The Astrophysical Journal* 766, no. 2 (April): 103.

Doyle, Laurance R., Joshua A. Carter, et al. 2011. 'Kepler-16: A Transiting Circumbinary Planet.' *Science* 333 (6049): 1602–1606.

Draine, B. T. 1978. 'Photoelectric heating of interstellar gas.' *The Astrophysical Journals* 36 (April): 595–619.

Drążkowska, J., and Y. Alibert. 2017. 'Planetesimal formation starts at the snow line.' *Astronomy and Astrophysics* 608 (December): A92.

Duffell, Paul C., Daniel D'Orazio, et al. 2020. 'Circumbinary Disks: Accretion and Torque as a Function of Mass Ratio and Disk Viscosity.' *The Astrophysical Journal* 901 (September): 25.

Duquennoy, A., and M. Mayor. 1991. 'Multiplicity among Solar Type Stars in the Solar Neighbourhood - Part Two - Distribution of the Orbital Elements in an Unbiased Sample.' *Astronomy and Astrophysics* 248 (August): 485.

Dutrey, A, S Guilloteau, and M Simon. 1994. 'Images of the GG Tauri rotating ring.' *Astronomy and Astrophysics* 286:149–159.

Dutrey, Anne, Emmanuel Di Folco, Tracy Beck, and Stéphane Guilloteau. 2016. 'GG Tau: the ringworld and beyond. Mass accretion and planetary formation in young multiple stellar systems.' *Astronomy and Astrophysicsr* 24 (January): 5.

Duvert, G., A. Dutrey, et al. 1998. 'Disks in the UY Aurigae binary.' *Astronomy and Astrophysics* 332 (April): 867–874.

Dvorak, R. 1982. 'Planetenbahnen in Doppelsternsystemen.' *Oesterreichische Akademie Wissenschaften Mathematisch naturwissenschaftliche Klasse Sitzungsberichte Abteilung* 191, no. 10 (January): 423–437.

Eckart, Carl. 1960. 'Variation Principles of Hydrodynamics.' *Physics of Fluids* 3, no. 3 (May): 421–427.

Eisner, J. A., H. G. Arce, et al. 2018. 'Protoplanetary Disk Properties in the Orion Nebula Cluster: Initial Results from Deep, High-resolution ALMA Observations.' *The Astrophysical Journal* 860, no. 1 (June): 77.

Elsender, Daniel, and Matthew R. Bate. 2021. 'The statistical properties of protostellar discs and their dependence on metallicity.' *Monthly Notices of the Royal Astronomical Society* 508, no. 4 (December): 5279–5295.

Ercolano, B., and C. J. Clarke. 2010. 'Metallicity, planet formation and disc lifetimes.' *Monthly Notices of the Royal Astronomical Society* 402, no. 4 (March): 2735–2743.

Facchini, Stefano, Giuseppe Lodato, and Daniel J. Price. 2013. 'Wave-like warp propagation in circumbinary discs - I. Analytic theory and numerical simulations.' *Monthly Notices of the Royal Astronomical Society* 433 (August): 2142–2156.

Fedele, D., M. Carney, et al. 2017. 'ALMA unveils rings and gaps in the protoplanetary system HD 169142: signatures of two giant protoplanets.' *A&A* 600 (April): A72.

Federrath, Christoph, Martin Schrön, Robi Banerjee, and Ralf S. Klessen. 2014. 'MODELING JET AND OUTFLOW FEEDBACK DURING STAR CLUSTER FORMATION.' *The Astrophysical Journal* 790, no. 2 (July): 128.

Fehlberg, Erwin. 1969. 'Low-order classical Runge-Kutta formulas with stepsize control and their application to some heat transfer problems.' *NASA Technical Report R-315.*

Ferguson, Jason W., David R. Alexander, et al. 2005. 'Low-Temperature Opacities.' *The Astrophysical Journal* 623, no. 1 (April): 585–596.

Fernández-López, M., L. A. Zapata, and R. Gabbasov. 2017. 'Strongly Misaligned Triple System in SR 24 Revealed by ALMA.' *ApJ* 845, no. 1 (August): 10.

Fischer, Debra A., and Geoffrey W. Marcy. 1992. 'Multiplicity among M Dwarfs.' *The Astrophysical Journal* 396 (September): 178.

Fischer, Debra A., and Jeff Valenti. 2005. 'The Planet-Metallicity Correlation.' *The Astrophysical Journal* 622, no. 2 (April): 1102–1117.

Fisher, Robert T. 2004. 'A Turbulent Interstellar Medium Origin of the Binary Period Distribution.' *The Astrophysical Journal* 600 (January): 769–780.

Flock, M., J. P. Ruge, et al. 2015. 'Gaps, rings, and non-axisymmetric structures in protoplanetary disks. From simulations to ALMA observations.' *Astronomy and Astrophysics* 574 (February): A68.

Frank, J., A. King, and D. Raine. 1992. *Accretion power in astrophysics.* Vol. 21. January.

Fu, Wen, Stephen H. Lubow, and Rebecca G. Martin. 2015. 'The Kozai-Lidov Mechanism in Hydrodynamical Disks. II. Effects of Binary and Disk Parameters.' *The Astrophysical Journal* 807 (July): 75.

Fung, Jeffrey, and Eugene Chiang. 2016. 'Gap Opening in 3D: Single-planet Gaps.' *The Astrophysical Journal* 832 (December): 105.

Gammie, Charles F. 1996. 'Layered Accretion in T Tauri Disks.' *The Astrophysical Journal* 457 (January): 355.

———. 2001. 'Nonlinear Outcome of Gravitational Instability in Cooling, Gaseous Disks.' *The Astrophysical Journal* 553 (May): 174–183.

Gárate, Matías, Paola Pinilla, Thomas J. Haworth, and Stefano Facchini. 2024. 'The external photoevaporation of structured protoplanetary disks.' *Astronomy and Astrophysics* 681 (January): A84.

Garufi, A., C. Ginski, et al. 2024. 'The SPHERE view of the Taurus star-forming region' (March).

Gaudi, B. Scott, Michael Meyer, and Jessie Christiansen. 2021. 'The Demographics of Exoplanets.' In *ExoFrontiers*, 2-1 to 2–21. 2514-3433. IOP Publishing.

Ghez, AM, G Neugebauer, and K Matthews. 1993. 'The multiplicity of T Tauri stars in the star forming regions Taurus-Auriga and Ophiuchus-Scorpius: A 2.2 micron speckle imaging survey.' *Astronomical Journal* 106 (5): 2005–2023.

Gillen, E., S. Aigrain, et al. 2014. 'CoRoT 223992193: A new, low-mass, pre-main sequence eclipsing binary with evidence of a circumbinary disk.' *Astronomy and Astrophysics* 562 (February): A50.

Gillen, E., S. Aigrain, et al. 2017. 'CoRoT 223992193: Investigating the variability in a low-mass, pre-main sequence eclipsing binary with evidence of a circumbinary disk.' *Astronomy and Astrophysics* 599 (March): A27.

Gingold, R. A., and J. J. Monaghan. 1977. 'Smoothed particle hydrodynamics: theory and application to non-spherical stars.' *Monthly Notices of the RAS* 181 (November): 375–389.

Glover, S. C. O., C. Federrath, M. -M. Mac Low, and R. S. Klessen. 2010. 'Modelling CO formation in the turbulent interstellar medium.' *Monthly Notices of the Royal Astronomical Society* 404, no. 1 (May): 2–29.

Glover, Simon C. O., and Paul C. Clark. 2012a. 'Is molecular gas necessary for star formation?' *Monthly Notices of the Royal Astronomical Society* 421, no. 1 (March): 9–19.

———. 2012b. 'Star formation in metal-poor gas clouds.' *Monthly Notices of the Royal Astronomical Society* 426, no. 1 (October): 377–388.

Goldreich, P., and S. Tremaine. 1979. 'The excitation of density waves at the Lindblad and corotation resonances by an external potential.' *The Astrophysical Journal* 233 (November): 857–871.

———. 1980. 'Disk-satellite interactions.' *The Astrophysical Journal* 241 (October): 425–441.

Goldsmith, Paul F. 2001. 'Molecular Depletion and Thermal Balance in Dark Cloud Cores.' *The Astrophysical Journal* 557, no. 2 (August): 736–746.

Gonzalez, Guillermo. 1997. 'The stellar metallicity-giant planet connection.' *Monthly Notices of the Royal Astronomical Society* 285, no. 2 (February): 403–412.

Gonzalez, J. -F., C. Pinte, S. T. Maddison, F. Ménard, and L. Fouchet. 2012. 'Planet gaps in the dust layer of 3D protoplanetary disks. II. Observability with ALMA.' *Astronomy and Astrophysics* 547 (November): A58.

Goodman, A. A., P. J. Benson, G. A. Fuller, and P. C. Myers. 1993. 'Dense Cores in Dark Clouds. VIII. Velocity Gradients.' *The Astrophysical Journal* 406 (April): 528.

Guthrie, B. N. G. 1985. 'The distribution of the rotation axes of A-type stars.' *Monthly Notices of the Royal Astronomical Society* 215 (August): 545–553.

Haffert, S. Y., A. J. Bohn, et al. 2019. 'Two accreting protoplanets around the young star PDS 70.' *Nature Astronomy* 3 (June): 749–754.

Hale, A. 1994. 'Orbital CoPlanetary in Solar-Type Binary Systems: Implications for Planetary System Formation and Detection.' *The Astronomical Journal* 107 (January): 306.

Hammond, Iain, Valentin Christiaens, et al. 2023. 'Confirmation and Keplerian motion of the gap-carving protoplanet HD 169142 b.' *Monthly Notices of the Royal Astronomical Society* 522 (June): L51–L55.

Harris, Robert J., Sean M. Andrews, David J. Wilner, and Adam L. Kraus. 2012. 'A Resolved Census of Millimeter Emission from Taurus Multiple Star Systems.' *The Astrophysical Journal* 751, no. 2 (June): 115.

Harris, Robert J., Erin G. Cox, et al. 2018. 'ALMA Observations of Polarized 872 μm Dust Emission from the Protostellar Systems VLA 1623 and L1527' [in en]. *The Astrophysical Journal* 861, no. 2 (July): 91.

Hartmann, Lee, Nuria Calvet, Erik Gullbring, and Paola D'Alessio. 1998. 'Accretion and the Evolution of T Tauri Disks.' *The Astrophysical Journal* 495 (March): 385–400.

Hayashi, C. 1981. 'Structure of the Solar Nebula, Growth and Decay of Magnetic Fields and Effects of Magnetic and Turbulent Viscosities on the Nebula.' *Progress of Theoretical Physics Supplement* 70 (January): 35–53.

Heath, R. M., and C. J. Nixon. 2020. 'On the orbital evolution of binaries with circumbinary discs.' *Astronomy and Astrophysics* 641 (September): A64.

Hildebrand, R. H. 1983. 'The determination of cloud masses and dust characteristics from submillimetre thermal emission.' *Quarterly Journal of the Royal Astronomical Society* 24 (September): 267–282.

Hollenbach, David, and Christopher F. McKee. 1989. 'Molecule Formation and Infrared Emission in Fast Interstellar Shocks. III. Results for J Shocks in Molecular Clouds.' *The Astrophysical Journal* 342 (July): 306.

Hsieh, Cheng-Han, Shih-Ping Lai, et al. 2020. 'Determining the Physical Conditions of an Extremely Young Class 0 Circumbinary Disk around VLA 1623A.' *The Astrophysical Journal* 894, no. 1 (May): 23.

Huang, Jane, Sean M. Andrews, et al. 2018a. 'CO and Dust Properties in the TW Hya Disk from High-resolution ALMA Observations.' *The Astrophysical Journal* 852 (January): 122.

Huang, Jane, Sean M. Andrews, et al. 2018b. 'The Disk Substructures at High Angular Resolution Project (DSHARP). II. Characteristics of Annular Substructures.' *The Astrophysical Journal* 869 (December): L42.

Hubber, D. A., S. P. Goodwin, and A. P. Whitworth. 2006. 'Resolution requirements for simulating gravitational fragmentation using SPH.' *Astronomy and Astrophysics* 450, no. 3 (May): 881–886.

Hutchison, Mark, Daniel J. Price, and Guillaume Laibe. 2018. 'MULTIGRAIN: a smoothed particle hydrodynamic algorithm for multiple small dust grains and gas.' *Monthly Notices of the Royal Astronomical Society* 476 (May): 2186–2198.

Hutchison, Mark A., Jean-David Bodénan, Lucio Mayer, and Maria Schönbächler. 2022. 'Presolar grain dynamics: Creating nucleosynthetic variations through a combination of drag and viscous evolution.' *Monthly Notices of the Royal Astronomical Society* 512 (June): 5874–5894.

Hutchison, Mark A., Daniel J. Price, Guillaume Laibe, and Sarah T. Maddison. 2016. 'On dust entrainment in photoevaporative winds.' *Monthly Notices of the Royal Astronomical Society* 461 (September): 742–759.

Ida, Shigeru, and D. N. C. Lin. 2004. 'Toward a Deterministic Model of Planetary Formation. II. The Formation and Retention of Gas Giant Planets around Stars with a Range of Metallicities.' *The Astrophysical Journal* 616, no. 1 (November): 567–572.

Isella, Andrea, Greta Guidi, et al. 2016. 'Ringed Structures of the HD 163296 Protoplanetary Disk Revealed by ALMA.' *Physical Review Letters* 117 (December): 251101.

Janson, Markus, Felix Hormuth, et al. 2012. 'The AstraLux Large M-dwarf Multiplicity Survey.' *The Astrophysical Journal* 754 (July): 44.

Jensen, Eric L. N., Saurav Dhital, et al. 2007. 'Periodic Accretion from a Circumbinary Disk in the Young Binary UZ Tau E.' AJ 134 (July): 241–251.

Jensen, Eric L. N., David W. Koerner, and Robert D. Mathieu. 1996a. 'High-Resolution Imaging of Circumstellar Gas and Dust in UZ Tauri: Comparing Binary and Single-Star Disk Properties.' AJ 111 (June): 2431.

Jensen, Eric L. N., and Robert D. Mathieu. 1997. 'Evidence for Cleared Regions in the Disks Around Pre-Main-Sequence Spectroscopic Binaries.' AJ 114 (July): 301–316.

Jensen, Eric L. N., Robert D. Mathieu, and Gary A. Fuller. 1996b. 'The Connection between Submillimeter Continuum Flux and Binary Separation in Young Binaries: Evidence of Interaction between Stars and Disks.' *The Astrophysical Journal* 458 (February): 312.

Johnson, John Asher, Kimberly M. Aller, Andrew W. Howard, and Justin R. Crepp. 2010. 'Giant Planet Occurrence in the Stellar Mass-Metallicity Plane.' PASP 122, no. 894 (August): 905.

Joos, M., P. Hennebelle, and A. Ciardi. 2012. 'Protostellar disk formation and transport of angular momentum during magnetized core collapse.' *Astronomy and Astrophysics* 543 (July): A128.

Kalyaan, Anusha, Paola Pinilla, Sebastiaan Krijt, Gijs D. Mulders, and Andrea Banzatti. 2021. 'Linking Outer Disk Pebble Dynamics and Gaps to Inner Disk Water Enrichment.' *The Astrophysical Journal* 921 (November): 84.

Kalyaan, Anusha, Paola Pinilla, et al. 2023. 'The Effect of Dust Evolution and Traps on Inner Disk Water Enrichment.' *The Astrophysical Journal* 954 (September): 66.

Kastner, Joel H. 2018. 'Candidate Wide-separation Companions to Nearby, Dusty Young Stars: Gaia Weighs In.' *Res. Notes Am. Astron. Soc.* 2 (August): 137.

Kastner, Joel H., C. Qi, et al. 2018. 'A Subarcsecond ALMA Molecular Line Imaging Survey of the Circumbinary, Protoplanetary Disk Orbiting V4046 Sgr.' *The Astrophysical Journal* 863 (August): 106.

Kawabe, R., M. Ishiguro, T. Omodaka, Y. Kitamura, and S. M. Miyama. 1993. 'Discovery of a Rotating Protoplanetary Gas Disk around the Young Star GG Tauri.' *The Astrophysical Journal* 404 (February): L63.

Kennedy, G. M. 2015. 'Nature or nurture of coplanar Tatooines: the aligned circumbinary Kuiper Belt analogue around HD 131511.' *Monthly Notices of the Royal Astronomical Society* 447 (February): L75–L79.

Kennedy, G. M., M. C. Wyatt, et al. 2012a. '99 Herculis: host to a circumbinary polar-ring debris disc.' *Monthly Notices of the Royal Astronomical Society* 421 (April): 2264–2276.

Kennedy, G. M., M. C. Wyatt, et al. 2012b. 'Coplanar circumbinary debris discs.' *Monthly Notices of the Royal Astronomical Society* 426 (November): 2115–2128.

Kennedy, Grant M., Luca Matrà, et al. 2019. 'A circumbinary protoplanetary disk in a polar configuration.' *Nature Astronomy* 3 (January): 230–235.

Kenworthy, M. A., D. González Picos, et al. 2022. 'Eclipse of the V773 Tau B circumbinary disc' [in en]. *Astronomy and Astrophysics* 666 (October): A61.

Keppler, M., M. Benisty, et al. 2018. 'Discovery of a planetary-mass companion within the gap of the transition disk around PDS 70.' *Astronomy and Astrophysics* 617 (September): A44.

Keto, Eric, and Paola Caselli. 2008. 'The Different Structures of the Two Classes of Starless Cores.' *The Astrophysical Journal* 683, no. 1 (August): 238–247.

Kley, W. 1999. 'Mass flow and accretion through gaps in accretion discs.' *Monthly Notices of the Royal Astronomical Society* 303 (March): 696–710.

Kley, W., and R. P. Nelson. 2012. 'Planet-Disk Interaction and Orbital Evolution.' *Annual Review of Astronomy and Astrophysics* 50 (September): 211–249.

Kostov, Veselin B., Jerome A. Orosz, et al. 2020. 'TOI-1338: TESS' First Transiting Circumbinary Planet.' AJ 159, no. 6 (June): 253.

Kostov, Veselin B., Brian P. Powell, et al. 2021. 'TIC 172900988: A Transiting Circumbinary Planet Detected in One Sector of TESS Data.' AJ 162, no. 6 (December): 234.

Kozai, Yoshihide. 1962. 'Secular perturbations of asteroids with high inclination and eccentricity.' AJ 67 (November): 591–598.

Krapp, Leonardo, Kaitlin M. Kratter, et al. 2024. 'A thermodynamic criterion for the formation of Circumplanetary Disks' (February).

Kratter, Kaitlin M., and Christopher D. Matzner. 2006. 'Fragmentation of massive protostellar discs.' *Monthly Notices of the Royal Astronomical Society* 373, no. 4 (December): 1563–1576.

Kraus, Adam L., Michael J. Ireland, Lynne A. Hillenbrand, and Frantz Martinache. 2012. 'The Role of Multiplicity in Disk Evolution and Planet Formation.' *The Astrophysical Journal* 745 (January): 19.

Kraus, Stefan, Alexander Kreplin, et al. 2020. 'A triple-star system with a misaligned and warped circumstellar disk shaped by disk tearing.' *Science* 369 (September): 1233–1238.

Krumholz, Mark R., Richard I. Klein, and Christopher F. McKee. 2007. 'Radiation-Hydrodynamic Simulations of Collapse and Fragmentation in Massive Protostellar Cores.' *The Astrophysical Journal* 656 (February): 959–979.

———. 2012. 'Radiation hydrodynamic Simulations of the Formation of Orion-like Star Clusters. II. The Initial Mass Function from Winds, Turbulence, and Radiation.' *The Astrophysical Journal* 754, no. 1 (July): 71.

Kuffmeier, M., H. Calcutt, and L. E. Kristensen. 2019. 'The bridge: a transient phenomenon of forming stellar multiples. Sequential formation of stellar companions in filaments around young protostars.' *Astronomy and Astrophysics* 628 (August): A112.

Kuffmeier, M., C. P. Dullemond, S. Reissl, and F. G. Goicovic. 2021. 'Misaligned disks induced by infall.' *Astronomy and Astrophysics* 656 (December): A161.

Kurosawa, R., T. J. Harries, M. R. Bate, and N. H. Symington. 2004. 'Synthetic infrared images and spectral energy distributions of a young low-mass stellar cluster.' *Monthly Notices of the Royal Astronomical Society* 351 (July): 1134–1150.

Kuruwita, Rajika L., and Christoph Federrath. 2019. 'The role of turbulence during the formation of circumbinary discs.' *Monthly Notices of the Royal Astronomical Society* 486 (July): 3647–3663.

Lacour, S., B. Biller, et al. 2016. 'An M-dwarf star in the transition disk of Herbig HD 142527. Physical parameters and orbital elements.' *Astronomy and Astrophysics* 590 (May): A90.

Lada, C. J., and B. A. Wilking. 1984. 'The nature of the embedded population in the rho Ophiuchi dark cloud : mid-infrared observations.' *The Astrophysical Journal* 287 (December): 610–621.

Lada, Charles J. 1987. 'Star formation: from OB associations to protostars.' 115 (January): 1.

Laibe, Guillaume, and Daniel J. Price. 2011. 'DUSTYBOX and DUSTYWAVE: two test problems for numerical simulations of two-fluid astrophysical dust-gas mixtures.' *Monthly Notices of the Royal Astronomical Society* 418 (December): 1491–1497.

———. 2012a. 'Dusty gas with smoothed particle hydrodynamics - I. Algorithm and test suite.' *Monthly Notices of the Royal Astronomical Society* 420 (March): 2345–2364.

———. 2012b. 'Dusty gas with smoothed particle hydrodynamics - II. Implicit timestepping and astrophysical drag regimes.' *Monthly Notices of the Royal Astronomical Society* 420 (March): 2365–2376.

———. 2014a. 'Dust and gas mixtures with multiple grain species - a one-fluid approach.' *Monthly Notices of the Royal Astronomical Society* 444 (October): 1940–1956.

———. 2014b. 'Dusty gas with one fluid.' *Monthly Notices of the Royal Astronomical Society* 440 (May): 2136–2146.

———. 2014c. 'Dusty gas with one fluid in smoothed particle hydrodynamics.' *Monthly Notices of the Royal Astronomical Society* 440 (May): 2147–2163.

Larson, R. B. 1981. 'Turbulence and star formation in molecular clouds.' *Monthly Notices of the Royal Astronomical Society* 194 (March): 809–826.

Larson, Richard B. 1969. 'Numerical calculations of the dynamics of collapsing proto-star.' *Monthly Notices of the Royal Astronomical Society* 145 (January): 271.

Lebreuilly, U., B. Commerçon, and G. Laibe. 2019. 'Small dust grain dynamics on adaptive mesh refinement grids. I. Methods.' *Astronomy and Astrophysics* 626 (June): A96.

Lebreuilly, U., P. Hennebelle, et al. 2024. 'Synthetic populations of protoplanetary disks: Impact of magnetic fields and radiative transfer.' *Astronomy and Astrophysics* 682 (February): A30.

Lebreuilly, Ugo, Patrick Hennebelle, et al. 2021. 'Protoplanetary Disk Birth in Massive Star-forming Clumps: The Essential Role of the Magnetic Field.' *The Astrophysical Journal* 917 (August): L10.

Lee, Chin-Fei, Naomi Hirano, et al. 2009. 'Rotation and Outflow Motions in the Very Low-Mass Class 0 Protostellar System HH 211 at Subarcsecond Resolution.' *The Astrophysical Journal* 699, no. 2 (July): 1584–1594.

Lidov, M. L. 1962. 'The evolution of orbits of artificial satellites of planets under the action of gravitational perturbations of external bodies.' *Planetary and Space Science* 9 (October): 719–759.

Lin, D. N. C., and J. Papaloizou. 1979a. 'On the structure of circumbinary accretion disks and the tidal evolution of commensurable satellites.' *Monthly Notices of the Royal Astronomical Society* 188 (July): 191–201.

———. 1979b. 'Tidal torques on accretion discs in binary systems with extreme mass ratios.' *Monthly Notices of the Royal Astronomical Society* 186 (March): 799–812.

Lin, D. N. C., and John Papaloizou. 1986. 'On the Tidal Interaction between Protoplanets and the Protoplanetary Disk. III. Orbital Migration of Protoplanets.' *The Astrophysical Journal* 309 (October): 846.

Lodato, Giuseppe, and Daniel J. Price. 2010. 'On the diffusive propagation of warps in thin accretion discs.' *Monthly Notices of the Royal Astronomical Society* 405 (June): 1212–1226.

Long, Feng, Sean M. Andrews, et al. 2021. 'The Architecture of the V892 Tau System: The Binary and Its Circumbinary Disk.' *The Astrophysical Journal* 915 (July): 131.

Long, Feng, Paola Pinilla, et al. 2018. 'Gaps and Rings in an ALMA Survey of Disks in the Taurus Star-forming Region.' *The Astrophysical Journal* 869 (December): 17.

Lorén-Aguilar, Pablo, and Matthew R. Bate. 2014. 'Two-fluid dust and gas mixtures in smoothed particle hydrodynamics: a semi-implicit approach.' *Monthly Notices of the Royal Astronomical Society* 443 (September): 927–945.

———. 2015. 'Two-fluid dust and gas mixtures in smoothed particle hydrodynamics II: an improved semi-implicit approach.' *Monthly Notices of the Royal Astronomical Society* 454 (December): 4114–4119.

Lubow, S. H., M. Seibert, and P. Artymowicz. 1999. 'Disk Accretion onto High-Mass Planets.' *The Astrophysical Journal* 526 (December): 1001–1012.

Lubow, Stephen H., and Rebecca G. Martin. 2018. 'Linear analysis of the evolution of nearly polar low-mass circumbinary discs.' *Monthly Notices of the Royal Astronomical Society* 473 (January): 3733–3746.

Lucy, L. B. 1977. 'A numerical approach to the testing of the fission hypothesis.' *Astronomical Journal* 82 (December): 1013–1024.

Lynden-Bell, D., and J. E. Pringle. 1974. 'The evolution of viscous discs and the origin of the nebular variables.' *Monthly Notices of the Royal Astronomical Society* 168 (September): 603–637.

Machida, M. N. 2008. 'Binary Formation in Star-forming Clouds with Various Metallicities.' *The Astrophysical Journall* 682 (July): L1–L4.

Machida, M. N., K. Omukai, T. Matsumoto, and S.-I. Inutsuka. 2009. 'Binary formation with different metallicities: dependence on initial conditions.' *Monthly Notices of the Royal Astronomical Society* 399 (November): 1255–1263.

Machida, Masahiro N., and Tomoaki Matsumoto. 2011. 'The origin and formation of the circumstellar disc.' *Monthly Notices of the Royal Astronomical Society* 413 (June): 2767–2784.

Maddison, S. T., R. J. Humble, and J. R. Murray. 2003. 'Building Planets with Dusty Gas.' In *Scientific Frontiers in Research on Extrasolar Planets,* edited by Drake Deming and Sara Seager, 294:307–310. Astronomical Society of the Pacific Conference Series. January.

Manara, C. F., M. Ansdell, et al. 2023. 'Demographics of Young Stars and their Protoplanetary Disks: Lessons Learned on Disk Evolution and its Connection to Planet Formation.' 534 (July): 539.

Marino, S., S. Perez, and S. Casassus. 2015. 'Shadows Cast by a Warp in the HD 142527 Protoplanetary Disk.' *The Astrophysical Journal* 798 (January): L44.

Martin, David V., and Amaury H. M. J. Triaud. 2014. 'Planets transiting non-eclipsing binaries.' *Astronomy and Astrophysics* 570 (October): A91.

———. 2015. 'Circumbinary planets - why they are so likely to transit.' *Monthly Notices of the Royal Astronomical Society* 449 (May): 781–793.

Martin, Rebecca G., Stephen Lepp, Bing Zhang, C. J. Nixon, and Anna C. Childs. 2024. 'Mergers of black hole binaries driven by misaligned circumbinary discs.' *Monthly Notices of the Royal Astronomical Society* 528 (February): L161–L167.

Martin, Rebecca G., and Stephen H. Lubow. 2017. 'Polar Alignment of a Protoplanetary Disk around an Eccentric Binary.' *The Astrophysical Journall* 835, no. 2 (February): L28.

———. 2019. 'Polar alignment of a protoplanetary disc around an eccentric binary - III. Effect of disc mass.' *Monthly Notices of the Royal Astronomical Society* 490 (November): 1332–1349.

———. 2022. 'Eccentric Dust-ring Formation in Kozai-Lidov Gas Disks.' *The Astrophysical Journal* 925 (January): L1.

Martin, Rebecca G., Chris Nixon, et al. 2014. 'The Kozai-Lidov Mechanism in Hydrodynamical Disks.' *The Astrophysical Journal* 792 (September): L33.

Mathieu, R. D., E. L. Martin, and A. Magazzu. 1996. 'UZ Tau E: A New Classical T Tauri Spectroscopic Binary.' 188 (September): 60.05.

Mathieu, Robert D., Fred C. Adams, et al. 1995. 'Submillimeter Continuum Observations of the T Tauri Spectroscopic Binary GW Orionis.' AJ 109 (June): 2655.

Mathieu, Robert D., Keivan Stassun, et al. 1997. 'The Classical T Tauri Spectroscopic Binary DQ Tau.I.Orbital Elements and Light Curves.' AJ 113 (May): 1841.

Matsumura, Soko, Ramon Brasser, and Shigeru Ida. 2021. 'N-body simulations of planet formation via pebble accretion II. How various giant planets form.' *arXiv e-prints* (April): arXiv:2104.07271.

Maureira, María José, Jaime E. Pineda, et al. 2020. 'Orbital and Mass Constraints of the Young Binary System IRAS 16293-2422 A' [in en]. *The Astrophysical Journal* 897, no. 1 (July): 59.

McCaughrean, M. J., and C. R. O'dell. 1996. 'Direct Imaging of Circumstellar Disks in the Orion Nebula.' AJ 111 (May): 1977.

McCaughrean, M. J., K. R. Stapelfeldt, and L. M. Close. 2000. 'High-Resolution Optical and Near-Infrared Imaging of Young Circumstellar Disks.' *Protostars and Planets IV* (May): 485.

McCaughrean, Mark J., and C. Robert O'Dell. 1996. 'Direct Imaging of Circumstellar Disks in the Orion Nebula.' *The Astronomical Journal* 111 (May): 1977.

McKee, Christopher F., and Eve C. Ostriker. 2007. 'Theory of Star Formation.' *Annual Review of Astronomy and Astrophysics* 45 (September): 565–687.

Ménard, F., N. Cuello, et al. 2020. 'Ongoing flyby in the young multiple system UX Tauri.' *Astronomy and Astrophysics* 639 (July): L1.

Mesa, D., M. Bonnefoy, et al. 2019. 'Exploring the R CrA environment with SPHERE. Discovery of a new stellar companion.' *Astronomy and Astrophysics* 624 (April): A4.

Mignone, A., C. Zanni, et al. 2012. 'The PLUTO Code for Adaptive Mesh Computations in Astrophysical Fluid Dynamics.' *The Astrophysical Journal Supplement Series* 198 (January): 7.

Mihalas, D., and B. W. Mihalas. 1984. *Foundations of radiation hydrodynamics.* January.

Miranda, Ryan, Diego J. Muñoz, and Dong Lai. 2017. 'Viscous hydrodynamics simulations of circumbinary accretion discs: variability, quasi-steady state and angular momentum transfer.' *Monthly Notices of the Royal Astronomical Society* 466 (April): 1170–1191.

Mizuno, H. 1980. 'Formation of the Giant Planets.' *Progress of Theoretical Physics* 64 (August): 544–557.

Moe, Maxwell, Kaitlin M. Kratter, and Carles Badenes. 2019. 'The Close Binary Fraction of Solar-type Stars Is Strongly Anticorrelated with Metallicity.' *The Astrophysical Journal* 875, no. 1 (April): 61.

Monaghan, J. J. 1992. 'Smoothed particle hydrodynamics.' *Annual Review of Astronomy and Astrophysics* 30 (January): 543–574.

———. 1997a. 'Implicit SPH Drag and Dusty Gas Dynamics.' *Journal of Computational Physics* 138 (December): 801–820.

———. 1997b. 'SPH and Riemann Solvers.' *Journal of Computational Physics* 136 (September): 298–307.

Monaghan, J. J., and A. Kocharyan. 1995. 'SPH simulation of multi-phase flow.' *Computer Physics Communications* 87 (May): 225–235.

Monaghan, J. J., and J. C. Lattanzio. 1985. 'A refined particle method for astrophysical problems.' *Astronomy and Astrophysics* 149 (August): 135–143.

Monnier, J. D., J. -P. Berger, et al. 2006. 'Few Skewed Disks Found in First Closure-Phase Survey of Herbig Ae/Be Stars.' *The Astrophysical Journal* 647 (August): 444–463.

Moody, Mackenzie S. L., Ji-Ming Shi, and James M. Stone. 2019. 'Hydrodynamic Torques in Circumbinary Accretion Disks.' *The Astrophysical Journal* 875 (April): 66.

Morbidelli, A., J. Szulágyi, et al. 2014. 'Meridional circulation of gas into gaps opened by giant planets in three-dimensional low-viscosity disks.' *Icarus* 232 (April): 266–270.

Morfill, G. E., and H. J. Voelk. 1984. 'Transport of dust and vapor and chemical fractionation in the early protosolar cloud.' *The Astrophysical Journal* 287 (December): 371–395.

Morris, J. P., and J. J. Monaghan. 1997. 'A Switch to Reduce SPH Viscosity.' *Journal of Computational Physics* 136, no. 1 (September): 41–50.

Muñoz, Diego J., Ryan Miranda, and Dong Lai. 2019. 'Hydrodynamics of Circumbinary Accretion: Angular Momentum Transfer and Binary Orbital Evolution.' *The Astrophysical Journal* 871 (January): 84.

Myers, Andrew T., Christopher F. McKee, Andrew J. Cunningham, Richard I. Klein, and Mark R. Krumholz. 2013. 'The Fragmentation of Magnetized, Massive Star-forming Cores with Radiative Feedback.' *The Astrophysical Journal* 766, no. 2 (April): 97.

Nixon, Chris, Andrew King, and Daniel Price. 2013. 'Tearing up the disc: misaligned accretion on to a binary.' *Monthly Notices of the Royal Astronomical Society* 434 (September): 1946–1954.

Nixon, Christopher J., and Andrew R. King. 2012. 'Broken discs: warp propagation in accretion discs.' *Monthly Notices of the Royal Astronomical Society* 421 (April): 1201–1208.

Nozawa, Takaya, Takashi Kozasa, and Ken'ichi Nomoto. 2012. 'Can the Growth of Dust Grains in Low metallicity Star forming Clouds Affect the Formation of Metal-poor Low-mass Stars?' *The Astrophysical Journall* 756, no. 2 (September): L35.

O'Dell, C. R. 1998. 'Observational Properties of the Orion Nebula Proplyds.' *The Astronomical Journal* 115 (January): 263–273.

O'Dell, C. R., Zheng Wen, and Xihai Hu. 1993. 'Discovery of New Objects in the Orion Nebula on HST Images: Shocks, Compact Sources, and Protoplanetary Disks.' *The Astrophysical Journal* 410 (June): 696.

O'dell, C. R., Zheng Wen, and Xihai Hu. 1993. 'Discovery of New Objects in the Orion Nebula on HST Images: Shocks, Compact Sources, and Protoplanetary Disks.' *The Astrophysical Journal* 410 (June): 696.

Offner, S. S. R., R. I. Klein, C. F. McKee, and M. R. Krumholz. 2009. 'The Effects of Radiative Transfer on Low-Mass Star Formation.' *The Astrophysical Journal* 703 (September): 131–149.

Offner, Stella S. R., Richard I. Klein, and Christopher F. McKee. 2008. 'Driven and Decaying Turbulence Simulations of Low-Mass Star Formation: From Clumps to Cores to Protostars.' *The Astrophysical Journal* 686 (October): 1174–1194.

Offner, Stella S. R., Thomas P. Robitaille, Charles E. Hansen, Christopher F. McKee, and Richard I. Klein. 2012. 'Observing Simulated Protostars with Outflows: How Accurate Are Protostellar Properties Inferred from SEDs?' *The Astrophysical Journal* 753, no. 2 (July): 98.

Ogilvie, G. I. 1999. 'The non-linear fluid dynamics of a warped accretion disc.' *Monthly Notices of the Royal Astronomical Society* 304 (April): 557–578.

Ohashi, Nagayoshi, Kazuya Saigo, et al. 2014. 'Formation of a Keplerian Disk in the Infalling Envelope around L1527 IRS: Transformation from Infalling Motions to Kepler Motions.' *The Astrophysical Journal* 796, no. 2 (December): 131.

Ohashi, Nagayoshi, John J. Tobin, et al. 2023. 'Early Planet Formation in Embedded Disks (eDisk). I. Overview of the Program and First Results.' *The Astrophysical Journal* 951 (July): 8.

Okamoto, Yoshiko Kataza, Hirokazu Kataza, et al. 2009. 'Direct Detection of a Flared Disk Around a Young Massive Star HD200775 and its 10 to 1000 AU Scale Properties.' *The Astrophysical Journal* 706 (November): 665–675.

Omukai, Kazuyuki. 2000. 'Protostellar Collapse with Various Metallicities.' *The Astrophysical Journal* 534, no. 2 (May): 809–824.

Ostriker, Eve C., James M. Stone, and Charles F. Gammie. 2001. 'Density, Velocity, and Magnetic Field Structure in Turbulent Molecular Cloud Models.' *The Astrophysical Journal* 546, no. 2 (January): 980–1005.

Paardekooper, S. -J., and G. Mellema. 2004. 'Planets opening dust gaps in gas disks.' *Astronomy and Astrophysics* 425 (October): L9–L12.

Papaloizou, J., and D. N. C. Lin. 1984. 'On the tidal interaction between protoplanets and the primordial solar nebula. I - Linear calculation of the role of angular momentum exchange.' *The Astrophysical Journal* 285 (October): 818–834.

Papaloizou, J., and J. E. Pringle. 1977. 'Tidal torques on accretion discs in close binary systems.' *Monthly Notices of the Royal Astronomical Society* 181 (November): 441–454.

Papaloizou, J. C. B., and J. E. Pringle. 1984. 'The dynamical stability of differentially rotating discs with constant specific angular momentum.' *Monthly Notices of the Royal Astronomical Society* 208 (June): 721–750.

Penzlin, Anna B. T., Wilhelm Kley, Hugo Audiffren, and Christoph M. Schäfer. 2022. 'Binary orbital evolution driven by a circumbinary disc.' *Astronomy and Astrophysics* 660 (April): A101.

Perri, F., and A. G. W. Cameron. 1974. 'Hydrodynamic Instability of the Solar Nebula in the Presence of a Planetary Core.' *Icarus* 22 (August): 416–425.

Pinilla, P., M. Benisty, and T. Birnstiel. 2012a. 'Ring shaped dust accumulation in transition disks.' *Astronomy and Astrophysics* 545 (September): A81.

Pinilla, P., T. Birnstiel, et al. 2012b. 'Trapping dust particles in the outer regions of protoplanetary disks.' *Astronomy and Astrophysics* 538 (February): A114.

Pinilla, Paola, Myriam Benisty, Rens Waters, Jaehan Bae, and Stefano Facchini. 2024. 'On the survival of the long-lived inner disk of PDS 70' (March).

Pinte, C., D. J. Price, et al. 2018. 'Kinematic Evidence for an Embedded Protoplanet in a Circumstellar Disk.' *The Astrophysical Journal* 860 (June): L13.

Pinte, C., D. J. Price, et al. 2020. 'Nine Localized Deviations from Keplerian Rotation in the DSHARP Circumstellar Disks: Kinematic Evidence for Protoplanets Carving the Gaps.' *ApJL* 890, no. 1 (February): L9.

Pollack, J. B., C. P. McKay, and B. M. Christofferson. 1985. 'A calculation of the Rosseland mean opacity of dust grains in primordial solar system nebulae.' *Icarus* 64, no. 3 (December): 471–492.

Pollack, James B., Olenka Hubickyj, et al. 1996. 'Formation of the Giant Planets by Concurrent Accretion of Solids and Gas.' *Icarus* 124 (November): 62–85.

Prato, L., M. Simon, T. Mazeh, S. Zucker, and I. S. McLean. 2002. 'Component Masses of the Young Spectroscopic Binary UZ Tau E.' *The Astrophysical Journal* 579 (November): L99–L102.

Press, William H. 1986. 'Techniques and tricks for N-body computation.' In *The Use of Supercomputers in Stellar Dynamics*, edited by Piet Hut and Stephen L. W. McMillan, 184–192. Berlin, Heidelberg: Springer Berlin Heidelberg.

Price, D. J., and J. J. Monaghan. 2005. 'Smoothed Particle Magnetohydrodynamics - III. Multidimensional tests and the ∇.B= 0 constraint.' *Monthly Notices of the Royal Astronomical Society* 364, no. 2 (December): 384–406.

———. 2007. 'An energy-conserving formalism for adaptive gravitational force softening in smoothed particle hydrodynamics and N-body codes.' *Monthly Notices of the Royal Astronomical Society* 374, no. 4 (February): 1347–1358.

Price, Daniel J. 2012. 'Smoothed particle hydrodynamics and magnetohydrodynamics.' *Journal of Computational Physics* 231 (February): 759–794.

Price, Daniel J., Nicolás Cuello, et al. 2018a. 'Circumbinary, not transitional: on the spiral arms, cavity, shadows, fast radial flows, streamers, and horseshoe in the HD 142527 disc.' *MNRAS* 477, no. 1 (June): 1270–1284.

Price, Daniel J., and Guillaume Laibe. 2015. 'A fast and explicit algorithm for simulating the dynamics of small dust grains with smoothed particle hydrodynamics.' *MNRAS* 451, no. 1 (July): 813–826.

———. 2020. 'A solution to the overdamping problem when simulating dust-gas mixtures with smoothed particle hydrodynamics.' *Monthly Notices of the Royal Astronomical Society* 495 (July): 3929–3934.

Price, Daniel J., James Wurster, et al. 2018b. 'Phantom: A Smoothed Particle Hydrodynamics and Magnetohydrodynamics Code for Astrophysics.' *Publications of the Astron. Soc. of Australia* 35 (September): e031.

Pringle, J. E. 1981. 'Accretion discs in astrophysics.' *Annual Review of Astronomy and Astrophysics* 19 (January): 137–162.

Qiao, Lin, Gavin A. L. Coleman, and Thomas J. Haworth. 2023. 'Planet formation via pebble accretion in externally photoevaporating discs.' *Monthly Notices of the Royal Astronomical Society* 522 (June): 1939–1950.

Qiao, Lin, Thomas J. Haworth, Andrew D. Sellek, and Ahmad A. Ali. 2022. 'The evolution of protoplanetary discs in star formation and feedback simulations.' *Monthly Notices of the Royal Astronomical Society* 512 (May): 3788–3805.

Rabago, Ian, Zhaohuan Zhu, Stephen Lubow, and Rebecca G. Martin. 2023. *Warps and Breaks in Circumbinary Discs*, September.

Raghavan, Deepak, Harold A. McAlister, et al. 2010. 'A Survey of Stellar Families: Multiplicity of Solar-type Stars.' *The Astrophysical Journals* 190, no. 1 (September): 1–42.

Rémy-Ruyer, A., S. C. Madden, et al. 2014. 'Gas-to-dust mass ratios in local galaxies over a 2 dex metallicity range.' *Astronomy and Astrophysics* 563 (March): A31.

Rice, W. K. M., Philip J. Armitage, Kenneth Wood, and G. Lodato. 2006. 'Dust filtration at gap edges: implications for the spectral energy distributions of discs with embedded planets.' *Monthly Notices of the Royal Astronomical Society* 373 (December): 1619–1626.

Rosenfeld, Katherine A., Sean M. Andrews, David J. Wilner, and H. C. Stempels. 2012. 'A Disk-based Dynamical Mass Estimate for the Young Binary V4046 Sgr.' *The Astrophysical Journal* 759 (November): 119.

Rosotti, Giovanni P. 2023. 'Empirical constraints on turbulence in proto-planetary discs.' *New Astronomy Reviews* 96 (June): 101674.

Rosotti, Giovanni P., Attila Juhasz, Richard A. Booth, and Cathie J. Clarke. 2016. 'The minimum mass of detectable planets in protoplanetary discs and the derivation of planetary masses from high-resolution observations.' *Monthly Notices of the Royal Astronomical Society* 459, no. 3 (May): 2790–2805.

Sadavoy, Sarah I., Philip C. Myers, et al. 2018. 'Dust Polarization toward Embedded Protostars in Ophiuchus with ALMA. I. VLA 1623' [in en]. *The Astrophysical Journal* 859, no. 2 (June): 165.

Sakai, Nami, Yoko Oya, et al. 2014. 'A Chemical View of Protostellar-disk Formation in L1527.' *The Astrophysical Journall* 791, no. 2 (August): L38.

Santos, N. C., G. Israelian, and M. Mayor. 2001. 'The metal-rich nature of stars with planets.' *Astronomy and Astrophysics* 373 (July): 1019–1031.

Schaefer, G. H., L. Prato, and M. Simon. 2018. 'Orbital Motion of Young Binaries in Ophiuchus and Upper Centaurus-Lupus.' AJ 155 (March): 109.

Schib, O., C. Mordasini, and R. Helled. 2022. 'Calibrated gas accretion and orbital migration of protoplanets in 1D disc models.' *Astronomy and Astrophysics* 664 (August): A138.

Segura-Cox, Dominique M., Robert J. Harris, et al. 2016. 'The VLA Nascent Disk and Multiplicity Survey: First Look at Resolved Candidate Disks around Class 0 and I Protostars in the Perseus Molecular Cloud.' *ApJL* 817, no. 2 (February): L14.

Seifried, D., R. Banerjee, R. E. Pudritz, and R. S. Klessen. 2013. 'Turbulence-induced disc formation in strongly magnetized cloud cores.' *Monthly Notices of the Royal Astronomical Society* 432 (July): 3320–3331.

Sellek, Andrew D., Richard A. Booth, and Cathie J. Clarke. 2020. 'The evolution of dust in discs influenced by external photoevaporation.' *Monthly Notices of the Royal Astronomical Society* 492 (February): 1279–1294.

Shakura, N. I., and R. A. Sunyaev. 1973. 'Black holes in binary systems. Observational appearance.' *Astronomy and Astrophysics* 24 (January): 337–355.

Sheehan, Patrick D., John J. Tobin, Leslie W. Looney, and S. Thomas Megeath. 2022. 'The VLA/ALMA Nascent Disk and Multiplicity (VANDAM) Survey of Orion Protostars. VI. Insights from Radiative Transfer Modeling.' *The Astrophysical Journal* 929 (April): 76.

Simon, M., A. Dutrey, and S. Guilloteau. 2000. 'Dynamical Masses of T Tauri Stars and Calibration of Pre-Main-Sequence Evolution.' *The Astrophysical Journal* 545, no. 2 (December): 1034–1043.

Siwek, Magdalena, Rainer Weinberger, and Lars Hernquist. 2023a. 'Orbital evolution of binaries in circumbinary discs.' *Monthly Notices of the Royal Astronomical Society* 522 (June): 2707–2717.

Siwek, Magdalena, Rainer Weinberger, Diego J. Muñoz, and Lars Hernquist. 2023b. 'Preferential accretion and circumbinary disc precession in eccentric binary systems.' *Monthly Notices of the Royal Astronomical Society* 518 (February): 5059–5071.

Smallwood, Jeremy L., Stephen H. Lubow, and Rebecca G. Martin. 2022. 'Accretion on to a binary from a polar circumbinary disc.' *Monthly Notices of the Royal Astronomical Society* 514 (July): 1249–1257.

Smith, B. A., and R. J. Terrile. 1984. 'A Circumstellar Disk around β Pictoris.' *Science* 226 (December): 1421–1424.

Sod, G. A. 1978. 'Review. A Survey of Several Finite Difference Methods for Systems of Nonlinear Hyperbolic Conservation Laws.' *Journal of Computational Physics* 27, no. 1 (April): 1–31.

Springel, Volker. 2010. 'E pur si muove: Galilean-invariant cosmological hydrodynamical simulations on a moving mesh.' *Monthly Notices of the Royal Astronomical Society* 401 (January): 791–851.

Stammler, Sebastian Markus, Tim Lichtenberg, Joanna Drążkowska, and Tilman Birnstiel. 2023. 'Leaky dust traps: How fragmentation impacts dust filtering by planets.' *Astronomy and Astrophysics* 670 (February): L5.

Standing, Matthew R., Lalitha Sairam, et al. 2023. 'The First Circumbinary Planet Discovered with Radial Velocities.' *arXiv e-prints* (January): arXiv:2301.10794.

Stempels, H. C., and G. F. Gahm. 2004. 'The close T Tauri binary V 4046 Sagittarii.' *Astronomy and Astrophysics* 421 (July): 1159–1168.

Sterzik, M. F., and A. A. Tokovinin. 2002. 'Relative orientation of orbits in triple stars.' *Astronomy and Astrophysics* 384 (March): 1030–1037.

Stone, James M., Kengo Tomida, Christopher J. White, and Kyle G. Felker. 2020. 'The Athena++ Adaptive Mesh Refinement Framework: Design and Magnetohydrodynamic Solvers.' *The Astrophysical Journal Supplement Series* 249 (July): 4.

Stoyanovskaya, O. P., T. A. Glushko, N. V. Snytnikov, and V. N. Snytnikov. 2018. 'Two-fluid dusty gas in smoothed particle hydrodynamics: Fast and implicit algorithm for stiff linear drag.' *Astronomy and Computing* 25 (October): 25–37.

Stoyanovskaya, O. P., F. A. Okladnikov, E. I. Vorobyov, Ya. N. Pavlyuchenkov, and V. V. Akimkin. 2020. 'Simulations of Dynamical Gas-Dust Circumstellar Disks: Going Beyond the Epstein Regime.' *Astronomy Reports* 64 (February): 107–125.

Strom, Karen M., Stephen E. Strom, Suzan Edwards, Sylvie Cabrit, and Michael F. Skrutskie. 1989. 'Circumstellar Material Associated with Solar-Type Pre-Main-Sequence Stars: A Possible Constraint on the Timescale for Planet Building.' *Astronomical Journal* 97 (May): 1451.

Syer, D., and C. J. Clarke. 1995. 'Satellites in discs: regulating the accretion luminosity.' *Monthly Notices of the Royal Astronomical Society* 277 (December): 758–766.

Szulágyi, J. 2017. 'Effects of the Planetary Temperature on the Circumplanetary Disk and on the Gap.' *The Astrophysical Journal* 842 (June): 103.

Szulágyi, J., F. Binkert, and C. Surville. 2022. 'Meridional Circulation of Dust and Gas in the Circumstellar Disk: Delivery of Solids onto the Circumplanetary Region.' *The Astrophysical Journal* 924 (January): 1.

Szulágyi, J., F. Masset, et al. 2016. 'Circumplanetary disc or circumplanetary envelope?' *Monthly Notices of the Royal Astronomical Society* 460 (August): 2853–2861.

Szulágyi, J., A. Morbidelli, A. Crida, and F. Masset. 2014. 'Accretion of Jupiter-mass Planets in the Limit of Vanishing Viscosity.' *The Astrophysical Journal* 782 (February): 65.

Takakuwa, Shigehisa, Masao Saito, et al. 2012. 'A Keplerian Circumbinary Disk around the Protostellar System L1551 NE.' *The Astrophysical Journal* 754, no. 1 (July): 52.

Tanaka, Kei E. I., and Kazuyuki Omukai. 2014. 'Gravitational instability in protostellar discs at low metallicities.' *Monthly Notices of the Royal Astronomical Society* 439, no. 2 (April): 1884–1896.

Tanaka, Yuki A., and Yusuke Tsukamoto. 2019. 'Pebble accretion in Class 0/I YSOs as a possible pathway for early planet formation.' *Monthly Notices of the Royal Astronomical Society* 484 (April): 1574–1588.

Tang, Ya-Wen, Anne Dutrey, et al. 2016. 'Mapping CO Gas in the GG Tauri A Triple System with 50 au Spatial Resolution.' *The Astrophysical Journal* 820 (March): 19.

Tazzari, M., L. Testi, et al. 2017. 'Physical properties of dusty protoplanetary disks in Lupus: evidence for viscous evolution?' *Astronomy and Astrophysics* 606 (October): A88.

Terquem, Caroline, Paul Magnus Sørensen-Clark, and Jérôme Bouvier. 2015. 'A circumbinary disc model for the variability of the eclipsing binary CoRoT 223992193.' *Monthly Notices of the Royal Astronomical Society* 454 (December): 3472–3479.

Tiede, Christopher, Jonathan Zrake, Andrew MacFadyen, and Zoltan Haiman. 2020. 'Gas-driven Inspiral of Binaries in Thin Accretion Disks.' *The Astrophysical Journal* 900 (September): 43.

Tobin, John, Kaitlin Kratter, et al. 2016a. 'A Triple Protostar System Formed via Fragmentation of a Gravitationally Unstable Disk' [in en]. *Nature* 538, no. 7626 (October): 483–486.

Tobin, John J., Lee Hartmann, et al. 2012. 'A ∼0.2-solar-mass protostar with a Keplerian disk in the very young L1527 IRS system.' Nature 492, no. 7427 (December): 83–85.

Tobin, John J., Leslie W. Looney, et al. 2016b. 'The VLA Nascent Disk and Multiplicity Survey of Perseus Protostars (VANDAM). II. Multiplicity of Protostars in the Perseus Molecular Cloud.' *The Astrophysical Journal* 818 (February): 73.

Tobin, John J., Leslie W. Looney, et al. 2018. 'The VLA/ALMA Nascent Disk and Multiplicity (VANDAM) Survey of Perseus Protostars. VI. Characterizing the Formation Mechanism for Close Multiple Systems.' *The Astrophysical Journal* 867 (November): 43.

Tobin, John J., Patrick D. Sheehan, et al. 2020. 'The VLA/ALMA Nascent Disk and Multiplicity (VANDAM) Survey of Orion Protostars. II. A Statistical Characterization of Class 0 and Class I Protostellar Disks.' *ApJ* 890, no. 2 (February): 130.

Tokovinin, Andrei, and Maxwell Moe. 2020. 'Formation of close binaries by disc fragmentation and migration, and its statistical modelling.' *Monthly Notices of the Royal Astronomical Society* 491 (February): 5158–5171.

Toomre, Alar. 1964. 'On the gravitational stability of a disk of stars.' *The Astrophysical Journal* 139:1217–1238.

Tripathi, Anjali, Sean M. Andrews, Tilman Birnstiel, and David J. Wilner. 2017. 'A millimeter Continuum Size-Luminosity Relationship for Protoplanetary Disks.' *The Astrophysical Journal* 845, no. 1 (August): 44.

Truelove, J. Kelly, Richard I. Klein, et al. 1997. 'The Jeans Condition: A New Constraint on Spatial Resolution in Simulations of Isothermal Self-gravitational Hydrodynamics.' *The Astrophysical Journall* 489, no. 2 (November): L179–L183.

Tscharnuter, W. 1975. 'On the Collapse of Rotating Protostars.' *Astronomy and Astrophysics* 39 (March): 207.

Tsukamoto, Yusuke, and Masahiro N. Machida. 2013. 'Formation and early evolution of circumstellar discs in turbulent molecular cloud cores.' *Monthly Notices of the Royal Astronomical Society* 428 (January): 1321–1334.

Tsuribe, Toru, and Kazuyuki Omukai. 2006. 'Dust-cooling-induced Fragmentation of Low-Metallicity Clouds.' *The Astrophysical Journall* 642, no. 1 (May): L61–L64.

Tung, Ngo-Duy, Leonardo Testi, et al. 2024. *Accuracy of ALMA estimates of young disk radii and masses. Predicted observations from numerical simulations,* January.

Tychoniec, Łukasz, Carlo F. Manara, et al. 2020. 'Dust masses of young disks: constraining the initial solid reservoir for planet formation.' *Astronomy and Astrophysics* 640 (August): A19.

Tychoniec, Łukasz, John J. Tobin, et al. 2018. 'The VLA Nascent Disk and Multiplicity Survey of Perseus Protostars (VANDAM). IV. Free-Free Emission from Protostars: Links to Infrared Properties, Outflow Tracers, and Protostellar Disk Masses.' *The Astrophysical Journals* 238, no. 2 (October): 19.

Valegard, P. -G., C. Ginski, et al. 2024. 'The SPHERE view of the Orion star-forming region' (March).

van Boekel, R., Th. Henning, et al. 2017. 'Three Radial Gaps in the Disk of TW Hydrae Imaged with SPHERE.' *ApJ* 837, no. 2 (March): 132.

van Terwisga, S. E., A. Hacar, and E. F. van Dishoeck. 2019. 'Disk masses in the Orion Molecular Cloud-2: distinguishing time and environment.' *Astronomy and Astrophysics* 628 (August): A85.

Von Neumann, J., and R. D. Richtmyer. 1950. 'A Method for the Numerical Calculation of Hydrodynamic Shocks.' *Journal of Applied Physics* 21 (March): 232–237.

Vorobyov, Eduard I., Vardan G. Elbakyan, et al. 2020. 'Accretion bursts in low-metallicity protostellar disks.' *Astronomy and Astrophysics* 641 (September): A72.

Vorobyov, Eduard I., D. N. C. Lin, and Manuel Guedel. 2015. 'The effect of external environment on the evolution of protostellar disks.' *Astronomy and Astrophysics* 573 (January): A5.

Walch, S., T. Naab, A. Whitworth, A. Burkert, and M. Gritschneder. 2010. 'Protostellar discs formed from turbulent cores.' *Monthly Notices of the Royal Astronomical Society* 402 (March): 2253–2263.

Weidenschilling, S. J. 1977a. 'Aerodynamics of solid bodies in the solar nebula.' *Monthly Notices of the Royal Astronomical Society* 180, no. 2 (September): 57–70.

———. 1977b. 'The Distribution of Mass in the Planetary System and Solar Nebula.' *Astrophysics and Space Science* 51, no. 1 (September): 153–158.

Weis, E. W. 1974. 'On the inclination of rotation axes in visual binaries.' *The Astrophysical Journal* 190 (June): 331–337.

Welsh, William F., Jerome A. Orosz, et al. 2012. 'Transiting circumbinary planets Kepler-34 b and Kepler-35 b.' Nature 481, no. 7382 (January): 475–479.

Whipple, F. L. 1972. *On certain aerodynamic processes for asteroids and comets.* January.

Whitehouse, Stuart C., and Matthew R. Bate. 2006. 'The thermodynamics of collapsing molecular cloud cores using smoothed particle hydrodynamics with radiative transfer.' *Monthly Notices of the Royal Astronomical Society* 367, no. 1 (March): 32–38.

Whitehouse, Stuart C., Matthew R. Bate, and Joe J. Monaghan. 2005. 'A faster algorithm for smoothed particle hydrodynamics with radiative transfer in the flux-limited diffusion approximation.' *Monthly Notices of the Royal Astronomical Society* 364, no. 4 (December): 1367–1377.

Whitworth, A. P. 1998. 'The Jeans instability in smoothed particle hydrodynamics.' *Monthly Notices of the Royal Astronomical Society* 296, no. 2 (May): 442–444.

Whitworth, A. P., S. J. Chapman, et al. 1995. 'Binary star formation: accretion-induced rotational fragmentation.' *Monthly Notices of the Royal Astronomical Society* 277 (November): 727–746.

Wilhelm, Martijn J. C., Simon Portegies Zwart, et al. 2023. 'Radiation shielding of protoplanetary discs in young star-forming regions.'

Williams, Jonathan P., and William M. J. Best. 2014. 'A Parametric Modeling Approach to Measuring the Gas Masses of Circumstellar Disks.' *The Astrophysical Journal* 788 (June): 59.

Wilson, Edwin B. 1927. 'Probable Inference, the Law of Succession, and Statistical Inference.' *J. Am. Stat. Assoc.* 22 (158): 209–212.

Wurster, James, Matthew R. Bate, and Daniel J. Price. 2019. 'There is no magnetic braking catastrophe: low-mass star cluster and protostellar disc formation with non-ideal magnetohydrodynamics.' *Monthly Notices of the Royal Astronomical Society* 489, no. 2 (October): 1719–1741.

Yasui, Chikako, Naoto Kobayashi, Masao Saito, and Natsuko Izumi. 2016. 'Low-metallicity Young Clusters in the Outer Galaxy. II. Sh 2-208.' AJ 151, no. 5 (May): 115.

Yasui, Chikako, Naoto Kobayashi, Masao Saito, Natsuko Izumi, and Warren Skidmore. 2021. 'Low-metallicity Young Clusters in the Outer Galaxy. III. Sh 2-127.' *The Astronomical Journal* 161, no. 3 (February): 139.

Yasui, Chikako, Naoto Kobayashi, Alan T. Tokunaga, Masao Saito, and Chihiro Tokoku. 2009. 'The Lifetime of Protoplanetary Disks in a Low-metallicity Environment.' *The Astrophysical Journal* 705, no. 1 (November): 54–63.

Yen, Hsi-Wei, Patrick M. Koch, et al. 2015. 'Observations of Infalling and Rotational Motions on a 1000 AU Scale around 17 Class 0 and 0/I Protostars: Hints of Disk Growth and Magnetic Braking?' *The Astrophysical Journal* 799, no. 2 (February): 193.

Yen, Hsi-Wei, Patrick M. Koch, et al. 2017. 'Signs of Early-stage Disk Growth Revealed with ALMA.' *ApJ* 834, no. 2 (January): 178.

Yen, Hsi-Wei, Shigehisa Takakuwa, Nagayoshi Ohashi, and Paul T. P. Ho. 2013. 'Unveiling the Evolutionary Sequence from Infalling Envelopes to Keplerian Disks around Low-mass Protostars.' *The Astrophysical Journal* 772, no. 1 (July): 22.

Yorke, Harold W., Peter Bodenheimer, and Gregory Laughlin. 1993. 'The Formation of Protostellar Disks. I. 1 M sub sun.' *The Astrophysical Journal* 411 (July): 274.

Youdin, Andrew N, and Jeremy Goodman. 2005. 'Streaming instabilities in protoplanetary disks.' *The Astrophysical Journal* 620 (1): 459.

Young, Alison K., Struan Stevenson, C. J. Nixon, and Ken Rice. 2023. 'On the conditions for warping and breaking protoplanetary discs.' *Monthly Notices of the Royal Astronomical Society* 525 (October): 2616–2631.

Zagaria, Francesco, Giovanni P. Rosotti, and Giuseppe Lodato. 2021. 'On dust evolution in planet-forming discs in binary systems - I. Theoretical and numerical modelling: radial drift is faster in binary discs.' *Monthly Notices of the Royal Astronomical Society* 504 (June): 2235–2252.

Zanazzi, J. J., and Dong Lai. 2018. 'Inclination evolution of protoplanetary discs around eccentric binaries.' *Monthly Notices of the Royal Astronomical Society* 473 (January): 603–615.

Zeipel, H. von. 1910. 'Sur l'application des séries de M. Lindstedt à l'étude du mouvement des comètes périodiques.' *Astronomische Nachrichten* 183 (March): 345.

Zhang, Shangjia, Zhaohuan Zhu, et al. 2018. 'The Disk Substructures at High Angular Resolution Project (DSHARP). VII. The Planet-Disk Interactions Interpretation.' *The Astrophysical Journal* 869 (December): L47.

Zrake, Jonathan, Christopher Tiede, Andrew MacFadyen, and Zoltán Haiman. 2021. 'Equilibrium Eccentricity of Accreting Binaries.' *The Astrophysical Journal* 909 (March): L13.

Zucconi, A., C. M. Walmsley, and D. Galli. 2001. 'The dust temperature distribution in prestellar cores.' *Astronomy and Astrophysics* 376 (September): 650–662.

Zúñiga-Fernández, S., J. Olofsson, et al. 2021. 'The HD 98800 quadruple pre-main sequence system: Towards full orbital characterisation using long-baseline infrared interferometry' [in en]. *Astronomy and Astrophysics* 655 (November): A15.